Title
Measuring and modeling the thermal conductivity of high temperature liquids

Permalink
https://escholarship.org/uc/item/7g0451vt

Author
Zhao, Andrew

Publication Date
2021

Peer reviewed|Thesis/dissertation

UNIVERSITY OF CALIFORNIA SAN DIEGO

MEASURING AND MODELING THE THERMAL CONDUCTIVITY OF HIGH TEMPERATURE LIQUIDS

A dissertation submitted in partial satisfaction of the
requirements for the degree Doctor of Philosophy

in

Materials Science and Engineering

by

Andrew Zigang Zhao

Committee in charge:

Professor Javier Garay, Chair
Professor Prabhakar Bandaru
Professor Nicholas Boechler
Professor Renkun Chen
Professor Shirley Meng

2021

The Dissertation of Andrew Zigang Zhao is approved, and it is acceptable in quality and form

for publication on microfilm and electronically.

University of California San Diego

2021

DEDICATION

To Ayla Ruhan Lim, my beloved niece.

EPIGRAPH

The practice of science was not itself a science; it was an art, to be passed from master to apprentice as the art of painting is passed or the skills and traditions of the law or of medicine are passed. You could not learn the law from books and classes alone. You could not learn medicine. No more could you learn science, because nothing in science ever quite fits; no experiment is ever final proof; everything is simplified and approximate.

– Richard Rhodes, *The Making of the Atomic Bomb*

TABLE OF CONTENTS

LIST OF FIGURES

LIST OF TABLES

ACKNOWLEDGEMENTS

The single most important person behind this dissertation, besides the author I suppose, is Professor Javier Garay. I'm endlessly grateful for his steadfast and patient support over the past five years as I dove deep into the oceanic cross currents of materials science, nanoscale heat transfer, clean energy, and liquids. He gave me the latitude to grow, foster my own ideas, and develop into an independent scientist. But he always shared a key theoretical insight, experimental trick, or calming wisdom whenever I needed it most. His joy from seeing new data and thinking about new ideas is a spark for scientific inquiry that was crucial for my research, and it will sustain the flames of future students for a long time to come – until he inevitably gets chosen to become the Dean of the School of Engineering or Chancellor of UC San Diego, unless, of course, he chooses to pursue his true passion, vacuum science and engineering.

I am standing on the gigantic shoulders of my mentors and teachers, who have offered me their time and deep expertise. Professor Prabhakar Bandaru has helped guide the Materials Science Program as the Chair for years, and he is the one that helped recruit me to UC San Diego years ago – though he might not remember our conversation since he meets with every prospective student, it is one of those tipping points in my life I think back to often, and I believe he helped manifest my present fortune. Professor Nicholas Boechler revitalized the Experimental Techniques lab class that I was a Teaching Assistant for, and it was an honor to work with him and be a part of revamping the curriculum for every aerospace, bio, chemical, and mechanical engineering undergrad on campus. Through Professor Boechler's immense osmotic pressure, I gained a deeper respect for careful experimentation and error propagation, a love of open source hardware and software, and a better understanding of what it takes to

create relatable and useful content for students. Professor Renkun Chen taught the most important class of my academic career – Nanoscale Heat Transfer. He laid the theoretical foundation for my understanding of heat and presented the cutting edge of the field. With Professor Chen's help, I began formulating the research questions that would guide me through my dissertation, and I had the privilege to collaborate with him on constructing a model for how heat conducts in liquids. Professor Shirley Meng is a force for clean energy and energy storage that I am indebted to for my broad perspective on energy and materials science. While teaching me how to examine what is happening at the nano-scale in energy materials with cutting edge synchrotron techniques, Professor Meng also inspired me to think bigger about the societal-scale impacts of my research, how it was influenced by history, and how it could initiate future excitations of the scientific field and beyond. Dr. Matt Wingert is the lead thermal engineer for PsiQuantum's photonic quantum computer, but while he was a postdoc in our lab, I was the luckiest PhD student in the world to have learned the art and science of doing research with him for three years. Matt took a stab at every question I threw at him with a surgeon's precision, he pointed out all the mistakes in my first drafts with kindness, and he took my crazy ideas seriously, which is the single most important gift for a young scientist.

My lab mates gave me a boost every day, providing me scientific sounding boards for what experiments to run next, sharing data analysis and modeling know-how, and teaching me the devlish details in their materials processing procedures. This dissertation would never have seen the light of day without our daily treks to acquire Diet Mountain Dew and boba. Wilson Xingzhong Wu joined AMPS lab with me from the beginning, and it was a pleasure to share the journey with him. I inherited the AMPS lab will from Kyle Chan, Matthew Duarte, Darren Dewitt, Meir Shachar, Gottlieb Uahengo, and Chad Warren. I did my best to contribute to our

culture of curious materials science misfits that love Korean barbeque, and I am now passing the baton to Wenbo Zhou, Ross Turner, Otis Statham, and Everbrook Zhou to surpass us all. Dr. Yasuhiro Kodera was always there to provide experimental support and the perfect analogy to explain a complex topic or philosophy – if I was lucky it was a food metaphor, which is my preferred way of consuming knowledge.

The undergrads I've mentored throughout the years have helped me develop as a scientist and leader. Whenever they didn't understand an idea I was presenting, I had to sharpen my thinking and explanation. Whenever they didn't know what to do next or how to explain their research to their friends or family, I had to clarify the vision and direction of what we were working towards. They forced me to distill my thoughts down to their essence, and I'm grateful for their budding minds of inquiry that made me admit "I don't know" more times than I can recall. The future is in the capable hands of Gwendolyn Wang, Genggeng Zhou, Ernesto Suarez, Kristin Hartsfield, Lwin Dumont, Jordan Wong, Amanda Kerlee, and Jolie Tran.

My EBU2 hallmates did research in a wide variety of topics, some vastly different from my own, but running into them in the hall and discussing the trials and tribulations of our experiments was a constant fountain of support and inspiration. Thank you, Audrey Velasco-Hogan, Rachel Flanagan, Keisuke Matsushita, Maritza Sanchez, Isaac Cabrera, Sunmi Shin, Jian Zeng, Ka Man Chung, Tianshi Feng, and Sarath Adapa.

Friendship was the sustaining force for my soul throughout it all. Having something to look forward to is what got me through the long days, long years, and certain failure that comes with doing research. I always had amazing meals, ice cold beverages, uncontrollable laughter, attentive ears and open hearts, and exciting travel plans to look forward to. Here's to the friends that would always carve out glacial valleys of time and space for me: Andrew Mitchell, Aaron

Oro, Alan Propp, Aly Cash, Anna Olson, Brandan La, Daf Szafer, Emily Bohl, Gaby Grieg, Jeff Sarsona, Katie Bick, Kristin Chesnutt Oro, Kyle Machicado, Lisa Su, Maki Tazawa, Margaret Tomaszczuk, Minna Xiao, Nicole Gurtler, Steven Losorelli, and Varun Datta. And here's to the friends that made San Diego feel like home: Cong Dinh, Quynh Nguyen, Olivia Dippo, Will McCarthy, Anthony Thomas, John Skubic, Lysha Matsumoto, Andrew Parlier, Nojan Sheybani, Austin Doughty, Sophia Xiao, Philip Belzeski, and Nancy Turtletaub. And thank you to anyone else who I shared a meal, beverage, or laugh with over the past five years.

As I attempt to pave my own path, I look down and realize the shoes on my feet, the tools in my hands, and the drive in my heart were carefully crafted by my family to propel me ever-forward. My older sister Holly Zhao watched over me as I grew up, and she is the sole reason that I'm capable of boiling water and socially competent enough to have any friends. Now, her and Jason Lim have built a home together in the Bay Area for Ayla, and they made sure to keep a room open for me, the family's other baby. Holly and Jason have always been my role models for how to traverse life's milestones with humor, passion, and care. My parents, Hong-Hong Zhu and Yusheng Zhao, will always be my heroes. They came to America with $50, a handful of English, and an iron grip of will-power. My scientific career descends from my dad making it to America on an academic scholarship to Berkeley and raising me in Los Alamos. My love of sharing food with friends was fostered by my mom cooking dinner every night and making sure Holly and I had enough to eat. My love for reading fell into my lap from the overflowing bookshelves that lined our home. My parents drove the same car and wore the same clothes for over 20 years, but they spared no expense for my books and education. When I make a mistake, I like to joke that nature vs. nurture, either way it's my parents' fault. But the

real implication is that every success and joy in my life can be traced back to my parents' love and sacrifice. I owe everything to them. I hope I make them proud.

And last, thank you to my collaborators, who have given me permission to use the following publications in my dissertation:

Chapter 1 and 5 are currently being prepared for submission as **Zhao, A. Z.** & Garay, J. E. High temperature liquid thermal conductivity: a review of measurement techniques, theoretical understanding, and energy applications (*In Preparation*). For this work, I performed the literature review and wrote the paper.

Chapter 2 is a reprint of **Zhao, A. Z.,** Wingert, M. C., Chen, R., & Garay, J. E. (2021). Phonon gas model for thermal conductivity of dense, strongly interacting liquids. *Journal of Applied Physics*, *129*(23), 235101. For this publication, I formulated the analytical model, performed the calculations, and wrote the paper.

Chapter 3 is a reprint of **Zhao, A. Z.,** Wingert, M. C., & Garay, J. E. (2020). Frequency-domain hot-wire measurements of molten nitrate salt thermal conductivity. *Journal of Chemical & Engineering Data*, *66*(1), 262-270. For this publication, I did the experimental work and wrote the paper.

Chapter 4 is a reprint of **Zhao, A. Z.,** Wingert, M. C., Levine, G., Obrey, S., & Garay, J. E. Evaluation of [emim]$^+$ and [bmim]$^+$ ionic liquid thermal conductivity models with frequency-domain hot-wire measurements (*In Preparation*). For this publication, I did the experimental work and wrote the paper.

VITA

2016   Bachelor of Science, Stanford University

2017   Master of Science, University of California San Diego

2021   Doctor of Philosophy, University of California San Diego

PUBLICATIONS

1. Wingert, M. C., **Zhao, A. Z.,** Kodera, Y., Obrey, S. J., & Garay, J. E. (2020). Frequency-domain hot-wire sensor and 3D model for thermal conductivity measurements of reactive and corrosive materials at high temperatures. *Review of Scientific Instruments*, *91*(5), 054904.

2. **Zhao, A. Z.,** Wingert, M. C., & Garay, J. E. (2020). Frequency-domain hot-wire measurements of molten nitrate salt thermal conductivity. *Journal of Chemical & Engineering Data*, *66*(1), 262-270.

3. **Zhao, A. Z.,** Wingert, M. C., Chen, R., & Garay, J. E. (2021). Phonon gas model for thermal conductivity of dense, strongly interacting liquids. *Journal of Applied Physics*, *129*(23), 235101.

4. **Zhao, A. Z.,** Wingert, M. C., Levine, G., Obrey, S.J., & Garay, J. E. Evaluation of [emim]$^+$ and [bmim]$^+$ ionic liquid thermal conductivity models with frequency-domain hot-wire measurements, (To be submitted).

5. **Zhao, A. Z.** & Garay, J. E. High temperature liquid thermal conductivity: a review of measurement techniques, theoretical understanding, and energy applications. (To be submitted).

ABSTRACT OF THE DISSERTATION

MEASURING AND MODELING THE
THERMAL CONDUCTIVITY OF HIGH
TEMPERATURE LIQUIDS

by

Andrew Zigang Zhao

Doctor of Philosophy in Materials Science and Engineering

University of California San Diego, 2021

Professor Javier Garay, Chair

The thermal conductivity of liquids is an integral part of the thermal design for future clean energy sources that can provide higher temperature heat and higher thermodynamic efficiencies. Molten salts and molten metals are leading candidates for heat-transfer fluids in next-generation concentrated solar power and nuclear plants, which can provide both clean electricity and industrial heat. However, the thermal conductivity of liquids at high temperature is not well understood since there is no well-established model for liquid thermal conductivity and because errors from convection, radiation, and

corrosion have created a large spread in experimental data at high temperatures. In **Chapter 1,** I review the various steady-state, time-domain, and frequency-domain experimental techniques used to measure liquid thermal conductivity at high temperature, as well as the various modified-gas and quasi-crystalline models of liquid thermal conductivity – rather than providing exhaustive lists of all previous methods, I provide frameworks for understanding the diverse approaches for measuring and modeling liquid thermal conductivity. In **Chapter 2**, I formulate a new phonon gas model for liquid thermal conductivity, which can accurately calculate the thermal conductivity of dense, strongly-interacting liquids like water and molten nitrate salts. The model is able to match reliable experimental results, explain the mechanism of heat conduction in certain liquids, and encapsulate previous quasi-crystalline models that took slightly different forms depending on which liquids they were formulated for. In **Chapter 3**, I present a newly developed frequency-domain hot-wire measurement technique – designed specifically to measure the thermal conductivity of high temperature liquids and minimize errors from convection, radiation, and corrosion. Using frequency-domain measurements, I show that the thermal conductivity of molten nitrate salts is ~15% higher than the current reference value. In **Chapter 4**, I use frequency-domain measurements and various models to better understand ionic liquid thermal conductivity, which have elements of both molten salts and long molecular chained liquids. And in **Chapter 5**, I provide a brief outlook on future research directions for enhancing the effective thermal conductivity of high-temperature liquids for clean energy applications

Chapter 1. High temperature liquid thermal conductivity: a review of measurement techniques, theoretical understanding, and energy applications

Clean energy sources must supplant the fossil fuels that have driven electricity generation and ignited industrial heat for the past century. Solar thermal energy and advanced nuclear reactors are clean energy sources that can provide electricity to the grid and high quality heat for industrial processes.[1] They are being designed to provide heat at temperatures above 600°C to unlock the supercritical CO_2 Brayton cycle that is $1/10^{th}$ the cost and $1/10^{th}$ the volume of the conventional steam Rankine cycle[2], as well as provide the high temperatures required for industrial chemical reactions and manufacturing processes[3]. Operating at temperatures above 600°C will require heat transfer fluids that are stable at high temperature with low vapor pressure.

Molten salts and molten metals are prime heat transfer fluids for next-generation, high-temperature energy applications, and their thermal conductivity is critical for designing and modeling systems that will use them to transport and store heat. However, it is difficult to accurately measure molten salt and molten metal thermal conductivity due to errors from convection, radiation, and corrosion that become magnified at higher temperatures; there is a large spread in experimental values for molten salts (275% spread in sodium chloride data) and metals (70% spread in molten iron data) – see **Figure 1.2**. Such widely varying experimental results and opposite temperature dependent trends in liquid thermal conductivity data have led to general confusion when trying to interpret and explain experimental measurements.

In addition, models of liquid thermal conductivity are not as well understood as gas or solid thermal conductivity. There are numerous models for explaining how heat conducts in liquids, ranging from modified kinetic gas to quasi-crystalline models that result in analytical equations that can calculate liquid thermal conductivity. But none are successful in capturing the wide ranging behavior of liquids with different intermolecular interactions[4]. Due to the shortcomings of analytical models for liquids, molecular dynamics has been used extensively to model liquids and their thermal conductivity.

In this chapter, we will first review high temperature experimental data of liquid thermal conductivity and discuss the various measurement techniques – steady state, time domain, and frequency domain – used to acquire liquid thermal conductivity data and examine how they have been modified to operate and reduce errors at high temperature. Then, we will compare the success of analytical and computational models in matching the best available experimental thermal conductivity data. Last, we provide an outlook of current trends and future research areas in high temperature liquids for next generation energy applications: engineering liquids with nanofluids to increase their heat capacity and thermal conductivity; materials and mechanical engineering challenges in harnessing high temperature liquids for energy storage and transport; and open experimental and theoretical problems in liquid heat transport. The 1964 state of the art in liquid thermal conductivity measurements and models was very well reviewed by McLaughlin[5]; here, we aim to highlight recent developments in high temperature liquid measurements and liquid thermal conductivity modeling, and put them in context with previous work.

1.1 Experimental techniques for measuring liquid thermal conductivity

Accurate thermal conductivity data for high temperature fluids is critical for designing next-generation energy systems and for testing liquid thermal conductivity theories. **Figure 1.1a** shows reference values for absolute liquid thermal conductivity drawn as lines – there is great diversity in liquid thermal conductivity that spans 4 orders of magnitude from 0.01 $Wm^{-1}K^{-1}$ to 100 $Wm^{-1}K^{-1}$ between 50 K to 2000 K. The general behavior of liquids is summarized by normalizing thermal conductivity by the highest value in the liquid's temperature range (from the melting point to boiling point/the maximum temperature measured) in **Figure 1.2**. Thermal conductivity drops as temperature increases for many liquids (e.g. Ar, CH_4, N_2, and molten salts); but the trend is the opposite for many molten metals and water, which increase in thermal conductivity as temperature increases.
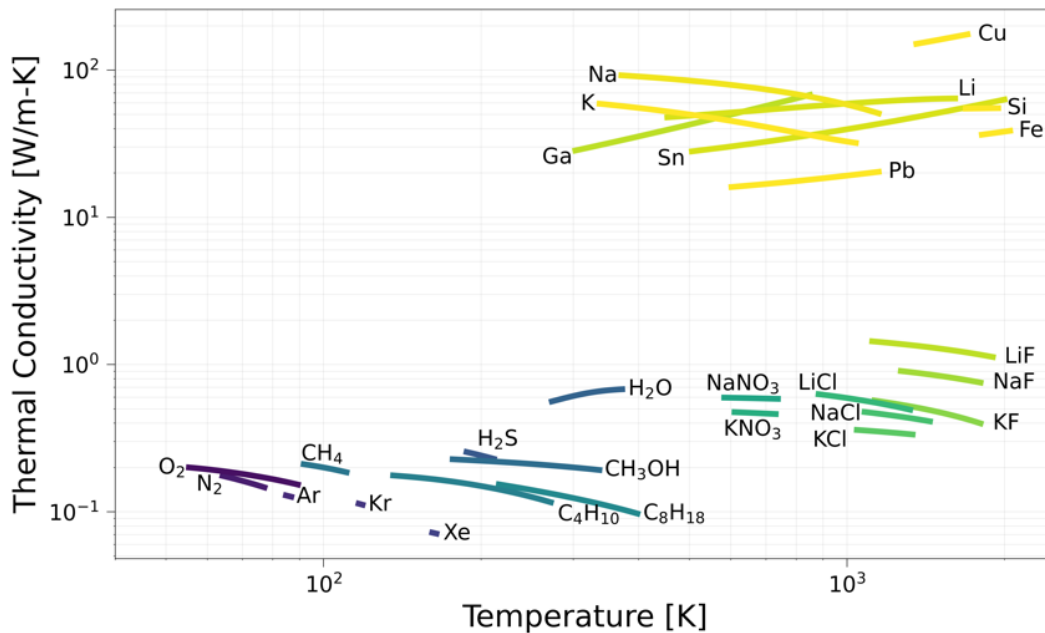
Figure 1.1. Liquid thermal conductivity of various liquids. Reference values are shown for O_2, N_2, Ar, Kr, Xe, CH_4, C_4H_{10}, C_8H_{18}, CH_3OH, H_2S, and H_2O from NIST Fluids database[6]; $NaNO_3$ and KNO_3 from Zhao et al.[7]; LiCl, NaCl, KCl from Chliatzou et al.[8]; LiF, NaF, and KF from Gheribi et al.[9]; Li, Na, and K from Agazhanov et al.[10]; Cu, Ga, Fe, Pb, and Sn from Assael et al.[11]; and Si from Assael et al.[12]
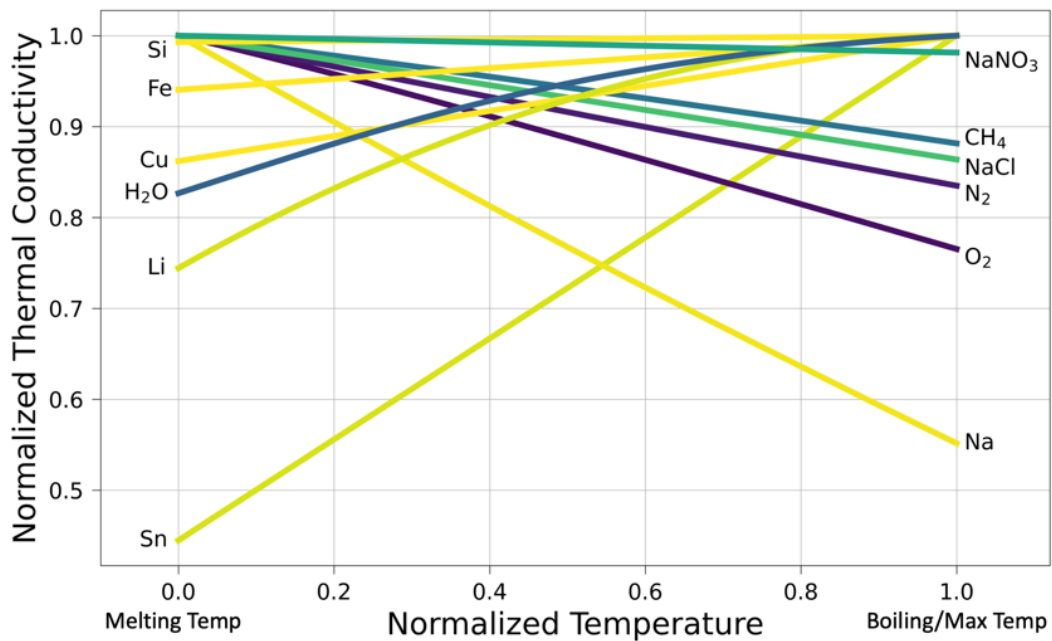
Figure 1.2. Normalized thermal conductivity of liquids with various interaction energies from their melting point to their boiling point or highest available temperature.

The lines drawn by the reference values in **Figure 1.1 and 1.2**, however, hide variations between liquid thermal conductivity measurements that can significantly exceed 25% from the lowest measured thermal conductivity value, shown in **Figure 1.3** – the percent spread is calculated as the difference between the highest and lowest measured thermal conductivity, divided by the lowest. If the heat transfer fluid's thermal conductivity is 25% lower than reported, the ideal area of the heat exchanger could be 16% larger with ramifications on the capital and operational cost of the exchanger.[13] In **Figure 1.3,** triangles are data from steady-state measurements, circles are from time-domain techniques, and diamonds are from frequency-domain measurements; solid lines show reference values used to draw Figure 1; and the lighter the color, the earlier the measurement was performed.
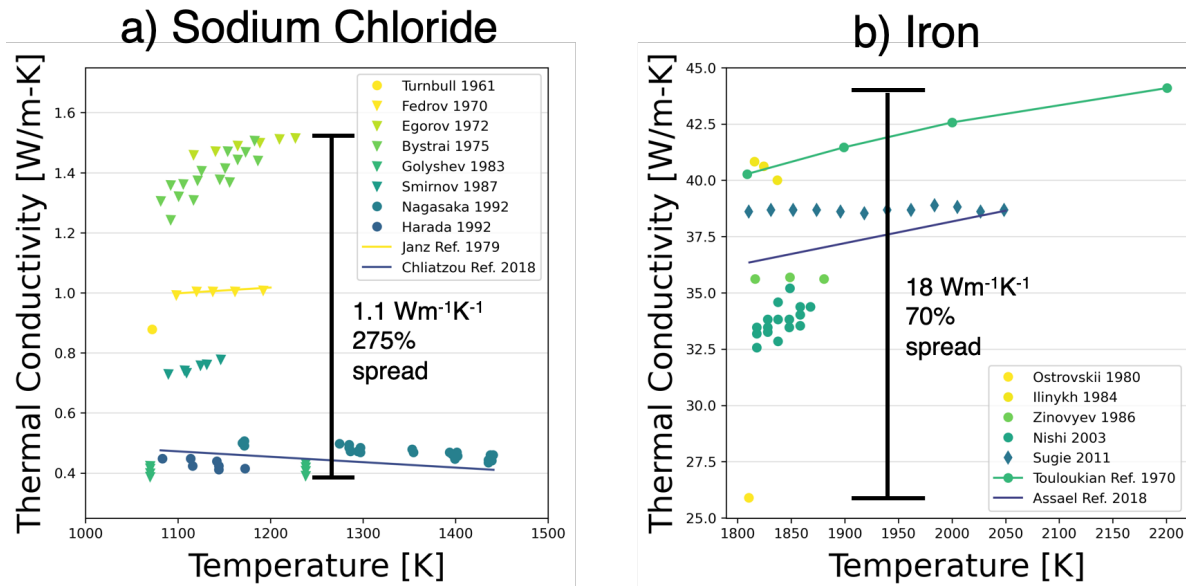
Figure 1.3. Spread in high temperature thermal conductivity measurements of a) molten sodium chloride adapted from Chliatzou et al.[8], and b) molten iron adapted from Assael et al.[11]

Further, early steady-state thermal conductivity experiments for the Molten Salt Reactor Experiment at Oak Ridge National Lab had significant errors from convection, and the measured thermal conductivity was 4 times higher than the reference value currently used – these experimental errors led to a significantly lower heat flux from the reactor than expected, which led to the incorrect conclusion that a thermally insulating film from fluoride corrosion was formed on the heat exchanger[14]. Fluoride corrosion studies in the following years found no films on metal surfaces, and the errors in thermal conductivity measurements were the root of the problem.

When there is such a large spread in experimental data, the natural questions arise – which measurements are the most accurate and what is the true thermal conductivity of these liquids? To get a better handle of the extensive experimental data, we briefly review the different measurement techniques, their underlying assumptions and equations, and strategies to

minimize error from corrosion, convection, and radiation that become more significant as temperature increases.

Liquid thermal conductivity measurement techniques can be grouped into 3 categories shown in **Table 1.1**: steady-state, time-domain, and frequency-domain. All measurement techniques aim to find a liquid's thermal conductivity, $\kappa\ [Wm^{-1}K^{-1}]$, which determines the conductive heat flux through a liquid, $\dot{q}\ [Wm^{-2}]$, in response to a temperature gradient, $\nabla T\ [Km^{-1}]$:

$$\dot{q} = -\kappa \nabla T \qquad (1.1)$$

This is Fourier's law, which lays the foundation for the study of heat transfer, and when combined with the conservation of energy leads to the heat equation for stationary liquids, assuming a stationary liquid and constant pressure:

$$\frac{dT}{dt} = \frac{\kappa \nabla^2 T}{\rho C_P} \qquad (1.2)$$

where $\frac{dT}{dt}$ is the change in temperature from a change in time, ρ is the density, and C_P is the specific heat at constant pressure.

Table 1.1. Comparison of high-temperature liquid thermal conductivity measurement techniques.

Category	Technique	Strengths	Challenges
Steady State	Parallel Plate[15–17] Concentric Cylinder[18,19]	Simple way to implement and understand Fourier's Law	- Long measurement time - Large gap sizes lead to convection
Time Domain	Transient Hot Wire[20,21]	Standard measurement technique for liquids	- Fragile wire - Data truncation needed to remove errors from convection
	Laser Flash[22,23]	High temperature sample not in contact with heating source or detector	- Expensive laser heater and temperature detector - Nonuniform liquid sample thickness in holder - Thick samples lead to convection
Frequency Domain	3ω Hot Wire[7,24]	- Probed volume less than $1\,\mu L$ to minimize convection - No data truncation required	- Fragile wire - Long measurement times
	Optical Techniques: - Modulated Photothermal Radiometry[25,26] - Electromagnetic Levitation[27,28]	- Non-contact measurement to heat and probe sample - Small sample volume probed to minimize convection	- Expensive laser heater and temperature detector - Long measurement times

Table 1.1 provides a list of common measurement techniques for high temperature liquid thermal conductivity based on our experience in reviewing the literature. It is not an exhaustive list of all previous techniques. There are, however, common challenges faced by

every high temperature thermal conductivity measurement technique that are the prime suspects for experimental error that has led to the spread in experimental data in **Figure 1.3**: convection, radiation, and corrosion. Recently, de Castro & Lourenço[29] also reviewed molten salt thermal conductivity measurement techniques and what adjustments need to be made at high temperature – in this review we want to highlight the recent developments in frequency-domain measurements.

The purity of the samples is also a significant source of error; purification techniques for molten salts and metals, as well as methods of measuring their purity, deserve their own review. There has been a recent push to report purity level since the manufacturer's purity level usually does not match measurements of purity upon arrival. Reference correlations of high temperature liquid thermal conductivity, which compile and sift through all previous measurements, exclude experiments from the primary data set used to draw the reference values that do not report their sample's purity. Further, removing water impurities in chloride salts has been shown to prevent hydrochloric acid formation that is a major source of corrosion[30]. And pure samples are essential to compare results across different data sets – there are ongoing round robin tests to measure the thermophysical properties of molten FLiNaK and NaCl-KCl salts, using the same source of well-purified and characterized salt samples, from the Molten Salt Thermal Properties Working Group with participation from national labs, universities, and companies that work with molten salts.

1.2 Experimental error at high temperature

Natural convection arises from a temperature gradient within a liquid that leads to a density gradient and a buoyancy force that drives bulk liquid motion. This hot liquid movement

can obscure a liquid's inherent thermal conductivity. Convection is limited in steady-state measurements by reducing the gap size and temperature difference between the heat source and heat sink; in time-domain measurements, once heat is applied to the sample, the measurement time window is truncated to remove the onset of convection; in frequency-domain measurements, the frequency of the modulated heat source keeps the thermal penetration depth within the no-slip boundary to remove convection. The Rayleigh number, Ra, can be used to determine what experimental conditions can lead to the onset of natural convection:

$$Ra = Gr \times Pr = \frac{d^3 g \alpha \Delta T \rho^2}{\eta^2} \times \frac{\eta C_P}{\kappa} \tag{1.3}$$

Where Gr is the Grashof number, Pr is the Prandtl number, d is the thickness of the liquid layer, g is the acceleration due to gravity, α is the liquid's thermal expansion coefficient, ΔT is the temperature difference across the liquid, ρ is the liquid density, η is the liquid viscosity, C_P is the liquid's specific heat, and κ is the liquid thermal conductivity. Rayleigh numbers below 1000 are demonstrated to be the conduction regime where conductive heat transfer is the predominant heat transfer mechanism – the governing equations of conduction and natural convection are derived and discussed by Kakaç & Yener[31]. Specific strategies to minimize convection will be discussed in the following sections.

Blackbody radiation leads to heat transfer between any objects at different temperatures according to

$$\dot{q}_{rad} = A_{surface} \sigma_{SB} \varepsilon (T_1^4 - T_2^4) \tag{1.4}$$

where $A_{surface}$ is the surface area in contact with the liquid, σ_{SB} is the Stefan-Boltzmann constant, T_1 and T_2 are the temperature of the hot and cold side of the system, and ε is the emissivity of the hot side solid. Increasing the temperature difference and exposed surface area

increases radiation. Generally, to minimize error from radiation, the emissivity of the solid should be low and temperature differences between surfaces should be small (same for minimizing convection). It is helpful to be conservative and assume blackbody radiation ($\varepsilon = 1$) to check the maximal radiative heat loss. To quantify the error from radiation, the ratio of heat fluxes due to radiation and conduction, $\frac{\dot{q}_{rad}}{\dot{q}_{cond}}$, can be calculated and it should be kept below 0.01 to ensure radiation is negligible. Radiation can be accounted for in the thermal model for any measurement technique, but it is more difficult to solve the differential equation analytically – so a check is usually done to ensure the radiative heat flux is less than 1% of conductive heat flux.

Corrosion is magnified at high temperature and can damage the sensors, degrade the sample holder, and alter the composition of the liquid sample. The ramifications of corrosion on the sample's thermal conductivity is not as easy to quantify as convection and radiation. For measurement techniques that use sensors immersed in the liquid sample, the main strategy is to coat the sensor with a robust ceramic film – borides, carbides, nitrides, and oxides can be chosen to be more chemically stable in the molten sample or match the thermal expansion coefficient of the sensor to prevent cracking upon heating and cooling cycles. Coatings may still react with the molten sample, but the kinetics can be slow enough so that the sensor can survive long enough to perform the measurement without significant degradation. The thickness in the coating has to be included in the thermal model along with the uncertainty in thickness due to potential corrosion – measuring the change in coating thickness before and after a measurement will show how stable the coating is in a sample, and also provides the error in coating thickness to propagate. It takes significant work to develop a proper coating to survive in molten samples and perform sensitive thermal conductivity measurements, so there have been several non-

contact techniques developed to use laser heating and infrared detectors/pyrometers to probe the temperature response of the molten sample without being in contact with the corrosive sample. The sample holder in these 'non-contact' measurements, however, are still in contact with the liquid, and they must be properly chosen so that the liquid properly wets the surface to form a uniform liquid layer, without balling up or wicking up the walls of the holder.

Now, we provide a brief overview of how the most popular steady-state, time-domain, and frequency-domain techniques in **Table 1.1** measure thermal conductivity of high temperature liquids, as well as their basic approach to minimizing errors from convection, radiation, and corrosion.

1.3 Steady-state measurements

Steady state measurements of thermal conductivity are relatively straightforward to understand and implement (see **Figure 1.4**). A known heat flux, $\dot{q}$, is applied to a liquid with a known thickness, d, until there is until a steady-state temperature difference, ΔT, is reached across the liquid sample, between the heater and the heat sink. For steady state measurements, **Equation 1.2** is simplified to

$$\kappa \nabla^2 T = 0 \qquad (1.5)$$

Solving for the liquid thermal conductivity results in different solutions depending on the liquid sample geometry. For a liquid sandwiched between parallel plates with a surface area of A, a heat flux is applied onto the top plate, diffusing heat through the liquid, and ultimately increasing the temperature of the back plate, resulting in a temperature difference between the top and bottom plate, ΔT. Thus, the liquid's thermal conductivity can be found using

$$\kappa = \frac{\dot{q} \cdot d}{A \cdot \Delta T} \qquad (1.6)$$

For further reading, Le Neindre et al.[15] provide in depth experimental details for how to build a steady state parallel plate measurement system, Wang et al.[16] review how the parallel plate method has been used to measure nanofluids, Santini et al.[17] describe their high temperature parallel plate setup to measure molten salts, and Cooke[32] reports the development of a variable gap measurement setup for molten fluorides at Oak Ridge National Laboratory.

The steady state concentric cylinder method (also referred to as the coaxial cylinder method), is more common than the steady state parallel plate method to measure liquid thermal conductivity. A liquid is loaded within the gap between two cylinders, and a heat flux is applied along the length of the inner cylinder, l, with an inner radius of r_1 to conduct heat through the liquid sample. After the temperature of the system stabilizes, the steady state temperature difference is measured between the inner cylinder and the outer cylinder with radius r_2, and the thermal conductivity of the liquid is given by

$$\kappa = \frac{\dot{q} \cdot \ln(r_2/r_1)}{2\pi l \Delta T} \qquad (1.7)$$

Le Neindre et al.[15], again, provide great experimental details for how to build a steady state concentric cylinder measurement system; Tufeu et al.[19] report their concentric cylinder setup and method for molten salts; and Sklyarchuk & Plevachuk[33] show their concentric cylinder setup for molten metals and semiconductors.

a) Parallel Plates

$$fluid\ thickness = d \qquad surface\ area = A$$

$$\kappa = \frac{\dot{q} \cdot d}{A \cdot \Delta T}$$

b) Concentric Cylinders

$$length\ of\ cylinder = l$$

$$\kappa = \frac{\dot{q} \cdot \ln(r_2/r_1)}{2\pi l \Delta T}$$
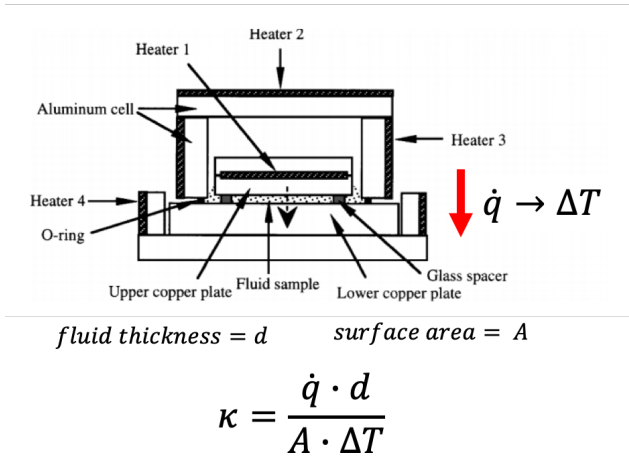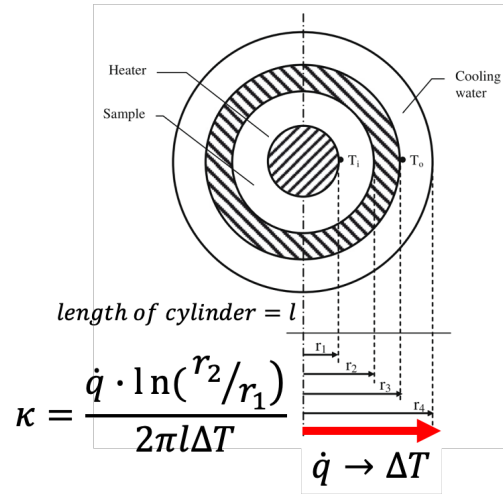
Figure 1.4. a) Schematic of steady-state parallel plates adapted from Wang et al.[16] and **b)** concentric cylinders adapted from Kurt & Kayfeci[34].

Despite the straightforward theory behind steady state measurements, the data varies widely between measurements and does not match results from more reliable and accurate measurement techniques. Zhao et al.[35] and Chliatzou et al.[8] discuss the potential sources of error in steady state measurements: natural convection within the liquid and radiation losses that lead to systematic errors for many early steady state measurements. To minimize errors due to convection in steady-state measurements, a general rule of thumb is to keep the gap's distance, where the fluid sample is encased, below 200 microns to minimize the temperature and density gradient in the liquid and suppress natural convection. However, this small 200-micron distance in the gap size, as well as how parallel the plates and concentric cylinders are aligned, are other potential sources for error to propagate to the measured thermal conductivity. The standard checks must be made to ensure convection is negligible: McLaughlin[5] provides a discussion of keeping the Rayleigh number below 1000 in steady-state concentric cylinder measurements to

prevent the onset of convection, and heat flux from radiation should be shown to be less than 1% compared to conductive heat flux for any steady-state measurement.

1.4 Time domain measurements

1.4 a) Transient hot-wire

Transient hot-wire provides a more reliable technique to measure thermal conductivity than steady-state setups, and it has become the standard liquid thermal conductivity measurement technique. While the fundamental concept of applying a heat flux and measuring the temperature response of the material is the same, the transient hot wire test takes a significantly shorter time to complete than a steady state measurement. A thin metallic wire, usually platinum, is used as a heater and as a temperature sensor. Direct current is applied to the platinum wire, which heats the wire and the surrounding fluid. The temperature versus time data is measured and fit to a thermal model, which describes the time dependent temperature rise surrounding the hot-wire sensor. The thermal model is a solution to **Equation 1.2**, given the initial and boundary conditions of a hot-wire, and provides the temperature as a function of radial distance and time

$$T(r,t) = \frac{-\dot{q}/l}{4\pi\kappa}\left\{Ei\left(\frac{-r^2\rho C_P}{4\kappa}\right)\right\} \tag{1.8}$$

where $\dot{q}/l$ is the heat conducted into the liquid sample from the length of the wire, and $Ei(-x)$ is the exponential integral that can be Taylor expanded as

$$T(r,t) = \frac{-\dot{q}/l}{4\pi\kappa}\left\{lnt + ln\frac{4\kappa}{r\rho C_P\gamma} + \frac{r^2\rho C_P}{4\kappa} + \cdots\right\} \tag{1.9}$$

where γ is Euler's constant. Finally, using the measured transient temperature rise will provide the liquid's thermal conductivity:

$$T(r, t_2) - T(r, t_1) \approx \frac{\dot{q}/l}{4\pi\kappa} \ln\frac{t_2}{t_1} \tag{10a}$$

$$\kappa = \frac{\dot{q}/l}{4\pi} \frac{dT}{d\ln t} \tag{10b}$$
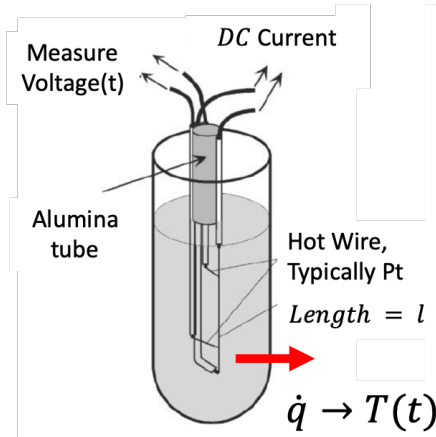
a) Transient Hot-Wire   b) H$_2$O Data and Model Fit
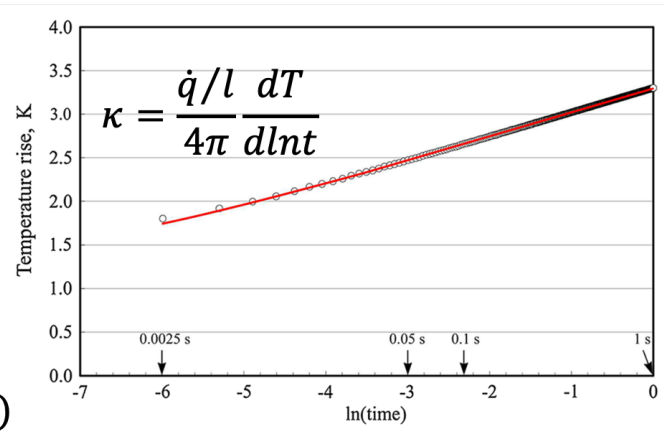
Figure 1.5. a) Schematic of transient hot-wire test setup adapted from Yamasue et al.[36] and b) experimental data and model fit of transient hot-wire measurement from Antoniadis et al.[37] in water.

To deal with high temperature corrosive and conductive environments, various coating strategies have been implemented to protect the sensor and prevent current leakage into conductive molten salt and metal samples. Nagasaka & Nagashima[38] first provided a method for coating the platinum wire with polyester to measure sodium chloride solutions up to 150°C and updated **Equation 1.8** to account for the new coating layer. To provide a high temperature coating for molten salt and metal measurements, tantalum-oxide has been deposited on the hot-wire sensor electrochemically[39], silicon-oxide deposited by dipping the sensor in a silica slurry and sintering[40], glass capillaries filled with liquid mercury probes[41], amongst many thin film coating techniques.

Errors from convection are still present in transient hot-wire, but they are accounted for in a more complex thermal model and by only using data before the onset of convection. Removing other errors from transient hot-wire measurements, such as end effects in the wire and radiation, are discussed in detail by Wakeham et al.[21] But still, transient hot wire measurement requires only fitting a small window in time of experimental data to prevent probing the heat capacity of the wire at very short times and natural convection and the sample's environment (sample holder, heating element, etc.) at long times – choosing the experimental window will affect the measured thermal conductivity[42].

Related time-domain techniques to transient hot-wire include the transient plane (aka hot-disc) and temperature wave methods. The transient plane method uses a resistive heating element in the shape of a plate or disc, made from a metal foil or a deposited thin film, which also acts as a temperature sensor. Similar to transient hot-wire, the hot plane heats the liquid sample and measures the temperature response versus time and finds the thermal conductivity of the liquid using a different thermal model for the different geometry.[43] The temperature wave technique uses a heat pulse at the center of a sample holder, and a temperature sensor at a set distance away from the heat source measures the time between the pulse and the sensor to find thermal conductivity[11].

1.4 b) Laser flash

The laser flash method utilizes a short high-intensity pulse of energy, usually from a laser or flash lamp, to heat a liquid sample, sandwiched in a container between two transducer surfaces with well-defined geometry, light absorption, and emissivity. After a known heat flux hits the first transducer, heat transfers through the liquid sample, and the time domain

temperature response, on the back side of the liquid cell, is measured using an infrared detector, pyranometer, or thermocouple.[44] Tada et al.[22,45] provide the details for laser flash's initial and boundary conditions, and solve **Equation 1.2** to provide temperature of each layer in the liquid cell (shown in **Figure 1.6**) as a function of time:

$$\frac{T(x,t)}{T_0} = \exp(h^2 t)\, erfc(ht^{\frac{1}{2}}) \tag{1.11a}$$

$$h = \frac{(\kappa_2 \rho_2 C_{P,2})^{1/2}}{\rho_1 C_{P,1} x} + \frac{(\kappa_3 \rho_3 C_{P,3})^{1/2}}{\rho_1 C_{P,1} x} \tag{1.11b}$$

There is a clear advantage for the heating source and the infrared detector to not be in physical contact with the high temperature, potentially corrosive and reactive liquid, whereas suspended hot-wire probes must be built to prevent current leakage and survive extreme conditions. The time to run a laser flash measurement is also comparable to the transient hot wire technique, with a flash shot and measurement occurring in less than a second (after the temperature of the system stabilizes), far shorter than steady state measurements.

The main drawback to the laser flash method, while short in duration, is that liquid sample are usually too thick to minimize convection. The liquid sample holders for laser flash usually contain a disc/film of liquid more than ~1mm thick, whereas steady-state and transient hot-wire measurements keep the probed liquid thickness below ~0.2 mm to suppress convection in the liquid. The error from convection influences the measured thermal conductivity of molten salts rather than molten metals – natural convection in a molten metal will not significantly change the effective thermal conductivity since the intrinsic electron dominated thermal conductivity is so high, but since the thermal conductivity of molten salts are orders of magnitude lower, natural convection can be comparable to conduction.

Adjustments to the thermal model and **Equation 1.11** also have to be made to deal with heat transfer from radiation that will affect the effective thermal conductivity, which is discussed by Srinivasan et al.[23]

Another practical difficultly in laser flash measurements, is to keep a uniform transducer layer and a uniform liquid throughout the high temperature measurements. Different liquids will wet the sample holder/transducer materials differently, and they may ball up or wick up the sides of the sample holder depending on the surface energy – many molten salts and molten metals bead up on graphite, so require platinum holders. There are also difficulties with evaporation changing the liquid thickness during the measurement – molten chlorides seem to have this issue more than molten nitrates, despite their strong ionic interaction energy. Experimental details for laser flash measurements of high temperature molten metals are discussed by Nishi et al.[46] and Agazhanov et al.[10]
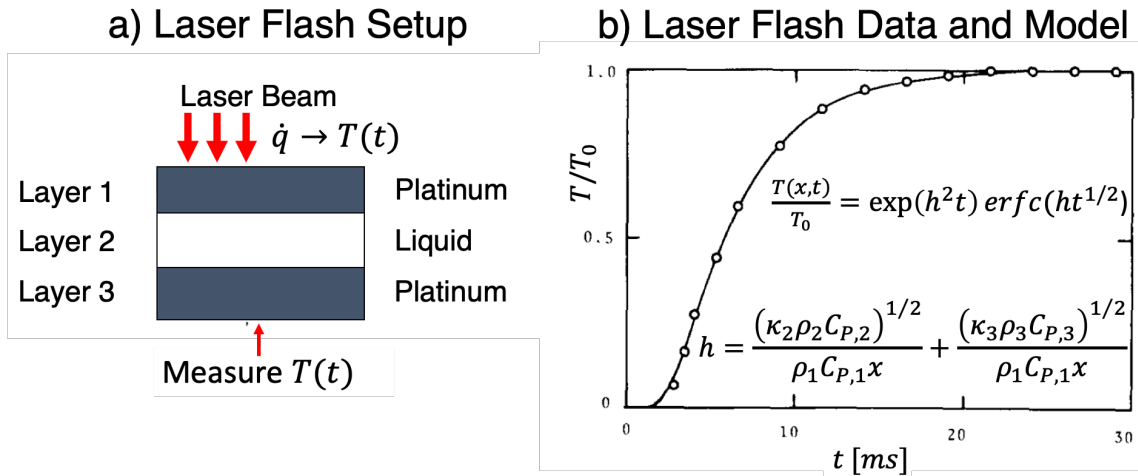
Figure 1.6. a) Schematic of laser flash setup adapted from Srinivasan et al.[23] and b) measured data and model adapted from Tada et al.[22]

Close relatives to laser flash are forced Rayleigh scattering and transient grating, which also use lasers to heat a sample and then measure the exponential decay in temperature as a

function of time. But rather than simply heating the sample as in laser flash, they both split the heating laser beam in two, and then cross them inside the liquid sample to create an interference pattern, with a sinusoidal temperature and density distribution induced by laser heating. Dyes are used to absorb the laser light and increase the sample temperature. The temperature then decays exponentially and can be measured as a function of time with a probe laser or thermocouple, and the time constant of the decay is used to extract the liquid's thermal conductivity. Forced Rayleigh scattering measurements of molten chloride salts is described by Nagasaka et al.[47,48] and transient grating measurements of ionic liquids are described by Frez et al.[49]

1.5 Frequency domain measurements

1.5 a) 3-Omega hot-wire

Frequency-domain hot-wire measurements are similar to transient hot-wire, but instead of a DC current, they use an AC current at 1ω to heat the platinum wire sensor and liquid sample. Joule heating in the wire is proportional to the current squared and leads to a temperature fluctuation of the wire and liquid sample at a frequency of 2ω. The oscillating temperature in the sample leads to a proportional oscillation in the sensor's resistance 2ω. Finally, the voltage of the wire, which oscillates at a frequency 3 times the input frequency – hence the name 3ω – is measured with a lock-in amplifier. 3ω was originally developed to measure the thermal conductivity of solids over wide temperature ranges and remove errors inherent to time-domain measurements, such as data truncation to remove self-heating of the sensor at short times and convection and environmental errors at long times. There has been significant work to develop 3ω to measure liquids[50–57] that is able to minimize error from

19

convection by controlling the thermal penetration depth and keeping the probed sample volume below 1μL. However, many previous 3ω measurements of liquids used sensors deposited on a solid substrate, which led to parasitic heat loss into the solid, or used incomplete thermal models that assumed an infinitely long wire that led to inaccurate results.

These difficulties were well discussed by Wingert et al.[24] and overcome through their full thermal model and solution to **Equation 1.2** , which provides the average temperature rise of a finite-length wire (length, L, and radius, r_0) from an input electrical heating power ($\tilde{P}_{RMS} = I_\omega^2 R$, with wire electrical resistance R) of varying frequency ($f = \omega/2\pi$) given by:

$$\tilde{T}_{2\omega,avg} \cong \sum_{n=1}^{\infty} \frac{8\tilde{P}_{RMS}}{\pi^3 r_0^2 L \kappa_0 (2n-1)^2 \varphi_0^2} \left\{ 1 + \left(\frac{\kappa_1 \varphi_1}{\kappa_0 \varphi_0} \right) \left(\frac{1}{\alpha\delta - \gamma\beta} \right) \left[\frac{\beta I_1(\varphi_1 r_0) - \alpha K_1(\varphi_1 r_0)}{I_1(\varphi_0 r_0)} \right] \right\} \qquad (1.12a)$$

$$\alpha = \kappa_1 \varphi_1 I_1(\varphi_1 r_1) \left(\frac{1}{\kappa_2 \varphi_2} \frac{K_0(\varphi_2 r_1)}{K_1(\varphi_2 r_1)} + \mathcal{R}_{1,2} \right) + I_0(\varphi_1 r_1) \qquad (1.12b)$$

$$\beta = \kappa_1 \varphi_1 K_1(\varphi_1 r_1) \left(\frac{1}{\kappa_2 \varphi_2} \frac{K_0(\varphi_2 r_1)}{K_1(\varphi_2 r_1)} + \mathcal{R}_{1,2} \right) - K_0(\varphi_1 r_1) \qquad (1.12c)$$

$$\delta = \kappa_1 \varphi_1 K_1(\varphi_1 r_0) \left(\frac{1}{\kappa_0 \varphi_0} \frac{I_0(\varphi_0 r_0)}{I_1(\varphi_0 r_0)} + \mathcal{R}_{0,1} \right) + K_0(\varphi_1 r_0) \qquad (1.12d)$$

$$\gamma = \kappa_1 \varphi_1 I_1(\varphi_1 r_0) \left(\frac{1}{\kappa_0 \varphi_0} \frac{I_0(\varphi_0 r_0)}{I_1(\varphi_0 r_0)} + \mathcal{R}_{0,1} \right) - I_0(\varphi_1 r_0) \qquad (1.12e)$$

$$\varphi_N = \sqrt{i \frac{4\pi f \rho_N C_N}{\kappa_N} + \left(\frac{\pi(2n-1)}{L} \right)^2} \qquad (1.12f)$$

where $I_j(x)$ and $K_j(x)$ are the jth order modified Bessel functions of the 1st and 2nd kind, respectively; κ_N is thermal conductivity and $\rho_N C_N$ is volumetric heat capacity of layer N; the subscripts $N = 0, 1$, and 2 represent the platinum, ceramic coating, and the surrounding liquid

sample, respectively; $\mathcal{R}_{0,1}$ and $\mathcal{R}_{1,2}$ are the interfacial thermal resistances between the wire-coating and coating-sample interfaces, respectively. The model includes an electrically insulating coating layer, with thickness $d = r_1 - r_0$, that are critical for measuring electrically conducting samples. Joule heating the platinum hot-wire leads to a radial thermal penetration depth into the sample, which is inversely proportional to heating frequency described by $\Delta_{p,N} = \sqrt{\kappa_N / 4\pi f \rho_N C_N}$.

This work made high temperature measurements feasible by allowing small sample sizes that are easier to keep at a uniform temperature, while rejecting ambient temperature fluctuations from the heater and environment, and also utilizing 4 orders of magnitude in varying input frequencies (1, 10, 100, and 1000 Hz) without arbitrary data truncation. **Figure 1.7 a)** shows the schematic setup of the sensor suspended in the liquid, and **Figure 1.7 b)** plots the measured frequency-dependent temperature rise in argon compared to various thermal model solutions that use hot-wire geometry and thermal properties of argon without data fitting – demonstrating the importance of using the newly developed finite length model rather than infinite length model to fit measured data from liquid's with unknown thermal conductivity. I will discuss the full details for calculating the wire temperature (**Eq. 1.12**), extracting the liquid sample's thermal conductivity, and show that convection, radiation, and convection are negligible in measurements of molten salts in **Chapter 3** and ionic liquids in **Chapter 4.**
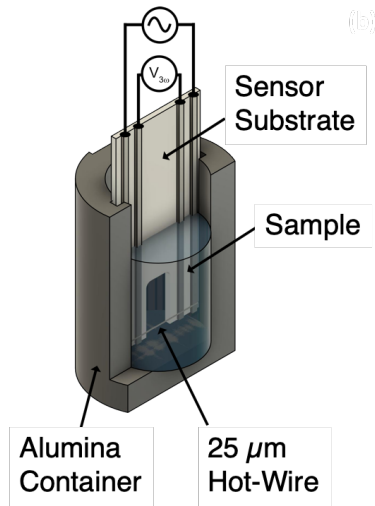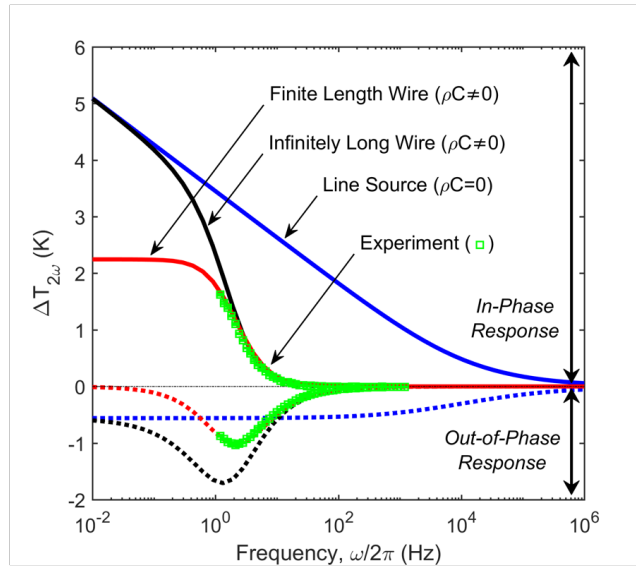
Figure 1.7. a) Schematic of hot-wire 3-Omega sensor, and b) frequency-domain experimental data of argon with various thermal models from Wingert et al.[24] Reprinted with permission from AIP Publishing.

1.5 b) Frequency-domain optical measurements

Similar to time-domain laser flash, frequency-domain optical measurements of liquid thermal conductivity use lasers to heat the liquid sample; rather than measuring the temperature response from laser heating as a function of time, the temperature response of the liquid sample is measured as a function of the input laser frequency. The intensity of the laser is modulated to a specific frequency that can control the thermal penetration depth into the liquid sample to remove error from convection, similar to 3ω hot-wire measurements. Modulated Photothermal Radiometry and Electromagnetic Levitation are examples of frequency-domain, non-contact, optical measurements of liquid thermal conductivity.

Modulated Photothermal Radiometry has recently been adapted by Zeng et al. for measuring high temperature solids[25], as well as flowing liquids[26]. It uses a laser to heat a

transducer in contact with a sample at varying frequencies, and an infrared detector measures the frequency-dependent temperature response of the system. Unpublished measurements of molten nitrate salts and molten sulfur using Modulated Photothermal Radiometry, match 3ω hot-wire measurements and provide promising support for frequency-domain measurements for high temperature liquids.

Electromagnetic Levitation uses a laser to heat the liquid sample, a pyrometer to measure the resulting temperature rise, and an electromagnetic field to suspend the liquid sample to remove any physical contact with a sample holder or transducer and prevents corrosion at high temperature (see **Figure 1.8a**), and it also uses periodic laser heating to measure the frequency domain response and ultimately the liquid's thermal conductivity (see **Figure 1.8b**). The phase lag, ϕ, between the oscillating laser heating and the measured temperature fluctuations, is measured as a function of the input laser frequency. Then a numerical solution to the thermal model for a suspended sphere (**Eq. 1.2**) is found by finite element analysis to give the phase lag ϕ with the parameter κ fit to the measured data. The following boundary conditions of the laser irradiated area (**Eq. 1.13a**), non-irradiated area (**Eq. 1.13b**), and center line of the suspended liquid spherical sample (**Eq. 1.13c**) are used:

$$-\kappa\frac{dT}{dn} = \sigma_{SB}\varepsilon(T^4 - T_{am}^4) - \frac{2P(t)}{\pi r_{laser}^2}exp\left[\frac{2R^2 sin^2\theta}{r_{laser}^2}\right] \times (-n \cdot e_{laser}) \tag{1.13a}$$

$$-\kappa\frac{dT}{dn} = \sigma_{SB}\varepsilon(T^4 - T_{am}^4) \tag{1.13b}$$

$$-\kappa\frac{dT}{d\theta} = 0 \tag{1.13c}$$

23

where n is the normal unit vector, r_{laser} is the radius of the laser, e_{laser} is the unit vector of the laser, T_{am} is the ambient temperature.

There are potential errors from convection – the standard temperature differences that lead to natural convection, as well as induced by electromagnetic forces – but there has been work to show convection is suppressed in magnetic fields greater than 2 Tesla[27].

a) Electromagnetic Levitation   b) Data and Numerical Fit
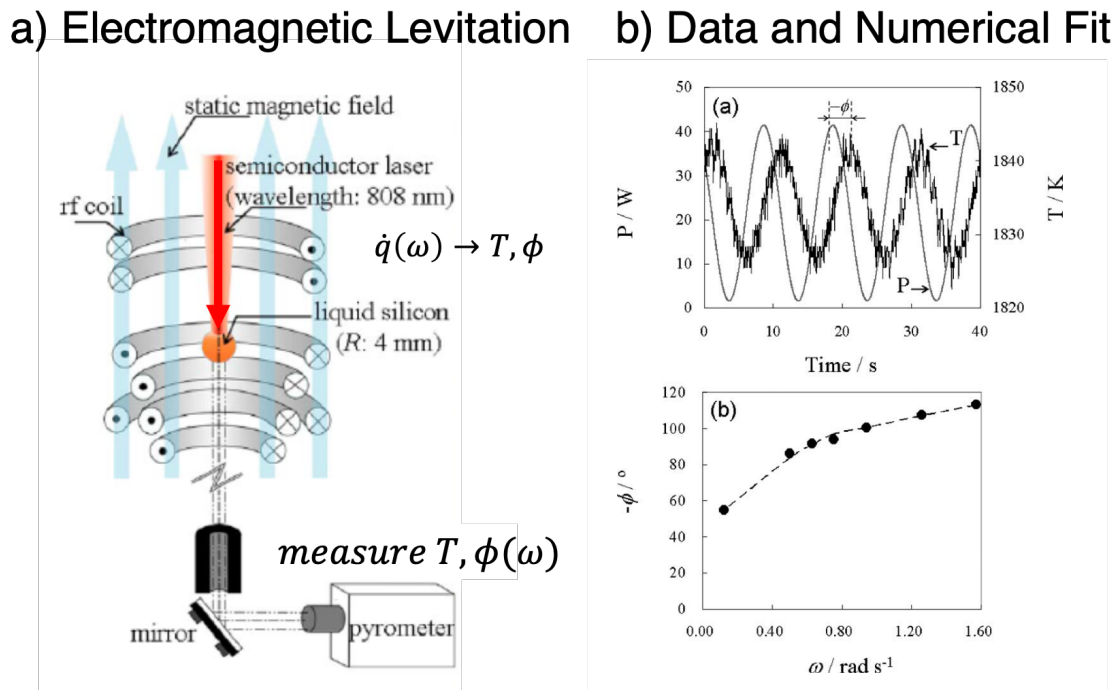
Figure 1.8. a) Schematic of electromagnetic levitation and **b)** measured data adapted from Kobatake et al.[27]

1.6 Theoretical models of liquid thermal conductivity

Analytical equations and molecular dynamics simulations can have explanatory and predictive power for how a liquid's thermal conductivity will behave from a change in its temperature, pressure, or chemical composition. High temperature liquid thermal conductivity measurements are difficult, and useful experimental data for many potential engineering conditions are not available. Thus, it is desirable to have models of liquid thermal conductivity that closely match reliable experimental data and have predictive power for liquid thermal conductivity in conditions that have not yet been experimentally tested. In the following sections, we provide a framework for understanding liquids through their intermolecular forces and structure that will provide insights into why certain models work well for specific liquids and not others. Then, we review analytical equations – modified kinetic gas theory, quasi-crystalline, and electron models – and examine how well they capture thermal conductivity. Last, we review how molecular dynamics is used to model liquid thermal conductivity through equilibrium and nonequilibrium approaches and compare its results to experimental measurements and analytical models.

1.7 Liquid framework: intermolecular forces and liquid structure

To understand how temperature affects thermal conductivity of different liquids, we first classify liquids based on their intermolecular forces into 4 categories: simple liquids held together by London dispersion energy, molecular liquids held together by dipole-dipole Keesom energy, molten salts held together by Coulombic energy, and molten metals held together by metallic bonding.[58] Different intermolecular interaction energies manifest in different liquid structures, which are well visualized by radial distribution functions in **Figure 1.8** that can be

measured by neutron and x-ray diffraction experiments. Radial distribution functions, $g(r)$, are defined so that if there is an atom at the origin $r = 0$, then the probability of finding a neighboring atom at a certain distance between r and $r + dr$, away from the origin atom is given by $g(r)4\pi r^2 dr$. The density of atoms in a liquid can then be calculated from the radial distribution function.

The radial distribution function for liquids serves a similar fingerprinting role that x-ray diffraction serves for crystalline solids. **Figure 1.9** clearly shows that there is short-range order between neighboring liquid molecules, as well as 2nd and 3rd nearest neighbors – this short-range order is due to the stronger intermolecular attraction, compared to gas molecules, that leads to relatively high density. While gas molecules are treated as independent particles with no volume in the Boltzmann kinetic theory of gases, liquid molecules take up space and interact strongly with their neighbors – such that when one molecule moves and vibrates, it influences its neighbors. But intermolecular interactions between liquid molecules are not strong enough to anchor them into time-independent equilibrium positions that define the crystal structure of solids with long-range order. Liquid molecules are arranged uniquely, different from gases and solids, based on their underlying intermolecular interaction energies that will provide clues to how heat conducts through a liquid and explain how liquid thermal conductivity changes with temperature, pressure, or composition.

Here, we briefly review intermolecular interaction energies and how they influence the structure of simple liquids (Ar), molecular liquids (H_2O), coulombic liquids ($NaNO_3$), and molten metals (Na) – more details about intermolecular forces can be found in a comprehensive textbook by Israelachvili[59].
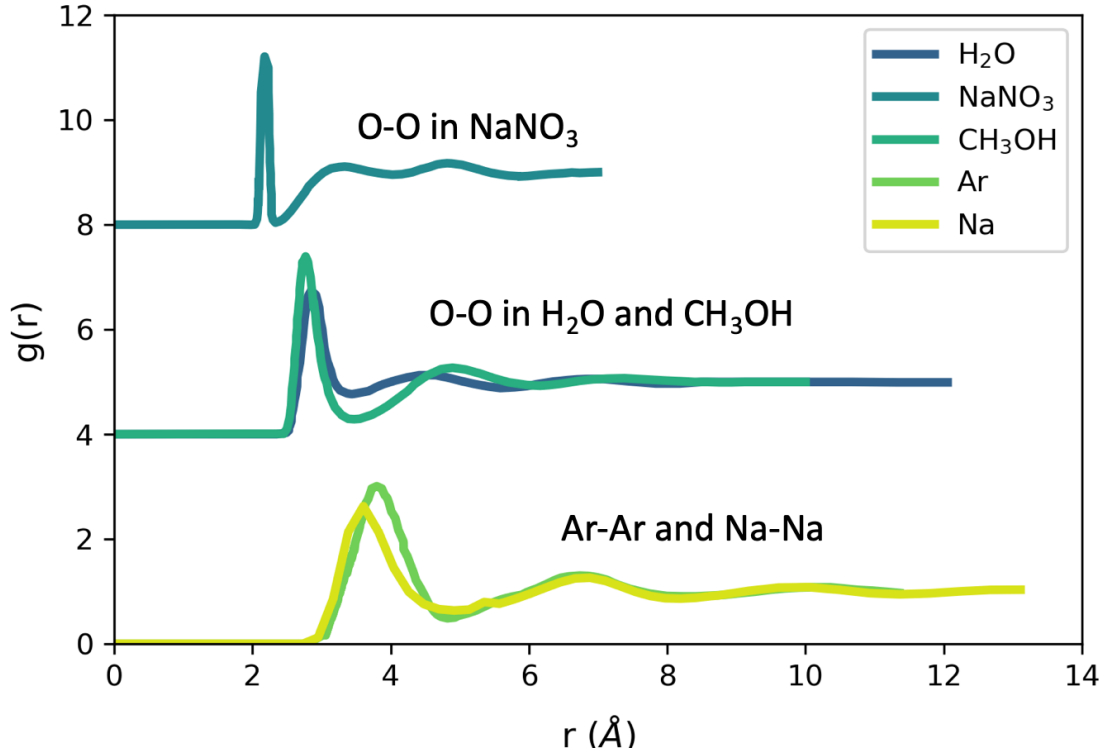
Figure 1.9. Radial distribution functions of liquid $NaNO_3$[60], H_2O[61], CH_3OH[62], Ar[63], and Na[64].

We first examine a simple liquid with only one atom: argon. Argon is nonpolar since its valence electron orbital is completely full, and London dispersion energy is the only interaction energy that holds liquid argon atoms together. Intermolecular interactions are all fundamentally electro-magnetic forces. London dispersion energy originates from a quantum mechanical fluctuation of an argon's electrons that leads to a temporary electron polarization, which induces an instantaneous dipole in a neighboring argon atom, which binds them together as a liquid with a potential energy given by

$$E_{London}(d) = \frac{-3}{4} \frac{h\nu\alpha^2}{(4\pi\varepsilon_0)^2 d^6} \tag{1.14}$$

where ν is the ionization frequency (s^{-1}), α is the electronic polarizability ($C^2 m^2 J^{-1}$), ε_0 is the dielectric permittivity of free space 8.854 $C^2 J^{-1} m^{-1}$, and d is the intermolecular distance. London dispersion energy exists in all molecules, but it is the weakest molecular interaction energy and results in low boiling points in simple liquids like argon. The London dispersion energy[58] of argon at 85K and 0.1 MPa is roughly $-0.86\ kJ\ mol^{-1}$, and methane at 92 K and 0.1 MPa is $-1.75\ kJ\ mol^{-1}$.

Within more complex molecules than argon, atoms are held together by covalent bonds that do not break when their solid form melts, and neighboring molecules are held together by intermolecular dipole-dipole interactions. The shape of the molecule and its atomic constituents create a permanent dipole moment; in H_2O and CH_3OH, electrons are concentrated around the oxygen atom leaving a partially positive charge on the hydrogen atom. This asymmetric distribution of electrons is the source of the permanent electric dipole moments, u ($u = 0.97\ D$ for hydrogen sulfide and $u = 1.85\ D$ for water[65], where $D = 3.336 \times 10^{-30} C\ m$). The dipole moment tells us how polar a molecule is and how far the positive and negative charges are separated within a molecule. Dipole-dipole interaction energy, also known as Keesom energy, arises when the charges of a polar molecule are attracted to a neighboring polar molecule, given by[58]

$$E_{Keesom}(d) = \frac{-u^4}{3 * (4\pi\varepsilon_0)^2 k_B T d^6} \qquad (1.15)$$

However, the bonding in hydrogen-bonded water and hydrogen sulfide is much more complicated than just Keesom energy; there are contributions from the covalency of electron orbitals between neighboring molecules, as well as London dispersion energy. Significant work has been done to find water's hydrogen bonding interaction energy ($-21\ kJ\ mol^{-1}$)[66], that

leads to the unique structure and properties of water. And hydrogen bonds have recently been detected in hydrogen sulfide to be weaker than water $(-7 \; kJ \; mol^{-1})$[67–69].

The Keesom attraction contributes to the similar short-range order of oxygen-oxygen neighbors in water and methanol shown in **Figure 1.9**. A schematic of how the radial distribution function relates to the physical arrangement of water molecules is shown in **Figure 1.10**. And as temperature increases, the dipole-dipole attraction between molecules diminishes due to thermal fluctuations of molecules that reduce alignment between neighboring molecules. Neutron diffraction measurements from Soper[61] show the declining short-range order of water as temperature increases – the first radial distribution function peak broadens, and it becomes less likely to find a neighboring water molecule a certain distance away. However, water becomes more thermally conductive at higher temperatures despite becoming less ordered and more gas-like.

It is intuitive to associate a decrease in local ordering with a decrease in thermal conductivity because gases are associated with a lack of order and have extremely low thermal conductivity while crystalline solids are associated with long-range order and thermal conductivities several orders of magnitude higher than gas. However, water's increasing thermal conductivity as temperature increases (**Figure 1.1)** is at odds with its decrease in order shown by Soper[61]. This provides an important lesson that intuition about the liquid phase drawn from the gas and solid phases does not always match experimental results, and a deeper dive into liquid structure, through phonon-dispersions, are necessary to explain thermal conductivity results.
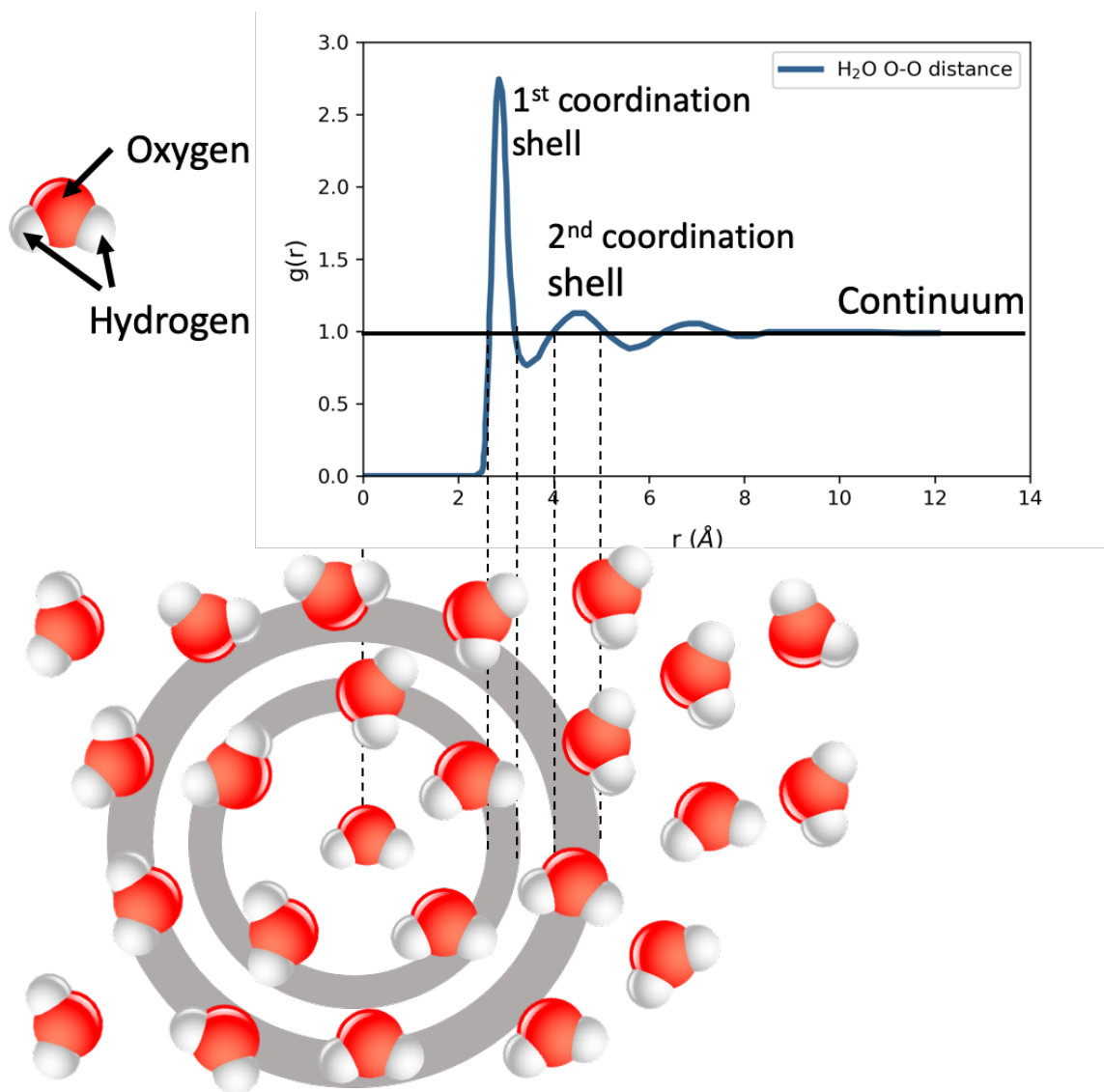
Figure 1.10. Visualized radial distribution function of water, measured with neutron diffraction by Soper[61]. Based on Ziman[70].

For molten salts, cations and anions in the liquid phase are held together by a strong Coulomb interaction energy given by

$$E_{Coulomb}(d) = \frac{q_1 q_2}{4\pi\varepsilon_0 d^2} \qquad (1.16)$$

where q_1 and q_2 are the charge of the species in Coulombs (C). Sodium nitrate's Coulomb interaction energy is 417 $kJ\ mol^{-1}$ and potassium nitrate's is 376 $kJ\ mol^{-1}$. While there are

nitrate molecules and other intermolecular forces present in molten sodium nitrate, the dominant intermolecular interaction energy is Coulomb, rather than Keesom or London, which are both temperature dependent and drop off much faster with increasing distance, r. The interactions and structure of molten salts mainly depend on the electric charge, q, which are independent of temperature. Thus, the thermal conductivity of molten salts should remain steady with respect to temperature, compared to liquids dominated by London and Keesom energy, since molten salt structure is dominated by Coulomb energy. The distinct radial distribution function between oxygen-oxygen neighbors in molten sodium nitrate, seen in **Figure 1.9 and 1.11**, can be attributed to the covalent bonding within the nitrate anion and coulombic forces.

Molten sodium and liquid argon are held together by different interatomic forces but their radial distribution functions are overlapping in **Figure 1.9**. They have both been modeled as hard spheres that are randomly close packed since neither has any molecular structure, only made up of atoms. But they have completely different temperature dependent thermal conductivity (**Figure 1.1**), and in the following sections, we will explore different models for interpreting liquid thermal conductivity with different intermolecular interactions and structure.
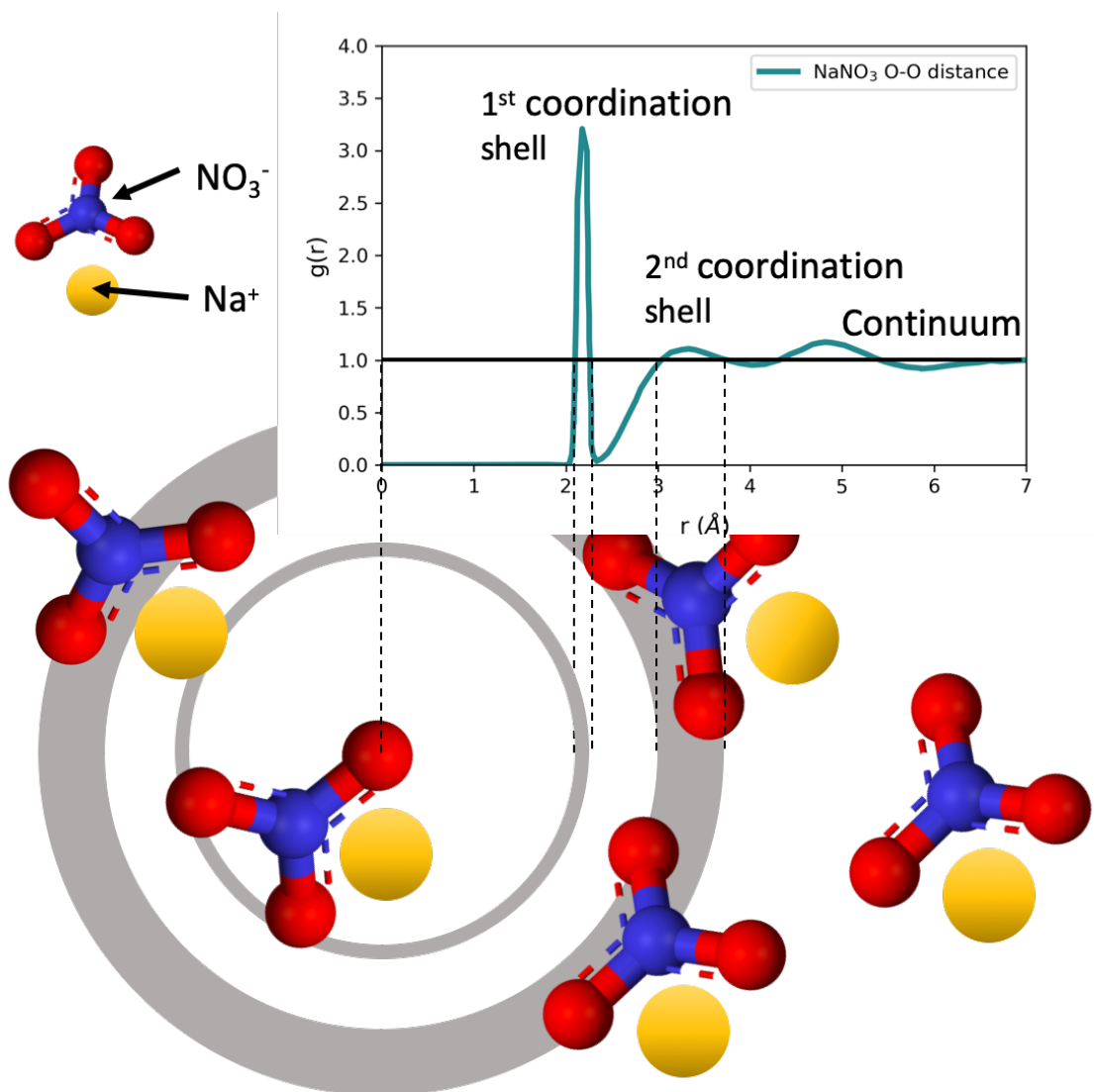
Figure 1.11. Visualized radial distribution function of $NaNO_3$[60] adapted from Ziman.[70]

1.8 Analytical models of liquid thermal conductivity

There has been a bounty of models of liquid thermal conductivity over the past century, but many models were developed to fit experimental data for a narrow set of liquids, and none are capable of matching experimental results for all types of liquids with different intermolecular interactions.

In this review, we categorize liquid thermal conductivity models into two broad categories: modified kinetic gas theories and quasi-crystalline models created to describe liquid thermal conductivity. The main tension between these two approaches is the contribution of diffusion, the source of heat conduction in gases, versus lattice vibrations, the source of heat conduction in crystalline dielectric solids. Liquids flow to fill up containers like gases, but the density of liquid molecules precludes kinetic gas-like conduction; liquids have similar density to solids, but the lack of long-range order precludes phonons from being well-defined. Here, we review models that are commonly used to interpret experimental data, discuss their assumptions and how they were formulated, and examine how well they fit experimental data for liquids of all types of intermolecular interactions. The dominant heat carriers in molten metals are electrons, rather than diffusion or vibrational modes, so we discuss Wiedemann-Franz law for molten metals after modified kinetic gas theories and quasi-crystalline models.

1.8 a) Modified kinetic theory of gas

The Boltzmann kinetic theory of gases provides the well-known result for the thermal conductivity of a gas:

$$\kappa = \frac{1}{3} C_V v l \qquad (17)$$

where C_V is the volumetric heat capacity, determined by the degrees of freedom of the gas molecules; v is the average speed of gas molecules directly related to the temperature; and l is the mean free path – the average distance a gas molecule travels between scattering events, dependent on the density of the gas molecules.

Previous attempts have been made to modify the kinetic theory of gases to account for the difference between a liquid and gas. Most notably, Chapman and Enskog independently

reformulated the kinetic theory of gases to account for the volume of liquid molecules and intermolecular interactions. The Chapman-Enskog framework was used to develop a new kinetic theory of liquids[71–74], where liquid molecules collide more frequently than gas molecules (visualized in **Figure 1.12**). An effective scattering diameter, D, of the liquid molecules can be extracted from the experimentally measured viscosity, $\mu_{Chapman-Enskog}$, and the resulting thermal conductivity and viscosity of a liquid are:

$$\kappa_{Chapman-Enskog} = \frac{k_0}{g(D)}\left[1 + \frac{2}{5}\pi\rho D^3 g(D)\right]^2 + \frac{3k_B}{2m}\Pi \tag{1.18a}$$

$$\mu_{Chapman-Enskog} = \frac{\mu_0}{g(D)}\left[1 + \frac{4}{15}\pi\rho D^3 g(D)\right]^2 + \frac{3}{5}\Pi \tag{1.18b}$$

$$k_0 = \frac{25}{32}\frac{\sqrt{\pi m k_B T}}{D^2\pi}\frac{3k_B}{2m} \tag{1.18c}$$

$$\mu_0 = \frac{5}{16}\frac{\sqrt{\pi m k_B T}}{D^2\pi} \tag{1.18d}$$

$$\Pi = \frac{4}{9}\sqrt{\pi m k_B T}\rho^2 D^4 g(D) \tag{1.18e}$$

$$g = \frac{\left(1 - \frac{11\rho b}{9}\right)}{1 - 2\rho b} \tag{1.18f}$$

$$b = \frac{2}{3}\pi D^3 \tag{1.18g}$$
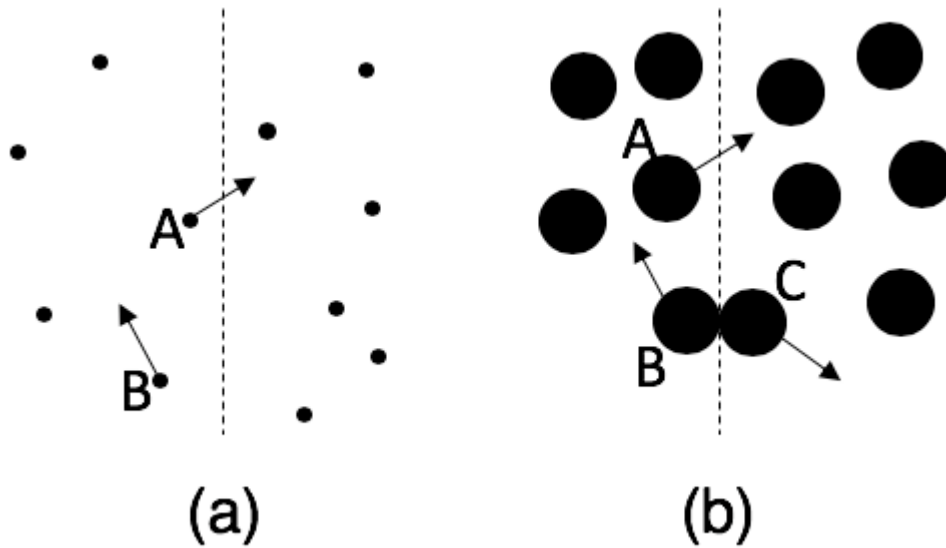
Figure 1.12. a) Schematic of Boltzmann kinetic gas where heat flows across the interface when molecules cross the interface. **b)** Schematic of Chapman-Enskog modified kinetic gas model for liquids where heat flows from molecules crossing the interface and collisions. Adapted from Chen[74].

Embedded inside Chapman-Enskog's expressions for liquid thermal conductivity (**Eq. 1.18a**) and viscosity (**Eq. 1.18b**) are the dilute-gas thermal conductivity k_0 (**Eq. 1.18c**) and viscosity μ_0 (**Eq. 1.18d**). The Chapman-Enskog kinetic theory of liquids has reasonable assumptions for how heat conducts in liquids, but it is not successful in capturing the temperature dependence and values of liquid thermal conductivity (shown in **Figs. 1.13 and 1.14**). Many researchers still interpret liquid thermal conductivity results using modified kinetic gas models since there are similarities between gases and liquids, and it is difficult to deal with the many-body interactions in liquids to create an analytical expression for thermal conductivity.

Another modified kinetic gas theory for liquids is currently used for several reference thermal conductivity values of several molecular liquids held together by Keesom dipole-dipole energy (ethanol[75], methanol[76], hexane[77], heptane[78]):

$$\lambda(\rho, T) = \lambda_0(T) + \Delta\lambda + \Delta\lambda_C \tag{1.19a}$$

$$\lambda_0(T) = 1000 \frac{5k_B(1 + r^2)T}{2m\langle v\rangle_0 S(10E)} f_\lambda \tag{1.19b}$$

where λ_0 is the thermal conductivity at the dilute gas limit, $\Delta\lambda$ is the contribution from intermolecular interactions towards thermal conductivity, and $\Delta\lambda_C$ is the enhancement in thermal conductivity at the critical point. $\langle v\rangle_0 = 4\sqrt{k_b T/\pi m}$, is the average relative thermal speed, $r^2 = 2C_v/5k_B$, and S(10E) is the generalized cross section. These reference correlations used to calculate thermal conductivity of commonly used solvents are extremely accurate, with reported uncertainties less than 5% and good agreement with experiments up to several hundred degrees Celsius and several hundred MPa. However, the authors state that there is no theoretical basis for $\Delta\lambda$, the intermolecular contribution to liquid thermal conductivity, and that it is a fitting parameter to match their primary experimental data.

1.8 b) Quasi-crystalline models of liquids

The other major approach to calculate liquid thermal conductivity is treating liquids like solids with quasi-crystalline lattices. McLaughlin presented a comprehensive review in 1968 of several quasi-crystalline approaches, their assumptions, and how well their models matched experimental data.[5] Here, we review models that are still used today that were previously discussed by McLaughlin, and include recent developments in the phonon gas model that can accurately calculate the thermal conductivity of molten salts – from Gheribi et al.[9,79] and Zhao et al.[4]

Bridgman developed an early quasi-crystalline model of liquid thermal conductivity[80] in 1923, which was further developed by Kincaid & Eyring[81] in 1938 and Powell et al.[82] in 1941. Bridgman treats liquids as a simple cubic lattice, with a molecule at each corner and side lengths of d, and each liquid molecule carries $2k_B$ of energy through a cubic cross-section d^2 at the speed of sound through the cubic lattice, leading to

$$\kappa_{Bridgman} = \frac{2k_B v_{sound}}{d^2} = 2k_B v_{sound} n^{2/3} \tag{1.20a}$$

$$\kappa_{Kincaid\,\&\,Eyring} = \left(\frac{0.931}{\gamma^{\frac{1}{2}}}\right) 3k_B v_{sound} n^{2/3} \tag{1.20b}$$

$$\kappa_{Powell\,et\,al.} = 2.8 k_B v_{sound} n^{2/3} \tag{1.20c}$$

where v_{sound} is the longitudinal speed of sound in the liquid, d is the mean distance between the centers of molecules and can be calculated from $d = n^{-1/3}$, and n is the number density of molecules in the liquid. The Bridgman model of liquid thermal conductivity is still used today to interpret measurement results because it is a simple analytical equation that can accurately calculate thermal conductivity of several liquids, and it provides a clear picture that a liquid's density and speed of sound strongly influence thermal conductivity. Bridgman's equation fit his experimental data for several molecular liquids, and we previously showed that it captures the general temperature-dependent trends in simple liquids and molten salts[4] that were not originally measured by Bridgman.

Horrocks & McLaughlin, in their quasi-crystalline model, treat liquids as a face-centered cubic lattice, where each liquid molecule interacts with its neighbors through a Leonard-Jones potential[83]. When one of the molecules is perturbed out of its quasi-lattice position, there is a restoring force with a spring constant. The restoring spring has vibrational frequency, *v,* and has a certain probability, *P*, of transferring energy to the next plane of liquid molecules (finding *v*

and P requires further calculations and fitting parameters). Horrocks & McLaughlin break liquid thermal conductivity into solid-like vibrational thermal conductivity, $\kappa(vib)$, and convective contributions to thermal conductivity, $\kappa(conv)$; they show that the convective component of liquid thermal conductivity, where one molecule moves into a vacancy in their quasi-lattice, to be negligible and less than 1% of the total thermal conductivity.

$$\kappa_{Horrocks-McLaughlin} = \kappa(vib) + \kappa(conv) \approx \kappa(vib) \qquad (1.21a)$$

$$\kappa(vib) = 2nPvlC_v \qquad (1.21b)$$

where n is the number of molecules per unit area of a lattice plane, P is the probability of transmitting energy to a neighboring molecules, l is the distance between lattice planes, and C_v is the specific heat per molecule. A face-centered cubic model of liquids is inaccurate, given the lack of long-range order in liquid radial distribution functions shown in **Figures 1.9, 1.10, and 1.11,** but Horrocks & McLaughlin's model showed good agreement with thermal conductivity measurements of simple liquids such as argon, nitrogen, benzene, and carbon tetrachloride – all nonpolar molecules with zero dipole moment. The major downside of the Horrocks & McLaughlin model, and many quasi-crystalline treatments of liquid thermal conductivity, is that they make unrealistic assumptions about liquid structure, have fitting parameters to calculate P, and are not applicable for a wider range of liquids.

A recently developed quasi-crystalline approach to liquids is the phonon-gas model. By analogy, the phonon gas model traditionally treats phonons in crystalline solids as gas particles to describe the thermal conductivity of a crystal lattice, and it is a powerful model for understanding heat transport in solids with long-range order[84]. The thermal conductivity of solids takes the same form as the kinetic gas model, but accounts for three phonon polarizations in solids (one longitudinal acoustic and two transverse acoustic branches, in addition to the

phonon frequency ω, dependent volumetric heat capacity of the solid $C_V(\omega)$, phonon group velocity $v_g(\omega)$, and mean free path $l(\omega)$.

$$\kappa = \sum_{n=1}^{3} \int_0^\infty \frac{1}{3} C_V(\omega) v_g(\omega) l(\omega) \, d\omega \qquad (1.22)$$

As previously stated, liquids are different from crystalline solids since they lack long-range order, but phonon-like vibrational modes exist at all frequencies for longitudinal waves, and transverse waves exist at frequencies above the Frenkel frequency since molecular rearrangement does not scatter them. Phonon dispersions in liquids can be obtained by neutron and x-ray scattering experiments, which we will discuss in more depth in **Chapter 2**. Measured phonon dispersions in liquids, along with Frenkel's theory of liquids, led Trachenko et al.[85–87] to develop a new solid-state formulation of liquid thermodynamics and accurate calculations of liquid heat capacity.

This inspired my work[4] to posit that vibrational modes in liquids behave like a phonon gas with frequency dependent heat capacity, velocity, and mean free path according to **Equation 1.22**, with the same adjustment Trachenko *et al.* made for liquid heat capacity, including transverse modes above the Frenkel frequency. We write the thermal conductivity of a liquid as:

$$\kappa = \int_0^{\omega_{Dl}} \frac{1}{3} C_l(\omega) v_l(\omega) l(\omega) \, d\omega + \int_{\omega_F}^{\omega_{Dt}} \frac{2}{3} C_t(\omega) v_t(\omega) l(\omega) \, d\omega \qquad (1.23)$$

where $C_l(\omega)$ and $C_t(\omega)$ are the frequency dependent specific heat due to the longitudinal and transverse modes, respectively; $v_T(\omega)$ is the transverse speed of sound, and $v_L(\omega)$ is the longitudinal speed of sound. We will discuss this model development in depth in **Chapter 2**. In short, to avoid the full spectral analysis of frequency-dependent properties of liquid vibrational modes, we assumed the experimental constant pressure heat capacity captured the vibrational contribution to specific heat, and we made the gray approximation for their speed of sound and

mean free path. Our simplifications of **Eq. 1.23** leads to the same result originally reported by Slack for liquids.

$$\kappa_{Slack} = \frac{1}{3} C_V v_{sound} n^{2/3} \qquad (1.24)$$

where C_V is the constant volume heat capacity both with the same units [JK^{-1}] and n is the molecular number density [m^{-3}]. I will discuss the assumptions of this model and its result in depth in **Chapter 2.**

Slack formulated his modified phonon gas model to calculate the thermal conductivity of liquids[88], where phonons in liquids conducted heat and moved at the speed of sound and had the shortest mean free path possible due to constant molecular rearrangement, the intermolecular distance that can be calculated from the number density of liquid molecules. Slack's model was never widely adopted or tested until our recent work on using the phonon gas model to calculate the thermal conductivity of liquids with varying intermolecular interaction energies and densities[4]. In fact, we only found Slack's original work after completing our calculations, and realized we used the same approach outlined by Slack. In **Chapter 2,** we will show that Slack's phonon gas model is successful in matching the experimental thermal conductivity of water and molten sodium nitrate across their entire temperature ranges. Further, the phonon gas model becomes more accurate as the density and intermolecular interaction energy of liquids increases.

The phonon gas model provides similar results to the analytical equations from Gheribi et al.[9] for molten salts and Xi et al.[89] for liquids and amorphous solids. Gheribi et al. derived molten salt thermal conductivity from the Boltzmann transport equation and the hard spheres theory; this work is related to the hard-spheres model developed by DiGuilio & Teja[90] for molten nitrate and chloride salts, which also provides a good review of previous molten salt

models that built upon results from Bridgman (**Eq. 1.20**) and Horrocks & McLaughlin (**Eq. 1.21**). Xi et al. derived a more general thermal conductivity equation for liquids and amorphous solids based on Einstein's random walk theory of coupled vibrational modes conducting heat through atoms and their nearest neighbors, and the heat flux changes depending on the molecular structure and short-range ordering of molecules.

$$\kappa_{Gheribi\ et\ al.} = \frac{1}{3} * 4.33 C_V v_{sound} \frac{(r_{cation} + r_{anion})}{N} \qquad (1.25)$$

$$\kappa_{Xi\ et\ al.} = \alpha \left(\frac{3}{2} + \frac{D_V}{2} \right) k_B v_{sound} n^{1/3} \qquad (1.26)$$

where r_{cation} and r_{anion} are the ionic radii of molten salts [m] and N is the number of atoms per molecule; α and D_V are parameters that change depending on the geometry of the liquid molecule. Note the similarity between the Bridgman model (**Eq. 1.20**) and phonon gas-like models from Slack (**Eq. 1.24**), Gheribi et al. (**Eq. 1.25**) and Xi et al. (**Eq. 1.26**) – the main difference being how much energy is transferred by vibrational modes between neighboring molecules and how the intermolecular distance is calculated. These discrepancies in the numerical coefficient, at the beginning of analytical equations, are likely due to the difference in the interaction energies of the liquids used to develop each respective model. The amount of heat that is transferred between neighboring molecules will change depending on how much energy can be stored locally within a molecule and the interaction strength between neighbors, which depends on the type of liquid. This is why certain equations fit better for specific types liquids than others, since they were built to explain those liquids. These differences can be clarified by future work in determining the frequency dependent properties of vibrational modes in liquids and their relative contributions to thermal conductivity, similar to work done in

amorphous solids[91,92] and in equilibrium molecular dynamics simulations of molten NaCl, MgO, and Mg_2SiO_4.[93]

Table 1.2. Analytical thermal conductivity models.

Model	Analytical Equation for Thermal Conductivity
Chapman-Enskog (Eq. 1.18)	$$\frac{k_0}{g(D)}\left[1+\frac{2}{5}\pi\rho D^3 g(D)\right]^2 + \frac{3k_B}{2m}\Pi$$
Modified Dilute Gas (Eq. 1.19)	$$\lambda_0(T) + \Delta\lambda + \Delta\lambda_C$$ $$\lambda_0(T) = 1000\frac{5k_B(1+r^2)T}{2m\langle v\rangle_0 S(10E)}f_\lambda$$
Bridgman (Eq. 1.20)	$$\frac{2k_B v_{sound}}{d^2} = 2k_B v_{sound} n^{2/3}$$
Horrocks & McLaughlin (Eq. 1.21)	$$2nPvlC_v$$
Zhao et al. (Eq. 1.23)	$$\kappa = \int_0^{\omega_{Dl}}\frac{1}{3}C_l(\omega)v_l(\omega)l(\omega)\,d\omega + \int_{\omega_F}^{\omega_{Dt}}\frac{2}{3}C_t(\omega)v_t(\omega)l(\omega)\,d\omega$$
Slack (Eq. 1.24)	$$\frac{1}{3}C_{P,volumetric}v_{sound}l = \frac{1}{3}C_P v_{sound} n^{2/3}$$
Gheribi et al. (Eq. 1.25)	$$\frac{1}{3}*4.33C_V v_{sound}\frac{(r_{cation}+r_{anion})}{N}$$
Xi et al. (Eq. 1.26)	$$\alpha\left(\frac{3}{2}+\frac{D_V}{2}\right)k_B v_{sound} n^{1/3}$$

1.8 c) Molten metal models

The thermal conductivity of molten metals has contributions from electron transport and vibrational modes, but electrons are usually the dominant heat carrier in molten metals.

$$\kappa_{metal} = \kappa_e + \kappa_{vib} \approx \kappa_e \qquad (1.27a)$$

$$\kappa_e = \frac{1}{3} C_e v_F^2 \tau_E \qquad (1.27a)$$

where C_e is the specific heat of electrons, v_F is the velocity of electrons at the Fermi level, and τ_E is the energy relaxation time of electrons. The Wiedemann-Franz law[74,94] relates the thermal conductivity from electron transport with the electrical conductivity through the Lorenz number, L.

$$L = \frac{\kappa_e}{\sigma T} \qquad (1.28)$$

The Lorenz number for various molten metals, however, has been measured[94] to be roughly between 2.1 to 2.8 – different from the constant Sommerfeld value, L_0.

$$L_0 = \frac{\kappa_e}{\sigma T} = \frac{m C_e v_F^2}{3 n T e^2} = \frac{\pi^2 k_B^2}{3 e^2} = 2.445 \times 10^{-8} [W\Omega K^{-2}] \qquad (1.29)$$

The Sommerfeld value only accounts for the electronic component to the thermal conductivity, κ_e, and the Lorenz number only equals the Sommerfeld value if $\kappa_e \gg \kappa_{vib}$, demonstrating the importance of electron-vibrational mode interactions for molten metal heat transport. To demonstrate that the Lorenz number is not constant, and that electrical conductivity measurements should not be used for thermal conductivity measurements, there has been work showing that the Lorenz number changes as a function of temperature, pressure, and composition in molten metals[10,46,95] (see **Figure 1.16**).
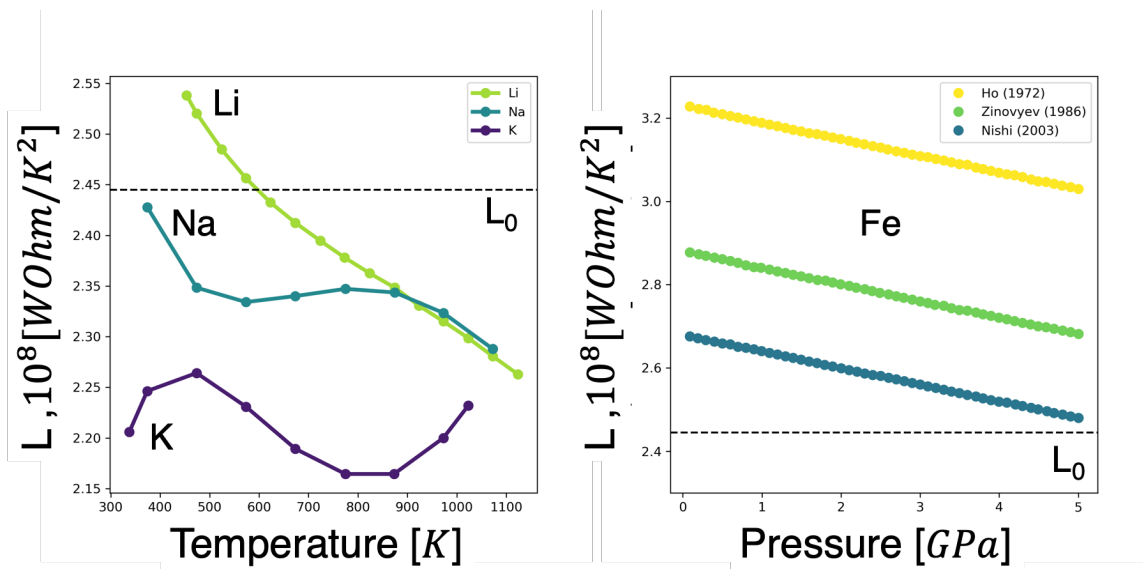
Figure 1.16. a) Lorenz number for molten alkali metals at varying temperatures adapted from Agazhanov et al.[10] and **b)** Lorenz number molten iron at varying pressures, from three independent measurements, adapted from Secco[95].

While some of the variation between measured Lorenz number can be attributed to experimental error, independent and reliable measurements of thermal conductivity for various molten metals have shown that the Lorenz number is not constant. Nishi et al.[46] measured molten iron, cobalt, and nickel thermal conductivity with laser flash, and showed how the Lorenz number for each metal changed for different metals and as a function of temperature. Secco[95] measured the Seebeck coefficient of molten iron, and along with previous reference values of thermal conductivity and electrical conductivity, they showed how the Lorenz number of molten iron changes with pressure, temperature, and the addition of silicon and silicates (the thermal properties of molten iron and its various alloys have large ramifications for the structure and composition of Earth's core[95,96]). Agazhanov et al.[10] measured the thermal conductivity using laser flash of molten alkali metals – lithium, sodium, potassium, cesium, and rubidium. They designed their sample cell to be sealed in argon to prevent chemical reactions and thin

44

enough to suppress error from convection – their results were repeatable, and their reported experimental error was 4 to 6%. Agazhanov et al.[10] demonstrated the precision and accuracy of laser flash for molten metals.

Previous modeling work on the temperature dependence of liquid thermal conductivity was done by Viswanath & Rao[97] and it was extended to molten metals by Viswanath & Mathur[98]. They start with the quasi-crystalline model from Horrocks & McLaughlin[83] (**Eq. 1.21**), and they take the derivative of thermal conductivity with respect to temperature, resulting in

$$\frac{\kappa}{\kappa_0} = \left(\frac{T}{T_0}\right)^{-N} \tag{1.30a}$$

$$N = \left[\frac{1}{3} - \left(\frac{\partial \ln v}{\partial \ln V}\right)_P\right] \tag{1.30b}$$

Their modeling results match old measurements of several molten metals within 4.25%, but old measurements were using unreliable steady-state techniques. There is room to examine the old liquid thermal conductivity model from Horrocks & McLaughlin[83] with more recent and reliable measurement data. It is possible to bridge it closer to the phonon gas model with its ideas of the transmission probability of vibrational energy between neighboring molecules, which is similar to work for modeling heat transport in polycrystalline silicon with nano-sized grains[99].

1.9 Molecular dynamics simulations

Computer simulations are a critical tool in modeling the behavior of high temperature liquids due to the difficulties of experimental measurements and formulating a satisfactory analytical model. The details of molecular dynamics (MD) simulations have incredible depth and history, and they are covered by comprehensive books[100,101], and the use of MD for thermal conductivity calculations have also been well reviewed[74,102]. Here, we provide a brief background in the two approaches to obtain thermal conductivity in MD simulations – equilibrium Green-Kubo calculations and non-equilibrium 'direct methods' – and show results comparing molten salt thermal conductivity from experimental measurements, analytical models, and MD simulations.

MD simulations begin with the Hamiltonian of a liquid system – the potential field (location of every particle and interaction potential between particles) and kinetic energy (mass and initial velocity). From the initial conditions, Newton's equations of motion of every particle are used to trace the trajectory of particles for the desired simulation time – the force exerted on each particle is calculated from the potential field, then the velocity of each particle is updated and multiplied by the time step to also obtain the new position of each particle. The forces are then recalculated based on the new positions to continue the sequence. If a particle crosses the simulation's geometric boundaries, it appears on the other side to conserve the number of particles. The particles in the system continue to take steps in time and space until the total simulation time is reached. There is a tremendous amount of data from recording the momentum and position of hundreds to thousands of particles for the simulation time, and there are many ways of using that data to calculate the thermophysical properties of interest. The main concerns that researchers must consider during an MD simulation are: using enough

particles to prevent size and surface effects from influencing the results meant for bulk liquids; running the simulation for a long enough time (~1 ns) with small enough time steps (~5-10 ps) to provide sufficient statistics for thermal transport calculations; and choosing a suitable potential and cutoff radius for calculating the force on each particle. Further subtleties arise depending on how thermal conductivity is obtained from an MD simulation.

The Green-Kubo equation, an equilibrium approach, for the thermal conductivity of an isotropic solid is

$$\kappa(T) = \frac{V}{3k_B T^2} \int_0^\infty \langle J_Q(t) \cdot J_Q(0) \rangle dt \qquad (1.31)$$

Where $J_Q(t)$ is the heat flux at time t, and $\langle J_Q(t) \cdot J_Q(0) \rangle$ is the autocorrelation of heat flux. A spectral analysis of the autocorrelation function can be done in MD to find the frequency dependent thermal conductivity and how much different vibrational modes contribute to the overall thermal conductivity[74].

$$\kappa(\omega) = \frac{V}{3k_B T^2} \int_0^\infty \langle J_Q(t) \cdot J_Q(0) \rangle e^{-i\omega t} dt \qquad (1.32a)$$

$$\kappa(\omega) = \frac{V}{3k_B T^2} \int_0^\infty \langle J_Q(0) \cdot J_Q(0) \rangle e^{-t/\tau} e^{-i\omega t} dt \qquad (1.32b)$$

$$\kappa(\omega) = \frac{V \langle |J_Q(0)|^2 \rangle}{3k_B T^2 (i\omega + 1/\tau)} \qquad (1.32c)$$

$$|\kappa(\omega)| = \frac{\kappa(0)}{\sqrt{1 + (\omega\tau)^2}} \qquad (1.32d)$$

Where τ is the decay time of the heat flux autocorrelation function and ω is the frequency of the vibrational mode.

In a non-equilbrium MD simulation, a temperature gradient can be imposed on a liquid system, and the resulting heat flux can be used to calculate the thermal conductivity of the system (**Eq. 1.1**). The reverse can also be done, where a heat flux is applied to a system, and the resulting temperature gradient is used to calculate the thermal conductivity (**Eq. 1.1**). These are direct methods of 'measuring' thermal conductivity in MD that put a liquid system out of equilibrium before extracting thermal conductivity.

Non-equilibrium MD simulations adjust several parameters that can change the modeling results. To name a few: altering the Boltzmann statistics by changing the momentum or energy distribution to induce a temperature gradient, using periodic boundary conditions or not when applying heat flux for nonequilibrium simulations, and measuring the temperature of the system in different areas and at different times leading to varying results.

1.10 Comparison of experimental, analytical models, and computer simulations

Gheribi et al.[9] compared their analytical model predictions (**Eq. 25**) with previous MD simulations and experimental measurements of molten chloride and fluoride salts (see **Figure 1.16** for lithium fluoride and sodium chloride). They showed that MD simulations generally overestimate experimental thermal conductivity measurements of molten salts by ~20-30%.
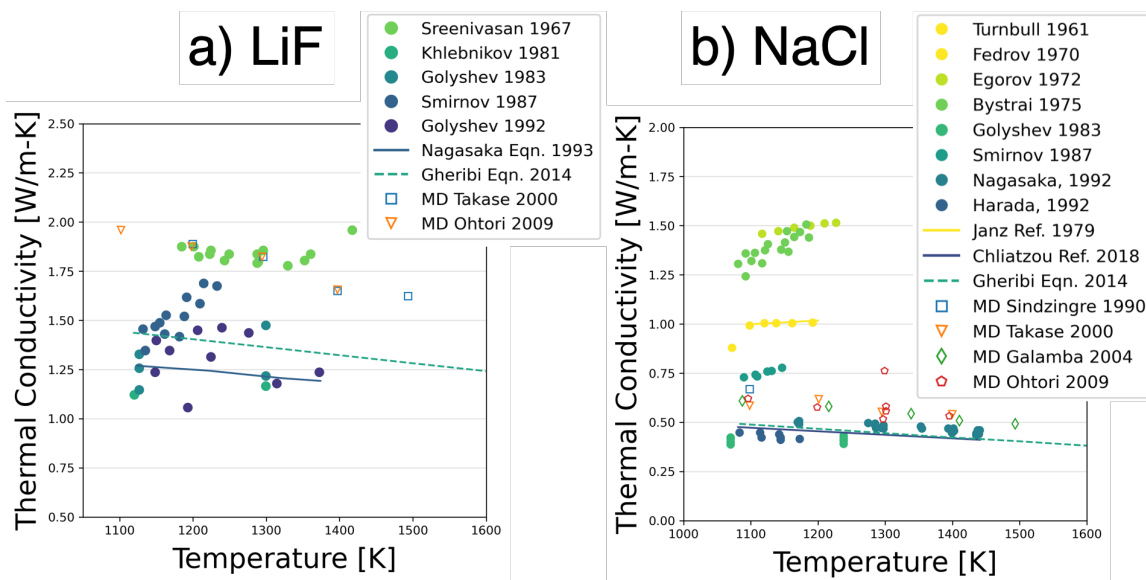
Figure 1.16. Molten salts – a) LiF and b) NaCl – comparison of thermal conductivity from experimental measurements, analytical model, and molecular dynamics from adapted from Gheribi et al.[9] and Chliatzou et al.[8]

Last, we highlight a few MD results for molten salts and metals. Ding et al.[103] used non-equilibrium MD simulations to obtain thermal conductivity of molten sodium and potassium carbonate that matched well with a single measurement from time-domain, forced Rayleigh scattering – more experimental measurements would help add confidence to these results. Smith et al.[104] used equilibrium MD simulations to find the thermal conductivity of molten LiF-BeF_2 – an important molten salt for advanced nuclear reactors; their MD results overestimate thermal

conductivity by ~0.384 W/m-K, which is again ~20-30% higher than experimental measurements and the analytical model from Gheribi et al. (**Eq. 1.25**). They proposed a constant offset of their MD results by 0.384 W/m-K across the entire temperature range to better match previous experimental results – this data fitting may turn out to be unnecessary if previous experimental results themselves are incorrect, and future results could be closer to their MD results. Yan et al.[105] performed non-equilibrium MD simulations of molten iron to find the 'phonon' contribution to the total thermal conductivity. They added the 'phonon' contribution to the electronic contribution, calculated from electrical conductivity measurements and the Wiedemann-Franz law, and their results were within 1.2% of experimental laser flash results from Nishi et al.[46]

Understanding high temperature liquid thermal conductivity is critical for next generation concentrated solar and nuclear plants that are run on molten salts and metals. However, high temperature experimental measurements are riddled with errors, and there is no well-established theoretical understanding for how heat conducts in liquids.

In this work, we reviewed thermal conductivity measurement techniques, and we grouped them into three buckets: steady-state, time-domain, and frequency-domain measurements. We discussed the various approaches used to minimize errors from convection, radiation, and corrosion that are critical for reliable measurements of high-temperature liquid thermal conductivity. Our general takeaway is that frequency-domain measurements are ideal for high-temperature liquid thermal conductivity measurements since the probed volume can be kept below 1 μL to minimize convection errors, and radiation and corrosion have also been shown to be negligible; the main disadvantage is the relatively long measurement times, which is worth it for reliable, and repeatable data. Careful time-domain measurements that

systematically account for convection, radiation, and corrosion are also reliable; their short measurement time and standard use for room-temperature liquids make them a reliable work-horse. Steady-state measurements can work for high temperature liquids in theory, if the gap size between the heating source and sink is kept below 200 µm to suppress convection, but in practice the long settling times to reach steady-state and the practical difficulties in creating such a small gap-size lead us to recommend avoiding steady-state measurements for high temperature liquids.

To make sense of experimental data, analytical models and computer simulations can be used to better understand the mechanism of heat conduction in various liquids and predict the thermal conductivity of liquids in different settings – higher pressure, different compositions, and more. Previous liquid thermal conductivity models were grouped into two main categories: modified kinetic gas and quasi-crystalline models. The most successful models for matching experimental data are quasi-crystalline models of liquids that posit that phonon-like vibrational modes conduct heat in liquids, and indeed phonon-like dispersions have been experimentally measured in liquids. We provided a framework to group liquids based on their intermolecular interaction energy – simple liquids with Van der Waals forces, molecular liquids with Keesom dipole-dipole interactions, molten salts with Coulombic forces, and molten metals with metallic bonding. Intermolecular interaction energy in a liquid dictates its short-range ordering and how vibrational-modes can be stored within its molecules and transferred to neighboring molecules. We discussed the variations between previous quasi-crystalline models of liquid thermal conductivity and how it could be due to how energy is stored and transferred differently for different types of liquids. Then, we discussed how frequency-dependent studies of a liquid's vibrational modes can further develop quasi-crystalline models of liquids. For

molten metals, we showed that the Wiedemann-Franz law provides a reasonable approximation of thermal conductivity from electron transport, but that the Lorenz number changes with temperature, pressure, and elemental composition – electrical conductivity measurements cannot be used to measure thermal conductivity. To provide a better atomistic picture of liquids, molecular dynamics is also a widely used tool to model liquid thermal conductivity, and we briefly described equilibrium versus non-equilibrium methods for extracting thermal conductivity from molecular dynamics simulations, as well as their use for providing frequency-dependent properties of vibrational modes in liquids.

Further experimental measurements and modeling of high temperature liquids are paramount for engineering applications that harness molten salts and molten metals, and we reviewed the cutting edge experimental and modeling techniques for researchers.

Acknowledgements

References

(1)   Chu, S.; Majumdar, A. Opportunities and Challenges for a Sustainable Energy Future. *Nature* **2012**, *488* (7411), 294–303. https://doi.org/10.1038/nature11475.

(2)   Gary E. Rochau; Jim J. Pasch; Glenn Cannon; Matt Carlson; Darryn Fleming; Alan Kruizenga; Rob Sharpe; Mollye Wi. *Supercritical CO2 Brayton Cycles*; 2014.

(3)   Thiel, G. P.; Stark, A. K. To Decarbonize Industry, We Must Decarbonize Heat. *Joule*. Cell Press March 17, 2021, pp 531–550. https://doi.org/10.1016/j.joule.2020.12.007.

(4)   Zhao, A. Z.; Wingert, M. C.; Chen, R.; Garay, J. E. Phonon Gas Model for Thermal Conductivity of Dense, Strongly Interacting Liquids. *J. Appl. Phys.* **2021**, *129* (23), 235101. https://doi.org/10.1063/5.0040734.

(5)   Mclaughlin, E. The Thermal Conductivity of Liquids and Dense Gases. *Chem. Rev.* **1964**, *64* (4), 389–428.

(6)   Lemmon, E. W.; McLinden, M. O.; Friend, D. G. *"Thermophysical Properties of Fluid Systems" in NIST Chemistry WebBook, NIST Standard Reference Database Number 69*; Linstrom, P. J., Mallard, W. G., Eds.; National Institute of Standards and Technology: Gaithersburg MD, 20899, 2020.

(7)   Zhao, A. Z.; Wingert, M. C.; Garay, J. E. Frequency-Domain Hot-Wire Measurements of Molten Nitrate Salt Thermal Conductivity. *J. Chem. Eng. Data* **2020**, acs.jced.0c00621. https://doi.org/10.1021/acs.jced.0c00621.

(8)   Chliatzou, C. D.; Assael, M. J.; Antoniadis, K. D.; Huber, M. L.; Wakeham, W. A. Reference Correlations for the Thermal Conductivity of 13 Inorganic Molten Salts. *J. Phys. Chem. Ref. Data* **2018**, *47*, 33104. https://doi.org/10.1063/1.5052343.

(9)   Gheribi, A. E.; Torres, J. A.; Chartrand, P. Recommended Values for the Thermal Conductivity of Molten Salts between the Melting and Boiling Points. *Sol. Energy Mater. Sol. Cells* **2014**, *126*, 11–25. https://doi.org/10.1016/J.SOLMAT.2014.03.028.

(10)   Agazhanov, A.; Abdullaev, R. N.; Samoshkin, D. A.; Stankus, S. V. Thermal Conductivity of Lithium, Sodium and Potassium in the Liquid State. *Phys. Chem. Liq.* **2020**, *58* (6), 760–768. https://doi.org/10.1080/00319104.2019.1636377.

(11)   Assael, M. J.; Chatzimichailidis, A.; Antoniadis, K. D.; Wakeham, W. A.; Huber, M. L.; Fukuyama, H. Reference Correlations for the Thermal Conductivity of Liquid Copper, Gallium, Indium, Iron, Lead, Nickel and Tin. *High Temp. - High Press.* **2017**, *46* (6), 391–416.

(12)   Assael, M. J.; Antoniadis, K. D.; Wakeham, W. A.; Huber, M. L.; Fukuyama, H. Reference Correlations for the Thermal Conductivity of Liquid Bismuth, Cobalt, Germanium, and Silicon. *J. Phys. Chem. Ref. Data* **2017**, *46* (3).

https://doi.org/10.1063/1.4991518.

(13)   Nunes, V. M. .; Lourenço, M. J. V.; Santos, F. J. V.; Nieto De Castro, C. A. Importance of Accurate Data on Viscosity and Thermal Conductivity in Molten Salts Applications. *J. Chem. Eng. Data* **2003**, *48* (3), 446–450. https://doi.org/10.1021/je020160l.

(14)   Holcomb, D. E.; Cetiner, S. M. *An Overview of Liquid-Fluoride-Salt Heat Transport Systems*; 2010.

(15)   Le Neindre, B.; Tufeu, R.; Sirota, A. M. Steady-State Methods for Thermal Conductivity. In *Measurement of the Transport Properties of Fluids*; Wakeham, W. A., Nagashima, A., Sengers, J. V., Eds.; Blackwell Scientific Publications: London, 1991; pp 111–160.

(16)   Wang, X.; Xu, X.; Choi, S. U. S. Thermal Conductivity of Nanoparticle – Fluid Mixture. *J. Thermophys. HEAT Transf.* **1999**, *13* (4), 474–480.

(17)   Santini, R.; Tadrist, L.; Pantaloni, J.; Cerisier, P. Measurement of Thermal Conductivity of Molten Salts in the Range 100-500°C. *Int. J. Heat Mass Transf.* **1984**, *27* (4), 623–626. https://doi.org/10.1016/0017-9310(84)90034-6.

(18)   Bloom, H.; Doroszkowski, A.; Tricklebank, S. B. Molten Salt Mixtures. IX. The Thermal Conductivities of Molten Nitrate Systems. *Aust. J. Chem.* **1965**, *18* (8), 1171–1176. https://doi.org/10.1071/CH9651171.

(19)   Tufeu, R.; Petitet, J. P.; Denielou, L.; Le Neindre, B. Experimental Determination of the Thermal Conductivity of Molten Pure Salts and Salt Mixtures. *Int. J. Thermophys.* **1985**, *6* (4), 315–330. https://doi.org/10.1007/BF00500266.

(20)   Nagasaka, Y.; Nagashima, A. Absolute Measurement of the Thermal Conductivity of Electrically Conducting Liquids by the Transient Hot-Wire Method. *J. Phys. E.* **1981**, *14* (12), 1435–1440. https://doi.org/10.1088/0022-3735/14/12/020.

(21)   Wakeham, W. A.; Nagashima, A. (Akira); Sengers, J. V. *Measurement of the Transport Properties of Fluids*; Blackwell Scientific Publications, 1991.

(22)   Tada, Y.; Harada, M.; Tanigaki, M.; Eguchi, W. Laser Flash Method for Measuring Thermal Conductivity of Liquids—Application to Low Thermal Conductivity Liquids. *Rev. Sci. Instrum.* **1978**, *49* (9), 1305–1314. https://doi.org/10.1063/1.1135573.

(23)   Srinivasan, N. S.; Xiao, X. G.; Seetharaman, S. Radiation Effects in High-temperature Thermal Diffusion Measurements Using the Laser-flash Method. *J. Appl. Phys.* **1994**, *75* (5), 2325–2331. https://doi.org/10.1063/1.356250.

(24)   Wingert, M. C.; Zhao, A. Z.; Kodera, Y.; Obrey, S. J.; Garay, J. E. Frequency-Domain Hot-Wire Sensor and 3D Model for Thermal Conductivity Measurements of Reactive and Corrosive Materials at High Temperatures. *Rev. Sci. Instrum.* **2020**, *91* (5), 054904.

https://doi.org/10.1063/1.5138915.

(25)   Zeng, J.; Chung, K. M.; Wang, Q.; Wang, X.; Pei, Y.; Li, P.; Chen, R. Measurement of High-Temperature Thermophysical Properties of Bulk and Coatings Using Modulated Photothermal Radiometry. *Int. J. Heat Mass Transf.* **2021**, *170* (May), 120989. https://doi.org/10.1016/j.ijheatmasstransfer.2021.120989.

(26)   Zeng, J.; Chung, K. M.; Adapa, S. R.; Feng, T.; Chen, R. In-Situ Thermal Transport Measurement of Flowing Fluid Using Modulated Photothermal Radiometry. *ArXiv* **2021**.

(27)   Kobatake, H.; Fukuyama, H.; Minato, I.; Tsukada, T.; Awaji, S. Noncontact Measurement of Thermal Conductivity of Liquid Silicon in a Static Magnetic Field. *Appl. Phys. Lett.* **2007**, *90* (9), 094102. https://doi.org/10.1063/1.2710220.

(28)   Tsukada, T.; Fukuyama, H.; Kobatake, H. Determination of Thermal Conductivity and Emissivity of Electromagnetically Levitated High-Temperature Droplet Based on the Periodic Laser-Heating Method: Theory. *Int. J. Heat Mass Transf.* **2007**, *50* (15–16), 3054–3061. https://doi.org/10.1016/J.IJHEATMASSTRANSFER.2006.12.026.

(29)   Nieto de Castro, C. A.; Lourenço, M. J. V. Towards the Correct Measurement of Thermal Conductivity of Ionic Melts and Nanofluids. *Energies* **2019**, *13* (1), 99. https://doi.org/10.3390/en13010099.

(30)   Raiman, S. S.; Lee, S. Aggregation and Data Analysis of Corrosion Studies in Molten Chloride and Fluoride Salts. *Journal of Nuclear Materials*. Elsevier B.V. December 1, 2018, pp 523–535. https://doi.org/10.1016/j.jnucmat.2018.07.036.

(31)   Kakaç, S. (Sadık); Yener, Y. *Convective Heat Transfer*, 2nd ed.; CRC Press: Boca Raton, 1995.

(32)   Cooke, J. W. *Development of the Variable-Gap Technique for Measuring the Thermal Conductivity of Fluoride Salt Mixtures*; 1973.

(33)   Sklyarchuk, V.; Plevachuk, Y. A Modified Steady State Apparatus for Thermal Conductivity Measurements of Liquid Metals and Semiconductors. *Meas. Sci. Technol.* **2005**, *16* (2), 467–471. https://doi.org/10.1088/0957-0233/16/2/019.

(34)   Kurt, H.; Kayfeci, M. Prediction of Thermal Conductivity of Ethylene Glycol-Water Solution by Using Artificial Neural Networks Prediction of Thermal Conductivity of Ethylene Glycol – Water Solutions by Using Artificial Neural Networks. *Appl. Energy* **2009**, *86* (10), 2244–2248. https://doi.org/10.1016/j.apenergy.2008.12.020.

(35)   Zhao, Q. G.; Hu, C. X.; Liu, S. J.; Guo, H.; Wu, Y. T. The Thermal Conductivity of Molten NaNO3, KNO3, and Their Mixtures. *Energy Procedia* **2017**, *143*, 774–779. https://doi.org/10.1016/j.egypro.2017.12.761.

(36) Yamasue, E.; Susa, M.; Fukuyama, H.; Nagata, K. Thermal Conductivities of Silicon and Germanium in Solid and Liquid States Measured by Non-Stationary Hot Wire Method with Silica Coated Probe. *J. Cryst. Growth* **2002**, *234* (1), 121–131. https://doi.org/10.1016/S0022-0248(01)01673-6.

(37) Antoniadis, K. D.; Tertsinidou, G. J.; Assael, M. J.; Wakeham, W. A. Necessary Conditions for Accurate, Transient Hot-Wire Measurements of the Apparent Thermal Conductivity of Nanofluids Are Seldom Satisfied. *Int. J. Thermophys.* **2016**, *37* (8), 78. https://doi.org/10.1007/s10765-016-2083-8.

(38) Nagasaka, Y.; Nagashima, A. Absolute Measurement of the Thermal Conductivity of Electrically Conducting Liquids by the Transient Hot-Wire Method. *J. Phys. E.* **1981**, *14* (12), 1435.

(39) Alloush, A.; Gosney, W. B.; Wakeham, W. A. A Transient Hot-Wire Instrument for Thermal Conductivity Measurements in Electrically Conducting Liquids at Elevated Temperatures. *Int. J. Thermophys.* **1982**, *3* (3), 225–235. https://doi.org/10.1007/BF00503318.

(40) Yamasue, E.; Susa, M.; Fukuyama, H.; Nagata, K. *Nonstationary Hot Wire Method with Silica-Coated Probe for Measuring Thermal Conductivities of Molten Metals*.

(41) Omotani, T.; Nagasaka, Y.; Nagashima, A. Measurement of the Thermal Conductivity of KNO3-NaNO3 Mixtures Using a Transient Hot-Wire Method with a Liquid Metal in a Capillary Probe. *Int. J. Thermophys.* **1982**, *3* (1).

(42) Schiffres, S. N.; Malen, J. A.; Schiffres, S. N.; Malen, J. A. Improved 3-Omega Measurement of Thermal Conductivity in Liquid , Gases , and Powders Using a Metal-Coated Optical Fiber Improved 3-Omega Measurement of Thermal Conductivity in Liquid , Gases , and Powders Using a Metal-Coated Optical Fiber. **2015**, *064903* (2011), 0–7. https://doi.org/10.1063/1.3593372.

(43) Nagai, H.; Mamiya, M.; Castillo, M.; Okutani, T. Development of Hot-Disk Sensor for Molten Metal, and the Thermal Conductivity Measurement of Molten Bismuth and Tin Using Hot-Disk Method. *Jpn. J. Appl. Phys.* **2006**, *45* (8R), 6455. https://doi.org/10.1143/JJAP.45.6455.

(44) Srinivasan, N. S.; Xiao, X. G.; Seetharaman, S. Laser-Flash Method Radiation Effects in High-Temperature Using the Laser-Flash Method t Ermal Diffusion Measurements. **1995**, *2325* (1994). https://doi.org/10.1063/1.356250.

(45) Tada, Y.; Harada, M.; Tanlgakl, M.; Eguchl, W. *Laser Flash Method for Measuring Thermal Conductivity of Liquids. Application to Molten Salts*; 1981; Vol. 20.

(46) Nishi, T.; Shibata, H.; Ohta, H.; Waseda, Y. Thermal Conductivities of Molten Iron, Cobalt, and Nickel by Laser Flash Method. *Metall. Mater. Trans. A Phys. Metall. Mater. Sci.* **2003**, *34* (12), 2801–2807. https://doi.org/10.1007/S11661-003-0181-2.

(47)   Nagasaka, Y.; Nakazawa, N.; Nagashima, A. Experimental Determination of the Thermal Diffusivity of Molten Alkali Halides by the Forced Rayleigh Scattering Method. I. Molten LiCl, NaCl, KCl, RbCl, and CsCl. *Int. J. Thermophys.* **1992**, *13* (4), 555–574. https://doi.org/10.1007/BF00501941.

(48)   Nagasaka, Y.; Nagashima, A. Measurement of the Thermal Diffusivity of Molten KCl up to 1000°C by the Forced Rayleigh Scattering Method. *Int. J. Thermophys. 1988 96* **1988**, *9* (6), 923–931. https://doi.org/10.1007/BF01133260.

(49)   Frez, C.; Diebold, G. J.; And, C. D. T.; Yu, S. Determination of Thermal Diffusivities, Thermal Conductivities, and Sound Speeds of Room-Temperature Ionic Liquids by the Transient Grating Technique. *J. Chem. Eng. Data* **2006**, *51* (4), 1250–1255. https://doi.org/10.1021/JE0600092.

(50)   Choi, S. R.; Kim, J.; Kim, D. 3ω Method to Measure Thermal Properties of Electrically Conducting Small-Volume Liquid. *Rev. Sci. Instrum.* **2007**, *78* (8), 084902. https://doi.org/10.1063/1.2777162.

(51)   Choi, S. R.; Kim, D. Real-Time Thermal Characterization of 12nl Fluid Samples in a Microchannel. *Rev. Sci. Instrum.* **2008**, *79* (6), 064901. https://doi.org/10.1063/1.2937180.

(52)   Roy-Panzer, S.; Kodama, T.; Lingamneni, S.; Panzer, M. A.; Asheghi, M.; Goodson, K. E. Thermal Characterization and Analysis of Microliter Liquid Volumes Using the Three-Omega Method. *Rev. Sci. Instrum.* **2015**, *86* (2), 024901. https://doi.org/10.1063/1.4907353.

(53)   Lee, S. Thermal Conductivity Measurement of Fluids Using the 3 ω Method. **2016**, *024901* (2009). https://doi.org/10.1063/1.3082036.

(54)   Heyd, R.; Hadaoui, A.; Fliyou, M.; Koumina, A.; Ameziane, L. E. H.; Outzourhit, A.; Saboungi, M.-L. Development of Absolute Hot-Wire Anemometry by the 3ω Method. *Rev. Sci. Instrum.* **2010**, *81* (4), 044901. https://doi.org/10.1063/1.3374015.

(55)   Karthik, R.; Harish Nagarajan, R.; Raja, B.; Damodharan, P. Thermal Conductivity of CuO–DI Water Nanofluids Using 3-ω Measurement Technique in a Suspended Micro-Wire. *Exp. Therm. Fluid Sci.* **2012**, *40*, 1–9. https://doi.org/10.1016/J.EXPTHERMFLUSCI.2012.01.006.

(56)   Yusibani, E.; Woodfield, P. L.; Fujii, M.; Shinzato, K.; Zhang, X.; Takata, Y. Application of the Three-Omega Method to Measurement of Thermal Conductivity and Thermal Diffusivity of Hydrogen Gas. *Int. J. Thermophys. 2009 302* **2009**, *30* (2), 397–415. https://doi.org/10.1007/S10765-009-0563-9.

(57)   López-Bueno, C.; Bugallo, D.; Leborán, V.; Rivadulla, F. Sub-ML Measurements of the Thermal Conductivity and Heat Capacity of Liquids. *Phys. Chem. Chem. Phys.* **2018**, *20* (10), 7277–7281. https://doi.org/10.1039/c8cp00165k.

(58) Israelachvili, J. N. *Intermolecular and Surface Forces*; Academic Press, 2011.

(59) Israelachvili, J. N. *Intermolecular and Surface Forces: Third Edition*; Elsevier Inc., 2011. https://doi.org/10.1016/C2011-0-05119-0.

(60) Wilding, M. C.; Wilson, M.; Ribeiro, M. C. C.; Benmore, C. J.; Weber, J. K. R.; Alderman, O. L. G.; Tamalonis, A.; Parise, J. B. The Structure of Liquid Alkali Nitrates and Nitrites. *Phys. Chem. Chem. Phys* **2017**, *19*, 21625. https://doi.org/10.1039/c7cp03465b.

(61) Soper, A. K. The Radial Distribution Functions of Water and Ice from 220 to 673 K and at Pressures up to 400 MPa. *Chem. Phys.* **2000**. https://doi.org/10.1016/S0301-0104(00)00179-8.

(62) Adya, A. K.; Kalugin, O. N.; Howells, S.; Bianchi, L.; Adya, A. K.; Kalugin, N.; Wormald, C. J. *The Structure of Liquid Methanol: A Molecular Dynamics Study Using a Six-Site Model Related Content Dynamics and Structure of Nickel Chloride-Methanol Solutions: Quasi-Elastic Neutronscattering and Molecular Dynamics Simulations The Structure of Liquid Methanol: A Molecular Dynamics Study Using a Six-Site Model*; 1999; Vol. 11.

(63) Yoon, B. J.; Jhon, M. S.; Eyring, H. *Radial Distribution Function of Liquid Argon According to Significant Structure Theory*; 1981; Vol. 78.

(64) Murphy, R. D.; Klein, M. L. Distribution Function of Liquid Sodium. *Phys. Rev. A* **1973**, *8* (5), 2640–2644.

(65) Rumble, J. R.; Lide, D. R.; Bruno, T. J. *"Dipole Moments," in CRC Handbook of Chemistry and Physics*, 100th Edit.; Rumble, J. R., Ed.; CRC Press/Taylor & Francis: Boca Raton, FL.

(66) Lane, J. R. CCSDTQ Optimized Geometry of Water Dimer. *J. Chem. Theory Comput.* **2013**, *9* (1), 316–323. https://doi.org/10.1021/ct300832f.

(67) Das, A.; Mandal, P. K.; Lovas, F. J.; Medcraft, C.; Walker, N. R.; Arunan, E. The H_2S Dimer Is Hydrogen-Bonded: Direct Confirmation from Microwave Spectroscopy. *Angew. Chemie Int. Ed.* **2018**, *57* (46), 15199–15203. https://doi.org/10.1002/anie.201808162.

(68) Perkins, M. A.; Barlow, K. R.; Dreux, K. M.; Tschumper, G. S. Anchoring the Hydrogen Sulfide Dimer Potential Energy Surface to Juxtapose (H2S)2 with (H2O)2. *J. Chem. Phys.* **2020**, *152* (21), 214306. https://doi.org/10.1063/5.0008929.

(69) Lousada, C. M.; Korzhavyi, P. A. The H2S Dimer Revisited – Insights from Wave-Function and Density Functional Theory Methods. Ab Initio Molecular Dynamics Simulations of Liquid H2S. *Comput. Theor. Chem.* **2020**, *1180*, 112821. https://doi.org/10.1016/j.comptc.2020.112821.

(70) Ziman, J. M. *Models of Disorder*; Cambridge University Press: Cambridge, 1979.

(71) Enskog, D. Kungliga Svenska Vatenskapsakademiens Handlingar (For English Translation, See Brush, S.G., 1972 Kinetic Theory, Vol. 3, Pergamon Press, Oxford.). *Ny Föld* **1922**, *63* (2).

(72) Chapman, S., and Cowling, T. G. *The Mathematical Theory of Non-Uniform Gases*; Cambridge University Press: London, 1953.

(73) Velarde, M. G. On the Enskog Hard-Sphere Kinetic Equation and the Transport Phenomena of Dense Simple Gases. In *Transport Phenomena*; Kirczenow, G., Marro, J., Eds.; Springer-Verlag: Berlin, 1974; pp 289–336.

(74) Chen, G. *Nanoscale Energy Transport and Conversion: A Parallel Treatment of Electrons, Molecules, Phonons, and Photons*; Oxford University Press: New York, 2005.

(75) Assael, M. J.; Sykioti, E. A.; Huber, M. L.; Perkins, R. A. Reference Correlation of the Thermal Conductivity of Ethanol from the Triple Point to 600 K and up to 245 MPa. *Therm. Conduct. ethanol J. Chem. Phys.* **2013**, *42*, 174503. https://doi.org/10.1063/1.4797368.

(76) Sykioti, E. A.; Assael, M. J.; Huber, M. L.; Perkins, R. A. Reference Correlation of the Thermal Conductivity of Methanol from the Triple Point to 660 K and up to 245 MPa. *J. Phys. Chem. Ref Data* **2013**, *42*, 43101. https://doi.org/10.1063/1.4829449.

(77) Assael, M. J.; Mylona, S. K.; TsiglifisiM L Huber, C. A.; Perkins, R. A.; Assael S K Mylona, M. J.; Tsiglifisi, C. A.; Huber, M. L. Reference Correlation of the Thermal Conductivity of N-Hexane from the Triple Point to 600 K and up to 500 MPa. *Cit. J. Phys. Chem. Ref. Data* **2013**, *42*, 13106. https://doi.org/10.1063/1.4793335.

(78) Assael, M. J.; Bogdanou, I.; MylonaM L Huber, S. K.; PerkinsV Vesovic, R. A.; Assael I Bogdanou, M. J.; Mylona, S. K.; Huber, M. L.; Perkins, R. A.; Vesovic, V. Reference Correlation of the Thermal Conductivity of N-Heptane from the Triple Point to 600 K and up to 250 MPa. *J. Phys. Chem. Ref. Data* **2013**, *42*, 23101. https://doi.org/10.1063/1.4794091.

(79) Gheribi, A. E.; Chartrand, P. Thermal Conductivity of Molten Salt Mixtures: Theoretical Model Supported by Equilibrium Molecular Dynamics Simulations. *J. Chem. Phys.* **2016**, *144* (8), 084506. https://doi.org/10.1063/1.4942197.

(80) Bridgman, P. W. The Thermal Conductivity of Liquids under Pressure. *Proc. Am. Acad. Arts Sci.* **1923**, *59* (7), 141–169.

(81) Kincaid, J. F.; Eyring, H. Free Volumes and Free Angle Ratios of Molecules in Liquids. *Struct. J. Chem. Phys.* **1938**, *6*, 283. https://doi.org/10.1063/1.1750134.

(82) Powell, R. E.; Roseveare, W. E.; Eyring, H. Diffusion, Thermal Conductivity, and Viscous Flow of Liquids. *Ind. Eng. Chem.* **1941**, *33* (4), 430–435.

(83)   Horrocks, J. K.; Mclaughlin, E. *Thermal Conductivity of Simple Molecules in the Condensed State*. 1959.

(84)   Toberer, E. S.; Baranowski, L. L.; Dames, C. Advances in Thermal Conductivity. *Annu. Rev. Mater. Res* **2012**, *42*, 179–209. https://doi.org/10.1146/annurev-matsci-070511-155040.

(85)   Trachenko, K. Heat Capacity of Liquids: An Approach from the Solid Phase. *Phys. Rev. B* **2008**, *78* (10). https://doi.org/10.1103/PhysRevB.78.104201.

(86)   Bolmatov, D.; Brazhkin, V. V.; Trachenko, K. The Phonon Theory of Liquid Thermodynamics. *Sci. Rep.* **2012**, *2*. https://doi.org/10.1038/SREP00421.

(87)   Trachenko, K.; Brazhkin, V. V. Collective Modes and Thermodynamics of the Liquid State. *Reports Prog. Phys.* **2016**, *79* (1), 016502. https://doi.org/10.1088/0034-4885/79/1/016502.

(88)   Slack, G. A. The Thermal Conductivity of Nonmetallic Crystals. *Solid State Phys. - Adv. Res. Appl.* **1979**, *34* (C), 1–71. https://doi.org/10.1016/S0081-1947(08)60359-8.

(89)   Xi, Q.; Zhong, J.; He, J.; Xu, X.; Nakayama, T.; Wang, Y.; Liu, J.; Zhou, J.; Li, B.; Li, and B.; Xi, Q.; Zhong, J.; He, J.; Xu, X.; Nakayama, T.; Wang, Y.; Liu, J.; Zhou, J.; Li, and B. A Ubiquitous Thermal Conductivity Formula for Liquids, Polymer Glass, and Amorphous Solids. *Chinese Phys. Lett.* **2020**, *37* (10), 1–6. https://doi.org/10.1088/0256-307X/37/10/104401.

(90)   DiGuilio, R. M.; Teja, A. S. A Rough Hard-Sphere Model for the Thermal Conductivity of Molten Salts. *Int. J. Thermophys.* **1992**, *13* (5), 855–871. https://doi.org/10.1007/BF00503912.

(91)   Larkin, J. M.; McGaughey, A. J. H. Thermal Conductivity Accumulation in Amorphous Silica and Amorphous Silicon. *Phys. Rev. B - Condens. Matter Mater. Phys.* **2014**, *89* (14), 144303. https://doi.org/10.1103/PhysRevB.89.144303.

(92)   DeAngelis, F.; Muraleedharan, M. G.; Moon, J.; Seyf, H. R.; Minnich, A. J.; McGaughey, A. J. H.; Henry, A. Thermal Transport in Disordered Materials. *Nanoscale Microscale Thermophys. Eng.* **2018**, 1–36. https://doi.org/10.1080/15567265.2018.1519004.

(93)   Salanne, M.; Marrocchelli, D.; Merlet, C.; Ohtori, N.; Madden, P. A. Thermal Conductivity of Ionic Systems from Equilibrium Molecular Dynamics. *J. Phys. Condens. Matter* **2011**, *23* (10), 102101. https://doi.org/10.1088/0953-8984/23/10/102101.

(94)   March, N. H. Liquid Metals: Concepts and Theory. *Liq. Met.* **1990**. https://doi.org/10.1017/CBO9780511563928.

(95)   Secco, R. A. Thermal Conductivity and Seebeck Coefficient of Fe and Fe-Si Alloys: Implications for Variable Lorenz Number. *Phys. Earth Planet. Inter.* **2017**, *265*, 23–34.

https://doi.org/10.1016/J.PEPI.2017.01.005.

(96) Pozzo, M.; Davies, C.; Gubbins, D.; Alfè, D. Thermal and Electrical Conductivity of Iron at Earth's Core Conditions. *Nature* **2012**, *485* (7398), 355–358. https://doi.org/10.1038/nature11031.

(97) Viswanath, D. S.; Rao, M. B. Thermal Conductivity of Liquids and Its Temperature Dependence. *J. Phys. D Appl. Phys.* **1970**, *3*.

(98) Viswanath, D. S.; Mathur, B. C. Thermal Conducivity of Liquid Metals and Alloys. **1972**, *3* (July).

(99) Wang, Z.; Alaniz, J. E.; Jang, W.; Garay, J. E.; Dames, C. Thermal Conductivity of Nanocrystalline Silicon- Importance of Grain Si. *Nano Lett.* **2011**, 2206–2213.

(100) Frenkel, D.; Smit, B. *Understanding Molecular Simulation: From Algorithms to Applications*, 2nd ed.; Elsevier, 2002. https://doi.org/10.1016/B978-0-12-267351-1.X5000-7.

(101) Allen, M. P.; Tildesley, D. J. Computer Simulation of Liquids: Second Edition. *Comput. Simul. Liq. Second Ed.* **2017**, 1–626. https://doi.org/10.1093/OSO/9780198803195.001.0001.

(102) McGaughey, A. J. H.; Kaviany, M. *Phonon Transport in Molecular Dynamics Simulations: Formulation and Thermal Conductivity Prediction*; Elsevier Masson SAS, 2006; Vol. 39. https://doi.org/10.1016/S0065-2717(06)39002-8.

(103) Ding, J.; Pan, G.; Du, L.; Lu, J.; Wang, W.; Wei, X.; Li, J. Molecular Dynamics Simulations of the Local Structures and Transport Properties of Na2CO3 and K2CO3. *Appl. Energy* **2018**, *227*, 555–563. https://doi.org/10.1016/J.APENERGY.2017.07.019.

(104) Smith, A. L.; Capelli, E.; Konings, R. J. M.; Gheribi, A. E. A New Approach for Coupled Modelling of the Structural and Thermo-Physical Properties of Molten Salts. Case of a Polymeric Liquid LiF-BeF2. *J. Mol. Liq.* **2020**, *299*, 112165. https://doi.org/10.1016/J.MOLLIQ.2019.112165.

(105) Yan, H. J.; Zhuang, J. C.; Zhou, P.; Li, Q.; Zhou, C. Q.; Fu, P. Molecular Dynamics Simulation of Thermal Physical Properties of Molten Iron. *Int. J. Heat Mass Transf.* **2017**, *109*, 755–760. https://doi.org/10.1016/J.IJHEATMASSTRANSFER.2017.02.027.

(106) Keblinski, P.; Prasher, R.; Eapen, J. Thermal Conductance of Nanofluids: Is the Controversy Over? *J. Nanoparticle Res.* **2008**, *10* (7), 1089–1097. https://doi.org/10.1007/s11051-007-9352-1.

(107) Elsheikh, A. H.; Sharshir, S. W.; Mostafa, M. E.; Essa, F. A.; Ahmed Ali, M. K. Applications of Nanofluids in Solar Energy: A Review of Recent Advances. *Renew. Sustain. Energy Rev.* **2018**, *82*, 3483–3502. https://doi.org/10.1016/J.RSER.2017.10.108.

(108) Chieruzzi, M.; Cerritelli, G. F.; Miliozzi, A.; Kenny, J. M. *Effect of Nanoparticles on Heat*

Capacity of Nanofluids Based on Molten Salts as PCM for Thermal Energy Storage; 2013. https://doi.org/10.1186/1556-276X-8-448.

(109) Shin, D.; Banerjee, D. Enhancement of Specific Heat Capacity of High-Temperature Silica-Nanofluids Synthesized in Alkali Chloride Salt Eutectics for Solar Thermal-Energy Storage Applications. **2011**. https://doi.org/10.1016/j.ijheatmasstransfer.2010.11.017.

(110) Ueki, Y.; Fujita, N.; Kawai, M.; Shibahara, M. Thermal Conductivity of Molten Salt-Based Nanofluid. *AIP Adv.* **2017**, *7* (5). https://doi.org/10.1063/1.4984770.

(111) Wang, W.; Wu, Z.; Li, B.; Sundén, B. A Review on Molten-Salt-Based and Ionic-Liquid-Based Nanofluids for Medium-to-High Temperature Heat Transfer. *J. Therm. Anal. Calorim. 2018 1363* **2018**, *136* (3), 1037–1051. https://doi.org/10.1007/S10973-018-7765-Y.

(112) Reid, R. S.; Merrigan, M. A.; Sena, J. T. Review of Liquid Metal Heat Pipe Work at Los Alamos. *AIP Conf. Proc.* **1991**, *217* (3), 999–1008. https://doi.org/10.1063/1.40058.

(113) Srimuang, W.; Amatachaya, P. A Review of the Applications of Heat Pipe Heat Exchangers for Heat Recovery. *Renew. Sustain. Energy Rev.* **2012**, *16* (6), 4303–4315. https://doi.org/10.1016/J.RSER.2012.03.030.

(114) Shafieian, A.; Khiadani, M.; Nosrati, A. A Review of Latest Developments, Progress, and Applications of Heat Pipe Solar Collectors. *Renew. Sustain. Energy Rev.* **2018**, *95*, 273–304. https://doi.org/10.1016/J.RSER.2018.07.014.

(115) El-Genk, M. S.; Tournier, J.-M. P. USES OF LIQUID-METAL AND WATER HEAT PIPES IN SPACE REACTOR POWER SYSTEMS. *Front. Heat Pipes* **2011**, *2* (1). https://doi.org/10.5098/FHP.V2.1.3002.

(116) Turchi, C.; Gage, S.; Martinek, J.; Jape, S.; Armijo, K.; Coventry, J.; Pye, J.; Asselineau, C.; Venn, F.; Logie, W.; Fontalvo, A.; Wang, S.; Mcnaughton, R.; Potter, D.; Steinberg, T.; Will, G.; Turchi, C.; Gage, S.; Martinek, J.; Jape, S.; Armijo, K.; Coventry, J.; Pye, J.; Asselineau, C.; Venn, F.; Logie, W.; Fontalvo, A.; Wang, S.; Mcnaughton, R.; Potter, D.; Steinberg, T.; Will, G. *CSP Gen3 : Liquid-Phase Pathway to SunShot*; Golden, CO, 2021.

(117) Amy, C.; Budenstein, D.; Bagepalli, M.; England, D.; DeAngelis, F.; Wilk, G.; Jarrett, C.; Kelsall, C.; Hirschey, J.; Wen, H.; Chavan, A.; Gilleland, B.; Yuan, C.; Chueh, W. C.; Sandhage, K. H.; Kawajiri, Y.; Henry, A. Pumping Liquid Metal at High Temperatures up to 1,673 Kelvin. *Nature* **2017**, *550* (7675), 199–203. https://doi.org/10.1038/nature24054.

(118) Elsheikh, B. M. Safety Assessment of Molten Salt Reactors in Comparison with Light Water Reactors. *https://doi.org/10.1016/j.jrras.2013.10.008* **2013**, *6* (2), 63–70. https://doi.org/10.1016/J.JRRAS.2013.10.008.

(119) Lane, J. A.; MacPherson, H. G.; Maslan, F. *Fluid Fuel Reactors: Molten Salt Reactors, Aqueous Homogeneous Reactors, Fluoride Reactors, Chloride Reactors, Liquid Metal Reactors and Why Liquid Fission*; Addison-Wesley Pub. Co., 1958.

(120) Magnusson, J.; Memmott, M.; Munro, T. Review of Thermophysical Property Methods Applied to Fueled and Un-Fueled Molten Salts. *Ann. Nucl. Energy* **2020**, *146*, 107608. https://doi.org/10.1016/J.ANUCENE.2020.107608.

(121) Abram, T.; Ion, S. Generation-IV Nuclear Power: A Review of the State of the Science. *Energy Policy* **2008**, *36* (12), 4323–4330. https://doi.org/10.1016/J.ENPOL.2008.09.059.

Chapter 2: Phonon gas model for dense, strongly interacting liquids

Developing predictive thermal property models for liquids based on microscopic principles has been elusive. The difficulty is that liquids have gas-like and solid-like attributes that are at odds when considering the frameworks of microscopic models: models for gases are simple due to randomness and low density, whereas models for crystalline solids rely on symmetry and long-range order for easier calculation. The short-range order in liquids does, however, provide structure to neighboring molecules similar to amorphous solids, and there have been recent advances indicating that collective vibrational modes store heat in liquids. Models combining Debye approximations from solid-state physics and Frenkel's theory of liquids can accurately predict the heat capacity of liquids. Phonon-like dispersions in liquids have also been widely observed in neutron scattering experiments. These developments motivate us to propose a model where high frequency vibrational modes, which travel at the speed of sound and have a mean free path on the order of the average intermolecular distance, conduct heat in liquids. We use this liquid phonon gas model to calculate the thermal conductivity of liquids with varying intermolecular interaction energies from strongest to weakest – Coulomb, hydrogen-bonding, Keesom, and London dispersion energy. Generally, the model is more accurate as the intermolecular interaction energy and density of liquids increase. The calculated thermal conductivity of Coulombic-bound molten sodium nitrate and hydrogen-bonded water is within 1.46% and 2.98% of the experimentally measured values, respectively, across their entire temperature ranges. Further modal analysis of the velocity and mean free path of collective vibrations could establish the liquid phonon gas model as an accurate model for weakly interacting liquids as well.

2.1 Introduction

Heat transfer fluids are the life blood of thermal energy technologies, transporting heat generated from energy sources – solar, fossil fuels, geothermal, and nuclear – to heat exchangers that power turbines to generate electricity or do useful work. Strongly interacting liquids, such as water and molten salts are crucial for heat transfer applications from 0°C up to 1600°C. Water is the most prevalent and important heat transfer fluid for many applications, but liquids that can operate at higher temperatures are required to achieve the higher thermodynamic efficiencies and energy densities needed for future energy technologies. Molten salts are desirable heat transfer fluids due to their high temperature stability, large heat capacity, and low vapor pressure; molten nitrates are currently being used as the heat transfer fluid and energy storage medium in concentrated solar plants[1], molten chlorides are being developed for next-generation concentrated solar plants[2,3], and molten fluorides are being developed for advanced nuclear reactors[4,5]. Fundamental properties of a liquid, such as thermal conductivity, κ and specific heat C_p, underpin the heat transfer coefficient and other performance metrics of heat transfer devices. The thermal conductivity of water has been measured extensively and a reference value has been well established[6], but the experimental thermal conductivity values of molten salts are less certain due to measurement errors caused by corrosion and convection at high temperature, leading to a large spread in thermal conductivity values and variations of its temperature dependence[7,8]. Experimental uncertainty is compounded by the lack of an established liquid thermal conductivity model, leading to general confusion for how to interpret widely varying experimental results for high temperature liquids.

Eighteen models of liquid thermal conductivity, using various interparticle potentials and assumptions about liquids, were well reviewed by McLaughlin in 1964[9]. Despite the bounty

of liquid thermal conductivity models, none of them accurately capture the behavior of a wide range of liquids governed by different interactions. For example, the Bridgman model, which we will discuss in detail later, closely matches the temperature dependent thermal conductivity of polar liquids, such as methanol and ethanol, but not that of hydrogen-bonded water and coulombic-bound molten nitrates. We believe that the strength of intermolecular interactions plays a key role in a model's ability to predict the experimental results of liquid thermal conductivity. To the best of the authors' knowledge, a simple analytical model that can accurately predict the thermal conductivity of strongly interacting liquids, hydrogen-bonded water and coulombic-bound molten nitrates, does not exist.

In this chapter, we present a phonon gas model of heat conduction in liquids, which can be used to calculate the temperature dependent thermal conductivity of strongly interacting liquids. In **Section 2.2,** we develop a model based on a phonon theory for liquid heat capacity, corroborated by experimental measurements of liquid phonon dispersions and speed of sound, and develop estimations regarding the mean free path of phonons in liquids. In **Section 2.3**, we examine how well calculations using the phonon gas model correspond to experimental measurements for liquids with varying intermolecular interaction types and strength: a) Coulombic-bound molten sodium nitrate and potassium nitrate; b) hydrogen-bonded water and hydrogen-sulfide; c) polar molecules with Keesom interaction energy, methanol and ethanol; d) non-polar molecules with London dispersion energy, n-alkanes with increasing chain length from methane to octane; and e) non-polar liquid argon with London dispersion energy under increasing pressure (0.1, 1, 10, and 100 MPa). We compare the phonon gas model results with calculations based on the Bridgman, Cahill-Pohl, and Chapman-Enskog models. We show that

the phonon gas model introduced here better captures the magnitude and the temperature dependence of liquids with strong intermolecular interaction energy.

2.2 Model development

The mechanism underlying heat conduction varies between different states of matter. Gases conduct heat through kinetic movement of gas molecules along the temperature gradient. Crystalline dielectric solids conduct heat through quantized lattice vibrations, known as phonons, which can be treated as free 'gas' particles – this is known as the phonon gas model[10]. Amorphous solids do not have long-range order, but still have vibrational modes that conduct heat. In liquids, molecules move and vibrate in response to a temperature gradient; however, the density of liquid molecules and strength of intermolecular interactions precludes kinetic gas-like conduction, which assumes gas particles are dilute and do not interact. Liquids lack time-independent, equilibrium atomic positions, but they do have short-range order similar to amorphous solids, and if intermolecular forces are strong enough to support a short-range network of liquid molecules for some time, such as in water or molten salts, phonon-like collective vibrations can potentially be the dominant heat conduction mechanism. We begin by exploring successful models for thermal conductivity in gases and solids to build a framework to describe liquid thermal conductivity.

The phonon gas model for solids is built upon the kinetic theory of gases, the classical treatment of gases used to derive important thermodynamic and transport properties, such as heat capacity, thermal conductivity, and viscosity. According to the kinetic gas theory, the thermal conductivity of a gas can be written as:

$$\kappa = \frac{1}{3} C_V v l \qquad (2.1)$$

where C_V, the volumetric heat capacity, is determined by the degrees of freedom of the gas molecules; v is the average speed of gas molecules directly related to the temperature; and l is the mean free path – the average distance a gas molecule travels between scattering events, which is dependent on the density of the gas molecules.

By analogy, the phonon gas model treats phonons in crystalline solids as gas particles to describe the thermal conductivity of a crystal lattice; it has proven to be a powerful model for understanding heat transport in solids from the nano to macro scale[11]. The thermal conductivity of solids takes the same form as the kinetic gas model, but takes into account three phonon polarizations in solids (one longitudinal acoustic and two transverse acoustic branches, excluding the optical modes which account for little to no heat transfer in most cases), as well as the phonon frequency (ω) dependence of the volumetric heat capacity of the solid (C_V), phonon group velocity (v_g) and mean free path (l):

$$\kappa = \sum_{n=1}^{3} \int_0^\infty \frac{1}{3} C_V(\omega) v_g(\omega) l(\omega) \, d\omega \qquad (2.2)$$

In amorphous solids, which lack the long-range order of crystals, heat moves through collective vibrations that are distinct from phonons – characterized as locons, diffusons, and propagons by Allen and Feldman[12]. Theories of heat transport in amorphous solids have been well reviewed elsewhere[13,14], but here we highlight the widely used minimum thermal conductivity model for amorphous solids[15], commonly referred to as the Cahill-Pohl model. It models the thermal conductivity of amorphous solids by assuming the mean free path of each vibrational mode to be half its wavelength. Agne et $al.$[16] simplified the minimum thermal conductivity result to:

$$\kappa_{Cahill-Pohl} = 1.21 k_B \frac{1}{3} (2v_T + v_L) n^{2/3} \qquad (2.3)$$

where, k_B is Boltzmann's constant n is the number density of atoms, v_T is the transverse speed of sound, and v_L is the longitudinal speed of sound. There is, however, similar short-range order in the structure of amorphous solids and liquids, which is reflected in the similarities between theories used to describe their thermal conductivity. For example, Xi *et al.* recently utilized the similarity between liquids and amorphous solids to present a unified formula to calculate both liquid and amorphous solid room-temperature thermal conductivity[17].

To extend the phonon gas model to liquids, we first examine the heat capacity of liquids and how energy is stored in the vibrations of liquid molecules. Trachenko *et al.* have recently formalized the vibrational modes in liquids to calculate theoretical liquid heat capacity[18–22] that matches very well with experimental data for a wide range of liquids by combining approaches from Debye's calculation of solid heat capacity[23,24] and Frenkel's theory of liquids[25]. Debye calculates the energy of a crystalline solid by integrating the energy of phonons with frequency, ω, up to a cut-off frequency known as the Debye frequency, ω_D. Assuming an ω^2 dependence for the phonon density of states, the energy of the solid can be written as:

$$E_{solid} = E_0 + \frac{9N}{\omega_D^3} \int_0^{\omega_D} \frac{\hbar \omega^3}{\exp\left(\frac{\hbar \omega}{k_B T}\right) - 1} \, d\omega \qquad (2.4)$$

$$\omega_D = (6\pi^2 n)^{1/3} v_{sound} \qquad (2.5)$$

where E_0 is the zero-point vibration energy, N is the number of atoms, and *n* is the number density of atoms. The heat capacity of a system can be obtained from **Equations 2.4** and **2.5** by using the definition that heat capacity is the derivative of energy with respect to temperature.

Frenkel's kinetic theory of liquids treats both amorphous solids and liquids as highly defected solids; however, the average time between diffusive hopping events, τ, of a molecule diffusing into a 'vacancy' within its network with short-range order is orders of magnitude

shorter in liquids. Contrary to typical assumptions, Frenkel theorized that liquids could support

transverse shear modes. In this framework, at frequencies higher than the Frenkel frequency,

$\omega_F = 1/\tau$, there is not enough time for liquid molecules to rearrange in response to a high

frequency perturbation – instead the high frequency vibration causes phonon-like excitations.

These phonon-like excitations are transferred along to neighboring liquid molecules until they

scatter due to defects, which are abundant in liquids. These high-frequency transverse modes in

liquids have been experimentally verified by x-ray and neutron scattering[26–30]. Recent molecular

dynamics work has also shown dispersive phonon-like modes in water with longitudinal and

transverse splitting[31], indicating that water dynamics are more similar to ice than previously

thought.

Trachenko *et al.* use Frenkel's theory of liquids to reformulate Debye's calculation of

energy for a liquid system. In their derivation of liquid heat capacity[18,19], they begin by summing

the energy contributions from longitudinal vibrational modes, transverse vibrational modes

above the Frenkel frequency, and the diffusive movement of liquid molecules:

$$E = K_l + P_l + K_t(\omega > \omega_F) + P_t(\omega > \omega_F) + K_d + P_d \quad (2.6)$$

$K_l + P_l$ are the kinetic and potential components of the longitudinal phonon energy,

$K_t(\omega > \omega_F) + P_t(\omega > \omega_F)$ are the kinetic and potential components of the transverse

phonon energy, and $K_d + P_d$ are the kinetic and potential energy of the diffusion. They first

note that P_d is negligible because if it were significant, it would result in a restorative force that

moves the liquid molecule back to its starting position, resulting in a low frequency vibrational

mode. They then use the virial theorem to write the liquid's total kinetic energy in terms of the

kinetic energy related to longitudinal and transverse waves, which accounts for the diffusive

kinetic energy, K_d, in the energy of shear waves with frequencies less than the Frenkel frequency,

$\omega < \omega_F$. The energy of a liquid system can then be written in terms of energy from longitudinal modes E_l and transverse modes E_t:

$$E = E_l + E_t(\omega > \omega_F) + \frac{E_t(\omega < \omega_F)}{2} \qquad (2.7)$$

Through further approximations and calculations detailed elsewhere[18,19], including the quasi-harmonic Grüneisen approximation, the Debye density of states approximation, the Debye frequency calculation, and calculating the energy $E_t(\omega < \omega_F)$, they achieve their ultimate result, that accurately predicts the temperature dependent heat capacity of liquids:

$$E_{liquid} = NT \left(3 - \left(\frac{\omega_F}{\omega_D} \right)^3 \right) \qquad (2.8a)$$

$$C_{V,liquid} = \frac{1}{N} \frac{dE_{liquid}}{dT} \bigg|_V \qquad (2.8b)$$

Equation 2.8a captures the general trend of energy in a liquid: at low temperatures just above the melting point, ω_F is at a minimum since liquid molecules vibrate and rearrange slowly, leading to a heat capacity per molecule, $C_{V,liquid}$, close to $3k_B$, the Dulong-Petit result for solids; at high temperatures, ω_F increases because liquid molecules vibrate and diffuse faster, cutting off lower frequency transverse modes from carrying energy in the liquid and decreasing $C_{V,liquid}$ close to $2k_B$.[19]

Trachenko *et al.* also wrote the liquid energy another way in terms of the vibrational energy of liquids, E_{vib}, as the sum of energies of quantum oscillators from longitudinal and

transverse modes. First integrating longitudinal vibrational modes, as done in solids, up to a longitudinal Debye frequency, ω_{Dl}; then integrating transverse modes with frequencies higher than ω_F up to a transverse Debye frequency, ω_{Dt}, because modes with frequencies lower than ω_F are excluded by liquid molecules rearranging too quickly. Thus, the vibrational energy of the liquid can be written as:

$$E_{vib} = E_0 + \frac{3N}{\omega_{Dl}^3} \int_0^{\omega_{Dl}} \frac{\hbar\omega^3}{\exp\left(\frac{\hbar\omega}{k_B T}\right) - 1} d\omega$$
$$+ \frac{6N}{\omega_{Dt}^3} \int_{\omega_F}^{\omega_{Dt}} \frac{\hbar\omega^3}{\exp\left(\frac{\hbar\omega}{k_B T}\right) - 1} d\omega \qquad (2.9)$$

Given the experimentally and theoretically observed phonon-like dispersion behavior in some liquids[26–31] and the success of Trachenko *et al.*'s phonon theory of liquid heat capacity at matching experimental liquid heat capacity, we assume that phonon-like vibrational modes also transport heat in liquids in response to a temperature gradient. While the vibrational modes in liquids cannot be strictly defined as phonons due to the lack of crystal lattice, to acknowledge inspiration from models used in solids, we use the term "phonon gas model" to describe our model to calculate liquid thermal conductivity from vibrational modes.

We hypothesize that the vibrational modes in liquids behave like a phonon gas with frequency dependent heat capacity, velocity, and mean free path according to **Equation 2.2**. By including the same adjustment Trachenko *et al.* make of only including transverse modes above the Frenkel frequency, we write the thermal conductivity of a liquid as:

$$\kappa = \int_0^{\omega_{Dl}} \frac{1}{3} C_l(\omega) v_l(\omega) l(\omega) \, d\omega + \int_{\omega_F}^{\omega_{Dt}} \frac{2}{3} C_t(\omega) v_t(\omega) l(\omega) \, d\omega \qquad (2.10)$$

where $C_l(\omega)$ and $C_t(\omega)$ are the frequency dependent specific heat due to the longitudinal and transverse modes, respectively. **Equation 2.10** is the full equation for liquid thermal

conductivity using a phonon gas model using the same modifications as the phonon model for liquid heat capacity (**Eq. 2.9)**. There has been a similar approach by Caplan et al.[32] to calculate the thermal boundary conductance between solids and liquids, which details calculations using **Equation 2.10**. In this work, we make further assumptions about the heat capacity, group velocity, and mean free path to calculate the thermal conductivity of liquids as discussed below.

In order to avoid the complexity of performing the full spectral analysis of phonon frequency contributions to thermal conductivity in **Equation 2.10** (see spectral analysis of crystalline silicon[33] or modal analysis in amorphous materials[34]), our approach is to assume the experimentally measured heat capacity of liquids accurately encapsulates contributions from the longitudinal and transverse modes at different frequencies. So, we combine both longitudinal and transverse components in **Equation 2.10** into one term represented by $C_{P,volumetric}$ (details discussed below). In addition, we use the gray approximation and assume the group velocity and mean free path of phonons are frequency independent; we will discuss our reasoning in selecting a representative velocity and mean free path for all phonon frequencies below.

We assume the group velocity, v_g (defined as $\partial\omega/\partial Q$, where Q is the wave vector), of vibrational modes that contribute to the thermal conductivity in a liquid can be closely approximated by the measured speed of sound, v_{sound}. This is a typical assumption for solids since v_{sound} is closely approximated by $\partial\omega/\partial Q$ of acoustic phonons near $Q = 0$. These phonons have the highest group velocity and are thus the dominant modes for heat conduction in bulk materials. As a partial validation of this assumption for liquids, we plot the phonon dispersion of liquid argon, measured by independent inelastic neutron scattering experiments and molecular dynamics simulations[35–37], in **Figure 2.1.** This data provides experimental

validation that there are phonon-like modes in liquids, each with a measured wavevector ($Q = 2\pi/\lambda$) that contains a corresponding energy, $\hbar\omega$. Despite constantly moving liquid molecules without long-range order, the slope of the dispersion curve show that vibrational modes store and transport energy in liquids. This has been well recognized by various inelastic neutron and x-ray scattering experiments that have reported "collective motion", "collective excitations", and "collective dynamics" in liquids[38–43]. Since there is no crystal lattice, the word "phonon" is avoided in previous work, but there is extensive discussion of transverse and longitudinal acoustic modes that transport energy in liquids, similar to terminology used in amorphous solids.

Also plotted in **Figure 2.1** is line of best fit for low Q inelastic neutron experiments[36] and the measured speed of sound, v_{sound}, of liquid argon. There is a good match between the best fit of the scattering results (815 m/s) and measured speed of sound (860 m/s) within 5% at a wide range of wavevectors. Thus, the dispersion for Ar suggests that the speed of sound is a good estimate for group velocity at a wide range of Q values (wavelengths). **Figure 2.1** also shows the Debye frequency calculated using **Equation 2.5** ($n = 35.377\frac{mol}{L}$, $v_{sound} = 860\frac{m}{s}$)[44], and Frenkel frequency from the Maxwell relationship ($\omega_F = \frac{2\pi}{\tau} = \frac{2\pi G_\infty}{\eta}$, where $G_\infty = 0.18\ GPa$, $\eta = 297\mu Pa \cdot s$)[19,44].
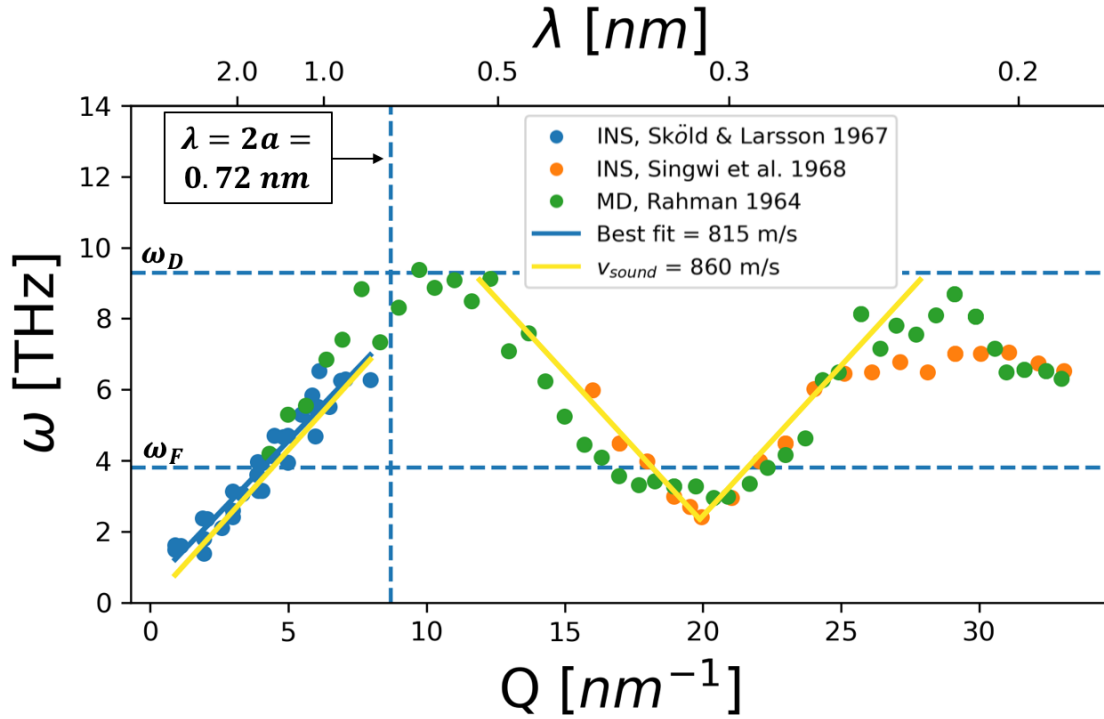
Figure 2.1. Experimental phonon dispersion of liquid argon[35–37] plotted along with the 860 m/s longitudinal speed of sound of in liquid argon at -189°C and 1 MPa[44].

It is likely that other liquids have dispersions similar to Ar, but the behavior is not universal. For example, the measured v_{sound} is not always a good approximation of the group velocity $\partial\omega/\partial Q$ at higher Q values, as seen in scattering experiments of water[45] and methanol[42]. The physical origin of this "fast sound" at high Q in liquids is discussed by Trachenko and Brazhkin[22]. Future work is required to better understand the frequency dependent vibrational mode group velocities in different liquids, so we simplify the analysis by using v_{sound} to approximate the speed of vibrational modes for all liquids in this study. Even though short-wavelength vibrational modes do not propagate long distances, we still assume their velocity is the same as the group velocity of propagating modes, or the sound velocity. In other words, the dispersion of propagating modes is used to estimate the velocity of the short-wavelength modes

that do not propagate – in amorphous solids these modes would be called diffusons or locons. This is analogous to the approach often used for amorphous solids. For example, Larkin & McGaughey[46] use the speed of sound for non-propagating vibrational modes to calculate thermal conductivity amorphous silicon and silica. Further work is needed to justify the assumption in liquids, but here it is treated as a postulate."

Using measured volumetric heat capacity and longitudinal speed of sound, **Equation 2.10** can be simplified as follows:

$$\kappa = \frac{1}{3} C_{P,volumetric} v_{sound} l \qquad (2.11)$$

We will us this analytical solution to calculate the thermal conductivity of various liquids in the following sections.

The final step to use **Equation 2.11** is to find l, the mean free path of vibrational modes. We posit that the dominant contributors to liquid thermal conductivity are short-wavelength, high-energy vibrational modes. Because of the fast rearrangement dynamics inherent to fluids, these vibrational modes should have short lifetimes and scatter frequently, preventing them from travelling far. So we take the intermolecular distance, the minimum step size a molecule or vibrational mode can travel in a liquid, as the mean free path – similar to the minimum thermal conductivity model in amorphous solids and Bridgman's model of liquid thermal conductivity, and equivalent to Slack's theory for phonons in liquids[47].

While vibrational modes with wavelengths much longer than the intermolecular distance should have mean free paths much longer than the intermolecular distance, those waves carry much less energy, as shown in the phonon dispersion in **Figure 2.1.** Note that in liquid molecules, atoms can be separated by distances shorter than the average intermolecular distance. This intramolecular distance could be for example the O-H bond distance in H_2O or the N-O

bond distance in a nitrate anion. In strongly interacting liquids, the vibrational modes might include both inter- and intra-molecular atoms (see **Figure 2.3a).** In future work, the accumulated thermal conductivity in liquids from vibrational modes with different wavelengths and mean free paths will be calculated.

Finding the proper intermolecular distance to use for the mean free path, l, is complicated by the lack of long-range order in liquids. A typical method used for determining structure in liquids is the radial distribution function (RDF) measured by inelastic neutron or x-ray scattering. The RDFs of liquid argon, water, and sodium nitrate in **Figure 2.2** show the short-range order in the spatial distribution of liquid molecules, and they can be used to find the average distance between nearest atomic neighbors and approximate the average intermolecular distance. In monatomic liquids, such as Ar, this is straight forward, but for molecular liquids like water it is more complicated to define an intermolecular distance; the oxygen-oxygen distance in water gives a rough idea of the spacing between water molecules, but since information about hydrogen atoms is missing, this does not give the complete picture. In ionic liquids like molten sodium nitrate, it is even more complicated since there are sodium cations and nitrate anions with different shapes, masses, and effective radii. Thus, we turn to other methods to calculate the intermolecular distance that reflect the average molecular spacing.
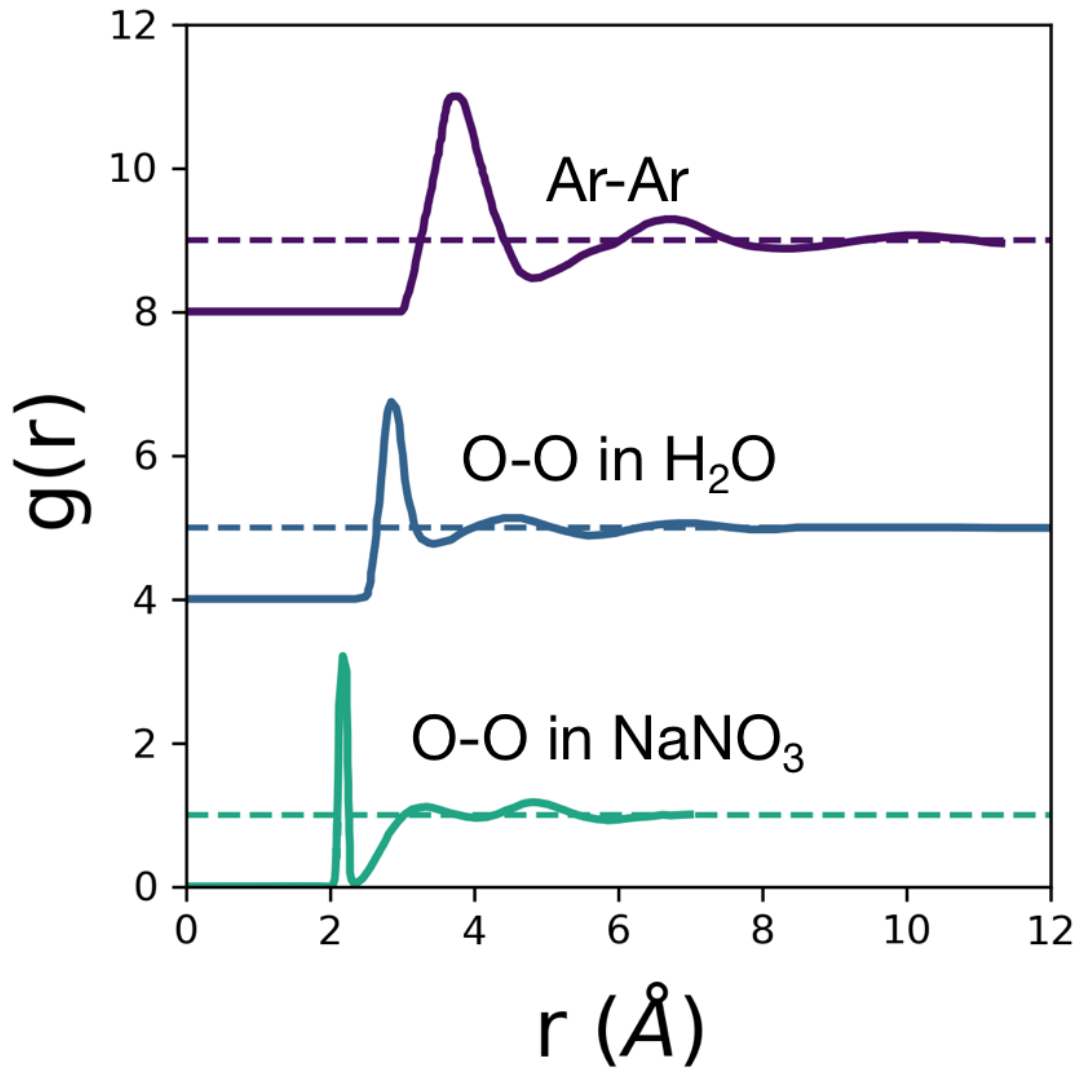
Figure 2.2. Radial distribution functions of liquid argon[48], water[49], and sodium nitrate[50] measured with neutron diffraction.

An alternate but equivalent formation of **Eq. 2.11** uses the phonon relaxation time, τ_{relax}. Since $l = v_{sound}\tau_{relax}$ we can write:

$$\kappa = \frac{1}{3} C_{P,volumetric} v_{sound}^2 \tau_{relax} \qquad (2.12)$$

To further explore the physical meaning of a vibrational mode's mean free path in a liquid, we examine the relaxation time after a scattering event. A vibrational mode can exist when atoms are located along periodic peaks and valleys that support a vibrational mode. This is shown schematically in **Fig. 2.3a**; when the liquid molecule moves by rotation or translation, the vibrational mode is no longer supported and 'scatters'. Thus, the relaxation time can also be viewed as a liquid vibrational mode's lifetime.
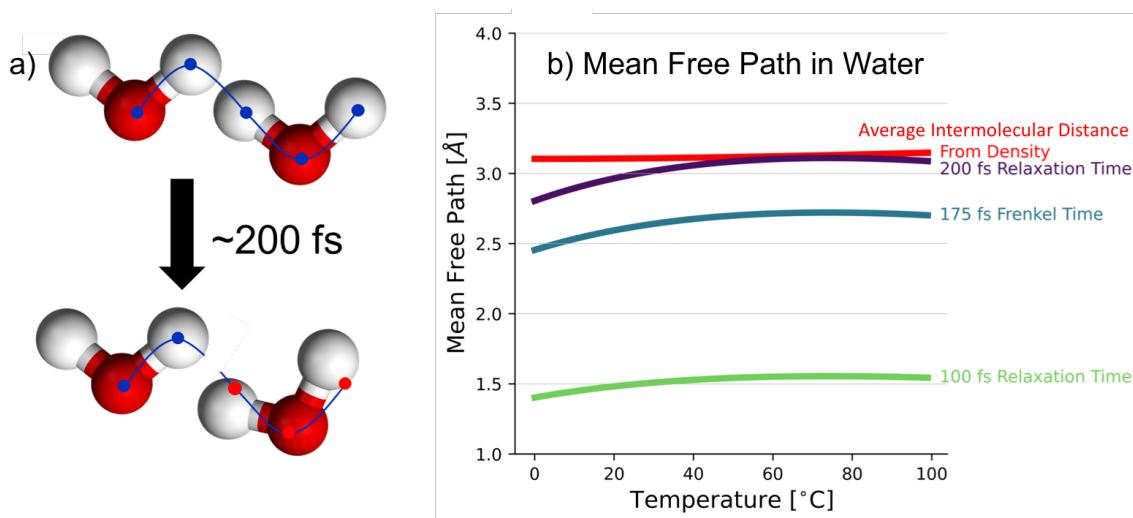
Figure 2.3. a) Schematic representation of a supported vibrational mode is (top). Vibrational mode lifetimes are ~200 fs, typical times for the reorientation of water molecules (bottom). **b)** Mean free path of vibrational modes calculated from density compared to different relaxation times.

We look to measurements of the structure and dynamics of water molecules using vibrational spectroscopy by Bakker and Skinner[41] to find a physical interpretation for the relaxation time in water. According to their work, the reorientation of water molecules occurs on two time scales. In the first very short time scales (< 200 femtoseconds), O-H groups rotate and move but keep their hydrogen bond intact. On longer time scales, the reorientation dynamics of water require rearrangements of the entire network. Bakker and Skinner discuss the "wobbling-in-a-cone model" that shows O-H groups in water take between 100 and 200 fs

to rotate around a confined cone. Within this time frame, there are both experimental measurements and molecular dynamics simulations showing an underdamped oscillation at about 180 fs due to a stretching intermolecular hydrogen-bond. Further, we calculate a Frenkel time of 175 fs for the time it takes for water molecules to rearrange using the Maxwell relationship $\tau_{Frenkel} = \frac{\eta}{G_\infty}$, where the viscosity $\eta = 1790.9 \, \mu Pa \cdot s$ (from NIST database[44]) and the infinite frequency shear modulus $G_\infty = \rho c_\infty = 10.24 \, GPa$ (from Ruocco & Sette[45]). In **Figure 2.3b** we show the mean free path of phonons in water based on calculations from $100 \, fs < \tau_{relax} < 200 fs$. The results show that mean free paths based on these very fast dynamics are indeed short (between ~1.5 to 3 Å). Note that some of the atoms within the average intermolecular distance are intramolecular atoms within the same molecule while others are in distinct molecules, intermolecular atoms. We believe both intermolecular and intramolecular dynamics should be important in liquid thermal conductivity, and we will discuss this more for n-alkane chains with increasing length in **Section 2.3d.**

We presented three independent approaches (density, radial distribution function, and lifetime) to approximate mean free path that lead to similar results, which gives us confidence in the approximations. But we understand that these approximations do not provide a complete picture of vibrational modes in liquids. The biggest concern with assuming the mean free path is equal to the intermolecular distance is that propagating modes should have mean free paths much longer than the intermolecular distance to propagate. To support the assumption that the mean free path of vibrational modes in liquids is equal to the intermolecular distance, we note that this is similar to treatments used in describing thermal conductivity in amorphous solids. Previous calculations of the frequency dependent mean free path of vibrational modes in amorphous silica by Larkin and McGaughey[46] found that propagating modes in amorphous

silica, with mean free paths longer than 10 nm, are negligible and only contribute ~6% to the total thermal conductivity. The non-propagating, high energy vibrational modes that move at the speed of sound and have a mean free path on the order of the lattice parameter are the dominant contributors. This modeling results matched previous experimental measurements that showed silica's thermal conductivity was independent from film thickness. Thus, our assumptions that the dominant contributors to the thermal conductivity of liquids can be non-propagating vibrational modes that travel at the speed of sound with short mean free paths, on the order of the intermolecular distance, are analogous to previous models used for amorphous solids. Future work is needed to calculate or measure the frequency dependent phonon density of states, velocity, and mean free path; these will provide a better idea of how different vibrational modes contribute to the total thermal conductivity in liquids.

In this work, to calculate mean free path for liquids with uniform molecules (e.g. Ar and H_2O, not $NaNO_3$), we use the approximation $l \approx d = n^{-1/3}$, where n is the atomic number density, in units [m^{-3}]. This result closely compares with l calculated using relation time of 200 fs for water as shown in **Fig 2.3b**. We can also compare the approximate mean free paths from the RDFs (shown in **Fig. 2.2)** and the atomic number density. For liquid argon at -189°C, the RDF shows the average distance between Ar-Ar nearest neighbors to be 3.70 Å, which is just 2% larger than the distance, $d = 3.61$ Å, calculated based on the density. For water at 25°C, the RDF shows the average O-O distance is 2.85 Å for nearest neighbors and 4.53 Å for second nearest neighbors, while the intermolecular distance calculated from the density is $d = 3.11$ Å. As expected, this discrepancy suggests the intermolecular spacing of H_2O molecules is not completely reflected in the O-O distance. Since intermolecular distances from RDFs are only accurate for simple spherical molecules like argon, we utilize experimental density data, which

81

are readily available for most liquids, to calculate their intermolecular distance and mean free path for liquids that are not molten salts. This is a reasonable assumption for most liquids with small, uniform molecules that can be approximated as spheres; this assumption breaks down as the length of molecules increases, which we will see in alkane chains in **Section 2.3 d**.

To calculate the mean free path in molten salts, we find the intermolecular distance, *d*, by adding the cation and anion radius. For sodium nitrate, we find the radii of a sodium cation (1.02 Å) and nitrate anion (2.31 Å) in literature[51,52], assuming a coordination number of 6, and add them together (3.33 Å). 3.33 Å is also the same distance as the O-O second nearest neighbor distance in sodium nitrate's RDF (see **Figure 2.2**), which is the distance between oxygen atoms of neighboring nitrate molecules. Since the coulombic forces that hold sodium nitrate together are temperature independent, we assume d in molten salts is also temperature independent. Gheribi *et al.*[52] previously employed the Boltzmann transport equation and hard spheres model to calculate the thermal conductivity of various molten salts, also using the sum of ionic radii as the mean free path, and reached the same equation as this work (**Eq. 2.11**) with the added assumption that $C_P = 4.33 C_V$. If one was to calculate the intermolecular distance using the measured density of sodium nitrate, $d = n^{-1/3}$, where n is the number density [m^{-3}], it would result in a significantly larger intermolecular distance (4.21 Å at 310°C compared to 3.33 Å from adding the ionic radii and using the RDF) than that used in this work due to the different sizes and shapes of the sodium cations and nitrate anions.

Beginning with the liquid phonon gas model in **Equation 2.10** using the experimental heat capacity, and implementing our previously stated assumptions – regarding phonon velocity as the speed of sound, and mean free path being approximated using the measured density – leads to a simplified result for liquid thermal conductivity:

$$\kappa = \frac{1}{3} C_{P,volumetric} v_{sound} n^{-1/3} \qquad (2.13)$$

We use experimental $C_{P,volumetric}$ values at constant pressure with units $[Jm^{-3}K^{-1}]$ because most thermal conductivity experiments are conducted at constant pressure, and when there is a temperature gradient the volume will not remain constant. We can convert C_P values into $[JK^{-1}]$ using $C_{P,volumetric} [Jm^{-3}K^{-1}] = n[m^{-3}] C_P [JK^{-1}]$ to our final expression for liquid thermal conductivity:

$$\kappa = \frac{1}{3} C_P v_{sound} n^{2/3} \qquad (2.14)$$

Equation 2.14 matches Slack's model for liquid thermal conductivity[47], and it is closely related to the Cahill-Pohl minimum thermal conductivity model for amorphous solids (**Eq. 2.3**) and Bridgman's theory of liquid thermal conductivity (**Eq. 1.20**). The only difference lies in how the heat capacity of the liquid is expressed. Our result recaptures Bridgman's result[53], $\kappa = 2k_B v_{sound} n^{2/3}$, if we assume $C_P = 2C_V$ (which matches closely with experimental results for noble liquids argon, krypton, and xenon) and $C_V = 3k_B$ (the Dulong-Petit law for solids). Further, if $C_P < 2C_V$, our result approaches Cahill *et al.*'s simplified result[16], $\kappa = 1.21 k_B v_{sound} n^{2/3}$ (note we only use the longitudinal speed of sound to calculate the theoretical thermal conductivity of liquids); experimentally measured C_P is less than $2C_V$ to varying degrees for different liquids, and the degree should depend on how C_P of different liquids changes due to volume expansion. Some of the variety in previous theories and models for liquid thermal conductivity can be traced back to the lack of clarity in how much energy is stored in the liquid; Trachenko *et al.* have provided a more solid theoretical grounding for liquid heat capacity. In this work, we will test how well **Equation 2.11** fits measured thermal

conductivity data and compare our results with Bridgman's, Cahill-Pohl's, and Chapman-Enkog's theoretical values.

2.3 Comparing models with experimental measurements of various liquids

In this section we examine the ability of models to capture the thermal conductivity of liquids with varying intermolecular interaction energy. We consider liquids with intermolecular interactions governed by Coulomb, Keesom, and London dispersion energies. Specifically, we test the phonon gas model (**Eq. 2.11**) for a variety of liquids with varying degrees of intermolecular interaction strength, from the strongest (Coulomb energy) to the weakest (London dispersion energy), and observe how the intermolecular interaction energy influences the accuracy of the liquid phonon gas model. We will show the results of our work in comparison to results from Cahill-Pohl, Bridgman, and Chapman-Enskog.

Table 2.1. Thermal conductivity model equations used to calculate results.

Model	Equation
This Work (Eq. 2.11, 2.14)	$\frac{1}{3} C_{P,volumetric} v_{sound} l = \frac{1}{3} C_P v_{sound} n^{2/3}$
Cahill-Pohl (Eq. 2.3)	$1.21 k_B \frac{1}{3} (2v_T + v_L) n^{2/3} \approx 1.21 k_B v_{sound} n^{2/3}$
Bridgman (Eq. 1.20)	$\frac{2 k_B v_{sound}}{d^2} = 2 k_B v_{sound} n^{2/3}$
Chapman-Enskog (Eq. 1.18)	$\frac{k_0}{g(D)} \left[1 + \frac{2}{5} \pi \rho D^3 g(D) \right]^2 + \frac{3 k_B}{2m} \Pi$

2.3 a) Molten nitrate salts with strong coulomb energy

To begin, in **Figure 2.3**, we examine the phonon gas model in strongly interacting molten salts, sodium nitrate and potassium nitrate, made up of sodium/potassium cations and nitrate anions, strongly attracted by Coulomb interaction, of which the energy can be written[54]:

$$E_{Coulomb}(d) = \frac{q_1 q_2}{4\pi\varepsilon_0 d^2} \tag{2.15}$$

where q_1 and q_2 are the charge of the species in Coulombs (C), ε_0 is the dielectric permittivity of free space 8.854 $C^2 J^{-1} m^{-1}$, and d is the intermolecular distance. Sodium nitrate's Coulomb interaction energy is 417 $kJ\ mol^{-1}$ and potassium nitrate's is 376 $kJ\ mol^{-1}$. There are other interactions present in molten salts, such as London dispersion, but we only consider the dominant interaction energy. Note that we do not use the calculated intermolecular interaction energy to calculate liquid thermal conductivity, but we will use it to observe trends in the performance of the models across different liquids in **Section 2.4.**

To quantify the deviation between calculated and experimentally measured results, we use the following relations to average the deviations over the n temperature points (T_i) evaluated:

$$Deviation = \frac{1}{n}\sum_{i=1}^{n} \kappa_{calculated(T_i)} - \kappa_{measured(T_i)} \tag{2.16a}$$

$$\%\ Deviation = 100\% \times \frac{1}{n}\sum_{i=1}^{n} \frac{\kappa_{calculated(T_i)} - \kappa_{measured(T_i)}}{\kappa_{measured(T_i)}} \tag{2.16b}$$

where $\kappa_{calculated}(T_i)$ and $\kappa_{measured}(T_i)$ are the calculated and the measured thermal conductivity values at T_i, respectively. The experimental thermal conductivity values of sodium nitrate and potassium nitrate are obtained from our recent measurement[7] utilizing a frequency domain hot wire method[55] that minimizes the potential systematic errors due to corrosion and

convection in previous steady-state and time-domain measurements[8]. $\kappa_{measured}$ of molten sodium nitrate, shown in **Figure 2.4**, remains very stable within the temperature window of 310 to 420°C. The $\kappa_{measured}$ values are compared to the various models discussed above. The model results were calculated using the various physical data needed for the models: experimental heat capacity[56], density[57], viscosity[58], and speed of sound[59] taken from literature. Note that density is used to calculate the mean free path for all liquids (see **Eq. 2.14**) except for molten salts, which use ionic radii/RDF to approximate mean free path (see **Eq. 2.11)**.

Our phonon gas model (**Eq.**) agrees well with the experimental steady state thermal conductivity measurements of sodium nitrate, and deviates from frequency-domain experimental thermal conductivity measurements by an average of 0.009 $Wm^{-1}K^{-1}$ (1.46%), which is within the experimental error. Similarly, our phonon gas model predicts a slightly decreasing thermal conductivity in potassium nitrate as temperature increases, but it overestimates the experimental results by 0.069 $Wm^{-1}K^{-1}$ (14.66%). The phonon gas model predicts the thermal conductivity of sodium nitrate more accurately than potassium nitrate, suggesting that stronger Coulomb energy correlates with higher accuracy for our model. The phonon gas model captures the magnitude and temperature dependent thermal conductivity significantly better than the other models also plotted in **Fig. 2.3**.

The Cahill-Pohl minimum thermal conductivity model (**Eq. 2.3**) and Bridgman's model (**Eq. 1.20**) both show a similar slope to the molten nitrate salt experimental data; Cahill-Pohl significantly underestimates the thermal conductivity by 72.50% for sodium nitrate and 69.93% for potassium nitrate; Bridgman underestimates sodium nitrate by 54.57% and potassium nitrate by 50.31%. Chapman-Enskog's calculation (**Eq. 1.18**) of molten nitrate thermal conductivity has a completely different temperature dependence than experimental measurements; at the

melting point, it significantly overestimates thermal conductivity, but at the higher temperatures it begins to converge with the experimental results. The deviations of all the models are reported in **Table 2.2**.
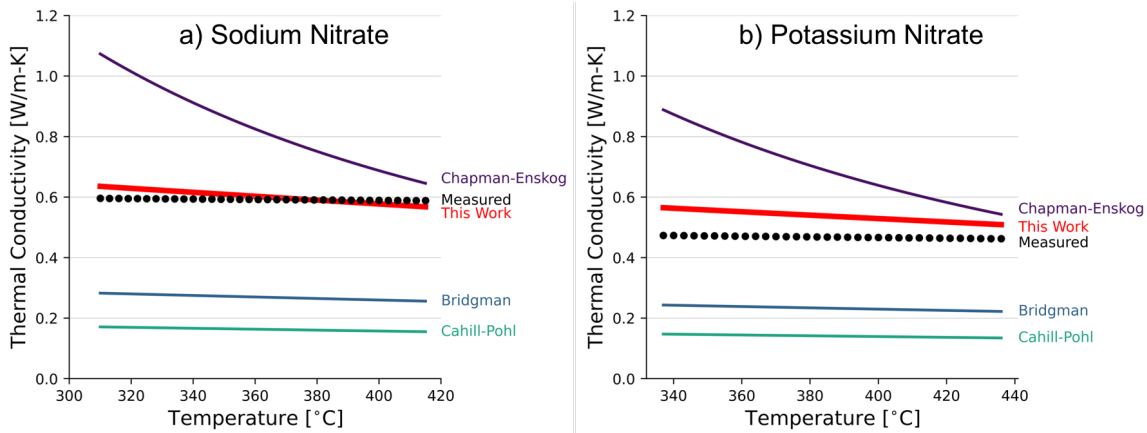
Figure 2.4. Experimentally measured and calculated thermal conductivity of molten a) sodium nitrate and b) potassium nitrate at 0.1 MPa.

2.3 b) Polar liquids with strong hydrogen bonding

Next, we test the phonon gas model in strongly interacting, hydrogen-bonded liquids. We examine the thermal conductivity of hydrogen sulfide and water; both have the same tetrahedral molecular structure with sulfur or oxygen at the center, two hydrogens bonded to the center atom, and two lone pairs of electrons on the center atom opposite from the two hydrogens. Due to their asymmetric distribution of electrons, hydrogen sulfide and water have permanent electric dipole moments, u ($u = 0.97$ D for hydrogen sulfide and $u = 1.85$ D for water[60], where $D = 3.336 \times 10^{-30} C\ m$). The dipole moment is a measure of how polar a molecule is, which is a function of how far the positive and negative charges are separated within a molecule. Dipole-dipole interactions arise when the charges of a polar molecule are attracted to the charges of a neighboring polar molecule; this is known as Keesom energy and is given by[54]

$$E_{Keesom}(d) = \frac{-u^4}{3 * (4\pi\varepsilon_0)^2 k_B T d^6} \qquad (2.17)$$

However, the bonding in water and hydrogen sulfide is much more complicated than just Keesom energy; there are also contributions from the covalency of electron orbitals in neighboring molecules and London dispersion energy. Extensive work has been done to calculate water's hydrogen bonding interaction energy $(21 \ kJ \ mol^{-1})$[61], which provides the unique structure and properties of water; hydrogen bonds have recently been measured in hydrogen sulfide to be weaker $(7 \ kJ \ mol^{-1})$[62–64].

In **Figure 2.5,** we compare the measured thermal conductivity of water and hydrogen sulfide with their calculated thermal conductivity values using **Equation 2.14** based on experimental heat capacity, density, viscosity, and speed of sound from the NIST fluids database[44]. In water, our liquid phonon gas model overlaps with the experimental thermal conductivity results that, uniquely, increases with increasing temperature, deviating from experimental results by an average of 0.018 $Wm^{-1}K^{-1}$(2.98%) – no other model comes close to capturing the thermal conductivity of water from melting to boiling point. In hydrogen sulfide, our work overestimates hydrogen-sulfide's thermal conductivity by an average of 0.105 $Wm^{-1}K^{-1}$ (43.49%). Once again, the stronger hydrogen bonding in water compared to that in hydrogen sulfide correlates with a decrease in the deviation between our phonon gas model and the experimental thermal conductivity. Bridgman's model underestimates water's thermal conductivity by an average of 0.204 (31.96%), but it overlaps with the experimental hydrogen sulfide thermal conductivity results[44] that gradually decrease with increasing temperature, overestimating by an average of 0.012 $Wm^{-1}K^{-1}$(4.76%). All the deviations between the various models and experimental results are summarized in **Table 2.2**, and in **Figure 2.5** we

show the corresponding thermal conductivities. In addition, water's modeled thermal conductivity from **Equation 2.12**, using a relaxation time of 200 fs, results in a 0.21% deviation from the measured results, even closer than **Equation 2.14** that uses the density to approximate mean free path shown in **Figure 2.5c.**
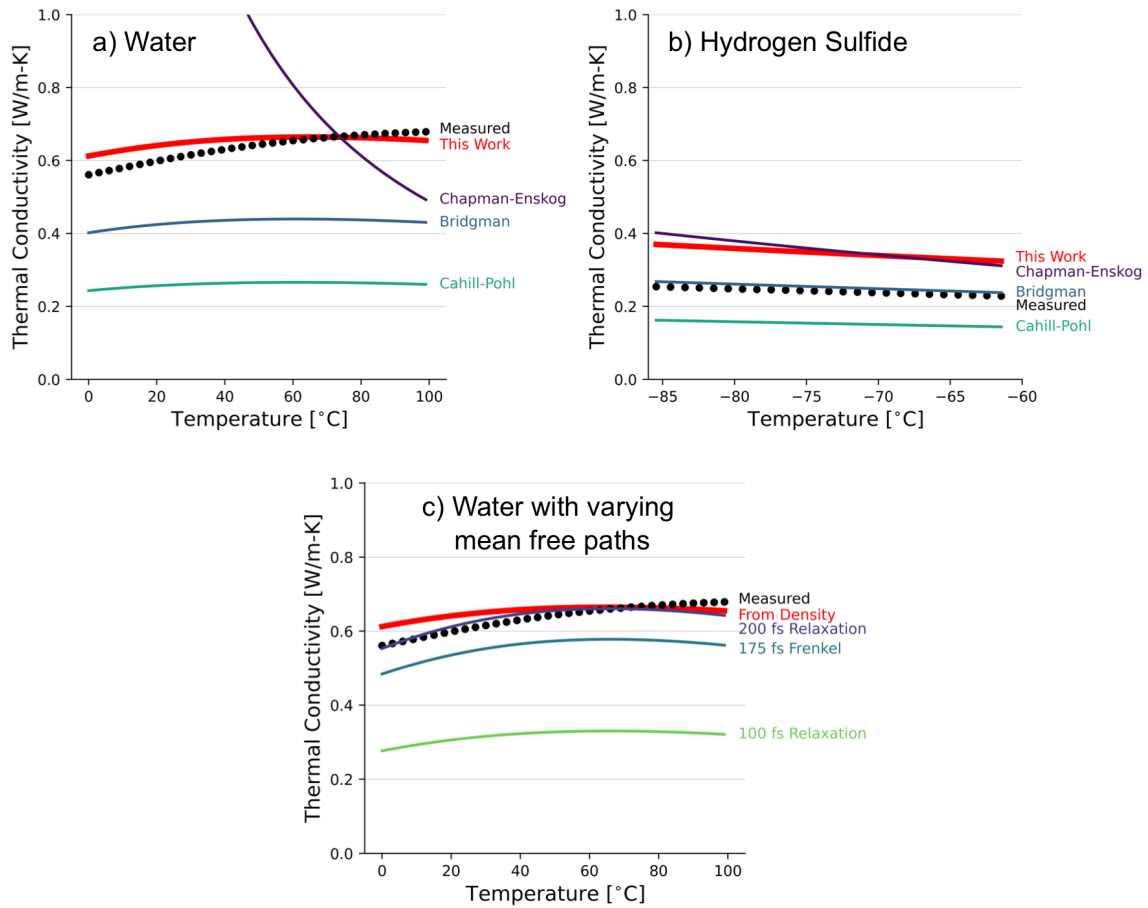
Figure 2.5. Thermal conductivity of a) hydrogen bonded water and b) hydrogen sulfide at 0.1 MPa. c) Thermal conductivity of water with varying mean free paths calculated from the density and relaxation times from 100-200 femtoseconds.

2.3 c) Polar liquids with Keesom energy

We next examine methanol and ethanol, which are polar liquids that have very similar dipole moments but have weaker intermolecular interactions than water's hydrogen bonding. We consider the Keesom energy, the dominant force attracting the liquid molecules together due to the dipole-dipole interactions in methanol ($u = 1.68$ D, $d = 4.01$ Å at -13ºC, which leads to $1.07 \ kJ \ mol^{-1}$ from **Eq. 2.17**)[60] and ethanol (1.69 D, $d = 4.56$ Å at 2ºC, $0.48 \ kJ \ mol^{-1}$ from **Eq. 2.17**)[60]. In **Figure 2.6**, the measured thermal conductivity of methanol[65] is compared to the calculated thermal conductivity from **Equation 2.14**, using the measured heat capacity, density, and speed of sound of methanol from the NIST fluids database[44], which did not include methanol's viscosity (for this reason we have excluded Chapman-Enskog's calculated result for methanol and ethanol from **Fig. 2.6**). Similarly, the calculated thermal conductivity values of ethanol are based on measurements of its heat capacity[66], density[67], and speed of sound[68] from literature, and is compared to the measured thermal conductivity value[69].

Bridgman's calculated thermal conductivity slightly underestimates the measured thermal conductivity of methanol by $0.017 \ Wm^{-1}K^{-1}$ (8.70%) and ethanol by 0.020 $Wm^{-1}K^{-1}$ (12.3%). Overall, Bridgman's model captures the temperature dependence of methanol and ethanol's thermal conductivity relatively accurately. The Cahill-Pohl model is again a lower estimate than Bridgman, underestimating methanol's measured thermal conductivity by $0.089 \ Wm^{-1}K^{-1}$(44.76%) and ethanol's measured thermal conductivity by $0.077 \ Wm^{-1}K^{-1}$ (46.99%). Our work vastly overestimates methanol's thermal conductivity by $0.099 \ Wm^{-1}K^{-1}$(49.24%) and ethanol's thermal conductivity by 0.171 $Wm^{-1}K^{-1}$(103.97%).

The deviations between the various models and measured results for methanol and ethanol are summarized in **Table 2.2**.
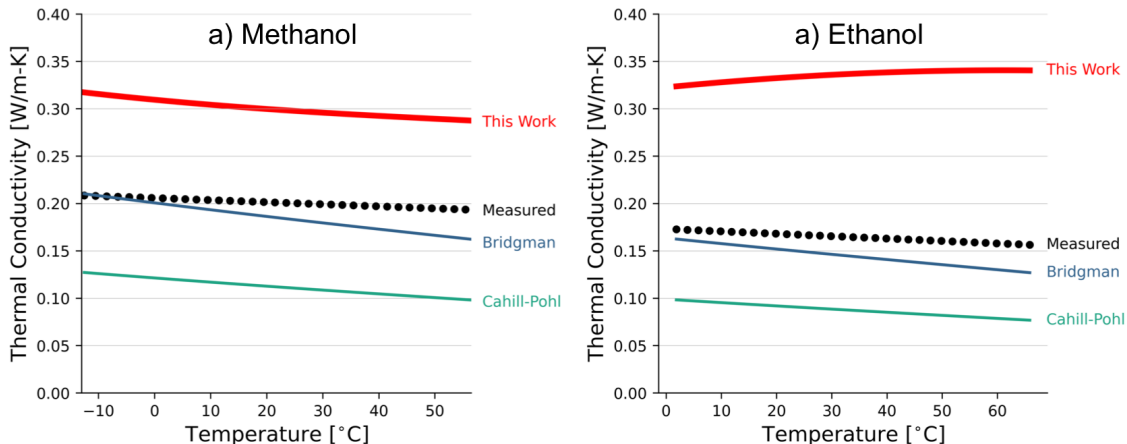
Figure 2.6. Thermal conductivity of a) methanol (dipole moment =1.68 D) at 0.1 MPa and b) ethanol (dipole moment =1.69 D) at 0.1 MPa.

2.3 d) Nonpolar liquids with increasing molecular chain length

To examine liquids with weaker intermolecular interactions than polar liquids, we calculate the thermal conductivity of nonpolar n-alkane chains (methane through octane) with zero dipole moment, which are only held together *via* London dispersion interaction (**Eq. 2.18**)[54]. Nonpolar molecules have no straightforward electrostatic interactions like Coulomb or Keesom energy, but due to quantum mechanical fluctuations of electron positions, there are instantaneous electric polarizations that attract other molecules – London dispersion energy – which hold liquid n-alkanes together and are present in all molecules:

$$E_{London}(d) = \frac{-3}{4} \frac{h\nu\alpha^2}{(4\pi\varepsilon_0)^2 d^6} \qquad (2.18)$$

where ν is the ionization frequency (s^{-1}) and α is the electronic polarizability ($C^2 m^2 J^{-1}$). The London dispersion energy attracting methane[54] molecules at 92 K equals $1.75 \; kJ \; mol^{-1}$ (for longer n-alkane chains, data was not found for ν and α).

Methane (CH_4) is a carbon atom bonded to four hydrogen atoms; due to the symmetric spread of carbon-hydrogen bonds and electrons in methane, there is no electric dipole moment. Ethane (C_2H_6) is also nonpolar and roughly longer than methane by a single carbon-carbon bond (1.54 Å); propane (C_3H_8), butane (C_4H_{10}), pentane (C_5H_{12}), hexane (C_6H_{14}), heptane (C_7H_{16}), and octane (C_8H_{18}) are all nonpolar and longer than their predecessors. As the length of the n-alkane chain increases, our assumption that the phonon mean free path is the intermolecular distance loses meaning as the chains become intertwined. Energy is stored and transported along chains (intramolecular energy) as well as between chains (intermolecular energy), and decoupling these energy transfer mechanisms in chain-like molecules is nontrivial and has been explored previously[70–73].

Despite the breakdown of our model's assumptions, we continue with the comparison between the measured and theoretical thermal conductivities of alkane chains (all data used for n-alkane chains are from the NIST fluids database[44]). **Figure 2.7** shows the measured and theoretical thermal conductivities of methane, butane, pentane, and octane. As chain length increases, the phonon gas model increasingly overestimates the thermal conductivity; in methane we overestimate by $0.084 \; Wm^{-1}K^{-1}$ (42.53%) and in octane we overestimate by $0.255 \; Wm^{-1}K^{-1}$ (206.82%). As chain length increases, the Cahill-Pohl model increasingly underestimates the thermal conductivity; in methane they underestimate by $0.043 \; Wm^{-1}K^{-1}$ (21.52%) and in octane they underestimate by $0.078 \; Wm^{-1}K^{-1}$ (64.18%). Bridgman's model begins by overestimating methane's measured thermal conductivity by $0.059 \; Wm^{-1}K^{-1}$

(29.71%), but it only deviates from butane's by 0.004 $Wm^{-1}K^{-1}$ (3.31%), and it eventually underestimates octane's by 0.049 $Wm^{-1}K^{-1}$ (40.80%). The deviations between the various models and measured results for methane, butane, pentane, and octane are summarized in **Table 2.2.**
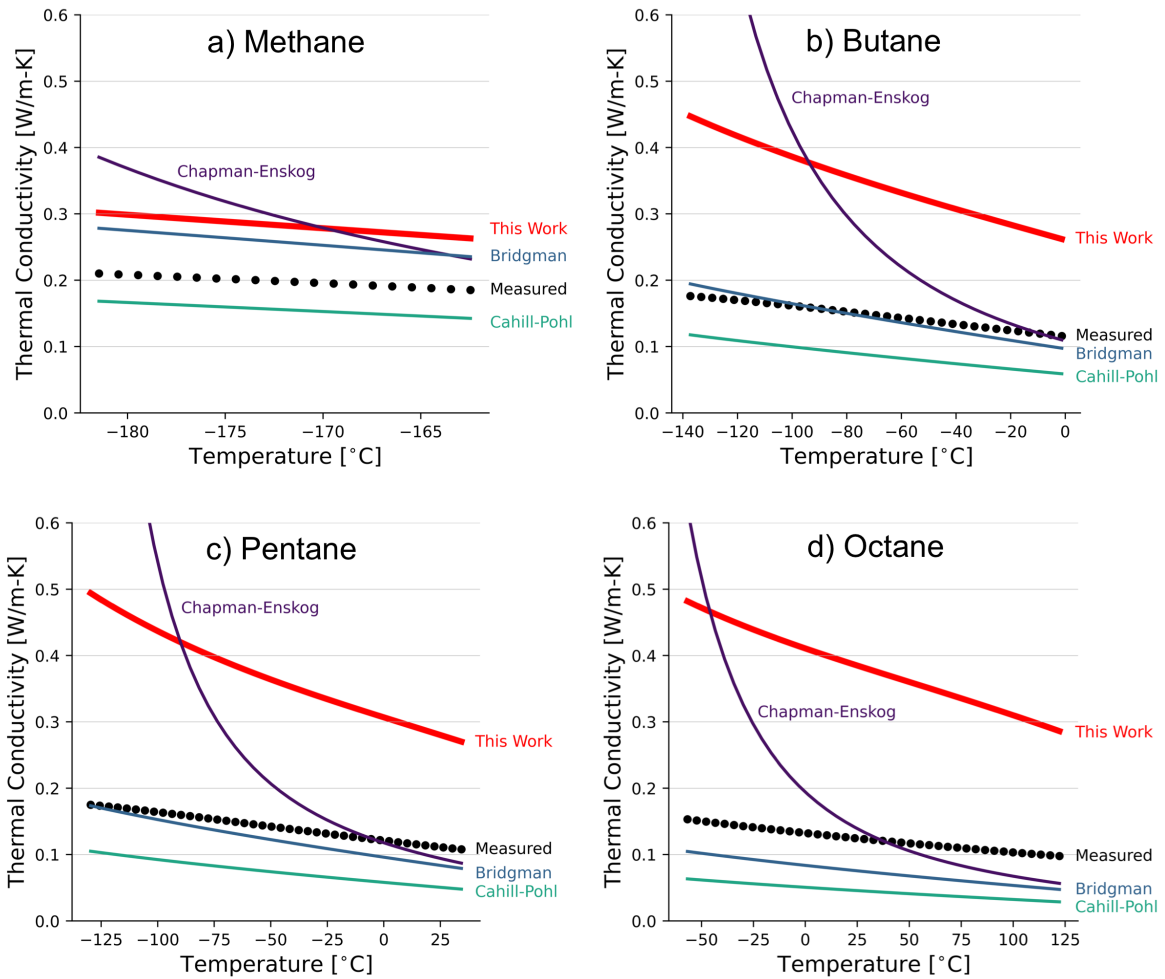
Figure 2.7. Thermal conductivity of nonpolar n-alkane liquids a) methane, b) butane, c) pentane, and d) octane at 0.1 MPa.

2.3 e) Nonpolar liquids with increasing pressure

Liquid argon molecules are nonpolar and thus held together by London dispersion energy (**Eq. 2.18**). Since the London dispersion energy is proportional to d^{-6}, increasing pressure from 0.1 to 100 MPa will decrease the intermolecular distance, d, which in turn increases the London dispersion energy. For Ar at 1 MPa and -189ºC, $d = 3.61$ Å and $E_{London} = 1.37\ kJmol^{-1}$; for Ar at 100 MPa and -165ºC, $d = 3.53$ Å and $E_{London} = 1.54\ kJmol^{-1}$.[54] In this section we observe how increasing pressure affects the deviation between the calculated and measured thermal conductivity.

We compare liquid argon's measured thermal conductivity with the calculated thermal conductivity results using experimental heat capacity, density, viscosity, and speed of sound from the NIST fluids database[44]. The measured thermal conductivity of liquid argon at a pressure of 1 MPa, shown in **Figure 2.8**, linearly decreases as temperature increases. Our phonon gas model captures the negative temperature dependence in argon's thermal conductivity but overestimates the value by an average of 0.031 $Wm^{-1}K^{-1}$ (28.85%). The Cahill-Pohl model has a similar negative slope that matches argon's experimental data, but underestimates the measured data by 0.018 $Wm^{-1}K^{-1}$ (16.35%); Bridgman's model has a similar negative slope but overestimates by 0.042 $Wm^{-1}K^{-1}$ (38.26%); Chapman-Enskog's thermal conductivity calculation has a completely different temperature dependence than the experimental measurements – at the melting point, Chapman-Enskog overestimates thermal conductivity by 0.096 $Wm^{-1}K^{-1}$ (74.84%), but at the boiling point it overestimates by just 0.006 $Wm^{-1}K^{-1}$ (7.02%).
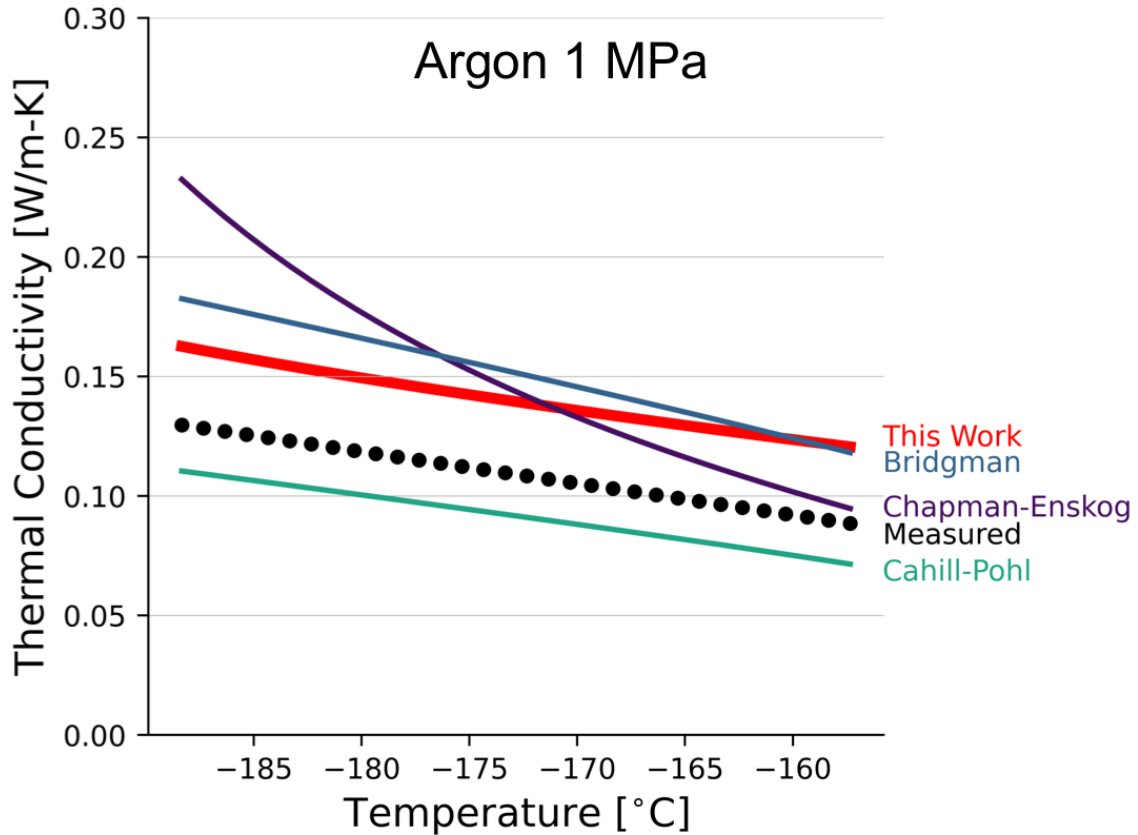
Figure 2.8. Thermal conductivity of liquid argon at 1 MPa.

Next, in **Figure 2.9,** we observe how increasing pressure on liquid argon changes our model's accuracy. Applying an external pressure forces the argon atoms closer together, increasing the density, and potentially making liquid argon more solid-like. At high enough temperature and pressure, above the critical point (-122.34°C at 4.87 MPa), argon enters a supercritical state where the densities of the liquid and vapor phases converge, and the phases become indistinguishable. Of interesting note, deep into the supercritical state (above -122.34°C at 100 MPa for example in **Fig. 2.9d**) our liquid phonon gas model increasingly overlaps with the measured thermal conductivity. Wang *et al.* recently presented evidence for propagating longitudinal phonon-like collective excitations in supercritical systems, with wavelengths and

mean free paths comparable to the interatomic separations[74] – suggestive that the phonon gas model presented here will be useful for predicting the thermal conductivity of supercritical fluids. At 0.1 MPa, 1 MPa, 10 MPa, and 100 MPa our model overestimates argon's measured thermal conductivity by an average of 0.033 $Wm^{-1}K^{-1}$, 0.031 $Wm^{-1}K^{-1}$, 0.028 $Wm^{-1}K^{-1}$, and 0.009 $Wm^{-1}K^{-1}$, respectively.
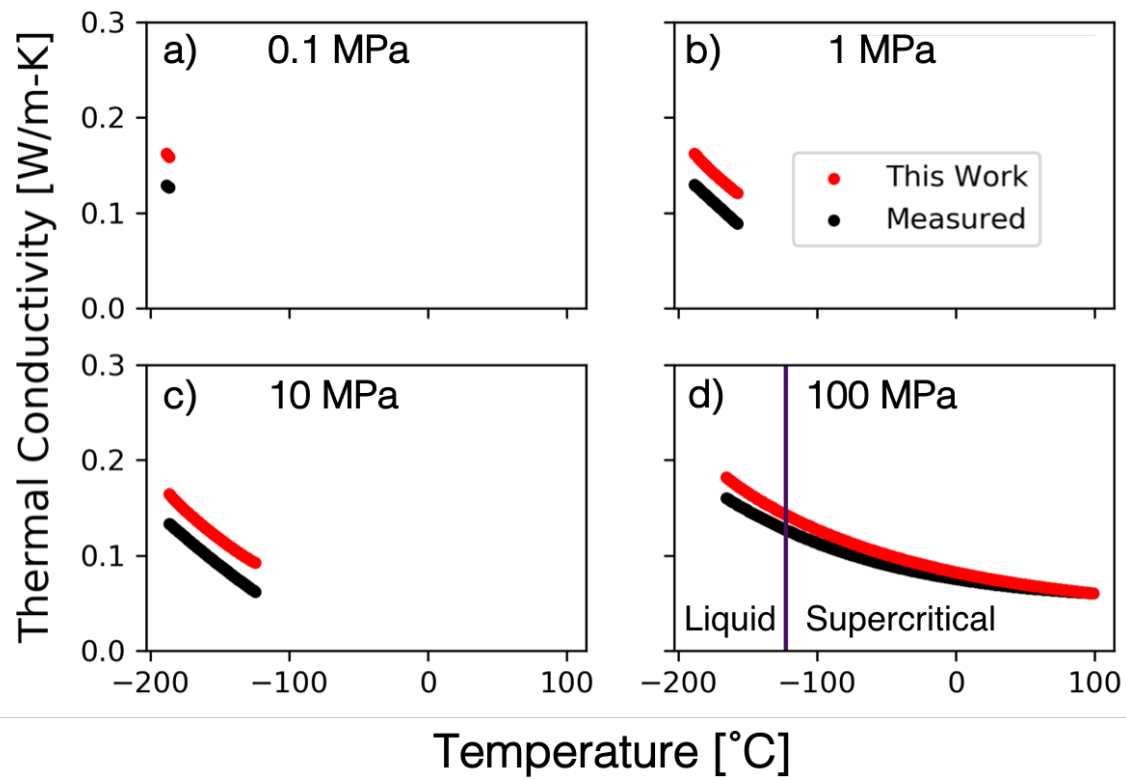
Figure 2.9. The effect of changing pressure on liquid argon's thermal conductivity. Measured and modeled results of argon under pressures of a) 0.1 MPa, b) 1 MPa, c) 10 MPa, and d) 100 MPa.

2.4 Evaluating the accuracy of the phonon gas model

The fundamental mechanism of heat conduction in liquids, foundational for liquid heat transfer applications, is not well understood. Previously, no model could adequately describe the experimental thermal conductivity results for important heat transfer fluids like water and molten sodium nitrate. In this work, we assumed that vibrational modes, which move at the speed of sound and have a mean free path on the order of the intermolecular distance, conduct heat in liquids. We formulated a simplified phonon gas model, **Eq. 13**, to calculate the theoretical thermal conductivity for liquids with varying intermolecular interaction energy. The calculated thermal conductivity from the liquid phonon gas model fits very well with experimental measurements for water (2.98% deviation), sodium nitrate (1.32% deviation), and argon under 100 MPa of pressure (9.31% deviation). We explored the limitations of the phonon gas model in liquids with weaker intermolecular interactions, such as argon (under varying lower pressures), hydrogen sulfide, alcohols, and long alkane chains (results summarized in **Table 2**). Our results suggest that the phonon gas model fits particularly well for liquids with very strong intermolecular interactions – Coulomb energy, hydrogen bonding, and high pressure – which indicates that these liquids exhibit more solid-like molecular vibrational character (see **Figure 10**). Increasing the liquid density [mol/L] similarly reduces the deviation of the predictions from the phonon gas model (see **Figure 11). Figures 10 and 11** show that when comparing any 2 liquids with the same interaction energy type (H_2O vs. H_2S, Ar 100 MPa vs. Ar 1 MPa, Methanol vs. Ethanol, or $NaNO_3$ vs. KNO_3), increasing the interaction energy or density leads the phonon gas model to more accurately predict the thermal conductivity. Also, it shows a general trend that the liquid phonon gas model becomes more accurate as the interaction energy and density increase. Whereas for other models shown in this work, there are no stand out trends.

Figure 2.10. Deviation between phonon gas model calculated thermal conductivity and measured thermal conductivity for liquids with varying interaction energies.

Figure 2.11. Deviation between phonon gas model calculated thermal conductivity and measured thermal conductivity for liquids with varying density. The density for each liquid was averaged over their respective temperature range.

Bridgman's model for liquid thermal conductivity successfully captures the value and temperature dependence of experimental results for liquids with Keesom energy holding them together with intermediate strength – hydrogen-sulfide (4.76% deviation), methanol (-8.70% deviation), and ethanol (-12.3% deviation) – shown in **Figure 2.12 and 2.13**. While the phonon gas model generally captures the temperature dependence of these liquids' thermal conductivity (except for ethanol), the thermal conductivity value is overestimated by over 40%. It is worth restating that our phonon gas model (**Eq. 2.14**) simplifies to Bridgman's result if we assume $C_P = 2C_V$ and $C_V = 3k_B$.
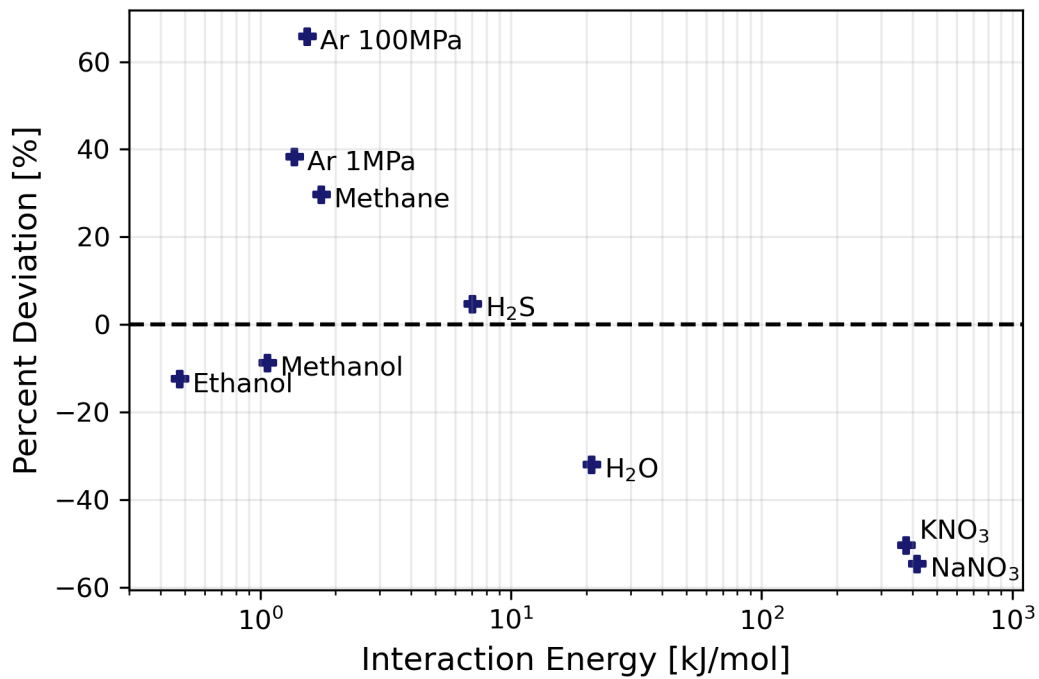
Figure 2.12 Deviation between Bridgman's calculated thermal conductivity and measured thermal conductivity for liquids with varying interaction energies.
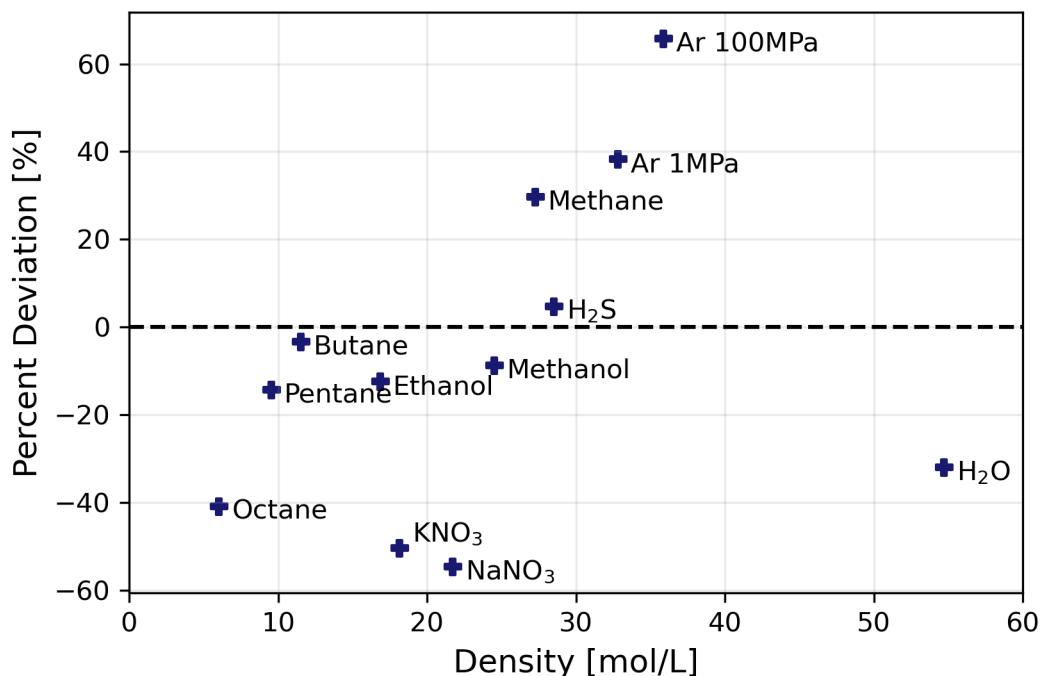
Figure 2.13 Deviation between Bridgman's calculated thermal conductivity and measured thermal conductivity for liquids with varying density.

Bridgman's model also accurately predicts the thermal conductivity of butane (-3.31% deviation), though it overestimates methane (29.71% deviation) and underestimates octane (-40.80% deviation). This suggests that for shorter alkane chain molecules, there is more energy transferred between molecules than the $2k_B$ Bridgman assumes to be constant across all liquids; for longer alkane chains, it suggests that less than $2k_B$ is transferred between neighboring molecules since more energy would remain within an individual molecular chain. The liquid phonon gas model is inaccurate in predicting the thermal conductivity for alkane chains with weak London dispersion holding them together, and as the molecular chains grow longer, the phonon gas model increasingly overestimates thermal conductivity (see **Fig. 2.14**). The growing overestimation could stem from the phonon gas model's use of experimental heat capacity to approximate how much energy the collective vibrations in a liquid transport. As molecular chain

length increases, more energy is stored in intramolecular vibrations that do not contribute to heat transport between molecules, leading our simplified phonon gas model to overestimate thermal conductivity. The deviation could also come from our assumption that mean free path is the intermolecular distance, which does not capture both intermolecular and intramolecular interactions as chains become entangled with several other chains.
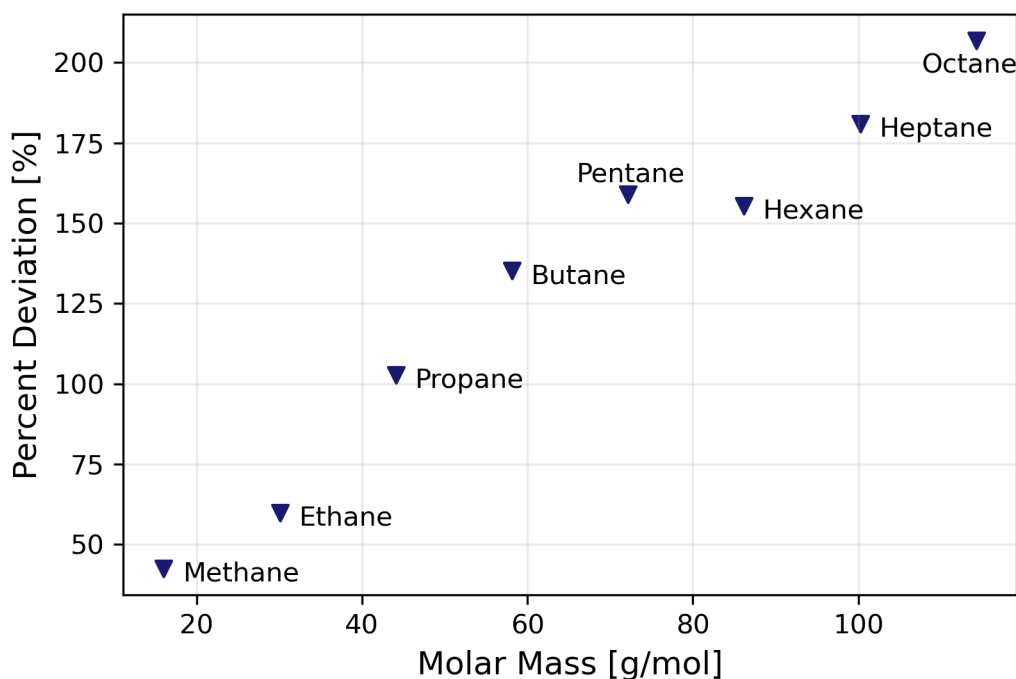
Figure 2.14. Deviation between phonon gas model calculated thermal conductivity and measured thermal conductivity for alkanes with varying molar masses.

For all liquids examined in this work, it is interesting that the Cahill-Pohl minimum thermal conductivity, formulated for amorphous solids, also serves as a lower limit for liquid thermal conductivity (see **Figure 2.15**). The Cahill-Pohl model also provides a fairly accurate prediction for liquid argon's thermal conductivity at high pressure (-0.29% for 100 MPa). The phonon gas model generally captures liquid argon's temperature dependent thermal

conductivity, but the value is always slightly overestimated (28.85% for 1 MPa and 9.31% for 100 MPa). It was reconfirmed that Chapman-Enskog's kinetic theory of liquids does not capture the thermal conductivity of liquids (see **Figure 2.16)**.

2.5 Conclusion

This work provides a helpful model for understanding heat conduction in dense, strongly interacting liquids and a tool to interpret experimental measurements of liquid thermal conductivity. Our formula (**Eq. 2.11**) based on the phonon gas model, only requires experimental inputs of heat capacity, speed of sound, and density (or ionic radii). By choosing representative liquids from all different types of intermolecular interactions, and then quantifying the interaction energy, we tested how well the liquid phonon gas model performs across a wide variety of liquids.

We find that the phonon gas model can accurately predict the temperature dependent thermal conductivity of strongly interacting fluids (with interaction energy greater than ~ 1 kJ/mol), such as water and molten nitrate salts – two of the most important heat transfer fluids. It is likely that the success of the model on dense strongly interacting fluids is related to the types intermolecular and intramolecular interactions in these fluids. Further study is required to determine if the full liquid phonon gas model in **Eq. 2.10**, taking into account the frequency dependent velocity and mean free path of phonons, as well as the Frenkel frequency for transverse modes, would more accurately predict the thermal conductivity of liquids with weaker intermolecular interactions.
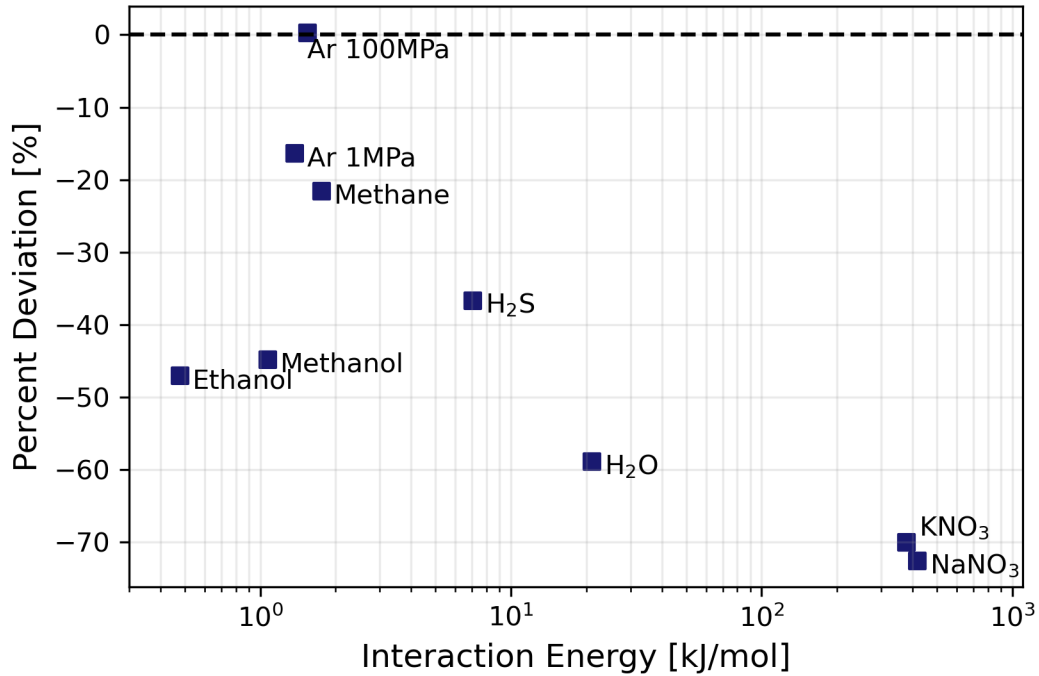
Figure 2.15. Deviation between the Cahill-Pohl calculated minimum thermal conductivity and measured thermal conductivity for liquids with varying interaction energies.
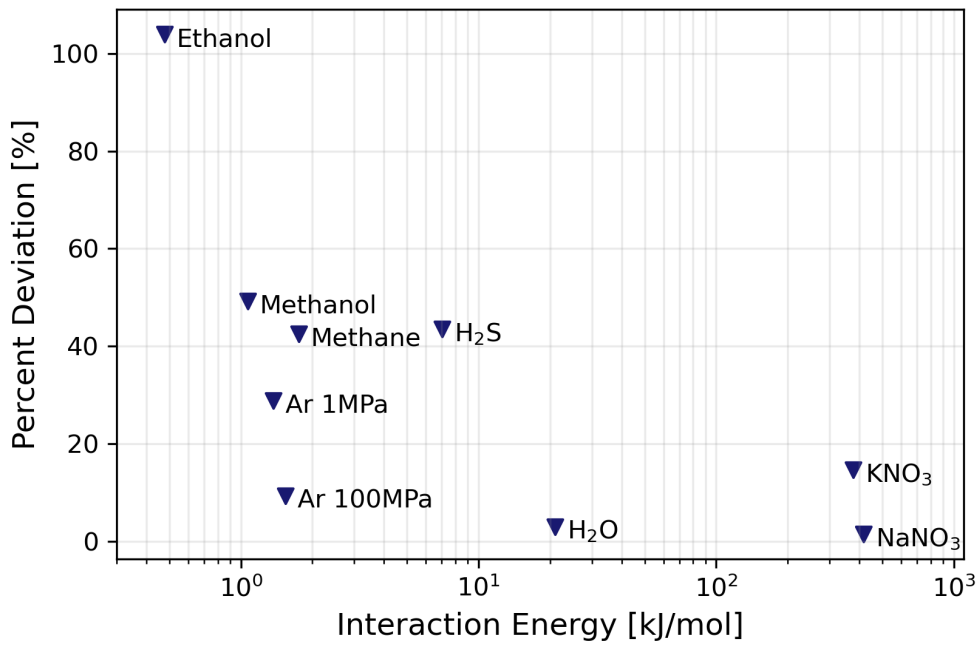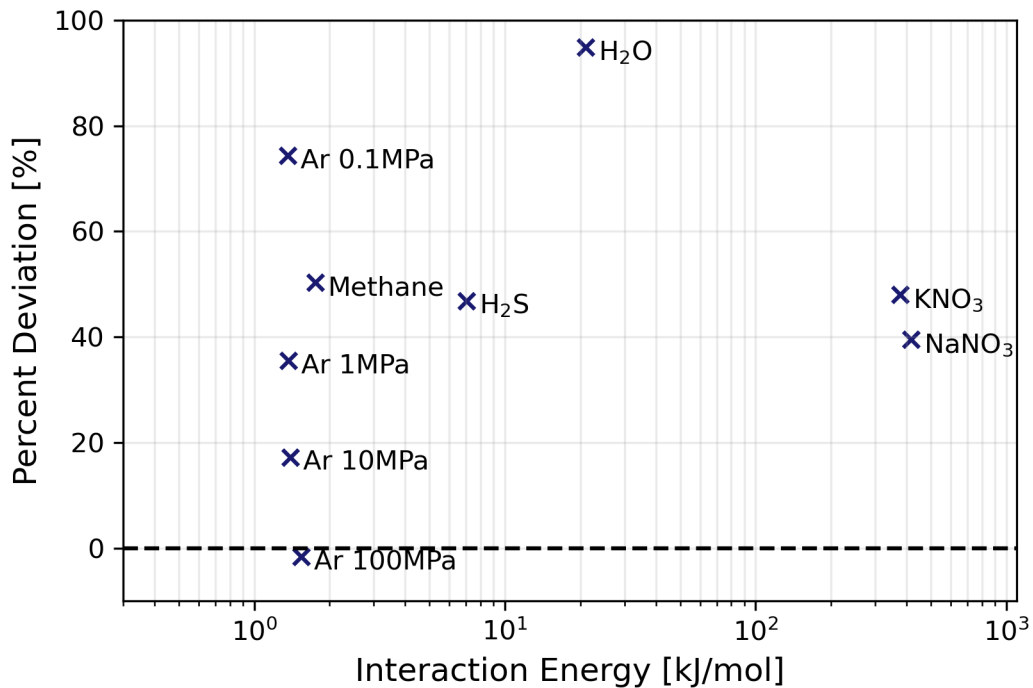

Figure 2.16. Deviation between the Chapman-Enskog thermal conductivity and measured thermal conductivity for liquids with varying interaction energies.

103

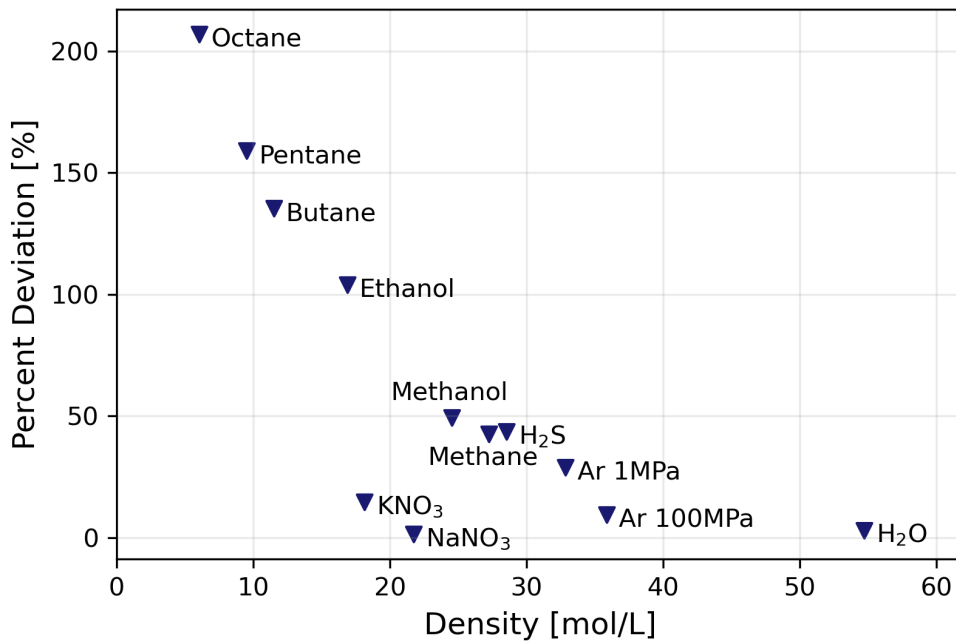**Table 2.2.** Average deviation of thermal conductivity modeling results from experimentally measured results. The percent error is listed in parentheses. Deviations less than or equal to ±15% are highlighted in green.

Liquid	Interaction Energy	Error [$\frac{W}{m-K}$]			
		This Work	Bridgman	Cahill-Pohl	Chapman & Enskog
Sodium Nitrate	Coulomb 417 kJ/mol	0.009 (1.46%)	-0.323 (-54.57%)	-0.429 (-72.50%)	0.235 (39.54%)
Potassium Nitrate	Coulomb 376 kJ/mol	0.069 (14.66%)	-0.235 (-50.31%)	-0.327 (-69.93%)	0.225 (48.02%)
Water	H-Bonding 21 kJ/mol	0.018 (2.98%)	-0.204 (-31.96%)	-0.374 (-58.83%)	0.560 (94.88%)
Hydrogen Sulfide	H-Bonding 7.02 kJ/mol	0.105 (43.49%)	0.012 (4.76%)	-0.088 (-36.62%)	0.113 (46.86%)
Methanol	Keesom 1.07 kJ/mol	0.099 (49.24%)	-0.017 (-8.70%)	-0.089 (-44.76%)	N/A
Ethanol	Keesom 0.48 kJ/mol	0.171 (103.97%)	-0.020 (-12.3%)	-0.077 (46.99%)	N/A
Methane	London 1.75 kJ/mol	0.084 (42.53%)	0.059 (29.71%)	-0.043 (-21.52%)	0.101 (50.34%)
Butane	London N/A	0.200 (135.20%)	-0.004 (-3.31%)	-0.060 (-41.50%)	0.203 (123.53%)
Pentane	London N/A	0.226 (158.91%)	-0.019 (-14.25%)	-0.067 (-48.12%)	0.197 (118.24%)
Octane	London N/A	0.255 (206.82%)	-0.049 (-40.80%)	-0.078 (-64.18%)	0.056 (35.78%)
Argon (1 MPa)	London 1.36 kJ/mol	0.031 (28.85%)	0.042 (38.26%)	-0.018 (-16.35%)	0.041 (35.58%)
Argon (100 MPa)	London 1.54 kJ/mol	0.010 (9.31%)	0.059 (65.76%)	-0.001 (-0.29%)	-0.004 (-1.67%)

Acknowledgements

Chapter 2 is a reprint of **Zhao, A. Z.,** Wingert, M. C., Chen, R., & Garay, J. E. (2021). Phonon gas model for thermal conductivity of dense, strongly interacting liquids. *Journal of Applied Physics*, *129*(23), 235101. For this publication, I formulated the analytical model, performed the calculations, and wrote the paper.

References

(1)   Nunes, V. M. B.; Queirós, C. S.; Lourenço, M. J. V.; Santos, F. J. V.; Nieto de Castro, C. A. Molten Salts as Engineering Fluids – A Review: Part I. Molten Alkali Nitrates. *Appl. Energy* **2016**, *183*, 603–611. https://doi.org/10.1016/j.apenergy.2016.09.003.

(2)   Ho, C. K. Advances in Central Receivers for Concentrating Solar Applications. *Sol. Energy* **2017**, *152*, 38–56. https://doi.org/10.1016/J.SOLENER.2017.03.048.

(3)   Mehos, M.; Turchi, C.; Vidal, J.; Wagner, M.; Ma, Z.; Ho, C.; Kolb, W.; Andraka, C.; Kruizenga, A. *Concentrating Solar Power Gen3 Demonstration Roadmap*; 2017.

(4)   Forsberg, C. W.; Peterson, P. F.; Pickard, P. S. Molten-Salt-Cooled Advanced High-Temperature Reactor for Production of Hydrogen and Electricity. *Nucl. Technol.* **2003**, *144* (3), 289–302. https://doi.org/10.13182/NT03-1.

(5)   Serp, J.; Allibert, M.; Beneš, O.; Delpech, S.; Feynberg, O.; Ghetta, V.; Heuer, D.; Holcomb, D.; Ignatiev, V.; Kloosterman, J. L.; Luzzi, L.; Merle-Lucotte, E.; Uhlíř, J.; Yoshioka, R.; Zhimin, D. The Molten Salt Reactor (MSR) in Generation IV: Overview and Perspectives. *Prog. Nucl. Energy* **2014**, *77*, 308–319. https://doi.org/10.1016/J.PNUCENE.2014.02.014.

(6)   Huber, M. L.; Perkins, R. A.; Friend, D. G.; Sengers, J. V.; Assael, M. J.; Metaxa, I. N.; Miyagawa, K.; Hellmann, R.; Vogel, E. New International Formulation for the Thermal Conductivity of H2O. *J. Phys. Chem. Ref. Data* **2012**, *41* (3), 21. https://doi.org/10.1063/1.4738955.

(7)   Zhao, A. Z.; Wingert, M. C.; Garay, J. E. Frequency-Domain Hot-Wire Measurements of Molten Nitrate Salt Thermal Conductivity. *J. Chem. Eng. Data* **2020**, acs.jced.0c00621. https://doi.org/10.1021/acs.jced.0c00621.

(8)   Chliatzou, C. D.; Assael, M. J.; Antoniadis, K. D.; Huber, M. L.; Wakeham, W. A. Reference Correlations for the Thermal Conductivity of 13 Inorganic Molten Salts. *J.*

Phys. Chem. Ref. Data **2018**, *47*, 33104. https://doi.org/10.1063/1.5052343.

(9)   Mclaughlin, E. The Thermal Conductivity of Liquids and Dense Gases. *Chem. Rev.* **1964**, *64* (4), 389–428.

(10)   Lv, W.; Henry, A. Examining the Validity of the Phonon Gas Model in Amorphous Materials. *Sci. Rep.* **2016**, *6* (1), 37675. https://doi.org/10.1038/srep37675.

(11)   Toberer, E. S.; Baranowski, L. L.; Dames, C. Advances in Thermal Conductivity. *Annu. Rev. Mater. Res* **2012**, *42*, 179–209. https://doi.org/10.1146/annurev-matsci-070511-155040.

(12)   Allen, P. B.; Feldman, J. L.; Fabian, J.; Wooten, F. Diffusons, Locons and Propagons: Character of Atomic Vibrations in Amorphous Si. *Philos. Mag. B Phys. Condens. Matter; Stat. Mech. Electron. Opt. Magn. Prop.* **1999**, *79* (11–12), 1715–1731. https://doi.org/10.1080/13642819908223054.

(13)   DeAngelis, F.; Muraleedharan, M. G.; Moon, J.; Seyf, H. R.; Minnich, A. J.; McGaughey, A. J. H.; Henry, A. Thermal Transport in Disordered Materials. *Nanoscale Microscale Thermophys. Eng.* **2018**, 1–36. https://doi.org/10.1080/15567265.2018.1519004.

(14)   Wingert, M. C.; Zheng, J.; Kwon, S.; Chen, R. Thermal Transport in Amorphous Materials : A Review. *Semicond. Sci. Technol.* **2016**, *31* (113003), 1–16.

(15)   Cahill, D. G.; Watson, S. K.; Pohl, R. O. Lower Limit to the Thermal Conductivity of Disordered Crystals. *Phys. Rev. B* **1992**, *46* (10), 6131–6140. https://doi.org/10.1103/PhysRevB.46.6131.

(16)   Agne, M. T.; Hanus, R.; Snyder, G. J. Minimum Thermal Conductivity in the Context of: Diffuson -Mediated Thermal Transport. *Energy Environ. Sci.* **2018**, *11* (3), 609–616. https://doi.org/10.1039/c7ee03256k.

(17)   Xi, Q.; Zhong, J.; He, J.; Xu, X.; Nakayama, T.; Wang, Y.; Liu, J.; Zhou, J.; Li, B.; Li, and B.; Xi, Q.; Zhong, J.; He, J.; Xu, X.; Nakayama, T.; Wang, Y.; Liu, J.; Zhou, J.; Li, and B. A Ubiquitous Thermal Conductivity Formula for Liquids, Polymer Glass, and Amorphous Solids. *Chinese Phys. Lett.* **2020**, *37* (10), 1–6. https://doi.org/10.1088/0256-307X/37/10/104401.

(18)   Trachenko, K. Heat Capacity of Liquids: An Approach from the Solid Phase. *Phys. Rev. B* **2008**, *78* (10). https://doi.org/10.1103/PhysRevB.78.104201.

(19)   Bolmatov, D.; Brazhkin, V. V.; Trachenko, K. The Phonon Theory of Liquid Thermodynamics. *Sci. Rep.* **2012**, *2*. https://doi.org/10.1038/SREP00421.

(20)   Brazhkin, V. V; Trachenko, K. Collective Excitations and Thermodynamics of Disordered State: New Insights into an Old Problem. *J. Phys. Chem. B* **2014**, *118*,

11417–11427. https://doi.org/10.1021/jp503647s.

(21)   Brazhkin, V. V.; Trachenko, K. Between Glass and Gas: Thermodynamics of Liquid Matter. *J. Non. Cryst. Solids* **2015**, *407*, 149–153. https://doi.org/10.1016/j.jnoncrysol.2014.09.030.

(22)   Trachenko, K.; Brazhkin, V. V. Collective Modes and Thermodynamics of the Liquid State. *Reports Prog. Phys.* **2016**, *79* (1), 016502. https://doi.org/10.1088/0034-4885/79/1/016502.

(23)   Debye, P. Zur Theorie Der Spezifischen Wärmen. *Ann. Phys.* **1912**, *344* (14), 789–839. https://doi.org/10.1002/andp.19123441404.

(24)   Kittel C. *Introduction to Solid State Physics, 8th Edition*; John Wiley & Sons, New York, 1996.

(25)   Frenkel, J. *Kinetic Theory of Liquids*; Oxford:Clarendon Press, 1946.

(26)   Burkel, E. Phonon Spectroscopy by Inelastic X-Ray Scattering. *Reports on Progress in Physics*. IOP Publishing February 1, 2000, pp 171–232. https://doi.org/10.1088/0034-4885/63/2/203.

(27)   Giordano, V. M.; Monaco, G. Inelastic X-Ray Scattering Study of Liquid Ga: Implications for the Short-Range Order. *Phys. Rev. B* **2011**, *84* (4), 52201–52202. https://doi.org/10.1103/PhysRevB.84.052201.

(28)   Hosokawa, S.; Munejiri, S.; Inui, M.; Kajihara, Y.; Pilgrim, W. C.; Ohmasa, Y.; Tsutsui, S.; Baron, A. Q. R.; Shimojo, F.; Hoshino, K. Transverse Excitations in Liquid Sn. *J. Phys. Condens. Matter* **2013**, *25* (11), 112101. https://doi.org/10.1088/0953-8984/25/11/112101.

(29)   Hosokawa, S.; Inui, M.; Kajihara, Y.; Tsutsui, S.; Baron, A. Q. R. Transverse Excitations in Liquid Fe, Cu and Zn. In *Journal of Physics Condensed Matter*; Institute of Physics Publishing, 2015; Vol. 27, p 194104. https://doi.org/10.1088/0953-8984/27/19/194104.

(30)   Cunsolo, A. The Terahertz Dynamics of Simplest Fluids Probed by Inelastic X-Ray Scattering The Terahertz Dynamics of Simplest Fluids Probed by Inelastic X-Ray Scattering. *Int. Rev. Phys. Chem.* **2017**, *36* (3), 433–539. https://doi.org/10.1080/0144235X.2017.1331900.

(31)   Elton, D. C.; Fernández-Serra, M. The Hydrogen-Bond Network of Water Supports Propagating Optical Phonon-like Modes. *Nat. Commun.* **2016**, *7* (1), 1–8. https://doi.org/10.1038/ncomms10193.

(32)   Caplan, M. E.; Giri, A.; Hopkins, P. E. Analytical Model for the Effects of Wetting on Thermal Boundary Conductance across Solid/Classical Liquid Interfaces. *J. Chem. Phys.* **2014**, *140* (15). https://doi.org/10.1063/1.4870778.

(33)   Henry, A. S.; Chen, G. Spectral Phonon Transport Properties of Silicon Based on Molecular Dynamics Simulations and Lattice Dynamics. *J. Comput. Theor. Nanosci.* **2008**, *5* (7), 1–12. https://doi.org/10.1166/jctn.2008.001.

(34)   Seyf, H. R.; Gordiz, K.; Deangelis, F.; Henry, A. Using Green-Kubo Modal Analysis (GKMA) and Interface Conductance Modal Analysis (ICMA) to Study Phonon Transport with Molecular Dynamics. *J. Appl. Phys.* **2019**, *125* (8), 081101. https://doi.org/10.1063/1.5081722.

(35)   Rahman, A. Correlations in the Motion of Atoms in Liquid Argon. *Phys. Rev.* **1964**, *136* (2A). https://doi.org/10.1103/PhysRev.136.A405.

(36)   Skold, K.; Larsson, K. E. Atomic Motion in Liquid Argon. *Phys. Rev.* **1967**, *161* (1), 102–116.

(37)   Singwi, K. S.; Sköld, K.; Tosi, M. P. Zero Sound in Classical Liquids. *Phys. Rev. Lett.* **1968**, *21* (13), 881–884. https://doi.org/10.1103/PhysRevLett.21.881.

(38)   Copley, J. R. D.; Lovesey, S. W. The Dynamic Properties of Monatomic Liquids. *Reports Prog. Phys.* **1975**, *38* (4), 461–563. https://doi.org/10.1088/0034-4885/38/4/001.

(39)   Ohmine, I. Liquid Water Dynamics: Collective Motions, Fluctuation, and Relaxation. *J. Phys. Chem.* **1995**, *99* (18), 6767–6776. https://doi.org/10.1021/j100018a004.

(40)   Scopigno, T.; Balucani, U.; Ruocco, G.; Sette, F. Evidence of Two Viscous Relaxation Processes in the Collective Dynamics of Liquid Lithium. *Phys. Rev. Lett.* **2000**, *85* (19), 4076–4079. https://doi.org/10.1103/PhysRevLett.85.4076.

(41)   Bakker, H. J.; Skinner, J. L. Vibrational Spectroscopy as a Probe of Structure and Dynamics in Liquid Water. *Chem. Rev.* **2010**, *110* (3), 1498–1517. https://doi.org/10.1021/cr9001879.

(42)   Yoshida, K.; Yamaguchi, T.; Yokoo, T.; Itoh, S. Collective Dynamics Measurement of Liquid Methanol by Inelastic Neutron Scattering. *J. Mol. Liq.* **2016**, *222*, 395–397. https://doi.org/10.1016/j.molliq.2016.07.038.

(43)   Amann-Winkel, K.; Bellissent-Funel, M.-C.; Bove, L. E.; Loerting, T.; Nilsson, A.; Paciaroni, A.; Schlesinger, D.; Skinner, L. X-Ray and Neutron Scattering of Water. **2016**. https://doi.org/10.1021/acs.chemrev.5b00663.

(44)   Lemmon, E. W.; McLinden, M. O.; Friend, D. G. *"Thermophysical Properties of Fluid Systems" in NIST Chemistry WebBook, NIST Standard Reference Database Number 69*; Linstrom, P. J., Mallard, W. G., Eds.; National Institute of Standards and Technology: Gaithersburg MD, 20899, 2020.

(45)   Ruocco, G.; Sette, F. The High-Frequency Dynamics of Liquid Water. *J. Phys. Condens. Matter* **1999**, *259*.

(46)   Larkin, J. M.; McGaughey, A. J. H. Thermal Conductivity Accumulation in Amorphous Silica and Amorphous Silicon. *Phys. Rev. B - Condens. Matter Mater. Phys.* **2014**, *89* (14), 144303. https://doi.org/10.1103/PhysRevB.89.144303.

(47)   Slack, G. A. The Thermal Conductivity of Nonmetallic Crystals. *Solid State Phys. - Adv. Res. Appl.* **1979**, *34* (C), 1–71. https://doi.org/10.1016/S0081-1947(08)60359-8.

(48)   Yoon, B. J.; Jhon, M. S.; Eyring, H. *Radial Distribution Function of Liquid Argon According to Significant Structure Theory*; 1981; Vol. 78.

(49)   Soper, A. K. The Radial Distribution Functions of Water and Ice from 220 to 673 K and at Pressures up to 400 MPa. *Chem. Phys.* **2000**. https://doi.org/10.1016/S0301-0104(00)00179-8.

(50)   Wilding, M. C.; Wilson, M.; Ribeiro, M. C. C.; Benmore, C. J.; Weber, J. K. R.; Alderman, O. L. G.; Tamalonis, A.; Parise, J. B. The Structure of Liquid Alkali Nitrates and Nitrites. *Phys. Chem. Chem. Phys* **2017**, *19*, 21625. https://doi.org/10.1039/c7cp03465b.

(51)   Shannon, R. D. Revised Effective Ionic Radii and Systematic Studies of Interatomic Distances in Halides and Chalcogenides. *Acta Crystallogr. Sect. A* **1976**, *32* (5), 751–767. https://doi.org/10.1107/S0567739476001551.

(52)   Gheribi, A. E.; Torres, J. A.; Chartrand, P. Recommended Values for the Thermal Conductivity of Molten Salts between the Melting and Boiling Points. *Sol. Energy Mater. Sol. Cells* **2014**, *126*, 11–25. https://doi.org/10.1016/J.SOLMAT.2014.03.028.

(53)   Bridgman, P. W. The Thermal Conductivity of Liquids. *Proc. Natl. Acad. Sci. U. S. A.* **1923**, *9* (10), 341–345.

(54)   Israelachvili, J. N. *Intermolecular and Surface Forces*; Academic Press, 2011.

(55)   Wingert, M. C.; Zhao, A. Z.; Kodera, Y.; Obrey, S. J.; Garay, J. E. Frequency-Domain Hot-Wire Sensor and 3D Model for Thermal Conductivity Measurements of Reactive and Corrosive Materials at High Temperatures. *Rev. Sci. Instrum.* **2020**, *91* (5), 054904. https://doi.org/10.1063/1.5138915.

(56)   Takahashi, Y.; Sakamoto, R.; Kamimoto, M. *Heat Capacities and Latent Heats of LiNO3, NaNO3, and KNO3*; 1988; Vol. 9.

(57)   Janz, G. J.; Allen, C. B.; Bansal, N. P.; Murphy, R. M.; Tomkins, R. P. T. *Physical Properties Data Compilations Relevant to Energy Storage. II. Molten Salts: Data on Single and Multi-Component Salt Systems*; United States Government Printing Office: Washington D.C., 1979.

(58)   Tasidou, K. A.; Chliatzou, C. D.; Assael, M. J.; Antoniadis, K. D.; Mylona, S. K.; Huber, M. L.; Wakeham, W. A. Reference Correlations for the Viscosity of 13 Inorganic Molten Salts. *J. Phys. Chem. Ref. Data* **2019**, *48* (1), 013101.

https://doi.org/10.1063/1.5091511.

(59)   Higgs, R. W.; Litovitz, T. A. Ultrasonic Absorption and Velocity in Molten Salts. *Cit. J. Acoust. Soc. Am.* **1960**, *32*, 1108. https://doi.org/10.1121/1.1908357.

(60)   Rumble, J. R.; Lide, D. R.; Bruno, T. J. *"Dipole Moments," in CRC Handbook of Chemistry and Physics*, 100th Edit.; Rumble, J. R., Ed.; CRC Press/Taylor & Francis: Boca Raton, FL.

(61)   Lane, J. R. CCSDTQ Optimized Geometry of Water Dimer. *J. Chem. Theory Comput.* **2013**, *9* (1), 316–323. https://doi.org/10.1021/ct300832f.

(62)   Das, A.; Mandal, P. K.; Lovas, F. J.; Medcraft, C.; Walker, N. R.; Arunan, E. The H$_2$S Dimer Is Hydrogen-Bonded: Direct Confirmation from Microwave Spectroscopy. *Angew. Chemie Int. Ed.* **2018**, *57* (46), 15199–15203. https://doi.org/10.1002/anie.201808162.

(63)   Perkins, M. A.; Barlow, K. R.; Dreux, K. M.; Tschumper, G. S. Anchoring the Hydrogen Sulfide Dimer Potential Energy Surface to Juxtapose (H2S)2 with (H2O)2. *J. Chem. Phys.* **2020**, *152* (21), 214306. https://doi.org/10.1063/5.0008929.

(64)   Lousada, C. M.; Korzhavyi, P. A. The H2S Dimer Revisited – Insights from Wave-Function and Density Functional Theory Methods. Ab Initio Molecular Dynamics Simulations of Liquid H2S. *Comput. Theor. Chem.* **2020**, *1180*, 112821. https://doi.org/10.1016/j.comptc.2020.112821.

(65)   Sykioti, E. A.; Assael, M. J.; Huber, M. L.; Perkins, R. A. Reference Correlation of the Thermal Conductivity of Methanol from the Triple Point to 660 K and up to 245 MPa. *J. Phys. Chem. Ref Data* **2013**, *42*, 43101. https://doi.org/10.1063/1.4829449.

(66)   Pedersen, M. J.; Kay, W. B.; Hershey, H. C. Excess Enthalpies, Heat Capacities, and Excess Heat Capacities as a Function of Temperature in Liquid Mixtures of Ethanol + Toluene, Ethanol + Hexamethyldisiloxane, and Hexamethyldisiloxane + Toluene. *J. Chem. Thermodyn.* **1975**, *7* (12), 1107–1118. https://doi.org/10.1016/0021-9614(75)90030-0.

(67)   Schroeder, J. A.; Penoncello, S. G.; Schroeder, J. S. A Fundamental Equation of State for Ethanol. *J. Phys. Chem. Ref. Data* **2014**, *43* (043102). https://doi.org/10.1063/1.4895394.

(68)   Khasanshin, T. S.; Aleksandrov, A. A. Thermodynamic Properties of Ethanol at Atmospheric Pressure. *J. Eng. Phys.* **1984**, *47* (3), 1046–1052. https://doi.org/10.1007/BF00873717.

(69)   Assael, M. J.; Sykioti, E. A.; Huber, M. L.; Perkins, R. A. Reference Correlation of the Thermal Conductivity of Ethanol from the Triple Point to 600 K and up to 245 MPa. *Therm. Conduct. ethanol J. Chem. Phys.* **2013**, *42*, 174503.

https://doi.org/10.1063/1.4797368.

(70)   Torii, D.; Nakano, T.; Ohara, T. Contribution of Inter- and Intramolecular Energy
         Transfers to Heat Conduction in Liquids. *J. Chem. Phys.* **2008**, *128*, 817.
         https://doi.org/10.1063/1.2821963.

(71)   Ohara, T.; Yuan, T. C.; Torii, D.; Kikugawa, G.; Kosugi, N. Heat Conduction in Chain
         Polymer Liquids: Molecular Dynamics Study on the Contributions of Inter-and
         Intramolecular Energy Transfer. *J. Chem. Phys* **2011**, *135*, 34507.
         https://doi.org/10.1063/1.3613648.

(72)   Matsubara, H.; Kikugawa, G.; Bessho, T.; Yamashita, S.; Ohara, T. Effects of
         Molecular Structure on Microscopic Heat Transport in Chain Polymer Liquids. *J. Chem.
         Phys.* **2015**, *142*, 164509. https://doi.org/10.1063/1.4919313.

(73)   Matsubara, H.; Kikugawa, G.; Bessho, T.; Yamashita, S.; Ohara, T. Understanding the
         Chain Length Dependence of Thermal Conductivity of Liquid Alcohols at 298 K on
         the Basis of Molecular-Scale Energy Transfer. *Fluid Phase Equilib.* **2017**, *441*, 24–32.
         https://doi.org/10.1016/J.FLUID.2016.12.019.

(74)   Wang, L.; Yang, C.; Dove, M. T.; Mokshin, A. V.; Brazhkin, V. V.; Trachenko, K. The
         Nature of Collective Excitations and Their Crossover at Extreme Supercritical
         Conditions. *Sci. Rep.* **2019**, *9* (1), 1–9. https://doi.org/10.1038/s41598-018-36178-6.

Chapter 3: Frequency-domain hot-wire measurements of molten nitrate salts

The thermal conductivity of liquids has traditionally been determined by measuring either the steady-state temperature gradient or time-dependent temperature rise in a sample due to an applied heat flux. The transient hot-wire method has become the standard for measuring liquid thermal conductivity; in this method, direct current Joule heats a long, thin wire immersed in a liquid sample, and the measured temperature rise over a particular time interval is fit to a heat transfer model to extract the thermal conductivity of the liquid. However, in the high-temperature environments of molten salts, long metal wires are vulnerable to corrosion, and convection errors are magnified in larger volumes of molten salts. Here, we utilize a new frequency-domain, corrosion-resistant, short hot-wire technique (sensor and model) to measure the thermal conductivity of molten $NaNO_3$ (2.78% standard uncertainty), KNO_3 (2.38% standard uncertainty), and Solar Salt mixture (2.66% standard uncertainty). Operating in the frequency domain and utilizing a full 3D model allows the use of short sensor wires, reducing the total contact area to minimize corrosion, and the use of small sample volumes, mitigating convection errors. An alternating current at varying frequencies Joule heats a short platinum wire sensor (6.5 mm), which is protected by a 1.6 μm thick Al_2O_3 coating, submerged in molten salt. The frequency-dependent temperature response of the sensor surrounded by salt is measured and fit to a 3D thermal model to obtain the thermal conductivity of the molten salt. Together, the new sensor design and 3D model keep the probed molten salt volume below 1 μL. Our frequency-domain measurements show an ~11-15% higher thermal conductivity of molten nitrate salts than the current reference correlations made from steady-state and time-domain measurements.

112

3.1 Introduction

Molten nitrate salts are important high temperature heat transfer and thermal energy storage fluids used in the solar and nuclear power industries due to their high temperature stability and low vapor pressure.[1] The thermal transport properties of molten nitrates are important to determine the rate at which heat energy can be extracted from a storage reservoir since a higher thermal conductivity fluid can allow the surface area required for an optimized heat exchanger to be reduced.[2] In addition to the magnitude of the thermal conductivity of molten nitrate salts, its temperature dependence is also important to understand how heat transfer changes across the entire operation range up to and above 773.15 Kelvin.

Reliable thermal conductivity measurements of molten salts are difficult due to convection and corrosion, which are magnified at high temperatures. The sample holder, temperature sensors, and electrical wiring must all be able to withstand high temperatures and corrosive molten salt environments. There must also be a way to minimize or account for errors due to natural convection and ambient temperature fluctuations of the heating system, which can alter the magnitude and temperature dependence of the measured thermal conductivity.

The importance and difficulty of measuring the thermal conductivity of nitrate salts is exemplified by the existence of at least 15 previous measurements of $NaNO_3$ in the literature. These measurements have been conducted using a variety of steady-state and time-domain techniques; the wide range in the magnitude and temperature dependence of the measured thermal conductivity of $NaNO_3$ is shown in **Fig. 3.1**. The gap in theoretical understanding of how heat is conducted in molten salts, and liquids in general, compared to gases and solids complicates interpretation of the measured results.

The spread in the available data make it difficult to select the correct magnitude and temperature dependence to use in device and system designs that use these materials. In this regard, reference correlations provide a very useful source for data[3–5]. Over the years, reference correlations have been updated considering newly available measurements and possible issues with previous measurements, which can include lack of protective sensor coatings and convection errors in liquids at high temperature.

Recently, Chliatzou et al.[5] reviewed previous measurements to compile primary data from five separate measurements, each with a reported error of 4% or less, to create a reference correlation for the thermal conductivity of molten $NaNO_3$. One steady-state measurement was included in the primary data since it had the smallest sample gap size of 200 μm[6]; decreasing the distance between temperature probes reduces the temperature gradients and natural convection in the sample. The remaining four measurements were conducted in the time-domain (transient hot-wire[7,8], pulse-heated flat plate[9], and wave-front interferometer[10]). Although the temperature rise is measured for relatively long times, only data in a certain time window is used for model analysis and data fitting to remove errors from the sensor's heat capacity at short times and natural convection in the molten salt and conduction through the containment materials at longer times. As a consequence, selecting the appropriate time window can affect the extracted measured thermal conductivity.[11]
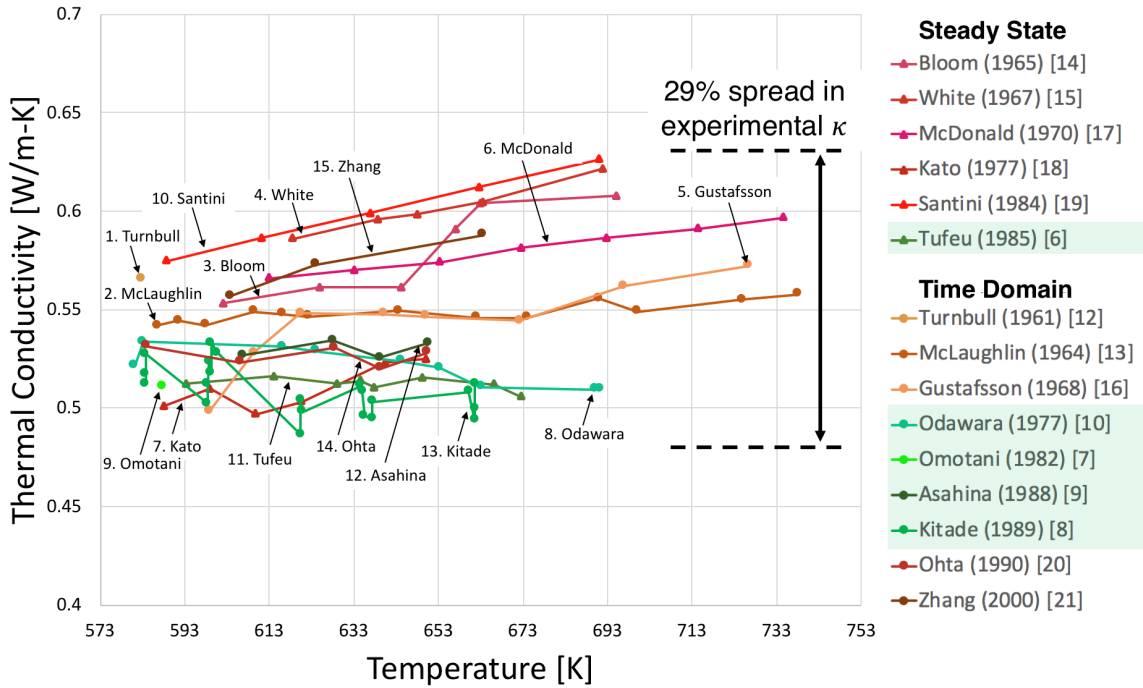
Figure 3.1. Previous thermal conductivity measurements of $NaNO_3$ labeled by first author's last name, in order of publication date from 1 to 15.[6–10,12–21] Steady-state measurements are shown as triangles, and time-domain measurements are shown as circles. Data points in shades of green were used to draw the most recent reference correlation by Chliatzou et al.[22]

Based on steady-state measurements performed by McDonald and Davis[17], Janz published the first reference correlation for the thermal conductivity of molten $NaNO_3$ in 1979.[3] Based on time-domain measurements by Kitade et al.[8], Nagasaka and Nagashima published an updated reference correlation in 1991.[23] Most recently, in 2018, Chliatzou et al. provided an updated reference correlation on what they define as the best available steady-state and time-domain data. They did not include measurements from McDonald and Davis (reported 5% uncertainty)[17] or Zhang and Fuji (reported 3% uncertainty)[21] in their primary data since they "were much higher than other reliable measurements" and "showed a positive increase with temperature". Neither do they include data from Bloom et al. (reported 5% uncertainty)[14] because they "seem to be affected by convection and radiation, increasing [thermal conductivity]

with measurement temperature" despite their use of "a very small sample gap size (0.9 mm)"; and they do not include measurements from McLaughlin[13] in their primary or secondary data sets.

Given the lack of accepted theoretical underpinnings for thermal conductivity in molten salts, it is difficult to provide a firm justification for disregarding careful thermal conductivity measurements that report different values or temperature dependencies. Thus, it is likely that new measurements and theories will refine our understanding of high temperature molten salt thermal conductivity. Here, to the best of the authors' knowledge, we provide the first frequency-domain measurements of molten $NaNO_3$, KNO3, and Solar Salt (60 wt.% $NaNO_3$, 40 wt.% KNO_3) thermal conductivity (see **Table 3.1** for details of salts used). We utilize a new frequency-domain hot-wire sensor with a protective coating to probe the thermal conductivity of molten nitrate salts while minimizing effects from corrosion and convection.[24]

Table 3.1. Nitrate salt chemical composition, CAS registry number, supplier, mass fraction purity measured by supplier using titration with NaOH on a gravimetric basis, and melting point[22].

Chemical Name	CAS Reg. No.	Supplier	Purity (Mass Fraction)	Melting Point
$NaNO_3$	7631-99-4	Sigma-Aldrich	≥ 0.99	583.15 K
KNO_3	7757-79-1	Sigma-Aldrich	≥ 0.99	610.15 K

3.2 Frequency-domain thermal model and sensor

The development of frequency-domain thermal measurements, particularly the 3-omega (3ω) method[25], have proven useful for removing errors inherent in time-domain and steady-state measurements and obtaining very accurate thermal measurement properties of solids over wide temperature ranges. We recently extended the 3ω technique to be used in a hot-wire geometry to measure molten and corrosive materials at high temperature (the full details are reported elsewhere by Wingert *et al.*[24]). The main advantages of operating in the frequency domain for molten materials are (1) convection is minimized by limiting the thermal penetration depth below 100 μm, which, combined with short-length sensors, allows probing of sample volumes less than 1μL, (2) ambient temperature fluctuations of the environment and heater are rejected by locking into the harmonic thermal response of the sample, and (3) a wide window of frequencies are utilized, without arbitrary data truncation, to measure thermal conductivity.

For the measurement, we apply an AC current (at 1ω frequency, I_ω) to Joule heat a platinum hot-wire and surrounding sample. This periodic heating induces temperature and subsequent resistance fluctuations at a 2nd harmonic (2ω), and finally, the voltage fluctuations at a 3rd harmonic (3ω, $V_{3\omega}$) are measured using an SR830 Lock-In Amplifier. The average temperature of the sensor is then calculated *via* the temperature coefficient of resistance (TCR, dR/dT) of the platinum sensor:

$$\tilde{T}_{2\omega,avg} = -2\frac{V_{3\omega}}{I_\omega}\left(\frac{dT}{dR}\right) \tag{3.1}$$

The frequency of I_ω is varied from 1000 Hz to 1 Hz to measure the frequency dependent thermal response of the sample.

The frequency dependent temperature rise in the platinum wire is fit to a solution of the 3D heat equation that we have described in detail previously in Ref [24]. Here we briefly describe the model concept and the final solution. **Fig. 3.2**, schematically depicts the average temperature rise of a finite-length wire (length, L, and radius, r_0) for electrical heating input power ($\tilde{P}_{RMS} = I_\omega^2 R$, with wire electrical resistance R) of varying frequency ($f = \omega/2\pi$). The solution to the 3D heat equation is:

$$\tilde{T}_{2\omega,avg} \cong \sum_{n=1}^{\infty} \frac{8\tilde{P}_{RMS}}{\pi^3 r_0^2 L \kappa_0 (2n-1)^2 \varphi_0^2} \left\{ 1 + \left(\frac{\kappa_1 \varphi_1}{\kappa_0 \varphi_0} \right) \left(\frac{1}{\alpha\delta - \gamma\beta} \right) \left[\frac{\beta I_1(\varphi_1 r_0) - \alpha K_1(\varphi_1 r_0)}{I_1(\varphi_0 r_0)} \right] \right\} \tag{3.2}$$

Where

$$\alpha = \kappa_1 \varphi_1 I_1(\varphi_1 r_1) \left(\frac{1}{\kappa_2 \varphi_2} \frac{K_0(\varphi_2 r_1)}{K_1(\varphi_2 r_1)} + \mathcal{R}_{1,2} \right) + I_0(\varphi_1 r_1) \tag{3.3a}$$

$$\beta = \kappa_1 \varphi_1 K_1(\varphi_1 r_1) \left(\frac{1}{\kappa_2 \varphi_2} \frac{K_0(\varphi_2 r_1)}{K_1(\varphi_2 r_1)} + \mathcal{R}_{1,2} \right) - K_0(\varphi_1 r_1) \tag{3.3b}$$

$$\delta = \kappa_1 \varphi_1 K_1(\varphi_1 r_0) \left(\frac{1}{\kappa_0 \varphi_0} \frac{I_0(\varphi_0 r_0)}{I_1(\varphi_0 r_0)} + \mathcal{R}_{0,1} \right) + K_0(\varphi_1 r_0) \tag{3.3c}$$

$$\gamma = \kappa_1 \varphi_1 I_1(\varphi_1 r_0) \left(\frac{1}{\kappa_0 \varphi_0} \frac{I_0(\varphi_0 r_0)}{I_1(\varphi_0 r_0)} + \mathcal{R}_{0,1} \right) - I_0(\varphi_1 r_0) \tag{3.3d}$$

$$\varphi_N = \sqrt{i \frac{4\pi f \rho_N C_N}{\kappa_N} + \left(\frac{\pi(2n-1)}{L} \right)^2} \tag{3.4}$$

Here $I_j(x)$ and $K_j(x)$ are the jth order modified Bessel functions of the 1ˢᵗ and 2ⁿᵈ kind, respectively, κ_N is thermal conductivity, $\rho_N C_N$ is volumetric heat capacity, and $\mathcal{R}_{0,1}$ and $\mathcal{R}_{1,2}$ are the wire-coating and coating-sample interfacial thermal resistances. The subscripts $N = 0$, 1, and 2 represent the wire, coating, and the surrounding sample, respectively. The model includes an electrically insulating coating layer of thickness $d = r_1 - r_0$. In this work, we assume $\mathcal{R}_{0,1}$ and $\mathcal{R}_{1,2}$ are both 0 since typical interfacial thermal resistances between metal-

alumina[26] and alumina-liquid interfaces are less than $5 \times 10^{-8} \, m^2 K W^{-1}$, which we have previously shown to have a negligible effect on measured thermal conductivity for our frequency-domain hot-wire measurements[24,26]. The radial thermal penetration depth over which the sample is measured decreases as the heating frequency increases according to $\Delta_{p,N} = \sqrt{\kappa_N / 4\pi f \rho_N C_N}$.
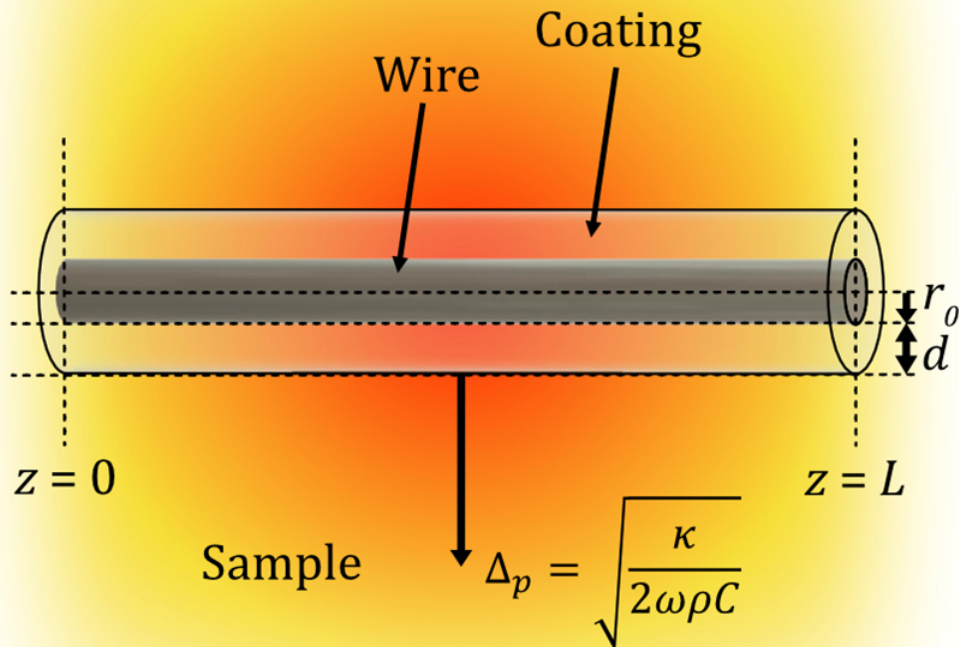
Figure 3.2. Schematic of hot-wire sensor with finite length (L), radius (r_0), and a protective coating (thickness d). The thermal penetration depth into the sample is shown as Δ_p and varies with frequency.

Previous attempts to measure liquid thermal conductivity using the frequency-domain made an infinite wire assumption to simplify the thermal model; however, that assumption can lead to significant error in the frequency-domain measured thermal conductivity, which is discussed in more detail by Wingert *et al.*[24] The finite length model facilitates the accurate measurement of liquids using short hot-wires. We previously validated the frequency-domain hot-wire technique by measuring the thermal conductivity of water, methanol, ethanol, silicone oil, and argon at ambient temperature and pressure, as well as sulfur at high temperatures; all frequency-domain measurements showed good agreement with reference values[24]. This new technique allows us to measure small amounts of molten salts, resulting in more uniform salt temperatures and negligible convection during measurements. Potential error due to radiative heat transfer between the hot-wire and molten salt is also negligible since radiative heat flux is always less than 1% of the conductive heat flux below 873.15 K (see **Appendix 1** of **Chapter 3**). Note that we assumed zero-temperature rise at the wire ends as a boundary condition for development of **Eq. 3.2** and assumed a uniform salt temperature during the measurement. The validity of these assumptions is shown in **Appendices 2 and 3** respectively at the end of **Chapter 3**.

The experimental setup, microfabricated sensor, and protective coating used in this study are shown in **Fig. 3.3**. The fabricated sensor is an Al_2O_3 substrate (can be polycrystalline or single crystal sapphire), with sputtered platinum leads using a titanium adhesion layer. A 6.5-7 mm long, 25.8 μm diameter platinum wire is bonded to the platinum leads using gold ball bonding or Tanaka Platinum Paste TR-7605. To prevent annealing of our sensors during the measurement, which could potentially change the dR/dT of our platinum wires, we anneal the sensors before the measurement by heating them up to 1173.15 K for 2 hours, holding them at

1173.15 K for 2 hours, and then cooling down to room temperature for 4 hours. Next a 1.6 μm thick Al_2O_3 coating is deposited with ALD/CVD/RF sputtering, which protects against corrosion and prevents any electrical leakage from the wire or electrodes into conductive samples.

The diameter of the platinum wire, $2r_0$, is measured to be 25.8 μm in SEM with a 0.4% standard uncertainty; the length of each wire, L, is measured from its room temperature electrical resistance to be between 6.5-7 mm, and there is 2% standard uncertainty from a 1 mm uncertainty in the 50 mm long Pt used for calibration; and the temperature coefficient of resistance (dR/dT) of each wire is measured during testing. The Al_2O_3 coating thickness, d, is measured in SEM before and after the measurement to be 1.6 μm with a standard uncertainty of 6.5%; the coating's thermal properties ($\kappa_1 = 1.5\ Wm^{-1}K^{-1}$ and $\rho_1 C_1 = 2.65 \times 10^6\ Jm^{-3}K^{-1}$) for amorphous alumina deposited with ALD) are taken from literature[27] with a 13% uncertainty in values. The molten salt density (1% reported uncertainty)[3] and heat capacity (1% reported uncertainty)[28], $\rho_2 C_2$, are taken from reference values.
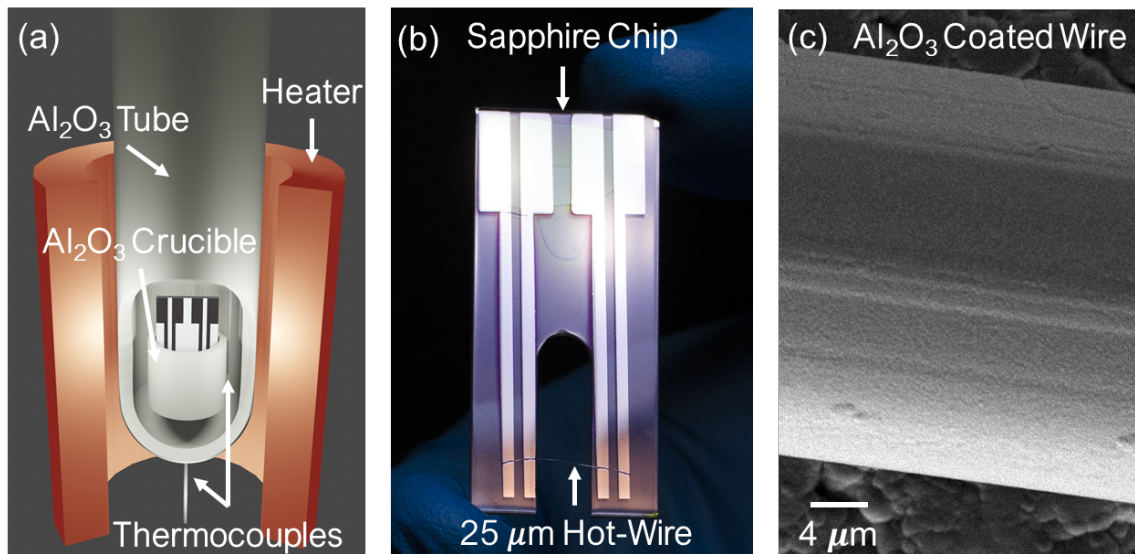
Figure 3.3. (a) 3D schematic of the experimental setup. The alumina tube and heater, which are actually continuous, are shown here with a cut-out for clarity. (b) photograph of coated hot-wire sensor on sapphire chip, (c) SEM of 1.6 μm thick Al_2O_3 coating on platinum hot-wire.

3.3 Measurement details and error analysis

To measure the thermal conductivity of a molten nitrate salt, we raise the temperature of the salt sample with an embedded coated sensor, shown in **Fig. 3.3 a)**, above the melting point in an argon environment, wait 30 minutes for the salt to completely melt and for the temperature to equilibrate, and then measure the molten salt's temperature response at 20 logarithmically spaced frequency points ranging from 1000 Hz to 1 Hz. We then raise the temperature of the furnace by ~20 K, wait 30 minutes for the temperature to equilibrate, and run another set of frequency response measurements, which takes ~1 hour and 20 minutes for the full frequency sweep. We continue to repeat this heating and measurement process until the thermal conductivity at the highest useful temperature for the molten nitrate salt is measured. Finally, we repeat this temperature dependent measurement for both molten $NaNO_3$ and KNO_3

with a new coated sensor, unused salt from the manufacturer, and an uncontaminated Al_2O_3 crucible (Solar Salt was only measured once).

Fig. 3.4 shows the measured ΔT vs. *frequency* for $NaNO_3$, KNO_3, and Solar Salt, each at 3 different temperatures (just above the melting point, the median temperature measured, and the highest temperature measured). The experimental in-phase temperature rise at each input frequency is positive and marked with an ×. The out-of-phase temperature response of the wire is also measured at each frequency and is negative and marked with a circle. The thermal conductivity of the surrounding molten salt is the only free parameter used to perform a least-squares fit for both the in-phase and out-of-phase experimental data. The in-phase and out-of-phase response model fits of the experimental results are plotted as solid and dotted lines, respectively, and both show good agreement with experimental measurements.

We use a Monte Carlo method to fit our thermal model (**Eq. 3.2**) to the measured frequency-dependent temperature rise (as in **Fig. 3.4**) to find the measured thermal conductivity and standard uncertainty. The parameters for the platinum wire, coating, and molten salt are randomly sampled from their Gaussian distributions (with their averages and standard uncertainties), then input into a least-squares regression of ΔT (**Eq. 3.2**) for varying thermal conductivity, κ_2, of the molten salt. This Monte Carlo simulation is run 200 times for each frequency-domain measurement to find the average thermal conductivity of the molten salt and its standard deviation, which is the standard uncertainty reported, at each temperature. The Monte Carlo method is used to account for the standard uncertainties in the parameters used in the thermal model (**Eq. 3.2**), specifically: the wire diameter ($2r_0$) length of the wire (L), coating thickness (d), coating density (ρ_1), heat capacity (C_1), salt density ρ_2, and salt heat capacity (C_2).

123
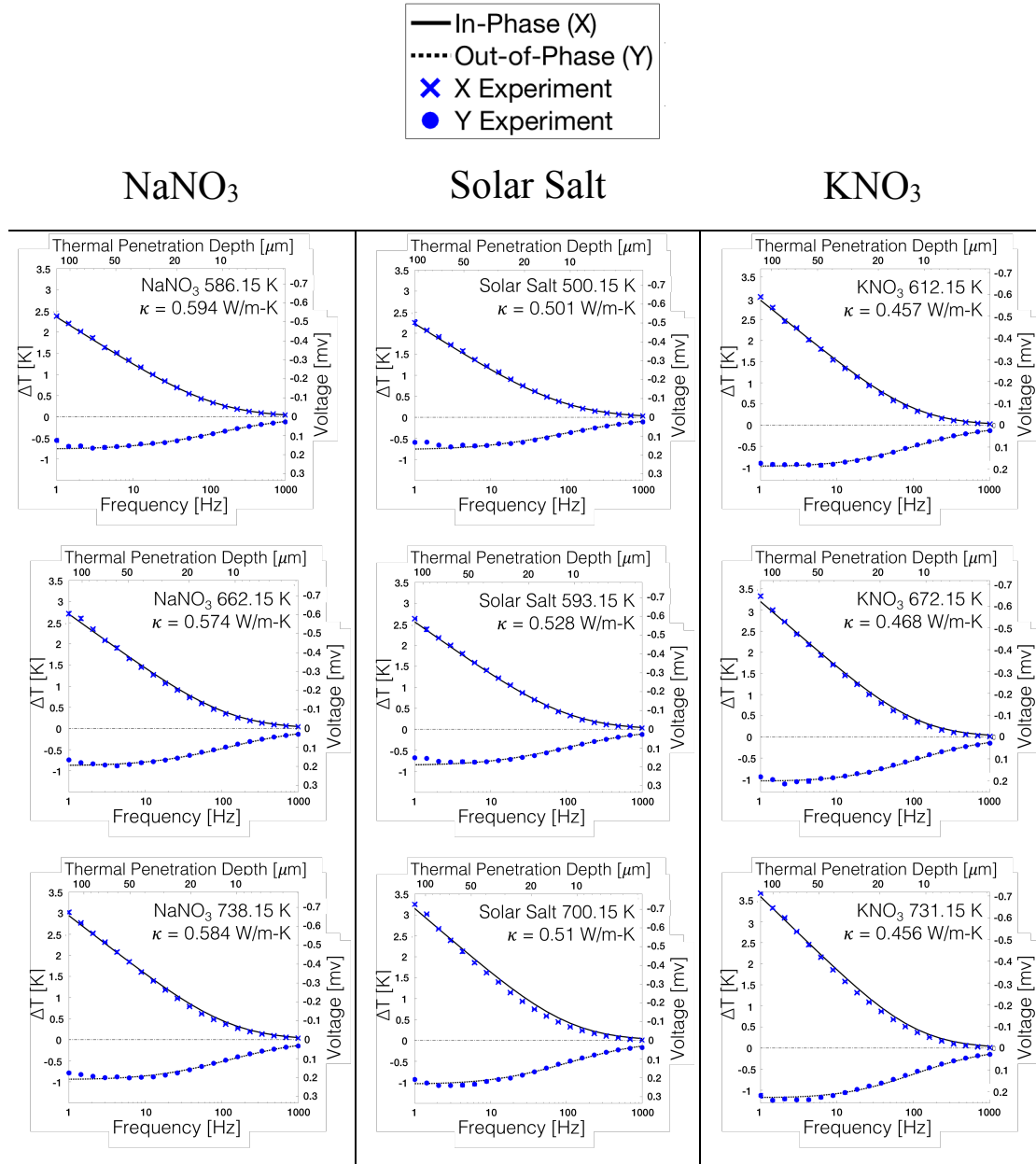
Figure 3.4. Frequency-domain measurements of NaNO₃ (1ˢᵗ column), Solar Salt (middle column), and KNO₃ (3ʳᵈ column) at just above the melting point, the median temperature measured, and the highest temperature measured.

3.4 Results and discussion

Fig. 3.5 and Table 3.2 show the frequency-domain $NaNO_3$ thermal conductivity measurements from two independent temperature sweeps using different sensors, fresh salt batches, and unused sample holders each time. The average standard uncertainty in thermal conductivity was found to be 2.78%. We find a very slight decreasing thermal conductivity as the temperature of $NaNO_3$ increases. The line of best fit of the measured thermal conductivity at varying temperature (T in kelvin) is given by the following equation:

$$\kappa = 0.637 - 7.152 \times 10^{-5}(\text{T}) \ [Wm^{-1}K^{-1}] \tag{3.5}$$

The residual sum of squares of the fit is 0.0012. Also plotted in Fig. 3.5 is data form Chliatzou *et al.'s* reference correlation. Comparison shows that the slope of the linear fits is similar. However, we find the magnitude of the thermal conductivity to be ~11% higher than the reference value. In addition to the difference in measurement techniques, our salt source and purity (Sigma-Aldrich ≥ 99%) could lead to some deviation between our measured thermal conductivity and previous literature or reference values. Of the 5 previous measurements used as primary data by Chliatzou *et al.*, only Omotani *et al.* (99.9%)[7] and Kitade *et al.* (99%)[8] report the purity of $NaNO_3$ used. The purity of $NaNO_3$ and concentration of different species present can affect the measured thermal conductivity. In addition, it has been shown that higher salt purity and lower water content in molten chlorides and fluorides is correlated with lower corrosion rates of metal alloys.[29] To remove water moisture that the salt absorbs, we heat the starting salt powder from room temperature to 673.15 K over two hours to evaporate off any water, then we submerge our hot-wire sensor into the salt, and the salt cools down and solidifies around the sensor. Next, we heat the salt and sensor in our vacuum tube furnace (see Fig. 3.3a)

above the melting point over 2 hours, pumping out any more moisture that comes off. And finally, we fill the furnace with argon before starting our measurements.

The decomposition temperature is also plotted at 669.15 K in **Fig. 3.5** for when the equilibrium constant of $NaNO_3$ decomposing into Na_2O, NO_2 gas, and O_2 gas is equal to 1×10^{-25}, as discussed by Pfleger *et al.*[30] and Stern[31]. Our measurements show that the thermal conductivity does not change substantially even above the decomposition temperature. However, these values should be used with caution. Since decomposition reactions are continuous, the thermal conductivity measured above the dashed line is likely time dependent.
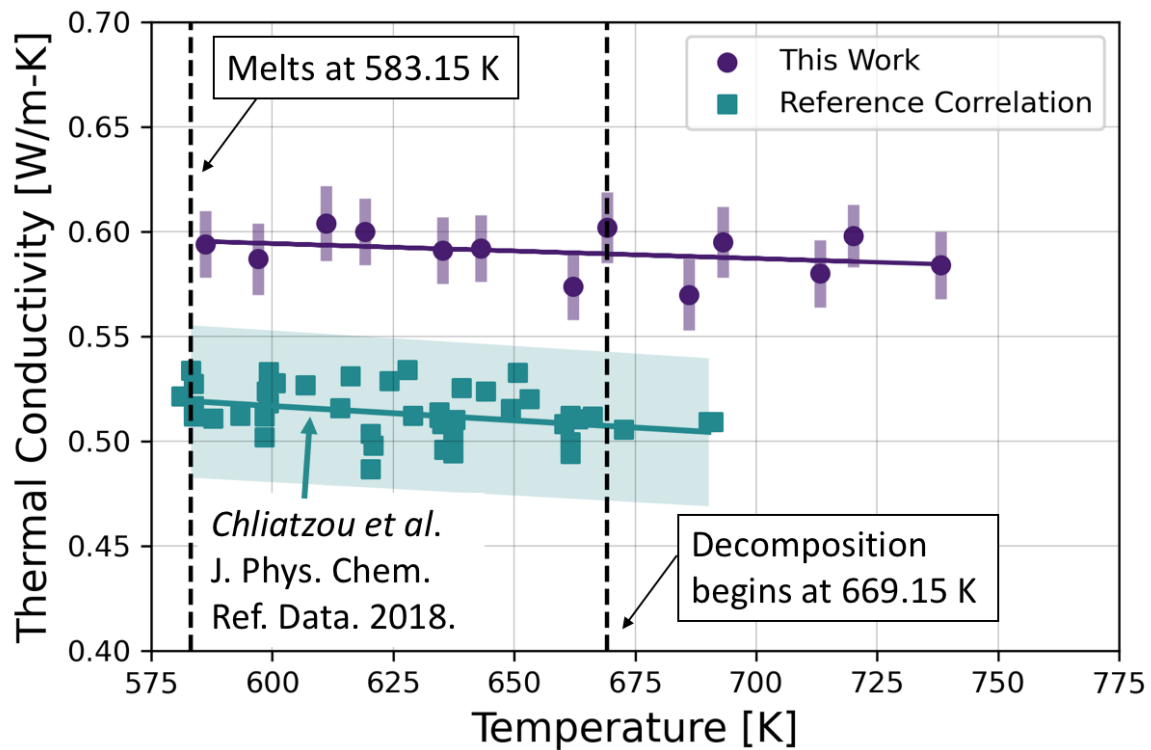
Figure 3.5. Frequency-domain $NaNO_3$ thermal conductivity measured values compared to the reference correlation of previous time-domain and steady-state measurements.

Table 3.2. NaNO$_3$ liquid thermal conductivity and standard uncertainty measured in argon environment at 0.142 ± 0.007 MPa. Uncertainty in temperature is ± 2 K from fluctuating furnace temperature.

Temperature [K]	Thermal Conductivity [Wm^{-1}K^{-1}]	Standard Uncertainty [Wm^{-1}K^{-1}]
597.15	0.587	0.017
619.15	0.6	0.016
643.15	0.592	0.016
669.15	0.602	0.017
693.15	0.595	0.017
720.15	0.598	0.015
586.15	0.594	0.016
611.15	0.604	0.018
635.15	0.591	0.016
662.15	0.574	0.016
686.15	0.57	0.017
713.15	0.58	0.016
738.15	0.584	0.016

Fig. 3.6 and **Table 3.3** show our frequency-domain measurements of thermal conductivity of KNO_3 from 2 independent temperature sweeps with two separate sensors, fresh salt batches, and unused sample holders. The average standard uncertainty in thermal conductivity was found to be 2.38%. We find a very slight decreasing thermal conductivity of molten KNO_3 across the whole temperature range. The line of best fit of our KNO_3 thermal conductivity measurements (T in Kelvin) is given by the following equation:

$$3 \times 10^{-4}(\text{T}) \left[Wm^{-1}K^{-1}\right] \tag{3.6}$$

The residual sum of squares of the fit is 0.0008. There is a small difference in slope from Chliatzou *et al.*'s reference correlation, and we measure the magnitude of thermal conductivity of KNO_3 to be ~15% higher than the reference value at 673.15 K. It is worth noting that time-domain measurements from Asahina *et al.*[9] and steady-state measurements from Tufeu *et al.*[6] used in the reference correlation overlap with our frequency-domain measurements of KNO_3's thermal conductivity.
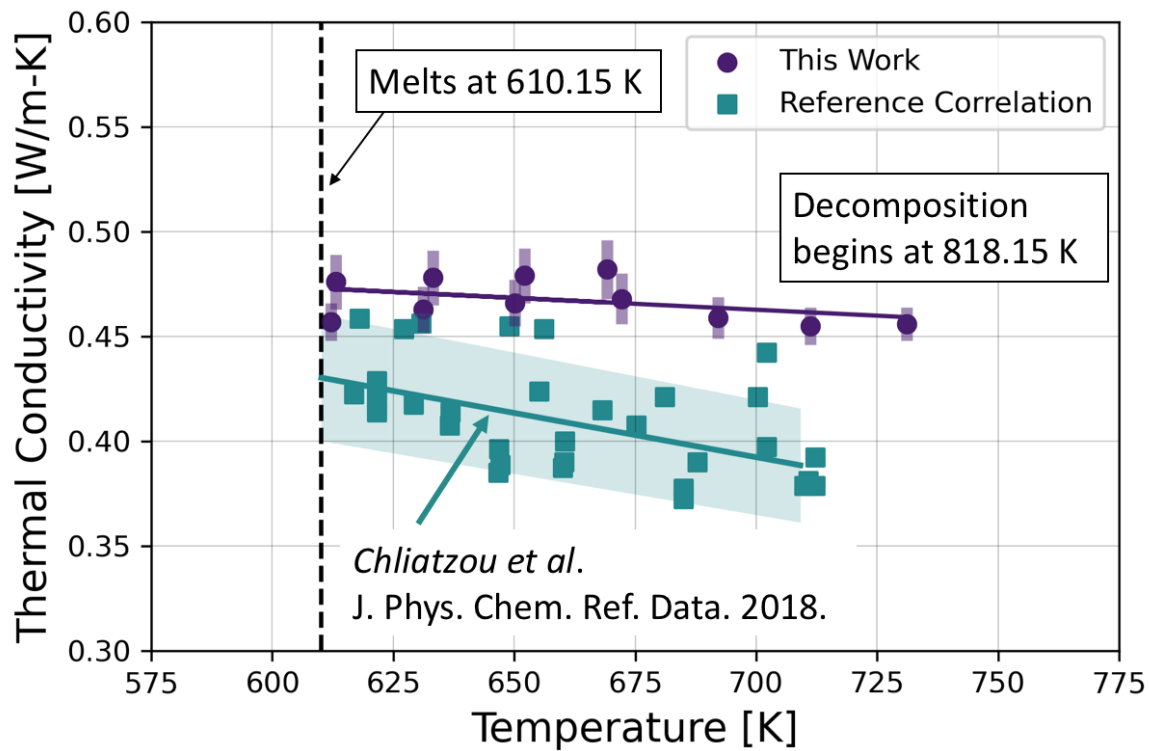
Figure 3.6. Frequency-domain KNO$_3$ thermal conductivity measured values compared to the reference correlation of previous time-domain and steady-state measurements.

Table 3.3. KNO$_3$ liquid thermal conductivity and standard uncertainty measured in argon environment at 0.142 $\pm$ 0.007 MPa. Uncertainty in temperature is $\pm$ 2 K from fluctuating furnace temperature.

Temperature [K]	Thermal Conductivity [Wm^{-1}K^{-1}]	Standard Uncertainty [Wm^{-1}K^{-1}]
613.15	0.476	0.013
633.15	0.478	0.013
652.15	0.479	0.013
669.15	0.482	0.014
612.15	0.457	0.009
631.15	0.463	0.011
650.15	0.466	0.011
672.15	0.468	0.012
692.15	0.459	0.01
711.15	0.455	0.009
731.15	0.456	0.008

Fig. 3.7 and Table 3.4 show our frequency-domain measurements of Solar Salt (60 wt.% $NaNO_3$, 40 wt.% KNO_3) from one temperature sweep. The average standard uncertainty in thermal conductivity was found to be 2.66%. Our measurements are plotted against the thermal conductivity of an effective medium of 60 wt.% $NaNO_3$ and 40 wt.% KNO_3, made using the lines of best fit from our frequency-domain measurements of $NaNO_3$ and KNO_3 (**Eqs. 5 and 6**), as well as the reference correlations of $NaNO_3$ and KNO_3. The rule of mixtures used is:

$$\kappa_{Solar\ Salt} = (0.6\kappa_{NaNO3}) + (0.4\kappa_{KNO3}) \qquad (3.7)$$

The residual sum of squares is 0.0086 for our frequency-domain measurements and 0.0151 for the reference correlation rule of mixtures. The first five measured data points up to 593.15 K overlap with the reference correlation's rule of mixtures within its 9.9% error (propagated from 2σ uncertainty of 7% in $NaNO_3$ and KNO_3 reference correlations). The rule of mixtures using our frequency-domain measurements of $NaNO_3$ and KNO_3 (**Eq. 3.7**) is higher than when using the reference correlation, and both correlations suggest a decreasing trend in Solar Salt's thermal conductivity with increasing temperature. However, there is a slight increase in the thermal conductivity measured from the melting point up to 642.15 K that cannot be explained by either correlation.
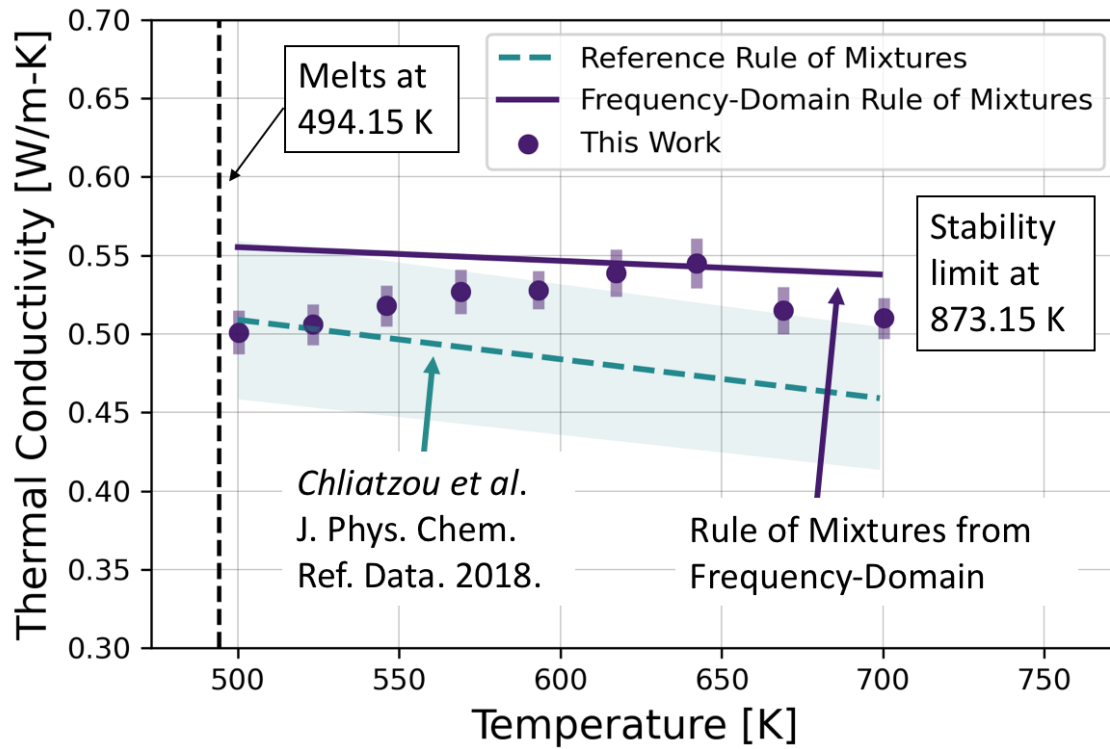
Figure 3.7. Frequency-domain thermal conductivity measurements of Solar Salt (60 wt.% $NaNO_3$, 40 wt.% KNO_3). A rule of mixtures from the frequency-domain measurements (**Eq. 7**) is drawn as a solid line, and a rule of mixtures using the reference correlations[5] is drawn as a dashed line.

Table 3.4. Solar Salt (60 ± 0.02 wt.% $NaNO_3$, 40 ± 0.02 wt.% KNO_3) liquid thermal conductivity and standard uncertainty measured in argon environment at 0.142 ± 0.007 MPa. Uncertainty in temperature is ± 2 K from fluctuating furnace temperature.

Temperature [K]	Thermal Conductivity [$Wm^{-1}K^{-1}$]	Standard Uncertainty [$Wm^{-1}K^{-1}$]
500.15	0.501	0.014
523.15	0.506	0.013
546.15	0.518	0.013
569.15	0.527	0.014
593.15	0.528	0.012
617.15	0.539	0.015
642.15	0.545	0.016
669.15	0.515	0.015
700.15	0.51	0.013

3.5 Conclusion

Frequency-domain hot-wire measurements provide a new method for determining the thermal conductivity of molten nitrate salts. The new measurements offer three advantages over previous measurements of nitrate salts at high temperature measurements. First, the thermal penetration depth into the sample is kept below 100 μm, which is crucial for minimizing the convection in the frequency-domain measurement. Second, there is no systematic error in our measurement system from the temperature fluctuations in the furnace or environment due to the lock-in amplifier only measuring harmonic signals coming from the platinum sensor probing the molten salt. And third, 4 orders of magnitude in frequency are utilized (1, 10, 100, and 1000 Hz) to measure the temperature response and ensure the data used to calculate thermal conductivity is not arbitrarily truncated.

Our frequency-domain measurements, shown all together in **Fig. 3.8**, have low standard uncertainty values for $NaNO_3$ (2.78%), KNO_3 (2.39%), and Solar Salt's thermal conductivity (2.66%), and they suggest that the current reference values for molten nitrate salts could be low, in some cases by over 10%. We measured nitrate salts sourced from Sigma-Aldrich with a reported purity ≥ 99%. Salt purity can influence the thermal conductivity (as shown in Solar Salt) and other molten salt properties, and it should be more consistently reported going forward. This new frequency-domain technique should be useful to those seeking accurate thermophysical and transport properties for designing new molten salt systems and to scientists developing new theories of heat transport in molten materials.
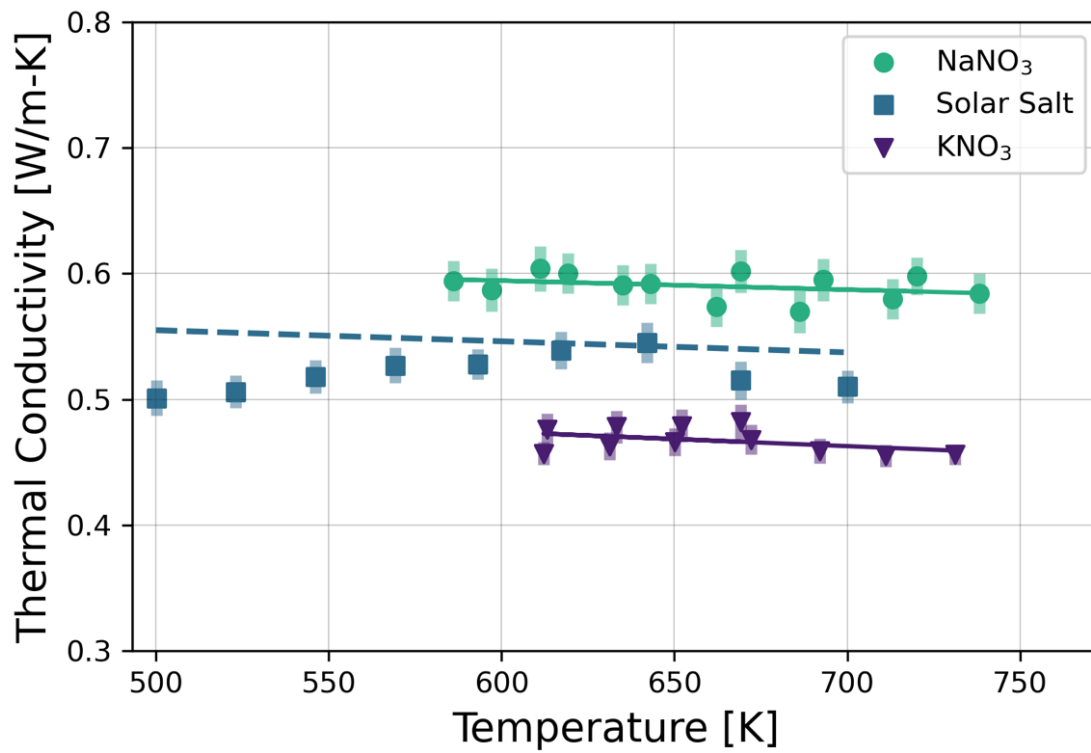
Figure 3.8. Thermal conductivity of molten $NaNO_3$, KNO_3, and Solar Salt (60 wt.% $NaNO_3$, 40 wt.% KNO_3) measured in the frequency-domain. Best fit lines are drawn for $NaNO_3$ and KNO_3 in solid lines, and their rule of mixtures for Solar Salt (60% $NaNO_3$, 40% KNO_3) is shown as a dashed line.

Supporting Information Available: Appendix 1 Validity of neglecting radiation in the thermal model; Appendix 2 Checking the boundary condition that there is no temperature rise at the ends of the hot-wire; Appendix 3 Validity of assuming a uniform salt temperature during the measurement.

3. Appendix 1: Validity of neglecting radiation in the thermal model

The model (Eqs. 2-4) we use to fit to measured data and extract sample thermal conductivity does not consider heat transfer by radiation. To confirm that radiation can be neglected in our thermal conductivity measurement, we calculate the relative significance of thermal radiation compared to thermal conduction between our sensor and molten salt during the measurement. Before the measurement, we let the temperature of our system equilibrate, so we assume the temperature of the sensor and the salt are equal. When we apply current to our hot-wire, joule heating leads to a temperature difference between the wire and salt that will lead to radiative heat transfer.

To quantify the effect of radiative and conductive heat transport, we can weigh the relative heat fluxes from radiation, Q_{rad} and conduction, Q_{cond} defined as:

$$Q_{rad} = A_{surface}\sigma\varepsilon(T_{wire}^4 - T_{amb}^4) \approx 4A_{surface}\sigma\varepsilon T_{amb}^3\Delta T_w \text{ (A1)}$$

$$Q_{cond} = \kappa_0 A_{surface}\frac{d\tilde{T}_{2\omega}}{dr}\bigg|_{r0} \qquad\qquad \text{(A2)}$$

where the temperature rise of the wire is $\Delta T_{wire} = \tilde{T}_{2\omega,avg}$ as defined in this work and [Ref. 24], σ is the Stefan-Boltzmann constant (5.67e-8 J/(m²sK⁴)), $A_{surface}$ is the surface area of the hot-wire, $r0$ is the radius of the hot-wire, T_{amb} is the ambient background temperature, and ε is the emissivity of the alumina surface of our hot-wire. We can assume blackbody radiation ($\varepsilon = 1$) to check the maximal radiative effect. The approximate ratio of heat fluxes due to radiation and conduction from the hot-wire is then:

$$\frac{Q_{rad}}{Q_{cond}} \approx \frac{4\sigma T_{amb}^3}{\kappa_0} \frac{\tilde{T}_{2\omega,avg}}{\left.\frac{d\tilde{T}_{2\omega}}{dr}\right|_{r0}} \qquad (A3)$$

As mentioned earlier, we define the temperature rise, $\tilde{T}_{2\omega,avg}$ in the hot-wire using **Eq.2**. To calculate the conductive heat flux from the hot-wire into the molten salt, we take the radial gradient at the wire surface of the temperature rise as described in Ref. 24 as follows:

$$\tilde{T}_{2\omega}(r) = \frac{1}{l}\int_0^l \tilde{T}_0(r,z)dz = \sum_{n=1}^{\infty}\left[\frac{1}{l}\int_0^l K_e(n,z)dz\right]\left[A_{c,0}I_0(\varphi_0 r) + \sqrt{\frac{2}{l}}\left(\frac{\tilde{P}_0}{\pi r_0^2 L\kappa_0\lambda_n\varphi_0^2}\right)\right]$$

(A4a)

$$\left.\frac{d\tilde{T}_{2\omega}}{dr}\right|_{r0} = \sum_{n=1}^{\infty}\left(\frac{8\tilde{P}_{RMS}}{\pi^3 r_0^2 L\kappa_0\varphi_0^2(2n-1)^2}\right)\left(\frac{\kappa_1\varphi_1}{\kappa_0}\right)\left(\frac{\beta I_1(\varphi_1 r_0)-\alpha K_1(\varphi_1 r_0)}{\alpha\delta-\gamma\beta}\right)$$

(A4b)

Finally, we calculate the ratio between radiation and conduction (Eq. A3**)**, plotted in **Figure S1.**
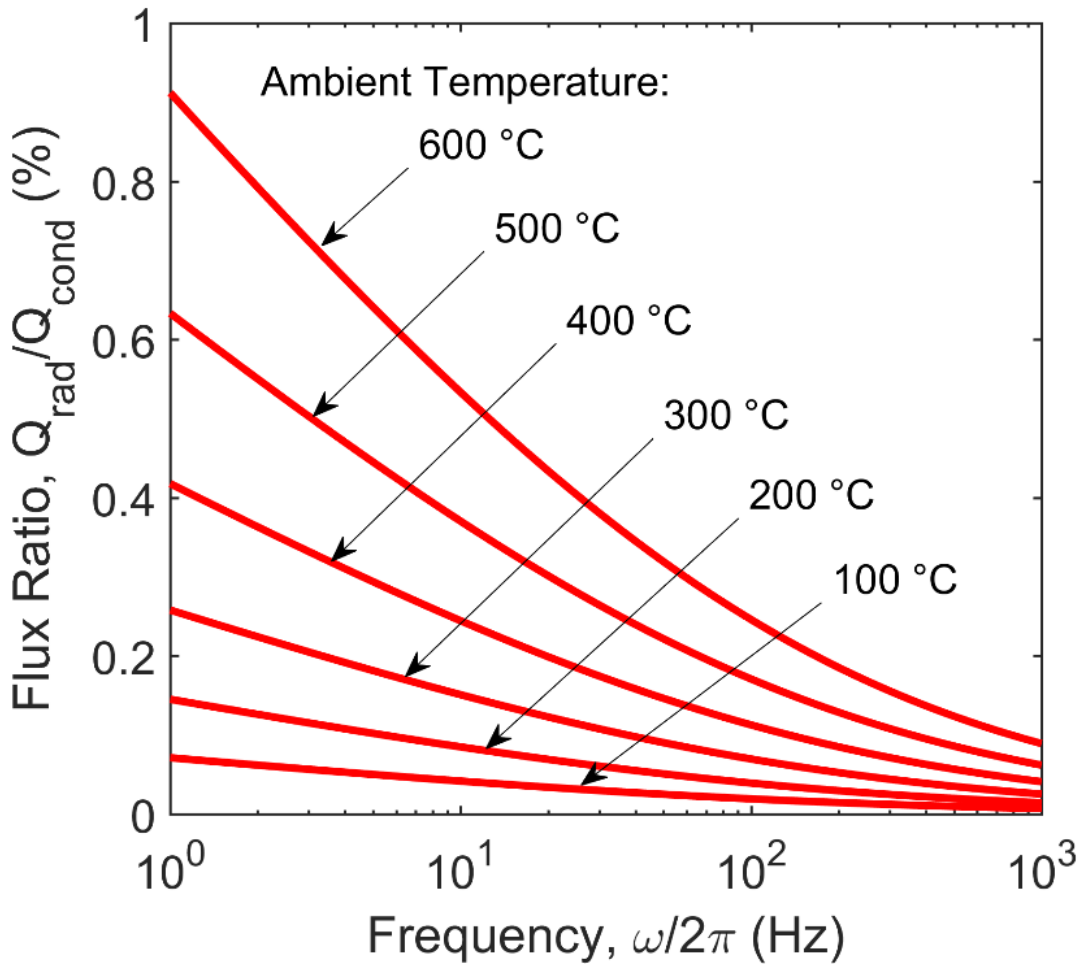
Figure 3. S1. The percentage of radiation flux compared to conduction flux for various ambient temperatures as a function of input frequency. The radiation flux is less than 1% of the conduction flux and thus considered negligible.

The highest temperature that our hot-wire system reached was 465℃ (738.15 K), shown in

Figure 3.4, which is well below the 600°C (873.15 K) upper limit shown in **Fig. 3. S1**. We find

that the Q_{rad} is less than 1% of Q_{cond} for the entire frequency range and for all salt

temperatures below 600ºC (873.15 K), validating our assumption that radiation does not play a

significant role in our measurement of molten salt thermal conductivity

3. Appendix 2: Checking the boundary condition at the wire ends

Here we discuss the validity of the assumption of zero-temperature rise at the wire ends as a boundary condition that was used to develop Equation 2. For a full discussion on the model development please see REF 24. If the thermal conductance at the ends of the wire into the substrate is significantly larger than the thermal conductance into the sample or along the wire, then the heat dissipates into the high thermal conductivity substrate fast enough to keep a negligible temperature rise at the wire ends , validating the boundary condition. Thus, we examine the ratio of heat conductance from the Pt wire into the substrate, $G_{substrate}$ to the heat conduction into the sample, G_{sample} as well as the heat conduction along the Pt wire, G_{wire}.

For our setup, the Pt wire is bonded/welded to the platinum leads on high thermal conductivity (alumina or sapphire) substrates. As conservative estimate, the heat conduction into the substrate, we assume conduction into the substrate is limited to the edge length of the welded portion of the wire, L_{weld}, and the thickness of the substrate, $d_{substrate}$. Therefore, for a molten salt thermal conductivity sample, $0.5 \ Wm^{-1}K^{-1}$, the conductance ratio is $G_{substrate}/G_{sample} \approx$

$$(2\pi D L_{weld}\kappa_{substrate}/d_{substrate})/(\pi D\kappa_{sample}) = (2L_{weld}\kappa_{substrate})/(\kappa_{sample}d_{substrate})$$

.

Using the dimensions and properties, $L_{weld} = 1$ mm, $d_{substrate} = 1$ mm, $\kappa_{substrate} = 30$ $Wm^{-1}K^{-1}$ and $\kappa_{substrate} = 0.5 \ Wm^{-1}K^{-1}$ gives $G_{substrate}/G_{sample} \approx 120.$

Similarly, for the conductance ratio into the substrate versus along the Pt wire we have

$$G_{substrate}/G_{wire} \approx (2\pi D L_{weld}\kappa_{substrate}/d_{substrate})/\left(\left(\frac{\pi}{2}\right)D^2\kappa_{wire}/L_{weld}\right) =$$

$(4L_{weld}^2\kappa_{substrate})/(D\kappa_{wire}d_{substrate})$. Using $D = 0.025$ mm and $\kappa_{wire} = 60\ Wm^{-1}K^{-1}$,

$G_{substrate}/G_{wire} \approx 80$. In both cases the estimated thermal conductance into the substrate is

~100 times larger than into the sample or past the substrate through the Pt wire. Thus, the

boundary condition that the temperature rise at the wire ends is zero is valid for the conditions

in this study

3. Appendix 3: Validity of assuming a uniform salt temperature

To check if the temperature of the sample is uniform, we use a lumped capacitance

model (REF 33). The criterion for negligible temperature gradients within an object from the

lumped capacitance model is that the Biot number (Bi) is less than 0.1, indicating that convective

heat loss to the environment is very small compared to the conductive heat transfer within the

sample.

The crucible containing the molten salt and sensor is a small volume of material and is

suspended in the tube furnace. The sample is radiatively heated from the tube furnace walls with

a primary cooling path of natural convection due to the Argon gas filling the tube furnace. For

this analysis, we measure the temperature of the larger alumina tube that encases the sample

holder in an argon environment, and we measure the temperature of the smaller alumina

crucible that holds our molten salt sample and sensor (see Figure 3a).

Next, we use the highest temperature of our system and an energy balance to calculate

the maximum convective heat transfer. During this work, the highest steady state temperature

of the sample ($T_{sample)}$) was $468°C\ (742K)$ and the outer alumina tube temperature

($T_{outer\ tube}$) was $500°C\ (773K)$. The energy balance of our sample, which includes the energy

in, Q_{in} from radiation from the larger alumina tube and the energy out, Q_{out} from convective heat loss from the surface of the sample holder, can be written: $Q_{in} - Q_{out} = 0$, where $Q_{in} = \sigma A \varepsilon_1 (T_{outer\ tube}^4 - T_{sample}^4)$ and $Q_{out} = hA(T_{sample} - T_\infty)$. Thus,

$$\sigma A \varepsilon_1 (T_{outer\ tube}^4 - T_{sample}^4) = hA(T_{sample} - T_\infty) \qquad (A5)$$

where σ is the Stefan-Boltzmann constant ($5.67 \times 10^{-8} \frac{J}{m^2 s K^4}$), A is the surface area of the sample holder (which cancels out), ε_1 is the emissivity of the alumina sample holder that we will conservatively assume to be 1, T_{sample} is the highest temperature that our molten salt reached ($T_{sample} = 468°C = 742K$ from Figure 4), $T_{outer\ tube}$ is the highest temperature we set for the outer tube ($T_{outer\ tube} = 500°C = 773K$), and T_∞ is the ambient argon gas temperature ($T_\infty = 30°C = 303K$).

Note the gas is static and not flowing, and thus according to Eq. A5 we find the heat transfer coefficient for natural convection $h = 6.96 \frac{W}{m^2 K}$. Next, we find the Biot number using the definition:

$$Bi = \frac{hL_c}{\kappa} = \frac{hD}{4\kappa} \qquad (A6)$$

where $L_c = Volume/Surface\ Area = D/4$ is the characteristic length scale of the cylindrical sample holder (0.025 m diameter) and κ is the thermal conductivity of the molten salt making up the majority of the volume of the sample holder ($\approx$0.5 Wm^{-1}K^{-1}). Eq. A6 gives: $Bi = 0.087$, which is less than 0.1, fulfilling the criterion of the lumped capacitance model uniform temperature for our molten salt.

Acknowledgements

References

(1)   Nunes, V. M. B.; Queirós, C. S.; Lourenço, M. J. V.; Santos, F. J. V.; Nieto de Castro, C. A. Molten Salts as Engineering Fluids – A Review: Part I. Molten Alkali Nitrates. *Appl. Energy* **2016**, *183*, 603–611.

(2)   Nunes, V. M. .; Lourenço, M. J. V.; Santos, F. J. V.; Nieto De Castro, C. A. Importance of Accurate Data on Viscosity and Thermal Conductivity in Molten Salts Applications. *J. Chem. Eng. Data* **2003**, *48*, 446–450.

(3)   Janz, G. J.; Allen, C. B.; Bansal, N. P.; Murphy, R. M.; Tomkins, R. P. T. *Physical Properties Data Compilations Relevant to Energy Storage. II. Molten Salts: Data on Single and Multi-Component Salt Systems*; U.S. National Bureau of Standards; Washington D.C.; **1979**.

(4)   Nagasaka, Y.; Nagashima, A. The Thermal Conductivity of Molten NaNO3 and KNO3. *Int. J. Thermophys.* **1991**, *12*, 769–781.

(5)   Chliatzou, C. D.; Assael, M. J.; Antoniadis, K. D.; Huber, M. L.; Wakeham, W. A. Reference Correlations for the Thermal Conductivity of 13 Inorganic Molten Salts. *J. Phys. Chem. Ref. Data* **2018**, *47*, 33104.

(6)   Tufeu, R.; Petitet, J. P.; Denielou, L.; Le Neindre, B. Experimental Determination of the Thermal Conductivity of Molten Pure Salts and Salt Mixtures. *Int. J. Thermophys.* **1985**, *6*, 315–330.

(7)   Omotani, T.; Nagasaka, Y.; Nagashima, A. Measurement of the Thermal Conductivity of KNO3-NaNO3 Mixtures Using a Transient Hot-Wire Method with a Liquid Metal in a Capillary Probe. *Int. J. Thermophys.* **1982**, *3,* 17-26.

(8)   Kitade, S.; Kobayashi, Y.; Nagasaka, Y.; Nagashima, A. Measurement of the Thermal Conductivity of Molten KNO3 and NaNO3 by the Transient Hot-Wire Method with Ceramic-Coated Probes. *High Temp. - High Press.* **1989**, *21*, 219–224.

(9)   Asahina, T.; Kosaka, M.; Tajiri, K. Thermal Diffusivity Measurement of Molten Nitrates by Pulse-Heated Flat Plate Method. *Kagaku Kogaku Ronbunshu* **1988**, *14*, 616–621.

(10)   Odawara, O.; Okada, I.; Kawamura, K. *Measurement of the Thermal Diffusivity of HTS (a Mixture of Molten Sodium Nitrate-Potassium Nitrate-Sodium Nitrite; 7-44-49 Mole %) by Optical Interferometry*; UTC, 1977; Vol. 22.

(11)   Bran-Anleu, G.; Lavine, A. S.; Wirz, R. E.; Pirouz Kavehpour, H. Algorithm to Optimize Transient Hot-Wire Thermal Property Measurement. *Rev. Sci. Instrum.* **2014**, *85*, 45105.

(12)   Turnbull, A. The Thermal Conductivity of Molten Salts. I. A Transient Measurement Method. *Austl. J. Appl. Sci.* **1961**, *12*.

(13)   Mclaughlin, E. The Thermal Conductivity of Liquids and Dense Gases. *Chem. Rev.* **1964**, *64*, 389–428.

(14)   Bloom, H.; Doroszkowski, A.; Tricklebank, S. B. Molten Salt Mixtures. IX. The Thermal Conductivities of Molten Nitrate Systems. *Aust. J. Chem.* **1965**, *18*, 1171–1176.

(15)   White, L. R.; Davis, H. T. Thermal Conductivity of Molten Alkali Nitrates. *J. Chem. Phys.* **1967**, *47*, 5433–5439.

(16)   Gustafsson, S. E.; Halling, N. O.; Kjellander, R. A. E. Optical Determination of Thermal Conductivity with a Plane Source Technique: I. Molten Sodium Nitrate and Potassium Nitrate. *Zeitschrift fur Naturforsch. - Sect. A J. Phys. Sci.* **1968**, *23*, 44–47.

(17)   McDonald, J.; Davis, H. T. Thermal Conductivity of Binary Mixtures of Alkali Nitrates. *J. Phys. Chem.* **1970**, *74*, 725–730.

(18)   Kato, Y.; Kobayasi, K.; Araki, N.; Furukawa, K. An Accuracy Analysis of the Thermal Diffusivity Measurement of Molten Salts by Stepwise Heating and Improved Apparatus. *J. Phys. E.* **1977**, *10*, 921–927.

(19)   Santini, R.; Tadrist, L.; Pantaloni, J.; Cerisier, P. Measurement of Thermal Conductivity of Molten Salts in the Range 100-500°C. *Int. J. Heat Mass Transf.* **1984**, *27*, 623–626.

(20)   Ohta, H.; Ogura, G.; Waseda, Y.; Suzuki, M. Thermal Diffusivity Measurements of Molten Salts Using a Three-layered Cell by the Laser Flash Method. *Rev. Sci. Instrum.* **1990**, *61*, 2645–2649.

(21)   Zhang, X.; Fujii, M. *Simultaneous Measurements of the Thermal Conductivity and Thermal Diffusivity of Molten Salts with a Transient Short-Hot-Wire Method*; 2000; Vol. 21.

(22)   Chliatzou, C. D.; Assael, M. J.; Antoniadis, K. D.; Huber, M. L.; Wakeham, W. A. Reference Correlations for the Thermal Conductivity of 13 Inorganic Molten Salts. *J. Phys. Chem. Ref. Data* **2018**, *47*.

(23) Y. Nagasaka, A. N. The Thermal Conductivity of NaNO3 and KNO3. *Int. J. Thermophys.* **1991**, *12*, 769–781.

(24) Wingert, M. C.; Zhao, A. Z.; Kodera, Y.; Obrey, S. J.; Garay, J. E. Frequency-Domain Hot-Wire Sensor and 3D Model for Thermal Conductivity Measurements of Reactive and Corrosive Materials at High Temperatures. *Rev. Sci. Instrum.* **2020**, *91*, 054904.

(25) Cahill, D. G. Thermal Conductivity Measurement from 30 to 750 K: The 3ω Method. *Rev. Sci. Instrum.* **1990**, *61*, 802–808.

(26) Li, X.; Park, W.; Wang, Y.; Chen, Y. P.; Ruan, X. Reducing Interfacial Thermal Resistance between Metal and Dielectric Materials by a Metal Interlayer. *J. Appl. Phys.* **2019**, *125*, 45302.

(27) Gorham, C. S.; Gaskins, J. T.; Parsons, G. N.; Losego, M. D.; Hopkins, P. E. Density Dependence of the Room Temperature Thermal Conductivity of Atomic Layer Deposition-Grown Amorphous Alumina (Al2O3). *Appl. Phys. Lett.* **2014**, *104*, 253107.

(28) Takahashi, Y.; Sakamoto, R.; Kamimoto, M. Heat Capacities and Latent Heats of LiNO3, NaNO3, and KNO3. *Int. J. Thermophys.* **1988**, *9*, 1081–1090.

(29) Raiman, S. S.; Lee, S. Aggregation and Data Analysis of Corrosion Studies in Molten Chloride and Fluoride Salts. *Journal of Nuclear Materials.* Elsevier B.V. December 1, 2018, pp 523–535.

(30) Pfleger, N.; Bauer, T.; Martin, C.; Eck, M.; Wörner, A. Thermal Energy Storage - Overview and Specific Insight into Nitrate Salts for Sensible and Latent Heat Storage. *Beilstein J. Nanotechnol.* **2015**, *6*, 1487–1497.

(31) Stern, H. K. *High Temperature Properties and Thermal Decomposition of Inorganic Salts with Oxyanions*; CRC Press: Boca Raton, FL, U.S.A.

(32) Vignarooban, K.; Xu, X.; Arvay, A.; Hsu, K.; Kannan, A. M. Heat Transfer Fluids for Concentrating Solar Power Systems - A Review. *Appl. Energy* **2015**, *146*, 383–396.

(33) Bergman, T.L., Lavine, S.A., Incropera, F.P. and Dewitt, D. . *Fundamentals of Heat and Mass Transfer. 7th Edition*; John Wiley & Sons: Hoboken, 2011.

Chapter 4: Evaluation of ionic liquid thermal conductivity models with frequency-domain hot-wire measurements

Ionic liquids are an extremely attractive replacement for volatile organic liquids and water for several technologies due to their superior chemical, thermal, and electrical stability. The thermal conductivity is a critical parameter for modeling the heat transfer in ionic liquid systems and understanding any desired temperature dependent property, such as chemical reaction rate or electrical and ionic conductivity. However, there are several models of ionic liquids that could be used to predict their thermal conductivity, and there is still no well-established understanding for the mechanism of heat conduction in ionic liquids. In this work, we examine how an ionic liquid's molar mass, density, speed of sound, and intermolecular distance are related to its thermal conductivity; then we test the accuracy of four ionic liquid thermal conductivity models from Mohanty, Bridgman, Fröba et al., and Zhao et al. We measure the thermal conductivity of 3 ionic liquids ($[bmim]^+ [I]^-$, $[bmim]^+ [BF_4]^-$, and $[bmim]^+ [TFS]^-$) with a recently developed frequency-domain hot-wire technique to minimize high temperature experimental error; our results are in good agreement with previous transient hot-wire measurements up to 200°C, and we report the first measurement of $[bmim]^+ [I]^-$ thermal conductivity. Utilizing our measurements and previous data of various $[emim]^+$ and $[NTF_2]^-$ ionic liquids, we find that while no individual parameter alone is predictive of thermal conductivity, combining multiple parameters together in the models of Bridgman and Fröba et al. provides accurate predictions of ionic liquid thermal conductivity. We also show how the liquid theory from Mohanty underpredicts ionic liquid thermal conductivity and the phonon gas model from Zhao et al. overpredicts ionic liquid thermal conductivity. This work provides

support for liquid thermal conductivity models from Bridgman and Fröba et al. and demonstrates the utility of frequency-domain measurements for high temperature liquids.

4.1 Introduction

Ionic liquids can be used in various applications as a replacement for volatile organic solvents since they are non-flammable and have excellent chemical, electrochemical, and thermal stability, negligible vapor pressure, and high ionic conductivity. These desirable properties of ionic liquids have led to their use in several clean technologies, well reviewed elsewhere[1–3]. Here we specifically highlight ionic liquids useful in applications for electrodepositing aluminum[4–6], electrolytes in new batteries[7–9], membranes in hydrogen fuel cells[10–12], electrochemical actuators for biomechanics[13–15], and next-generation heat transfer fluids and IoNanofluids[16–18]. In all ionic liquid applications, their performance changes with temperature, dictated by the ionic liquid thermal conductivity, which is not well understood.

Previous measurements and studies on ionic liquid thermal conductivity[16,19–23] aimed to understand how different ionic liquids conduct heat and what liquid parameters, such as density, molar mass, and viscosity, affect thermal conductivity, however there is no clear consensus regarding how the thermal conductivity changes with these parameters. Van Valkenburg et al.[19] found that increasing the cation's molecular weight from 1-ethyl-3-methylimadazolium [emim]$^+$ to 1-butyl-3-methylimadazolium [bmim]$^+$ for BF$_4^-$ anions led to a decrease in thermal conductivity. On the other hand, Tomida et al.[20] found that increasing the alkyl chain length of ionic liquids from 1-butyl-3-methylimadazolium [bmim]$^+$ to 1-octyl-3-methylimadazolium [omim]$^+$ with PF$_6^-$ anions did not change thermal conductivity. In addition, Ge et al.[24] found that increasing the alkyl chain length of ionic liquids from 1-ethyl-3-methylimadazolium

[emim]$^+$ to 1-decane-3-methylimadazolium [dmim]$^+$ with [NTF$_2$]$^-$ anions also had no measurable effect on the thermal conductivity; however, using an atomistic and vibrational model of liquid thermal conductivity and viscosity developed by Mohanty[25] in 1951, there was a noticeable relationship between the thermal conductivity, κ, and molar mass divided by viscosity, M/η, of ionic liquids. Fröba et al.[21] brought all the above together in their study of [NTF$_2$]$^-$ ionic liquids; they also found that thermal conductivity was relatively independent from the molecular weight of the cation; however, they found that thermal conductivity is directly proportional to an ionic liquid's molar mass times density, $M \times \rho$, much more than Mohanty's equation for liquids, M/η. More recently, there have been new ionic liquid measurements and modeling by López-Bueno et al.[23] that clearly show that ionic liquid thermal conductivity is dependent on the speed of sound in and density of ionic liquids which resembles other models for liquid thermal conductivity by Bridgman[26], Kincaid et al.[27], and our recent work developing a phonon gas model for dense, strongly interacting liquids[28]. There has also been recent discussion of how well different molecular theories can predict ionic liquid thermal conductivity in their pure form, as well as after adding nanoparticles to create IoNanofluids[18].

In **Section 4.2** of this work, we compile and compare all previous thermal conductivity measurements of 1-ethyl-3-methylimidazolium [emim]$^+$ and 1-butyl-3-methylimidazolium [bmim]$^+$ ionic liquids with 4 different anions each: iodide [I]$^-$, tetrafluoroborate [BF$_4$]$^-$, trifluoromethanesulfonate [TFS]$^-$, and bis(trifluoromethylsulfonyl)imide [NTF$_2$]$^-$ (see **Fig. 4.1**). In **Section 4.4**, we show our own frequency-domain hot-wire thermal conductivity measurements of the ionic liquids highlighted in green in **Fig. 4.1** (see **Table 4.1** for supplier details on the ionic liquids used). Then, in **Section 4.5**, we compare our measurements with previous time-domain measurements. Last, in **Section 4.6**, we combine our measurements and

previous data sets to assess the influence of various parameters (molar mass, density, speed of sound, and intermolecular distance) and models (Mohanty[25], Bridgman[26], Fröba et al.[21], and Zhao et al.[28]) to validate the accuracy with which they predict thermal conductivity for ionic liquids.
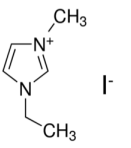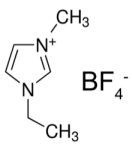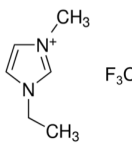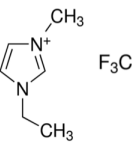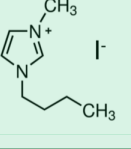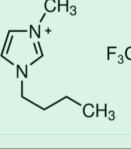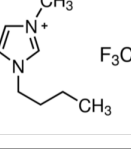
	$[I]^-$ iodide	$[BF_4]^-$ tetrafluoroborate	$[TFS]^-$ trifluoromethanesulfonate	$[NTF_2]^-$ bis(trifluoromethylsulfonyl)imide
[emim]$^+$ 1-ethyl-3-methylimidazolium				
[bmim]$^+$ 1-butyl-3-methylimidazolium				

Figure 4.1. Ionic liquids examined in this work. For ionic liquids highlighted in green, their thermal conductivities were measured with a frequency-domain hot-wire technique described in this work.

Table 4.1. Ionic liquid chemical composition, CAS registry number, mass fraction purity measured by supplier Sigma-Aldrich using HPLC, melting point. molecular weight, and density at 20°C.

Chemical Name	CAS Reg. No.	Purity (Mass Fraction)	Melting Point	Molecular Weight	Density (g/mL)
[bmim]$^+$ [I]$^-$	65039-05-6	0.99	-72°C	266.12	1.46
[bmim]$^+$ [BF$_4$]$^-$	174501-65-6	≥0.98	-71°C	226.02	1.21
[bmim]$^+$ [TFS]$^-$	174899-66-2	0.97	16°C	288.29	1.29

4.2 Background on previous ionic liquid measurements

Previous thermal conductivity measurements of 1-ethyl-3-methylimidazolium [emim]$^+$ and 1-butyl-3-methylimidazolium [bmim]$^+$ ionic liquids utilized various steady-state and time-domain measurements. [emim]$^+$ [I]$^-$ has never been measured before, most likely because it is solid at room temperature; [emim]$^+$ [BF$_4$]$^-$ was previously measured by Van Valkenburg et al.[19] with a time-domain hot-wire method; [emim]$^+$ [TFS]$^-$ was previously measured by Tenney et al.[29] with a steady-state parallel plate method; [emim]$^+$ [NTF$_2$]$^-$ was previously measured by Ge et al.[24] with a time-domain hot-wire method and Fröba et al.[21] with a steady-state parallel plate method. [bmim]$^+$ [I]$^-$ has never been measured before, but it is liquid at room temperature; [bmim]$^+$ [BF$_4$]$^-$ was previously measured by Van Valkenburg et al.[19], Tomida et al.[20], and Jorjani et al.[17] each with time-domain hot-wire methods; [bmim]$^+$ [TFS]$^-$ was previously measured by Ge et al.[24] and de Castro et al.[16], both with time-domain hot-wire methods; [bmim]$^+$ [NTF$_2$]$^-$ was previously measured by Ge et al.[24] and Chen et al.[30], both with time-domain hot-wire methods.

Previous measurements of [emim]$^+$ ionic liquids (shown in **Figure 4.2 a**) and of [bmim]$^+$ ionic liquids (shown in **Figure 4.2 b**) support the hypothesis that smaller, lighter anions have higher thermal conductivity. This is also the case in solid-state heat conduction, where lighter elements conduct heat faster than heavier elements. But this trend does not hold for all ionic liquids, as shown in previous measurements of [NTF$_2$]$^-$ ionic liquids with varying cations by Ge et al.[24] and Fröba et al.[21] In this work, we reexamine this trend and various other thermal conductivity models by comparing previous experiments with our own measurements of 3 [bmim]$^+$ ionic liquids.
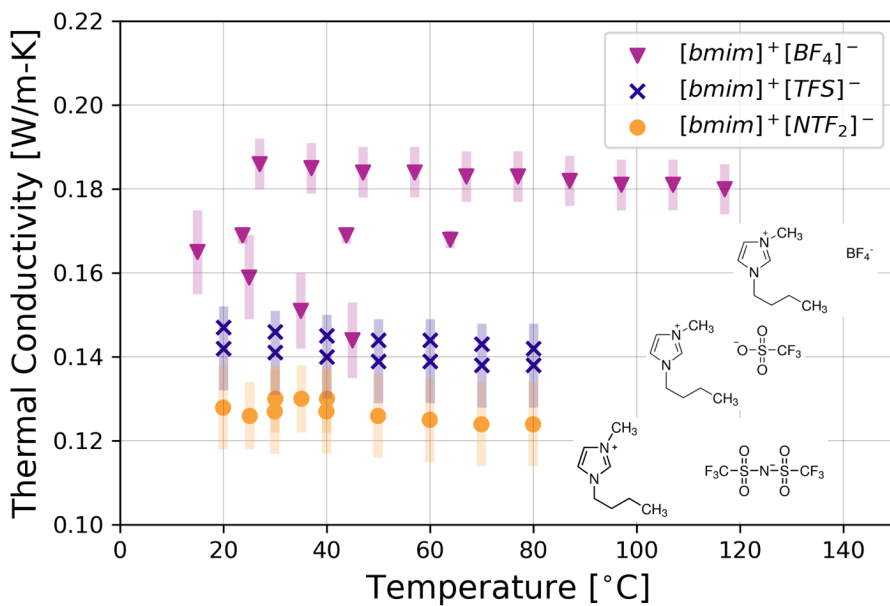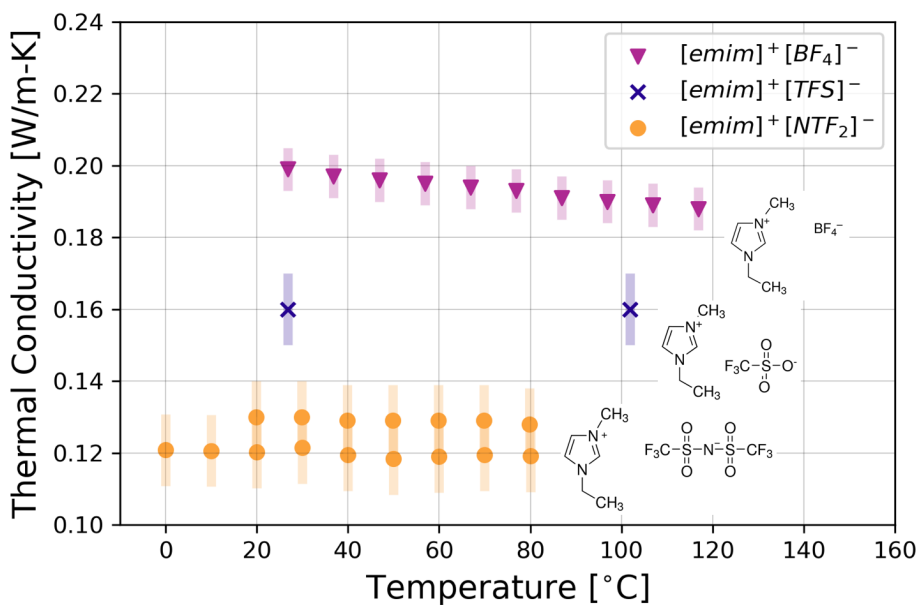
Figure 4.2 a) Previous measurements of [emim]⁺ (1-ethyl-3-methylimidazolium) ionic liquids with 3 different anions: BF₄ (tetrafluorborate)[19], TFS (trifluoromethanesulfonate)[29], and NTF₂ (bis(trifluoromethylsulfonyl)imide)[21,24]. **b)** Previous measurements of [bmim]⁺ (1-butyl-3-methylimidazolium) ionic liquids with 3 different anions: BF₄ (tetrafluorborate)[17,19,20], TFS (trifluoromethanesulfonate)[16], and NTF₂ (bis(trifluoromethylsulfonyl)imide)[24,30]. Shows that smaller, lighter anions have higher thermal conductivity.

4.3 Frequency-domain measurement setup for ionic liquids

In **Chapter 3**, we previously discussed how the 3ω hot-wire technique was used to accurately measure high temperature liquids – the full details of the experimental setup, microfabricated sensor, and protective coating are shown in my previous work – Wingert *et al.*[32] and Zhao *et al.*[33]. Here, we provide an schematic of the setup for 3-omega measurements for ionic liquids in **Figure 4.3**. We also restate the three main advantages of operating in the frequency domain for high temperature liquid measurements: (1) minimizing convection by keeping the probed sample volume below 1μL, (2) using a wide range of input frequencies for $I_{1\omega}$ from 1-1000 Hz, without arbitrary data truncation, to measure thermal conductivity, and (3) rejecting ambient temperature fluctuations from the environment and external heat sources by locking into the 2nd harmonic thermal response ($T_{2\omega}$) of the ionic liquid sample.
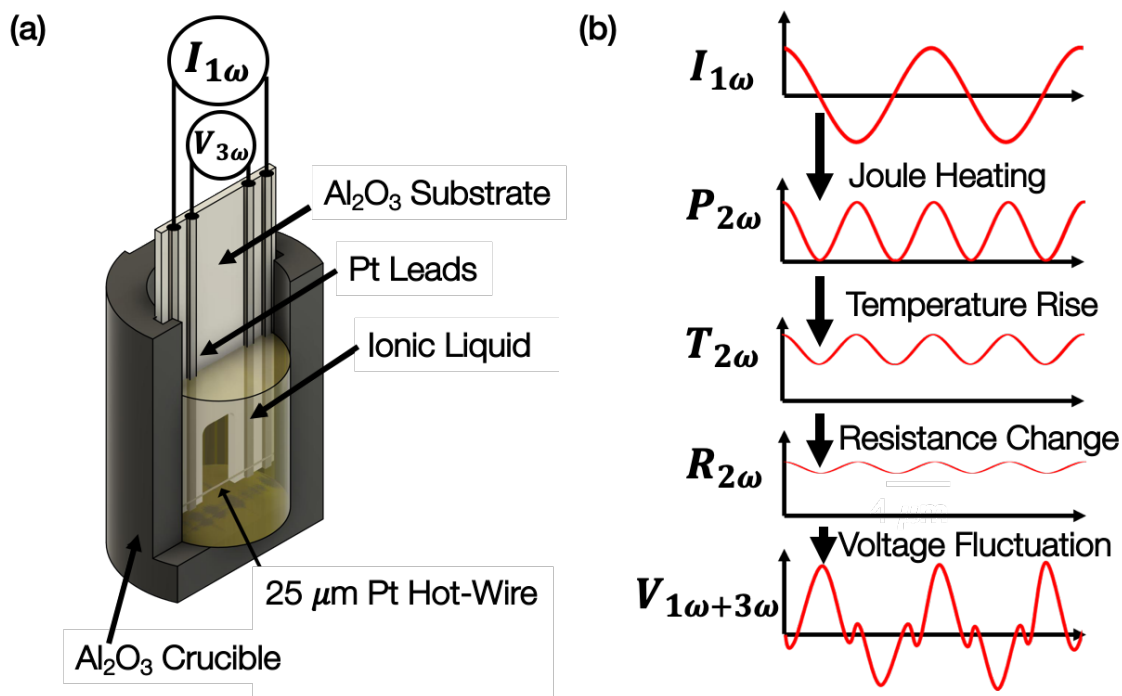
Figure 4.3. a. Schematic of Al_2O_3 sample holder cut out to show the hot-wire immersed in the ionic liquid sample. **b.** Diagram of a 3-omega measurement, and how an AC current through a hot-wire leads to a voltage fluctuation at 3 times the frequency (3-omega) of the input current.

Before our recent development of the 3-dimensional, finite-length, multilayer thermal model for frequency-domain hot-wire sensors, previous frequency-domain liquid thermal conductivity measurements used an infinite wire assumption to simplify the thermal model; however, that assumption can lead to significant error in the frequency-domain measured thermal conductivity, discussed in detail by Wingert *et al.*[32] The finite length model is critical for accurate measurement of liquids using short ~5 mm hot-wires that also minimize convection and temperature gradients in the sample. We validated our frequency-domain hot-wire technique by measuring the thermal conductivity of water, methanol, ethanol, silicone oil, and argon – all agreed with reference values at ambient temperature and pressure[32]. However, our frequency-domain measurements differed from previous steady-state and time-domain measurements in molten sulfur and molten nitrate salts above ~200°C, which we hypothesize to be due to sources of error inherent in steady-state and time-domain measurement techniques. Since ionic liquid measurements are mostly used below 200°C, our frequency-domain measurements match well with most transient hot-wire measurements, which we will show in **Section 4.5.**

4.4 Measurement details and error analysis

To measure the thermal conductivity of ionic liquids, we apply an AC current (I_ω) to our sensor and measure the ionic liquid's temperature response at 20 logarithmically spaced frequency points ranging from 1000 Hz to 1 Hz. Measuring the temperature response across the full frequency range, takes roughly 80 minutes. We then raise the temperature of the furnace by ~20 K, wait 30 minutes for the temperature to stabilize, and conduct another frequency-domain measurement. We continue to repeat this heating and measurement process until the

thermal conductivity at the highest useful temperature for the ionic liquid is measured. To ensure the reliability of our measurements, for each ionic liquid ($[bmim]^+$ $[I]^-$, $[bmim]^+$ $[BF_4]^-$, and $[bmim]^+$ $[TFS]^-$), we conduct multiple temperature dependent measurements with a new sensor, fresh unused ionic liquid from the manufacturer, and an uncontaminated Al_2O_3 crucible for each temperature sweep.

Fig. 4.4 shows the measured ΔT vs. *frequency* for $[bmim]^+$ $[I]^-$, $[bmim]^+$ $[BF_4]^-$, and $[bmim]^+$ $[TFS]^-$, each at 3 different temperatures (room temperature, the median temperature measured, and the highest temperature measured). The experimental in-phase temperature rise at each frequency is positive and marked with an ×. The out-of-phase temperature response of the hot-wire is negative and marked with a circle. The thermal conductivity of the surrounding ionic liquid is the only free parameter of **Eq. 4.2** and is used to perform a least-squares fit for both the in-phase and out-of-phase temperature data. The thermal model using the extracted thermal conductivity is plotted as a solid line (in-phase) and dotted line (out-of-phase), and they show good agreement with experimental measurements.

We use a Monte Carlo method to fit our thermal model (**Eq. 3.2**) to the measured frequency-dependent temperature rise (as in **Fig. 4.4**) to find the measured thermal conductivity and standard uncertainty. The parameters for the platinum wire, coating, and ionic liquid are randomly sampled from their Gaussian distributions (using their average values and standard uncertainties from literature and our own measurements), then input into a least-squares regression of ΔT (**Eq. 3.2**) for varying thermal conductivity, κ_2, of the ionic liquid. To find the average thermal conductivity and standard deviation (the reported standard uncertainty) at each temperature, we run the Monte Carlo simulation 200 times for each frequency-domain measurement. The Monte Carlo method is used to account for the standard uncertainties in the

parameters used in the thermal model (**Eq. 3.2**), specifically: the wire diameter ($2r_0$) length of the wire (L), coating thickness (d), coating density (ρ_1), heat capacity (C_1), salt density ρ_2, and salt heat capacity (C_2).
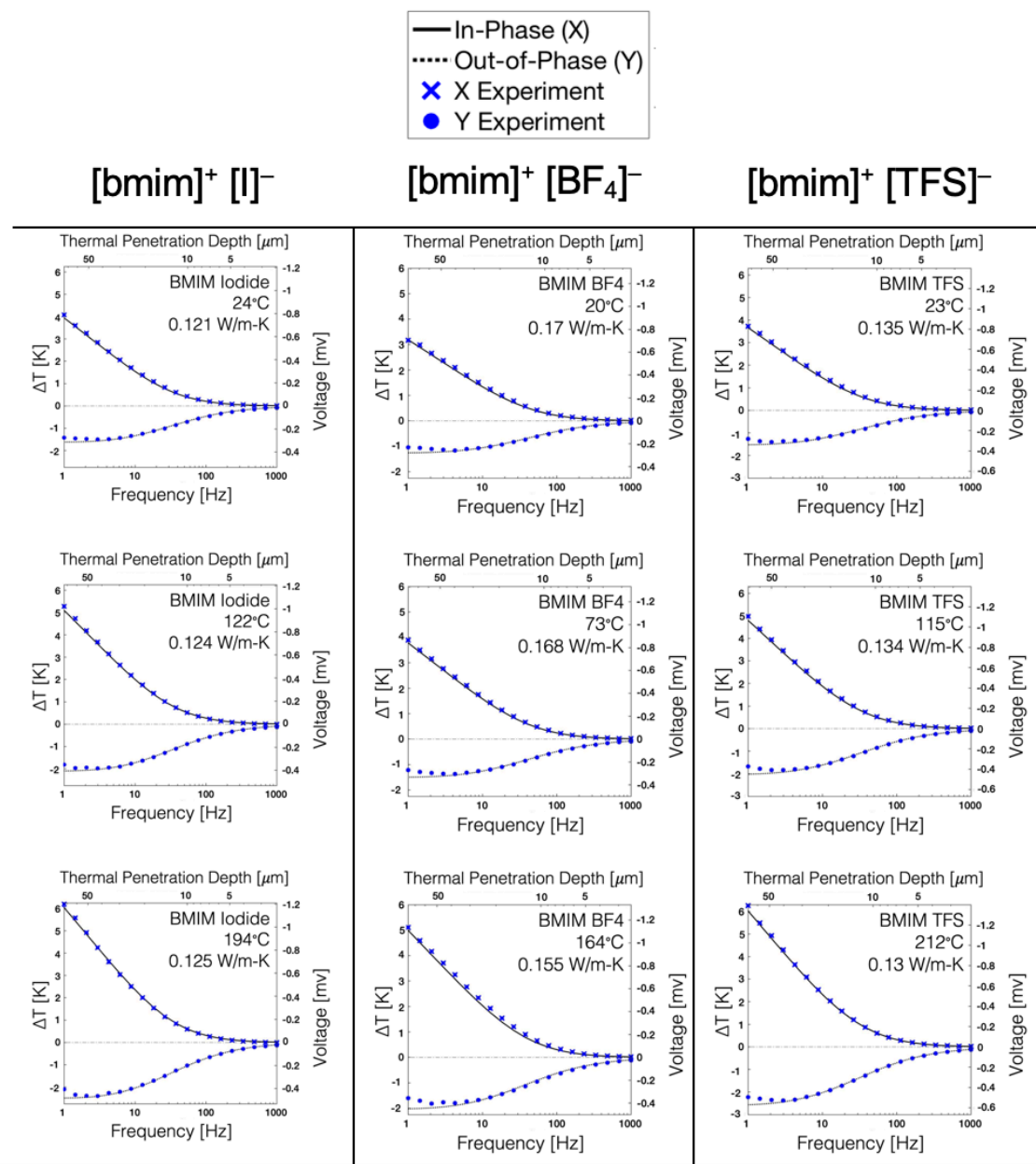
Figure 4.4. Frequency-domain measurements of [bmim]$^+$ [I]$^-$, [bmim]$^+$ [BF$_4$]$^-$, and [bmim]$^+$ [TFS]$^-$.

4.5 Comparing 3-omega hot-wire measurements with previous measurements

Here, we report the first thermal conductivity measurement of [bmim]$^+$ [I]$^-$, shown in **Fig. 4.5** and reported in **Table 4.2**. The line of best fit of the measured thermal conductivity at varying temperature (T in Celsius) is given by the following equation:

$$\kappa = 0.124 + 5.711 \times 10^{-6}(\text{T}) \; [Wm^{-1}K^{-1}] \tag{4.1}$$

Figure 4.5. Temperature dependent thermal conductivity of [bmim]$^+$ [I]$^-$ measured with frequency-domain hot-wire, shown as circles with the line of best fit (**Eq. 4.1**) and 1σ standard uncertainty. This is the first thermal conductivity measurement of [bmim]$^+$ [I]$^-$.

Table 4.2. [bmim]$^+$ [I]$^-$ liquid thermal conductivity and standard uncertainty measured in argon environment at 0.142 ± 0.007 MPa. Uncertainty in temperature is ± 2 K from fluctuating furnace temperature. Horizontal line signifies an independent measurement with a new sensor, alumina crucible, and replenished ionic liquid.

Temperature [°C]	Thermal Conductivity [Wm^{-1}K^{-1}]	Standard Uncertainty [Wm^{-1}K^{-1}]
25	0.124	0.0049
49	0.127	0.0048
79	0.126	0.0051
81	0.126	0.0051
88	0.127	0.0047
99	0.128	0.0046
25	0.125	0.0051
39	0.125	0.005
60	0.126	0.0049
73	0.125	0.005
89	0.127	0.0049
108	0.127	0.0048
23	0.1202	0.0034
24	0.1214	0.0034
75	0.1234	0.0034
122	0.1239	0.0035
146	0.1228	0.0038
168	0.1231	0.0034
194	0.1246	0.0033

Next, we report the measurement of [bmim]$^+$[BF$_4$]$^-$ thermal conductivity, shown in **Fig. 4.6** with all previous measurements, and reported in **Table 4.3**. The line of best fit of the measured thermal conductivity at varying temperature (T in Celsius) is given by the following equation:

$$\kappa = 0.170 - 6.722 \times 10^{-5}(\mathrm{T}) \ [Wm^{-1}K^{-1}] \qquad (4.2)$$

Figure 4.6. Thermal conductivity of [bmim]$^+$[BF$_4$]$^-$ measured with frequency-domain hot-wire, shown as purple circles with the line of best fit (**Eq. 4.2**) and 1σ standard uncertainty, compared with previous time-domain (Van Valkenburg et al.[19], Tomida et al.[20], and Jorjani et al.[17] all with time-domain hot-wire methods.)

Table 4.3. [bmim]$^+$ [BF$_4$]$^-$ liquid thermal conductivity and standard uncertainty measured in argon environment at 0.142 ± 0.007 MPa. Uncertainty in temperature is ± 2 K from fluctuating furnace temperature. Horizontal line signifies an independent measurement with a new sensor, alumina crucible, and replenished ionic liquid.

Temperature [°C]	Thermal Conductivity [Wm^{-1}K^{-1}]	Standard Uncertainty [Wm^{-1}K^{-1}]
20	0.17	0.0047
24	0.165	0.0047
73	0.168	0.0043
116	0.165	0.0045
164	0.155	0.0048
23	0.167	0.005
51	0.166	0.0044
72	0.168	0.0049
96	0.167	0.0044
123	0.164	0.0045
146	0.159	0.0045

Last, we report our frequency-domain hot-wire measurement of [bmim]$^+$[TFS]$^-$ thermal conductivity, shown in **Fig. 4.7** along with previous measurements, and reported in **Table 4.4**. The line of best fit of the measured thermal conductivity at varying temperature (T in Celsius) is given by the following equation:

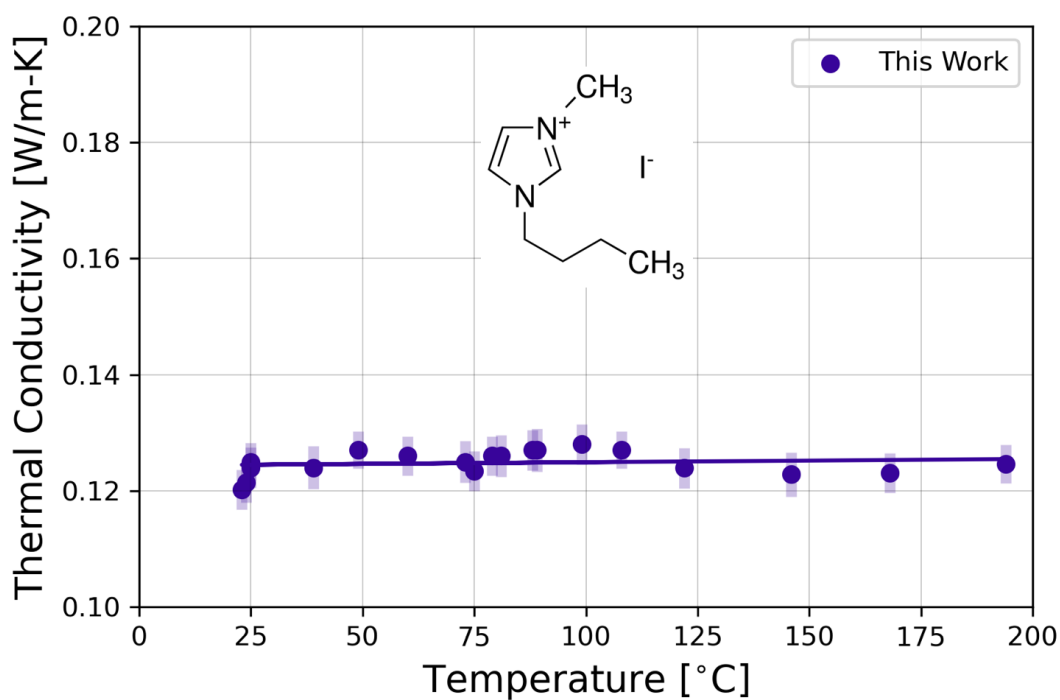$$\kappa = 0.141 - 4.269 \times 10^{-5}(T) \ [Wm^{-1}K^{-1}] \qquad (4.3)$$

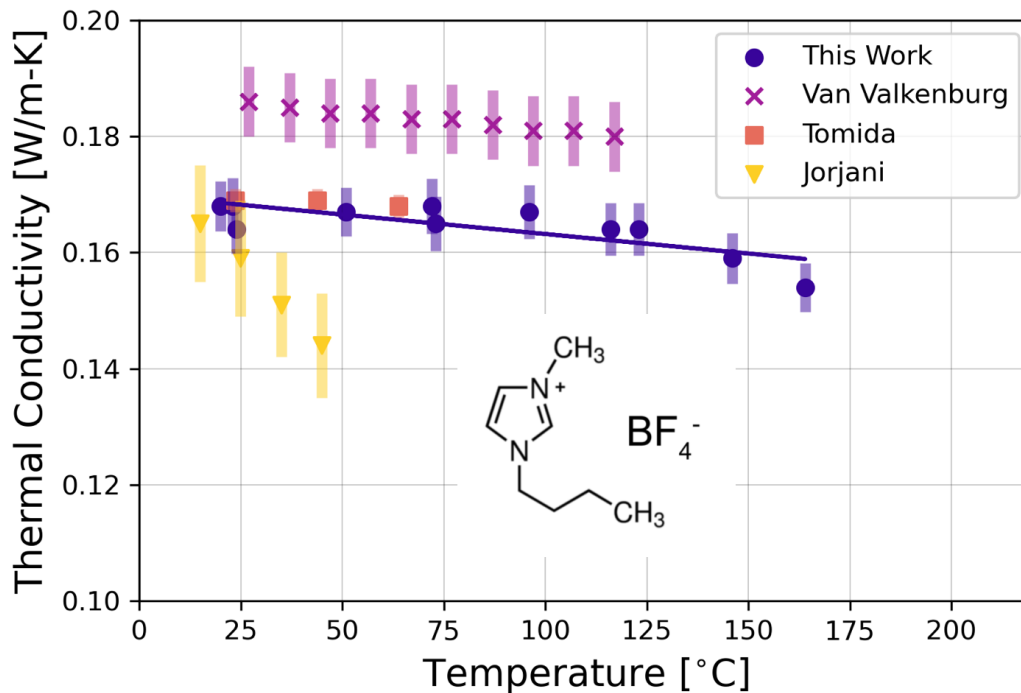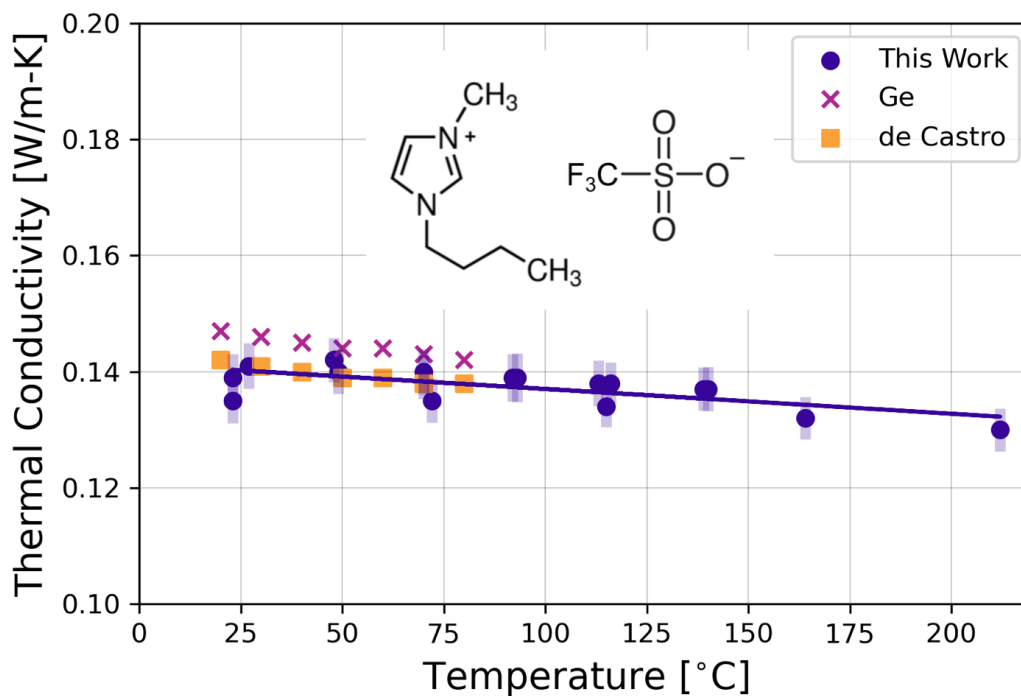**Figure 4.7.** Thermal conductivity of [bmim]$^+$[TFS]$^-$ measured with frequency-domain hot-wire, shown as purple circles with the line of best fit (**Eq. 4.3**) and 1σ standard uncertainty, compared with previous time-domain (Ge et al.[24] and de Castro et al.[16], both with time-domain hot-wire methods).

Table 4.4. [bmim]⁺ [TFS]⁻ liquid thermal conductivity and standard uncertainty measured in argon environment at 0.142 ± 0.007 MPa. Uncertainty in temperature is ± 2 K from fluctuating furnace temperature. Horizontal line signifies an independent measurement with a new sensor, alumina crucible, and replenished ionic liquid.

Temperature [°C]	Thermal Conductivity [Wm⁻¹K⁻¹]	Standard Uncertainty [Wm⁻¹K⁻¹]
23	0.135	0.0052
72	0.135	0.0052
115	0.134	0.005
164	0.132	0.0046
212	0.13	0.0035
23	0.139	0.0042
48	0.143	0.0049
70	0.14	0.0045
93	0.139	0.0047
113	0.138	0.005
140	0.138	0.0046
27	0.14	0.0044
49	0.14	0.0049
70	0.14	0.0043
92	0.14	0.0043
116	0.139	0.0053
139	0.137	0.005

Our temperature dependent thermal conductivity measurements of 3 [bmim]$^+$ ionic liquids are shown together in **Figure 4.8**. Together, they disprove the hypothesis that a heavier ionic liquid should have a lower thermal conductivity than a lighter ionic liquid; we measured the heavier [bmim]$^+$[TFS]$^-$ (288.29 g/mol) to have a higher thermal conductivity than the lighter [bmim]$^+$[I]$^-$ (266.12 g/mol) from room temperature up to 200°C.
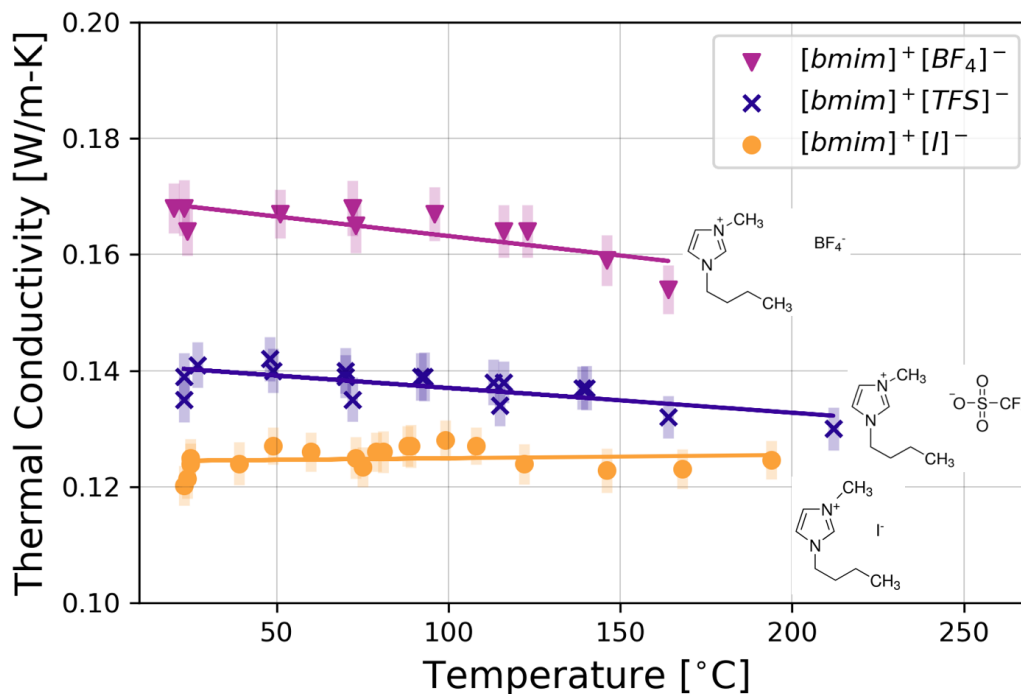
Figure 4.8. Thermal conductivity of [bmim]$^+$[I]$^-$, [BF$_4$], and [TFS]$^-$, measured in the frequency-domain with best fit lines are drawn as solid lines.

4.6 Evaluating the accuracy of liquid thermal conductivity models for ionic liquids

To broaden the scope of our analysis, we combine our thermal conductivity measurements of [bmim]$^+$ ionic liquids with other [emim]$^+$ and [bmim]$^+$ ionic liquids from **Figure 4.1** at 25°C (excluding [emim]$^+$ [I]$^-$ which is solid at 25°C). In **Figure 4.9**, we examine the effect of increasing molar mass, density, speed of sound, and intermolecular distance on 7 ionic liquids. We find that increasing the molar mass and intermolecular distance of ionic liquids generally leads to a decrease in ionic liquid thermal conductivity. The intermolecular distance is approximated using experimental density measurements, $\rho(\frac{kg}{m^3})$, from $d = \left(\frac{1}{\rho}\left[\frac{m^3}{mol}\right] * \frac{1\ mol}{6.022 \times 10^{23}\ molecules}\right)^{1/3} [m]$.

We also show in **Figure 4.9** that a higher density and speed of sound generally leads to a higher thermal conductivity. But there are not consistent trends, and no simple relationship can accurately predict thermal conductivity since there are outliers. Namely, [bmim]$^+$ [I]$^-$ has a lower thermal conductivity than the trends predict, and [NTF$_2$]$^-$ ionic liquids have a constant thermal conductivity (within measurement error) despite changing the cation from [emim]$^+$ to [bmim]$^+$, along with the molar mass, density, speed of sound, and intermolecular distance.

Figure 4.9. Thermal conductivity at 25°C, as a function of molar mass, density, speed of sound, and intermolecular distance.

Table 4.5. Ionic liquid thermophysical properties at 25°C used to create **Figures 4.9 and 4.10.** Values from literature are shown with references in square brackets; NIST ionic liquid database[34,35] used to find values and references.

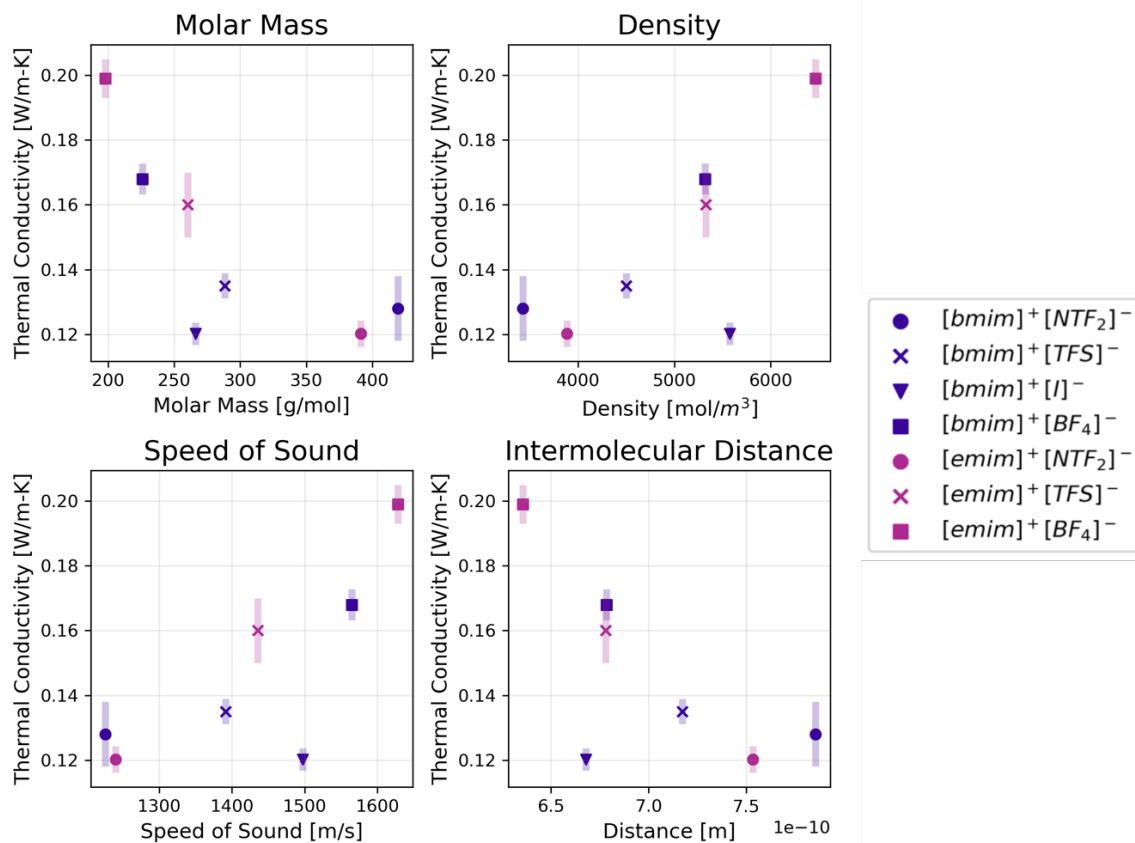|	Molar Mass [g/mol]	Density [kg/m³]	Speed of Sound [m/s]	Heat Capacity C_P [J/mol-K]	Thermal Conductivity [W/m-K]
[bmim]$^+$ [NTF$_2$]$^-$	419.4	1436.8[36]	1226[37]	531[38]	0.128[24]
[bmim]$^+$ [TFS]$^-$	288.29	1297.9[39]	1391[40]	427.7[41]	0.135[this work]
[bmim]$^+$ [I]$^-$	266.12	1483.8[42]	1497.5[43]	309.9[41]	0.120[this work]
[bmim]$^+$ [BF$_4$]$^-$	226.02	1201.8[44]	1564.7[45]	366.7[46]	0.168[this work]
[emim]$^+$ [NTF$_2$]$^-$	391.31	1519.5[47]	1240.3[48]	462[38]	0.120[21]
[emim]$^+$ [TFS]$^-$	260.23	1386.0[49]	1435.8[50]	363.2[51]	0.16[29]
[emim]$^+$ [BF$_4$]$^-$	197.97	1280.5[52]	1628.4[53]	305[54]	0.199[19]

Figure 4.9 suggests there are underlying mechanisms that affect the thermal conductivity of ionic liquids, such as molar mass, density, and speed of sound. Indeed, previous researchers have combined various thermophysical properties together in attempts to better predict liquid thermal conductivity than any single parameter can on its own. Bridgman[26] originally found a simple equation using Boltzmann's constant, speed of sound, and density, which fit closely with his thermal conductivity measurements in 1923, and was expanded upon by Powell et al.[55] In 1951, Mohanty[25] found a relation between liquid thermal conductivity with Boltzmann's constant, viscosity, and molar mass, which was explored in ionic liquids and liquid alkanes by Tomida et al.[20] More recently in 2010, Fröba et al.[21] found an empirical relationship between ionic liquid thermal conductivity with molar mass and density. And in 2021, Zhao et

al.[28] recently used the phonon gas model to calculate the thermal conductivity of dense, strongly interacting liquids. Models used to calculate ionic liquid thermal conductivity in this work are shown in **Table 4.6,** and the calculated values are plotted against experimentally measured values at 25°C in **Figure 4.10**.

Table 4.6. Thermal conductivity model equations used to calculate results in **Figure 4.10.**

Model	Equation
Mohanty[25]	$$\kappa = \frac{3N_A k_B \cdot \eta}{M}$$
Fröba et al.[21]	$$\kappa = \frac{AM + B}{M\rho}$$ $$A = 0.1130 \left[g \cdot cm^{-3} \cdot W \cdot m^{-1} \cdot K^{-1}\right]$$ $$B = 22.65 \left[g^2 \cdot cm^{-3} \cdot W \cdot m^{-1} \cdot K^{-1} \cdot mol^{-1}\right]$$
Bridgman[26] → Powell et al.[55]	$$\kappa = 2k_B v_{sound} n^{2/3} \rightarrow 2.8 k_B v_{sound} n^{2/3}$$
Zhao et al.[28]	$$\kappa = \frac{1}{3} C_{P,volumetric} v_{sound} l = \frac{1}{3} C_P v_{sound} n^{2/3}$$

Figure 4.10 shows that the thermal conductivity model from Mohanty dramatically underestimates the measured thermal conductivity of ionic liquids, and that the Mohanty model should not be used to predict ionic liquid thermal conductivity without fitting parameters and adjustments as described by Tomida et al.[20] The phonon gas model from Zhao et al. calculates the thermal conductivity of ionic liquids to be close to 0.6 W/m-K, significantly higher than the measured ~0.15 W/m-K for ionic liquids; this is similar to how the phonon gas model

significantly overestimates the thermal conductivity of n-alkane chains due to the breakdown of the phonon gas model for long molecular chains that store significant energy in intramolecular vibrations rather than intermolecular vibrational modes, and also since the mean free path approximations break down for longer molecular chains. Bridgman's theory, related to the phonon gas model, and modified by Powell et al.[55], captures the thermal conductivity of ionic liquids relatively well. However, Fröba et al. provide the most accurate model examined in this work; it is an empirically derived equation based on measurements of other ionic liquids, but it has great predictive power for the 7 ionic liquids shown here.
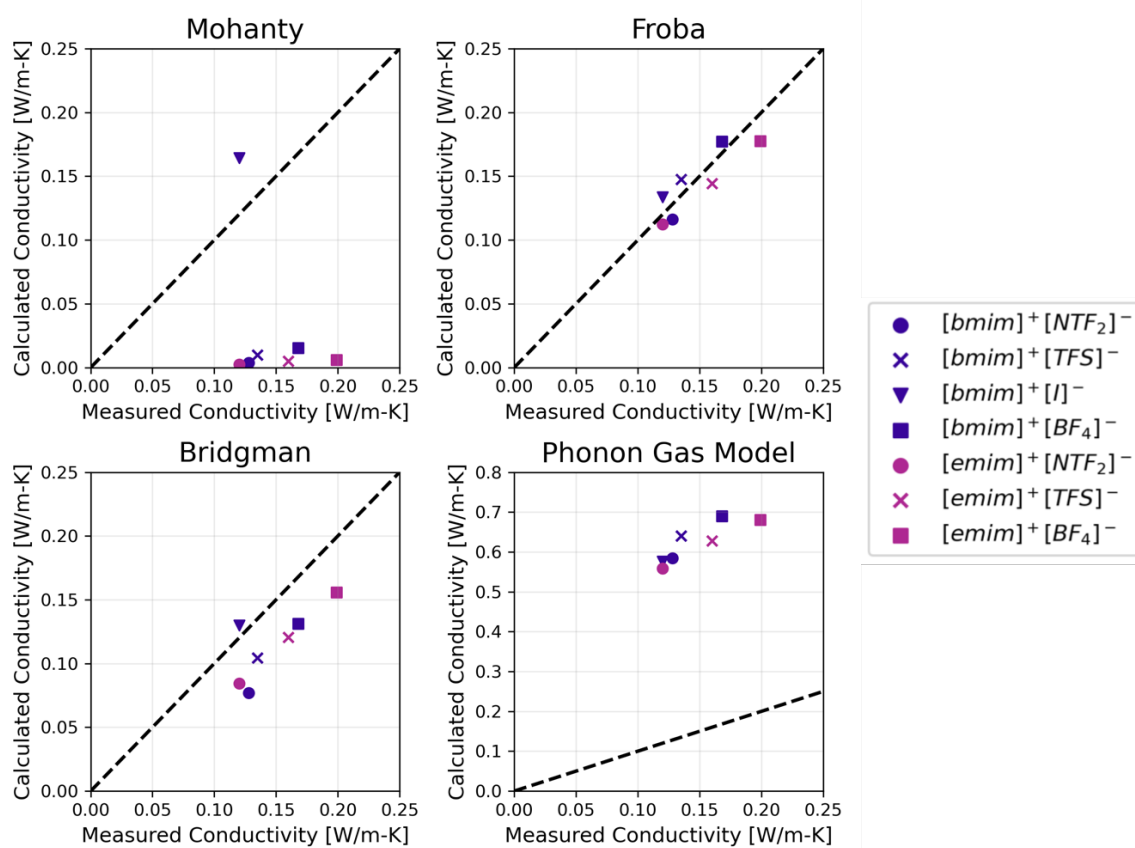

Figure 4.10. Measured thermal conductivity at 25°C compared to various thermal conductivity models.

4.7 Conclusion

There are several models of ionic liquids that aim to describe how fast heat conducts as a function of temperature, which is important for several industrial applications – such as electrochemical metal deposition and battery electrolytes that utilize ionic liquids. However, there is no well-established model for liquid thermal conductivity, let alone for ionic liquids. Furthermore, it is difficult to accurately measure ionic liquid thermal conductivity at high temperatures. In this work we measured 3 [bmim]$^+$ ionic liquids, [bmim]$^+$ [I]$^-$, [bmim]$^+$ [BF$_4$]$^-$, and [bmim]$^+$ [TFS]$^-$, with a recently developed 3-omega hot-wire measurement; our frequency-domain measurement is designed to provide accurate, high temperature liquid thermal conductivity data by reducing error from convection, radiation, and corrosion. Using our measurements, in addition to reliable transient hot-wire measurements of [NTF$_2$]$^-$ and [emim]$^+$ ionic liquids from literature, we evaluated how accurate various models are at predicting ionic liquid thermal conductivity.

We found there are general trends that predict the behavior of ionic liquids examined in this work. Increasing molar mass and intermolecular distance decreases thermal conductivity and increasing the speed of sound and density increases thermal conductivity. But there are exceptions to those general rules; we found [bmim]$^+$ [I]$^-$ thermal conductivity deviates significantly from these trends, and the thermal conductivity of [NTF$_2$]$^-$ with varying cations behave independently from individual physical parameters. Thermal conductivity models that incorporate different parameters, from Bridgman and Fröba et al., accurately capture the behavior of the [emim]$^+$ and [bmim]$^+$ ionic liquids examined in this work. Whereas, the liquid model from Mohanty significantly underestimates ionic liquid thermal conductivity and the phonon gas model significantly overestimates ionic liquid thermal conductivity. This work

167

demonstrates the value of frequency-domain measurements to evaluate thermal conductivity models by eliminating errors inherent to high temperature liquid measurements, as well as showing the need to further develop the liquid phonon gas model for long-chained molecular liquids.

Acknowledgements

Chapter 4 is a reprint of **Zhao, A. Z.,** Wingert, M. C., Levine, G., Obrey, S., & Garay, J. E. Evaluation of [emim]$^+$ and [bmim]$^+$ ionic liquid thermal conductivity models with frequency-domain hot-wire measurements, (*In Preparation*). For this publication, I did the experimental work and wrote the paper.

References

(1)   Seddon, K. R. Ionic Liquids for Clean Technology. *J. Chem. Technol. Biotechnol.* **1997**, *68* (4), 351–356. https://doi.org/10.1002/(SICI)1097-4660(199704)68:4<351::AID-JCTB613>3.0.CO;2-4.

(2)   Armand, M.; Endres, F.; MacFarlane, D. R.; Ohno, H.; Scrosati, B. Ionic-Liquid Materials for the Electrochemical Challenges of the Future. *Nat. Mater.* **2009**, *8*, 621–629. https://doi.org/10.1097/00019616-199307000-00001.

(3)   MacFarlane, D. R.; Tachikawa, N.; Forsyth, M.; Pringle, J. M.; Howlett, P. C.; Elliott, G. D.; Davis, J. H.; Watanabe, M.; Simon, P.; Angell, C. A. Energy Applications of Ionic Liquids. *Energy Environ. Sci.* **2014**, *7* (1), 232–250. https://doi.org/10.1039/C3EE42099J.

(4)   Liu, Q. X.; El Abedin, S. Z.; Endres, F. Electroplating of Mild Steel by Aluminium in a First Generation Ionic Liquid: A Green Alternative to Commercial Al-Plating in Organic Solvents. *Surf. Coatings Technol.* **2006**, *201* (3–4), 1352–1356. https://doi.org/10.1016/j.surfcoat.2006.01.065.

(5)   Abedin, S. Z. El. Coating of Mild Steel by Aluminium in the Ionic Liquid [EMIm]Tf2N and Its Corrosion Performance. *Zeitschrift fur Phys. Chemie* **2006**, *220* (10), 1293–1308. https://doi.org/10.1524/zpch.2006.220.10.1293.

(6)   Caporali, S.; Fossati, A.; Lavacchi, A.; Perissi, I.; Tolstogouzov, A.; Bardi, U. Aluminium Electroplated from Ionic Liquids as Protective Coating against Steel Corrosion. *Corros. Sci.* **2008**, *50* (2), 534–539. https://doi.org/10.1016/j.corsci.2007.08.001.

(7)   Lin, M. C.; Gong, M.; Lu, B.; Wu, Y.; Wang, D. Y.; Guan, M.; Angell, M.; Chen, C.; Yang, J.; Hwang, B. J.; Dai, H. An Ultrafast Rechargeable Aluminium-Ion Battery. *Nature* **2015**, *520* (7547), 325–328. https://doi.org/10.1038/nature14340.

(8)   Sun, H.; Zhu, G.; Xu, X.; Liao, M.; Li, Y. Y.; Angell, M.; Gu, M.; Zhu, Y.; Hung, W. H.; Li, J.; Kuang, Y.; Meng, Y.; Lin, M. C.; Peng, H.; Dai, H. A Safe and Non-Flammable Sodium Metal Battery Based on an Ionic Liquid Electrolyte. *Nat. Commun.* **2019**, *10* (1), 1–11. https://doi.org/10.1038/s41467-019-11102-2.

(9)   Sun, H.; Zhu, G.; Zhu, Y.; Lin, M.; Chen, H.; Li, Y.; Hung, W. H.; Zhou, B.; Wang, X.; Bai, Y.; Gu, M.; Huang, C.; Tai, H.; Xu, X.; Angell, M.; Shyue, J.; Dai, H. High‐Safety and High‐Energy‐Density Lithium Metal Batteries in a Novel Ionic‐Liquid Electrolyte. *Adv. Mater.* **2020**, *32* (26), 2001741. https://doi.org/10.1002/adma.202001741.

(10)   De Souza, R. F.; Padilha, J. C.; Gonçalves, R. S.; Dupont, J. Room Temperature Dialkylimidazolium Ionic Liquid-Based Fuel Cells. *Electrochem. commun.* **2003**, *5* (8), 728–731. https://doi.org/10.1016/S1388-2481(03)00173-5.

(11)   Nakamoto, H.; Watanabe, M. Brønsted Acid-Base Ionic Liquids for Fuel Cell Electrolytes. *Chem. Commun.* **2007**, No. 24, 2539–2541. https://doi.org/10.1039/b618953a.

(12)   Díaz, M.; Ortiz, A.; Ortiz, I. Progress in the Use of Ionic Liquids as Electrolyte Membranes in Fuel Cells. *Journal of Membrane Science*. Elsevier November 1, 2014, pp 379–396. https://doi.org/10.1016/j.memsci.2014.06.033.

(13)   Lu, W.; Fadeev, A. G.; Qi, B.; Smela, E.; Mattes, B. R.; Ding, J.; Spinks, G. M.; Mazurkiewicz, J.; Zhou, D.; Wallace, G. G.; MacFarlane, D. R.; Forsyth, S. A.; Forsyth, M. Use of Ionic Liquids for π-Conjugated Polymer Electrochemical Devices. *Science (80-.)*. **2002**, *297* (5583), 983–987. https://doi.org/10.1126/science.1072651.

(14)   Ding, J.; Zhou, D.; Spinks, G.; Wallace, G.; Forsyth, S.; Forsyth, M.; MacFarlane, D. Use of Ionic Liquids as Electrolytes in Electromechanical Actuator Systems Based on Inherently Conducting Polymers. *Chem. Mater.* **2003**, *15* (12), 2392–2398. https://doi.org/10.1021/cm020918k.

(15)   Almomani, A.; Hong, W.; Hong, W.; Montazami, R. Influence of Temperature on the Electromechanical Properties of Ionic Liquid-Doped Ionic Polymer-Metal Composite Actuators. *Polymers (Basel)*. **2017**, *9* (12), 358. https://doi.org/10.3390/polym9080358.

(16)   Nieto De Castro, C. A.; Lourenço, M. J. V; Ribeiro, A. P. C.; Langa, E.; Vieira, S. I. C.; Goodrich, P.; Hardacre, C. Thermal Properties of Ionic Liquids and IoNanofluids of

Imidazolium and Pyrrolidinium Liquids. *J. Chem. Eng. Data* **2010**, *55* (2), 653–661. https://doi.org/10.1021/je900648p.

(17) Jorjani, S.; Mozaffarian, M.; Pazuki, G. A Novel Nanodiamond Based IoNanofluid: Experimental and Mathematical Study of Thermal Properties. *J. Mol. Liq.* **2018**, *271*, 211–219. https://doi.org/10.1016/j.molliq.2018.08.116.

(18) Paredes, X.; Lourenço, M.; Nieto de Castro, C.; Wakeham, W. Thermal Conductivity of Ionic Liquids and IoNanofluids. Can Molecular Theory Help? *Fluids* **2021**, *6* (3), 116. https://doi.org/10.3390/fluids6030116.

(19) Valkenburg, M. E. V.; Vaughn, R. L.; Williams, M.; Wilkes, J. S. Thermochemistry of Ionic Liquid Heat-Transfer Fluids. In *Thermochimica Acta*; Elsevier, 2005; Vol. 425, pp 181–188. https://doi.org/10.1016/j.tca.2004.11.013.

(20) Tomida, D.; Kenmochi, S.; Tsukada, T.; Qiao, K.; Yokoyama, C. Thermal Conductivities of [Bmim][PF6], [Hmim][PF6], and [Omim][PF6] from 294 to 335 K at Pressures up to 20 MPa. *Int. J. Thermophys.* **2007**, *28* (4), 1147–1160. https://doi.org/10.1007/s10765-007-0241-8.

(21) Fröba, A. P.; Rausch, M. H.; Krzeminski, K.; Assenbaum, D.; Wasserscheid, P.; Leipertz, A. Thermal Conductivity of Ionic Liquids: Measurement and Prediction. *Int. J. Thermophys.* **2010**, *31* (11–12), 2059–2077. https://doi.org/10.1007/s10765-010-0889-3.

(22) Liu, H.; Maginn, E.; Visser, A. E.; Bridges, N. J.; Fox, E. B. Thermal and Transport Properties of Six Ionic Liquids: An Experimental and Molecular Dynamics Study. **2012**. https://doi.org/10.1021/ie300222a.

(23) López-Bueno, C.; Bugallo, D.; Leborán, V.; Rivadulla, F. Sub-ML Measurements of the Thermal Conductivity and Heat Capacity of Liquids. *Phys. Chem. Chem. Phys.* **2018**, *20* (10), 7277–7281. https://doi.org/10.1039/c8cp00165k.

(24) Ge, R.; Hardacre, C.; Nancarrow, P.; Rooney, D. W. Thermal Conductivities of Ionic Liquids over the Temperature Range from 293 K to 353 K. **2007**. https://doi.org/10.1021/je700176d.

(25) Mohanty, S. R. A Relationship between Heat Conductivity and Viscosity of Liquids. *Nature* **1951**, *168* (42), 1951.

(26) Bridgman, P. W. The Thermal Conductivity of Liquids under Pressure. *Proc. Am. Acad. Arts Sci.* **1923**, *59* (7), 141–169.

(27) Kincaid, J. F.; Eyring, H. Free Volumes and Free Angle Ratios of Molecules in Liquids. *Struct. J. Chem. Phys.* **1938**, *6*, 283. https://doi.org/10.1063/1.1750134.

(28) Zhao, A. Z.; Wingert, M. C.; Chen, R.; Garay, J. E. Phonon Gas Model for Thermal Conductivity of Dense, Strongly Interacting Liquids. *J. Appl. Phys.* **2021**, *129* (23), 235101. https://doi.org/10.1063/5.0040734.

(29)   Tenney, C. M.; Massel, M.; Mayes, J. M.; Sen, M.; Brennecke, J. F.; Maginn, E. J. A Computational and Experimental Study of the Heat Transfer Properties of Nine Different Ionic Liquids. *J. Chem. Eng. Data* **2014**, *59* (2), 391–399. https://doi.org/10.1021/je400858t.

(30)   Chen, H.; He, Y.; Zhu, J.; Alias, H.; Ding, Y.; Nancarrow, P.; Hardacre, C.; Rooney, D.; Tan, C. Rheological and Heat Transfer Behaviour of the Ionic Liquid, [C4mim][NTf2]. *Int. J. Heat Fluid Flow* **2008**, *29* (1), 149–155. https://doi.org/10.1016/j.ijheatfluidflow.2007.05.002.

(31)   Cahill, D. G. Thermal Conductivity Measurement from 30 to 750 K: The 3ω Method. *Rev. Sci. Instrum.* **1990**, *61* (2), 802–808. https://doi.org/10.1063/1.1141498.

(32)   Wingert, M. C.; Zhao, A. Z.; Kodera, Y.; Obrey, S. J.; Garay, J. E. Frequency-Domain Hot-Wire Sensor and 3D Model for Thermal Conductivity Measurements of Reactive and Corrosive Materials at High Temperatures. *Rev. Sci. Instrum.* **2020**, *91* (5), 054904. https://doi.org/10.1063/1.5138915.

(33)   Zhao, A. Z.; Wingert, M. C.; Garay, J. E. Frequency-Domain Hot-Wire Measurements of Molten Nitrate Salt Thermal Conductivity. *J. Chem. Eng. Data* **2020**, acs.jced.0c00621. https://doi.org/10.1021/acs.jced.0c00621.

(34)   Kazakov, A.; Magee, J. W.; Chirico, R. D.; Paulechka, E.; Diky, V.; Muzny, C. D.; Kroenlein, K.; Frenkel, M. *NIST Standard Reference Database 147: NIST Ionic Liquids Database - (ILThermo)*; Gaithersburg MD, 20899.

(35)   Dong, Q.; Muzny, C. D.; Kazakov, A.; Diky, V.; Magee, J. W.; Widegren, J. A.; Chirico, R. D.; Marsh, K. N.; Frenkel, M. ILThermo: A Free-Access Web Database for Thermodynamic Properties of Ionic Liquids. *Journal of Chemical and Engineering Data.* American Chemical Society July 2007, pp 1151–1159. https://doi.org/10.1021/je700171f.

(36)   Hamidova, R.; Kul, I.; Safarov, J.; Shahverdiyev, A.; Hassel, E. Thermophysical Properties of 1-Butyl-3-Methylimidazolium Bis(Trifluoromethylsulfonyl)Imide at High Temperatures and Pressures. *Brazilian J. Chem. Eng.* **2015**, *32* (1), 303–316. https://doi.org/10.1590/0104-6632.20150321s00003120.

(37)   Zorebski, M.; Zorebski, E.; Dzida, M.; Skowronek, J.; Jezak, S.; Goodrich, P.; Jacquemin, J. Ultrasonic Relaxation Study of 1-Alkyl-3-Methylimidazolium-Based Room-Temperature Ionic Liquids: Probing the Role of Alkyl Chain Length in the Cation. *J. Phys. Chem. B* **2016**, *120* (14), 3569–3581. https://doi.org/10.1021/acs.jpcb.5b12635.

(38)   Gómez, E.; Calvar, N.; Domínguez, Á.; MacEdo, E. A. Thermal Analysis and Heat Capacities of 1-Alkyl-3-Methylimidazolium Ionic Liquids with NTf2-, TFO-, and DCA- Anions. *Ind. Eng. Chem. Res.* **2013**, *52* (5), 2103–2110. https://doi.org/10.1021/ie3012193.

(39) Safarov, J.; Guluzade, A.; Hassel, E. Thermophysical Properties of 1-Butyl-3-Methylimidazolium Trifluoromethanesulfonate in a Wide Range of Temperatures and Pressures. *J. Chem. Eng. Data* **2019**, *64* (6), 2247–2258. https://doi.org/10.1021/acs.jced.8b00837.

(40) Seoane, R. G.; Corderí, S.; Gómez, E.; Calvar, N.; González, E. J.; MacEdo, E. A.; Domínguez, Á. Temperature Dependence and Structural Influence on the Thermophysical Properties of Eleven Commercial Ionic Liquids. *Ind. Eng. Chem. Res.* **2012**, *51* (5), 2492–2504. https://doi.org/10.1021/ie2029255.

(41) Paulechka, Y. U. Heat Capacity of Room-Temperature Ionic Liquids: A Critical Review. *J. Phys. Chem. Ref. Data* **2010**, *39* (3), 033108. https://doi.org/10.1063/1.3463478.

(42) Součková, M.; Klomfar, J.; Pátek, J. Surface Tension and 0.1 MPa Density Data for 1-C n-3-Methylimidazolium Iodides with n = 3, 4, and 6, Validated Using a Parachor and Group Contribution Model. *J. Chem. Thermodyn.* **2015**, *83*, 52–60. https://doi.org/10.1016/j.jct.2014.11.016.

(43) Teodorescu, M. Isothermal (Vapour + Liquid) Equilibrium and Thermophysical Properties for (1-Butyl-3-Methylimidazolium Iodide + 1-Butanol) Binary System. *J. Chem. Thermodyn.* **2015**, *87*, 58–64. https://doi.org/10.1016/j.jct.2015.03.023.

(44) Součková, M.; Klomfar, J.; Pátek, J. Surface Tension and 0.1 MPa Density of 1-Alkyl-3-Methylimidazolium Tetrafluoroborates in a Homologous Series Perspective. *J. Chem. Thermodyn.* **2016**, *100*, 79–88. https://doi.org/10.1016/j.jct.2016.04.008.

(45) Ebrahiminejadhasanabadi, M.; Nelson, W. M.; Naidoo, P.; Mohammadi, A. H.; Ramjugernath, D. Experimental Measurement of Carbon Dioxide Solubility in 1-Methylpyrrolidin-2-One (NMP) + 1-Butyl-3-Methyl-1H-Imidazol-3-Ium Tetrafluoroborate ([Bmim][BF4]) Mixtures Using a New Static-Synthetic Cell. *Fluid Phase Equilib.* **2018**, *477*, 62–77. https://doi.org/10.1016/j.fluid.2018.08.017.

(46) Paulechka, Y. U.; Blokhin, A. V.; Kabo, G. J. Evaluation of Thermodynamic Properties for Non-Crystallizable Ionic Liquids. *Thermochim. Acta* **2015**, *604*, 122–128. https://doi.org/10.1016/j.tca.2015.01.022.

(47) Součková, M.; Klomfar, J.; Pátek, J. Measurements and Group Contribution Analysis of 0.1 MPa Densities for Still Poorly Studied Ionic Liquids with the [PF6] and [NTf2] Anions. *J. Chem. Thermodyn.* **2014**, *77*, 31–39. https://doi.org/10.1016/j.jct.2014.04.017.

(48) Bansal, S.; Kaur, N.; Chaudhary, G. R.; Mehta, S. K.; Ahluwalia, A. S. Physiochemical Properties of New Formulations of 1-Ethyl-3-Methylimidazolium Bis(Trifluoromethylsulfonyl)Imide with Tritons. *J. Chem. Eng. Data* **2014**, *59* (12), 3988–3999. https://doi.org/10.1021/je500502a.

(49) Harris, K. R.; Kanakubo, M. Self-Diffusion Coefficients and Related Transport

Properties for a Number of Fragile Ionic Liquids. *J. Chem. Eng. Data* **2016**, *61* (7), 2399–2411. https://doi.org/10.1021/acs.jced.6b00021.

(50) Srinivasa Reddy, M.; Khan, I.; Raju, K. T. S. S.; Suresh, P.; Hari Babu, B. The Study of Molecular Interactions in 1-Ethyl-3-Methylimidazolium Trifluoromethanesulfonate + 1-Pentanol from Density, Speed of Sound and Refractive Index Measurements. *J. Chem. Thermodyn.* **2016**, *98*, 298–308. https://doi.org/10.1016/j.jct.2016.03.014.

(51) García-Miaja, G.; Troncoso, J.; Romaní, L. Excess Properties for Binary Systems Ionic Liquid + Ethanol: Experimental Results and Theoretical Description Using the ERAS Model. *Fluid Phase Equilib.* **2008**, *274* (1–2), 59–67. https://doi.org/10.1016/j.fluid.2008.09.004.

(52) Seki, S.; Tsuzuki, S.; Hayamizu, K.; Umebayashi, Y.; Serizawa, N.; Takei, K.; Miyashiro, H. Comprehensive Refractive Index Property for Room-Temperature Ionic Liquids. *J. Chem. Eng. Data* **2012**, *57* (8), 2211–2216. https://doi.org/10.1021/je201289w.

(53) Zarei, H.; Keley, V. Density and Speed of Sound of Binary Mixtures of Ionic Liquid 1-Ethyl-3-Methylimidazolium Tetrafluoroborate, N,N-Dimethylformamide, and N,N-Dimethylacetamide at Temperature Range of 293.15-343.15 K: Measurement and PC-SAFT Modeling. *J. Chem. Eng. Data* **2017**, *62* (3), 913–923. https://doi.org/10.1021/acs.jced.6b00496.

(54) Gupta, H.; Malik, S.; Chandrasekhar, M.; Sharma, V. K. Thermodynamic Investigations of Excess Heat Capacities of Ternary Liquid Mixtures Containing [Bmmim][BF4] + [Bmim][BF4] or [Emim][BF4] + Cyclopentanone or Cyclohexanone. *J. Therm. Anal. Calorim.* **2018**, *131* (2), 1653–1669. https://doi.org/10.1007/s10973-017-6587-7.

(55) Powell, R. E.; Roseveare, W. E.; Eyring, H. Diffusion, Thermal Conductivity, and Viscous Flow of Liquids. *Ind. Eng. Chem.* **1941**, *33* (4), 430–435.

Chapter 5: Future directions and applications

High temperature liquids, such as molten salts and molten metals, are central to next generation concentrated solar power and advanced nuclear plants. Their thermal properties will dictate how much heat can be stored in a high temperature system and how fast heat can be extracted to do useful work – designing molten salt and metal systems will require reliable temperature and pressure dependent data for a multitude of potential composition mixtures. In the previous chapters, I presented my work on developing experimental and theoretical methods for probing high temperature liquid thermal conductivity. In this last chapter, I highlight research areas of high temperature liquid thermal conductivity that require further development and discuss potential ways to increase the efficiency and power output of concentrated solar and advanced nuclear technologies.

5.1 Next generation energy applications

The U.S. Department of Energy is running the Concentrating Solar Power Generation 3 program to reduce the levelized cost of electricity below $60/MWh. The key to the reduction in cost for concentrated solar power is higher temperature systems, which have intrinsically higher thermodynamic efficiency to convert heat into electricity. There were three paths explored to storing heat at temperatures above 700°C – compressed gas, liquid, and solid particles. The liquid pathway designed a power plant with a solar absorber operating at ~740°C that uses molten sodium metal to transfer heat to storage tanks filled with molten chlorides that are dispatched to supercritical CO_2 power cycles to provide electricity to the grid[1]. The solid falling particle pathway was ultimately chosen to construct a pilot plant, but the liquid pathway

was paved for private companies to pursue in addition to providing cross-cutting knowledge of molten salt engineering for advanced nuclear reactors.

There have been recent developments in advanced nuclear reactors due to safety concerns and high costs associated with the fleet of standard light water reactors. Water cooling of nuclear fuel rods is essential for the safety of light water reactors, and if the water pumps fail due to a natural disaster like Fukushima, water vapor can build up to dangerous level that can escape containment structures and expel radioactive materials into the environment – a nuclear meltdown. Countries from around the world have been participating in developing Generation IV advanced nuclear reactors, with several different designs using various molten salts and metals being pursued, to replace light water reactors. Molten salt reactors use molten salts as heat transfer fluids that are inherently safer than light water reactors – if the flow of molten salts stops, they can absorb all the heat from fission without vaporizing, eventually solidifying without contaminating the environment[2]. The molten salt reactor using $LiF-BeF_2$ was successfully demonstrated in the 1960's at Oak Ridge National lab, and the history of its development was well documented by Oak Ridge National Lab[3]. Other molten salts have also been studied as potential heat transfer fluids for nuclear reactors – the thermophysical properties of LiF, $LiF-BeF_2$, $LiF-NaF-KF$, $KCl-MgCl_2$, $KF-ZrF_4$, and $NaF-KF-MgF_2$ were well reviewed by Magnusson et al.[4] The use of molten sodium and a molten lead-bismuth eutectic have also been explored for Generation IV nuclear reactors[5].

175

5.2 Outlook for thermal conductivity measurements and modeling of high temperature liquids

Frequency-domain measurement techniques provide an accurate and reliable thermal conductivity data that can assist in the design of future high temperature systems. In **Chapter 3**, I presented evidence for the accuracy and reliability of frequency-domain measurements for molten salts. But more research groups must invest in and build frequency-domain measurement setups to independently test our results and continue to build confidence in a new measurement technique. The barriers to overcome are money and time – infrastructure for steady-state and time-domain techniques already exists and it is expensive to build new measurement setups. It is also faster to buy a commercially available laser flash measurement system to provide a plug and play system that does not require expertise to operate, and laser flash has been shown to work well for molten metals since convection and radiation are negligible compared to electron transport.

Future work is also needed to incorporate the frequency-dependent behavior of vibrational modes in liquids to the phonon gas model. In **Chapter 2**, I showed that a simplified phonon gas model can predict the thermal conductivity for dense and strongly interacting liquids. The simplified gray model assumed all vibrational modes had the same group velocity and mean free path, and the assumptions about mean free path broke down for certain types of molecular liquids, shown in **Chapter 2 and 4**. A complete, frequency-dependent phonon gas model calculation could be capable of predicting the thermal conductivity of any liquid – modal analysis in molecular dynamics could test this hypothesis. In addition, more work is required to explain the thermal conductivity of molten metals – specifically why the Lorenz number varies with temperature, pressure, and composition in molten metals. Electron-phonon interactions

are likely at play, which provides further impetus to examine the frequency-dependent behavior of vibrational modes in liquids.

5.3 Enhancing liquid thermal conductivity with nanoparticles

Adding a small fraction of nanoparticles (~1%) to liquids has been reported to significantly enhance the thermal conductivity of liquids by 40-150%, far beyond any rule-of-mixture predictions. There has been controversy surrounding experimental errors in measuring nanofluid thermal conductivity[6], but that has not stopped a significant amount of work trying to boost the heat transfer coefficient and efficiency of solar energy systems with nanofluids[7]. Due to the difficulty in measuring molten salt thermal conductivity, most work on molten salt based nanofluids have focused on the enhancement of specific heat. 1.0 wt. % of Al_2O_3, SiO_2, and TiO_2 nanoparticles were added to solar salt (60% KNO_3, 40% $NaNO_3$), and the specific heat of the nanofluid was shown to increase by 1% to 22%.[8] Similarly, alkali metal chloride salts were doped with 1 wt. % SiO_2 nanoparticles and the specific heat was increased by 14.5%.[9] There has been work that showed 0.72 vol. % of SiC nanoparticles in Heat Transfer Salt (40 wt% $NaNO_2$, 7 wt% $NaNO_3$, and 53 wt% KNO_3) increased the thermal conductivity by 13%, which was measured by a ceramic coated transient hot-wire method by Ueki et al.[10] Work on lower temperature ionic liquid based nanofluids[11], has shown 0.06 wt. % of graphene can increase the thermal conductivity of the base fluid by 15-26%. There has also been work on modeling nanofluids[12] using the phonon based theory of liquids to examine the interactions between nanoparticles and the base liquid explain nanofluid thermal conductivity. There are interesting results in molten salt based nanofluids, and future work demonstrating their use in

real world applications will be important since the cost of nanoparticles and the practical problems with nanoparticle agglomeration have yet to been overcome.

5.4 Moving high temperature liquids with heat pipes and fluid pumps

If heat conduction is still the limiting factor in a system, it can be boosted by using mass transfer with heat pipes or liquid pumps. Heat pipes passively transfer heat through vapor mass transfer driven by a temperature gradient from an evaporator to a condenser, and the cool liquid wicks back to the evaporator through surface tension. Liquid metal heat pipes have been developed for various applications for over 50 years[13], and the recent use of heat pipes in heat exchangers[14], solar collectors[15], and space applications[16] are reviewed elsewhere. Molten nitrate salts are being mechanically pumped for commercial solar power applications, and further engineering work must be done to ensure the robustness of molten chloride and fluoride pumps for higher temperature systems[1]. A ceramic pump that is capable of moving molten metals at temperatures up to 1,673 Kelvin has also recently been demonstrated[17].

Acknowledgements

References

(1) Turchi, C.; Gage, S.; Martinek, J.; Jape, S.; Armijo, K.; Coventry, J.; Pye, J.; Asselineau, C.; Venn, F.; Logie, W.; Fontalvo, A.; Wang, S.; Mcnaughton, R.; Potter, D.; Steinberg, T.; Will, G.; Turchi, C.; Gage, S.; Martinek, J.; Jape, S.; Armijo, K.; Coventry, J.; Pye, J.; Asselineau, C.; Venn, F.; Logie, W.; Fontalvo, A.; Wang, S.; Mcnaughton, R.; Potter, D.; Steinberg, T.; Will, G. *CSP Gen3 : Liquid-Phase Pathway to SunShot*; Golden, CO, 2021.

(2) Elsheikh, B. M. Safety Assessment of Molten Salt Reactors in Comparison with Light Water Reactors. *https://doi.org/10.1016/j.jrras.2013.10.008* **2013**, *6* (2), 63–70. https://doi.org/10.1016/J.JRRAS.2013.10.008.

(3) Lane, J. A.; MacPherson, H. G.; Maslan, F. *Fluid Fuel Reactors: Molten Salt Reactors, Aqueous Homogeneous Reactors, Fluoride Reactors, Chloride Reactors, Liquid Metal Reactors and Why Liquid Fission*; Addison-Wesley Pub. Co., 1958.

(4) Magnusson, J.; Memmott, M.; Munro, T. Review of Thermophysical Property Methods Applied to Fueled and Un-Fueled Molten Salts. *Ann. Nucl. Energy* **2020**, *146*, 107608. https://doi.org/10.1016/J.ANUCENE.2020.107608.

(5) Abram, T.; Ion, S. Generation-IV Nuclear Power: A Review of the State of the Science. *Energy Policy* **2008**, *36* (12), 4323–4330. https://doi.org/10.1016/J.ENPOL.2008.09.059.

(6) Keblinski, P.; Prasher, R.; Eapen, J. Thermal Conductance of Nanofluids: Is the Controversy Over? *J. Nanoparticle Res.* **2008**, *10* (7), 1089–1097. https://doi.org/10.1007/s11051-007-9352-1.

(7) Elsheikh, A. H.; Sharshir, S. W.; Mostafa, M. E.; Essa, F. A.; Ahmed Ali, M. K. Applications of Nanofluids in Solar Energy: A Review of Recent Advances. *Renew. Sustain. Energy Rev.* **2018**, *82*, 3483–3502. https://doi.org/10.1016/J.RSER.2017.10.108.

(8) Chieruzzi, M.; Cerritelli, G. F.; Miliozzi, A.; Kenny, J. M. *Effect of Nanoparticles on Heat Capacity of Nanofluids Based on Molten Salts as PCM for Thermal Energy Storage*; 2013. https://doi.org/10.1186/1556-276X-8-448.

(9) Shin, D.; Banerjee, D. Enhancement of Specific Heat Capacity of High-Temperature Silica-Nanofluids Synthesized in Alkali Chloride Salt Eutectics for Solar Thermal-Energy Storage Applications. **2011**. https://doi.org/10.1016/j.ijheatmasstransfer.2010.11.017.

(10) Ueki, Y.; Fujita, N.; Kawai, M.; Shibahara, M. Thermal Conductivity of Molten Salt-Based Nanofluid. *AIP Adv.* **2017**, *7* (5). https://doi.org/10.1063/1.4984770.

(11) Wang, W.; Wu, Z.; Li, B.; Sundén, B. A Review on Molten-Salt-Based and Ionic-Liquid-Based Nanofluids for Medium-to-High Temperature Heat Transfer. *J. Therm.*

Anal. Calorim. 2018 1363 **2018**, *136* (3), 1037–1051. https://doi.org/10.1007/S10973-018-7765-Y.

(12)   Iacobazzi, F.; Milanese, M.; Colangelo, G.; Lomascolo, M.; de Risi, A. An Explanation of the Al2O3 Nanofluid Thermal Conductivity Based on the Phonon Theory of Liquid. *Energy* **2016**, *116*, 786–794. https://doi.org/10.1016/j.energy.2016.10.027.

(13)   Reid, R. S.; Merrigan, M. A.; Sena, J. T. Review of Liquid Metal Heat Pipe Work at Los Alamos. *AIP Conf. Proc.* **1991**, *217* (3), 999–1008. https://doi.org/10.1063/1.40058.

(14)   Srimuang, W.; Amatachaya, P. A Review of the Applications of Heat Pipe Heat Exchangers for Heat Recovery. *Renew. Sustain. Energy Rev.* **2012**, *16* (6), 4303–4315. https://doi.org/10.1016/J.RSER.2012.03.030.

(15)   Shafieian, A.; Khiadani, M.; Nosrati, A. A Review of Latest Developments, Progress, and Applications of Heat Pipe Solar Collectors. *Renew. Sustain. Energy Rev.* **2018**, *95*, 273–304. https://doi.org/10.1016/J.RSER.2018.07.014.

(16)   El-Genk, M. S.; Tournier, J.-M. P. USES OF LIQUID-METAL AND WATER HEAT PIPES IN SPACE REACTOR POWER SYSTEMS. *Front. Heat Pipes* **2011**, *2* (1). https://doi.org/10.5098/FHP.V2.1.3002.

(17)   Amy, C.; Budenstein, D.; Bagepalli, M.; England, D.; DeAngelis, F.; Wilk, G.; Jarrett, C.; Kelsall, C.; Hirschey, J.; Wen, H.; Chavan, A.; Gilleland, B.; Yuan, C.; Chueh, W. C.; Sandhage, K. H.; Kawajiri, Y.; Henry, A. Pumping Liquid Metal at High Temperatures up to 1,673 Kelvin. *Nature* **2017**, *550* (7675), 199–203. https://doi.org/10.1038/nature24054.